Stochastic Modeling and Optimal Control for Colloidal Organization, Navigation, and Machines

by
Yuguang Yang

A dissertation submitted to Johns Hopkins University in conformity with
the requirements for the degree of Doctor of Philosophy

Baltimore, Maryland
Feb 2017

© 2017 Yuguang Yang
All Rights Reserved

ABSTRACT

Colloidal suspensions consisting of particles undergoing Brownian motion are ubiquitous in scientific research and emerging technologies. Longstanding challenges in strategic control of complex colloidal systems are to investigate the principle of optimal control, overcome the curse of dimensionality, design efficient algorithms, and develop generalizable control strategies. In the first part of this dissertation, we present methods and results from three case studies to illustrate how these challenges are addressed from the perspectives of modeling and optimal control.

Single-agent optimal navigation in complex mazes. We investigate the optimal navigation principle of a self-propelled colloidal particle in complex mazes. We construct approximate Markov chain model and use the Markov decision process framework to obtain the general principle of optimal navigation.

Multiple-agent cooperation and coordination for colloidal machines. Using self-propelled Janus motors as the model system, we illustrate a new paradigm for cargo capture and transport based on multiple-agent feedback control. The control algorithm can coordinate multiple motors to cooperate on forming a reconfigurable machine for cargo capture and transport.

Low-dimensional modeling and ensemble control. Optimal control in a high dimensional self-assembly processes with limited actuations presents a challenge in both modelling and controller design. We use colloidal crystallization in an electric field as a model system to illustrate the methodologies of low-dimensional modeling and control for self-assembly processes. We use a nonlinear machine learning algorithm to characterize the dimensionality and parametrize the low-dimension manifold on which the system evolves. A low-dimensional Smoluchowski model is constructed and calibrated to illustrate the dynamic pathways of the assembly process. The resulting model is further leveraged to perform optimal control of the assembly process.

In the second part of dissertation, we report three additional relevant research projects on colloidal interaction, dynamics, and control. The first project extends ensemble control from finite-size systems to infinite-size systems using feedback control in sedimentation. The second project develops a computational method to model depletion interactions between general geometric objects The third project develops modified Stokesian dynamics methods to investigate the colloidal rod motion near a planar wall with hydrodynamic interactions.

Committee:

Prof. Michael A. Bevan (academic advisor, committee chair, Chemical & Biomolecular Engineering)

Prof. Joelle Frechette (Chemical & Biomolecular Engineering)

Prof. Rebecca Schulman(Chemical & Biomolecular Engineering)

Prof. Jeffrey J. Gray(Chemical & Biomolecular Engineering)

Prof. Dennice Gayme (Mechanical Engineering)

Prof. Margarita Herrera-Alonso(Material Science & Engineering)

Prof. Robert L. Leheny (Physics & Astronomy)

For my parents

ACKNOWLEDGEMENTS

I have many people to thank for their kind support during my PhD studies. Without them, the completion of my PhD studies would not be possible.

I first want to thank my parents for their constant love.

I must thank my PhD advisor, Prof. Michael Bevan, for his guidance throughout my whole PhD research. He taught me not only the hard skills on how to conduct research, but also soft skills on communication, leadership and life experience.

I want to thank the past and current members of the Bevan research group: Daniel Beltran, Tara Edward, Gregg Duncan, Swavola Julia, Julie Bitter, Xiaoqing Hua, Brad Rupple, Anna Coughlan, Nikki Neibloom, Matt Petroff, Isaac Torres, Xue Li, and Jianli Zhan. We help each other, directly or indirectly, on many research projects; we shared food, happiness, knowledge, and life experience with each other.

I want to thank collaborators on several of my PhD research projects: David Ford, Raghuram Thyagarajan, Ray M. Sehgal, and Dimitrios Maroudas from University of Massachusetts, Xun Tang and Martha A. Grover from Georgia Institute of Technology, and Benjamin Shapiro from University of Maryland. They either contributed directly to research projects or provided experience and help on problems I encountered.

I want to thank many professors in Johns Hopkins University (JHU) for the courses they delivered and their valuable discussion with me: Prof. Daniel Robinson for nonlinear optimization, Prof. Andrea Prosperetti for advanced engineering maths, Prof. Gregory Chirikjian for stochastic process on manifolds and Lie group, Prof. Michael Kahadan for group representation and Fourier transform, Prof. James C. Spall for Stochastic optimization, Prof. Marin Kobilarov for optimal control and estimation, Prof. Suchi Saria for machine learning, Prof. Michael Dimitz for algorithms, Prof. Sean Sun and Prof. Ari Turner for statistical mechanics, Prof. Gregory Eyink for dynamic systems and advanced parametrization methods, and Prof. Amitabh Basu for convexity analysis.

Finally, I want to thank friends and classmates at JHU and the library services at JHU.

Table of Contents

LIST OF TABLES .... *xii*

LIST OF FIGURES .... *xiii*

1 INTRODUCTION *1*

1.1 Significance and objective **1**

1.2 Background **3**

1.2.1 Self-propelled colloidal systems and optimal control 3
1.2.2 Low dimensional modeling and control of self-assembly processes 4
1.2.3 Depletion in colloidal systems 6
1.2.4 Hydrodynamics in colloidal rod systems 6

1.3 Summary and dissertation outline **7**

2 THEORY *9*

2.1 Colloidal and surface interactions **9**

2.1.1 Net potential energy interactions 9
2.1.2 Gravitational interactions 9
2.1.3 Electrostatic interactions 10
2.1.4 Depletion potentials 11
2.1.5 Induced-dipole interactions 12

2.2 Common order parameters for colloidal assembly **13**

2.2.1 Radius of gyration 13
2.2.2 Global and local order parameters 13

2.3 Stochastic process theory **14**

2.3.1 Ito stochastic differential equation 14
2.3.2 Fokker-planck equation 16
2.3.3 Smoluchowski equation 16

2.4 Stochastic optimal control theory **17**

3 METHODS *19*

3.1 Parameter estimation in multi-dimensional smoluchcowski equation **19**

3.2 Value iteration method for infinite horizon optimal control **20**

4 OPTIMAL NAVIGATION OF SELF-PROPELLED COLLOIDAL RODS IN MAZES *22*

4.1 Abstract **22**

4.2 Introduction **22**

4.3 Methods **25**

4.3.1 Equation of motion 25
4.3.2 Optimal control framework & probability evolution 27

4.4 Results & discussion **30**

4.4.1 Transition probability in free space 30
4.4.2 Rod navigation in free space 31
4.4.3 Rod navigation in simple mazes 34
4.4.4 Rod navigation in complex mazes 36

4.4.5 Scaling of performance 39
4.4.6 Generalization of optimal control principle 41

4.5 Conclusion & outlook 44

5 CARGO CAPTURE AND TRANSPORT VIA OPTIMALLY CONTROLLED SELF-PROPELLED COLLOIDAL MOTORS 46

5.1 Abstract 46

5.2 Introduction 46

5.3 Theory 49
5.3.1 Equation of motion for motors 49
5.3.2 Optimal multi-agent control framework 50
5.3.3 The cargo capture and transport algorithm 52
5.3.4 Measuring tracking performance 53
5.3.5 Capture characterization 54
5.3.6 Governing equation on steady state structures 54
5.3.7 Conservation of momentum and transport speed 55
5.3.8 Theoretical maximum velocity 56

5.4 Methods 57
5.4.1 Simulated experiments 57
5.4.2 Construction of first passage time from simulation 57
5.4.3 Transport speed measurement 58
5.4.4 Statistics for active velocity, density, and area fraction 58

5.5 Results & discussion 58
5.5.1 Capture time characterization 58
5.5.2 Multiple particle tracking multiple targets 61
5.5.3 Transient process in capture 61
5.5.4 Steady state structure during capture 63
5.5.5 Steady state structure during transport 65

5.6 Conclusion 69

5.7 Supplemental methods & theory 69
5.7.1 Brownian dynamics of colloidal motors and cargos 69
5.7.2 Calculation of optimal control policy 71
5.7.3 Sedimentation equilibrium 78

6 COLLOIDAL CRYSTAL GRAIN BOUNDARY FORMATION AND MOTION 80

6.1 Abstract 80

6.2 Introduction 81

6.3 Results 83

6.4 Discussion 92

6.5 Methods 98

6.6 Supplementary materials 99

7 DYNAMIC COLLOIDAL ASSEMBLY PATHWAYS VIA LOW DIMENSIONAL MODELS 114

7.1 Abstract 114

7.2 Introduction 114

7.3 Theory 118
7.3.1 Interaction potentials 118
7.3.2 Colloidal particle dynamics 120
7.3.3 Diffusion mapping 120
7.3.4 Order parameters 122
7.3.5 Low-dimensional smoluchowski & langevin equations 123

7.4 Methods 125
7.4.1 Brownian & langevin dynamic simulations 125
7.4.2 Diffusion mapping 126
7.4.3 Smoluchowski equation solution 127
7.4.4 First passage time distributions 128

7.5 Results & discussion 129
7.5.1 Dimensionality from diffusion mapping 129
7.5.2 Smoluchowski analysis of assembly trajectories 131
7.5.3 Field dependent landscapes (for fixed system size) 133
7.5.4 Field dependent assembly pathways 135
7.5.5 System size dependent assembly pathways 142

7.6 Conclusions 147

8 OPTIMAL FEEDBACK CONTROLLED ASSEMBLY OF PERFECT CRYSTALS 150

8.1 Abstract 150

8.2 Introduction 151

8.3 Methods 153

8.4 Results and discussion 160
8.4.1 Stochastic polycrystal assembly 160
8.4.2 Polycrystallinity versus uncontrolled ramp rate 161
8.4.3 Feedback controlled navigation of energy landscapes 162
8.4.4 Controlled versus uncontrolled assembly 166

8.5 Conclusions & outlook 168

8.6 Supplementary materials 170

9 CONTROLLED FINITE-SIZED COLLOIDAL CRYSTALLIZATION IN SEDIMENTATION WITH TUNABLE ATTRACTIONS 181

9.1 Abstract 181

9.2 Introduction 181

9.3 Equilibrium sedimentation model 184
9.3.1 Interaction potentials and brownian dynamics (bd) simulation 184
9.3.2 Colloidal sedimentation equilibrium 185
9.3.3 Sediment structure order parameters 186
9.3.4 Sedimentation equilibrium simulation 187
9.3.5 Dynamics and microstructure near the growth front 190

9.4 Controller design 192
9.4.1 Defective structures in direct deep quench 192
9.4.2 Quench-relax controller for crystal growth 194

9.5 Conclusion and outlook 199

10 MODELING DEPLETION MEDIATED COLLOIDAL ASSEMBLY ON TOPOGRAPHICAL PATTERNS 201

10.1 Abstract 201

10.2 Introduction 201

10.3 Theory 205
10.3.1 Net interaction potential 205
10.3.2 Gravitational potential 205
10.3.3 Electrostatic interaction potentials 205
10.3.4 A0 depletion potentials 206
10.3.5 Quasi-two dimensional models 208

10.4 Methods 209
10.4.1 Excluded volume calculation 209
10.4.2 Monte carlo simulations 210

10.5 Results & discussion 211
10.5.1 2d density landscapes 211
10.5.2 2d free energy landscapes 213
10.5.3 1d density & free energy landscapes 215
10.5.4 Potential Energy Landscapes 217

10.6 Conclusions 221

11 COLLOIDAL ROD MOTION NEAR A PLANAR WALL: TRANSPORT, SIMULATIONS AND TRAJECTORY ANALYSIS 223

11.1 Abstract 223

11.2 Introduction 223

11.3 Theory 228
11.3.1 Coordinate system 228
11.3.2 Grand resistance and mobility tensor for spheres 229
11.3.3 Calcuclating diffusivities for sphere-chain rod in bulk and above wall 231
11.3.4 Mid-step algorithm for equation of motion under constraint 234
11.3.5 Equilibrium and dynamical analysis 237

11.4 Results and discussion 241
11.4.1 Diffusivities of rod-shaped particle in bulk 241
11.4.2 Diffusivities of sphere-chain rod particle parallel above a planar wall 243
11.4.3 Diffusivities and couplings of sphere-chain rod particle inclined above a planar wall ... 247
11.4.4 Dynamic analysis for single rod diffusion in the bulk 250
11.4.5 Single rod levitated above a planar wall: equilibrium configuration and dynamics 251

11.5 Conclusion 254

11.6 Supplementary materials 255

12 CONCLUSIONS 275

12.1 Optimal control of self-propelled colloids for maze navigation and machines ... 275

12.2 Low dimensional modeling and optimal control for colloidal assembly 276

12.3 Advanced stochastic modeling methods 280

13 FUTURE DIRECTIONS 282

13.1 Reinforcement learning for stochastic optimal control 282

13.2 Multiple agent control framework for active assembly 285

References 287

14 CURRICULUM VITAE... 314

LIST OF TABLES

TABLE Page

S6.1 Parameters for BD simulations and experiments. a, colloidal particle size, b, Debye screening length, c, particle and wall Stern potential, d peak voltage applied to electrodes, e, Clausius-Mosotti factor for an AC field frequency at 1 MHz, f, medium dielectric permittivity, h electrode spacing........................... 106

7.1 Table 1. Parameters for simulations of colloidal particles in a quadrupole electrode: (a) number of particles, (b) particle size, (c) Debye screening length, (d) electrostatic potential pre-factor, (e) Clausius-Mossotti factor for 1 MHz AC field, (f) medium permittivity, (g) electrode spacing, (h) temperature, (i) radius of gyration for 2D HCP particles within regular hexagon morphologies, (j) lowest voltage to crystallize system, (k) applied voltage, (l) normalized voltage, (m) non-dimensional field strength.. 149

S8.1 Parameters for experiments and simulations. a. particle diameter, b. Debye screening length, c. particle and wall Stern potential, d. applied peak-to-peak voltage, e. dimensionless electric field strengths used for policy control, f. Clausius-Mossotti factor for an AC field frequency at 1 MHz, g. medium dielectric permittivity, h. electrode spacing. 172

10.1 Parameters for MC simulations to match with experiments. (a) colloidal particle size, (b) Debye screening length, (c) particle and wall electrostatic potential, (d) temperature, (e) patterned circle diameter, (f) center-to-center pattern spacing, (g) patterned depth, (h) depletant size, (i) osmotic pressure, (j) most probable height, (k) area fraction, (l) number of particles........................... 221

11.1 We label the *N* spheres comprising the rod as 1,2,…,*N*, and set the position vector for sphere *i* as (2*a*i, 0, *h*+*a*), then the velocity for each sphere is specified in the following table to calculate the $\mathbf{R}_{\text{rod}}$.... 233

LIST OF FIGURES

FIGURE Page

4.1 Schematics of navigating self-propelled rod in a maze with feedback control. (A) The imaging system feed the state information (x, y, ϕ) into the controller (here represented by a Maxwell demon), which decides turning on or off the stimulating light. The stimulating light will enable the rod to generate self-propulsion along its long axis. (B) The coordinate system used to measure the position and orientation of the rod. The self-propelled rod has a length of L, and diameter of 2a, and it will propel itself along its long axis with speed v as function of light intensity I. 30

4.2 Schematics of calculating optimal control policy using Markov decision process framework offline and execute optimal control plan online. (A) Markov decision process framework takes state space S, action space A, state transition probability P and a cost function C as input, and produce an optimal control policy. (B) Execute the optimal policy using feedback loop with every 1s control interval. The current state (x, y, ϕ) is feed back to update the current control action. 33

4.3 Plot of transition probability $p(s_{n+1}|s_n,a)$ under different actions a with discrete time step 1s starting from initial state (0, 0, 0). (A)(B) Probability distribution of position (x, y) after one discrete time step under actions of off mode (A) and on mode(C). (D) Probability distribution of angular displacement after one discrete time step. Note that the choice of action will not affect this angular distribution. 35

4.4 Optimal navigation of self-propelled rod in free space. (A) Simulated optimally controlled trajectory of 200s with starting state (x, y, ϕ)=(30, 30, 0) and target position (x, y) = (0, 0) (B) Optimal control policy calculated using Eq. (4.3) as a function of discretized state (x, y,ϕ). 8 subplots corresponds to states with angles falling into 8 different angular intervals [-π/8, π/8], [π/8, 3π/8], [3π/8, 5π/8], [5π/8, 7π/8], [7π/8, 9π/8], [9π/8, 11π/8], [11π/8, 13π/8], [13π/8, 15π/8]. (C) First passage time distribution obtained from simulation trajectory statistics (symbols) and theoretical predictions from Eq. (4.5) (solid lines): optimal control (black), off mode (red), and on mode (blue). Dash line is the asymptotic distribution (D) Theoretical probability evolution from Eq. (4.4) under optimal control as function of time.......... 37

4.5 Optimal navigation of self-propelled rod in free space. (A) Simulated optimally controlled trajectory of 200s with starting state (x, y, ϕ)=(30, 30, 0) and target position (x, y) = (0, 0) (B) Optimal control policy calculated using Eq. (4.3) as a function of discretized state (x, y,ϕ). 8 subplots corresponds to states with angles falling into 8 different angular intervals [-π/8, π/8], [π/8, 3π/8], [3π/8, 5π/8], [5π/8, 7π/8], [7π/8, 9π/8], [9π/8, 11π/8], [11π/8, 13π/8], [13π/8, 15π/8]. (C) First passage time distribution obtained from simulation trajectory statistics (symbols) and theoretical predictions from Eq. (4.5) (solid lines): optimal control (black), off mode (red), and on mode (blue). Dash line is the asymptotic distribution (D) Theoretical probability evolution from Eq. (4.4) under optimal control as function of time.. 39

4.6 Optimal navigation of self-propelled rod in a complex mazes (A)(B)(C)(D) and (E)(F)(G)(H), with the same descriptions as in Figure 5............................... 41

4.7 Scaling analysis for mean first passage time for rod navigation under different strategies in mazes of increasing length scales. (A) Mazes of increasing sizes, starting point and ending points are marked by cross symbol and pentagram. Shortest geometric path are plotted as solid lines. (B) The mean first passage for rod under optimal control is linear with the shortest path length. (C) Approximate scaling relationship between mean first passage time and maze length scale for rod under different control strategies... 43

4.8 Generalization of optimal control. (A) Positioning error (σ/L) as a function of λ and Pe. The contour line with triangle symbols denotes the isoline with $\sigma/L=10$. The black dash line passes through the minimum point on each contour line, indicating the optimal choice of Pe (in terms of minimizing positioning error) at different value of λ. (B) Intrinsic position error as a function of D_r and D_t. The contour line with triangle symbols denotes the isoline with $\sigma/L=10$. (A) Schematics for different navigation tasks characterized by geometric parameter η. (B) Summary of mean first passage time under optimal strategies in different navigation tasks as a function of control system setting Pe and λ. The black dash line passes through the minimum point on each contour line, indicating the optimal choice of Pe (in terms of minimizing navigation time cost) at different value of λ....................... 47

5.1 Schematics of navigating self-propelled rod in a maze with feedback control. (A) The imaging system feed the information of system state $S=(x, y, \phi)$ containing positions and orientation of the motor and the positions of the target into the online control policy module, which outputs velocities to use for the motors. The control policy is executed by the actuator module containing the illuminator(light bulb) and a selective phone mask such that each motor can be tuned to desired velocities. This feedback control procedure will loop at every interval of Δt_c. (B) Schemes of using optimal controlled colloidal motors to perform cargo capture and transport. Targets are designed to dynamically located around the cargo. And optimally controlled motors are controlled using feedback system in (A) to track these targets. When motors are localized to their target sites via optimal controlled, the cargo will be caged, and hence captured. After the cargo are captured, the controller will maintain the motor to the target sites and selectively activate motors in the transport direction (the dash black arrow) such that the motors will move with the cargo in the transport direction.. 49

5.2 (A) Optimal control policy for motors under speed constraint v ∈ [0, 5 a/s]. The optimal control policy specifies the self-propulsion speed v to be used given target position (x, y) with respect to the local coordinate system, which is centered on the motor center and has its y axis aligning with the motor's orientation vector n (the arrow). (B) Representative trajectory (blue solid line) of an optimally controlled motor (starting with initial state (x, y, ϕ)=(30,30,0)) tracking a target (initially located at position (0,0)) undergoing Brownian motion with the black solid line as the trajectory. The black dashed line around the target represents the target region used to calculate first passage time. (C) The distribution of first passage time τ for an optimally controlled single motor tracking a Brownian moving target as described in (B). (D) Design of target sites (dashed circles) for multiple motors to capture and transport cargo. Five different design schemes for different number of motors are demonstrated. Target sites are dynamically placed around the cargo such that when motors are perfectly localized at the target sites, cargo will be caged, therefore captured. (E) The representative trajectories of 6 optimally controlled motors tracking 6 dynamic targets moving simultaneous with the Brownian cargo. The cargo (yellow circle) is initially located at position (0, 0). The motors are initially equally spaced on a circle (dash blue) with radial distance 30a to the cargo. The targets are drawn as dashed circles around the cargo. Solid lines are trajectories of motors and the cargo. (F) The distribution of first passage time τ for a N motor tracking N dynamic targets (initially located at position (0,0)) with initial distance of 300a . From left to right are N=1, 6, 18, 36, 60, 90.. 60

5.3 Trajectory for capture and transport process. Cargo initially located at (0,0), after 1300s, cargo is transported to position at (90,0) (A) The black solid line represents the cargo. The color spectrum from blue to red represents the time scale. Other solid lines denote the trajectories of the motors. (B) The distance of each motor to its optimally assigned target position surrounding the cargo as a function of time. Each red line represents one motor. The black denotes the mean value. 0 to 300 s is the capture process, and 300s – 1500s is the transport process. The left part of the arrow is capture process and the right part is the transport process. (C) The distance of cargo to the mass center of all motors as a function of time. (D) The cargo's position in the x axis as a function of time. 63

5.4 (A) The normalized mean deviation of cargo to the mass center of motor as a number of number of motors N (from top to bottom: N=6, 18, 36, 60, 90) and attraction strength U_{att} between motors. (B) (upper row)2D steady state position distribution of 90 motors tracking 90 targets sites surrounding a Brownian moving cargo and (lower row) the steady state active force distribution in radial direction distribution. The coordinate in the 2D plot is with respect to a local coordinate system centering on the mass center of the system. Interactions between motors are: (left) 0 kT attraction, (middle) 3.2 kT attraction, and (right) 5.3 kT attraction. (C) The pressure estimated from the integrated active force in 1D radial direction (Eq. (5.11)) for N=90 motor system. Different colors represent motor interactions of: (black) 0 kT attraction, (red) 1.8 kT attraction, (green) 3.2 kT attraction, and (blue) 5.3 kT attraction.. 65

5.5 (A) 2D steady state position distribution of 90 motors tracking 90 targets sites surrounding a Brownian moving cargo, (middle column) the steady state active force distribution in positive horizontal direction distribution, and (right column) the steady state residual active force distribution in radial direction distribution. The coordinate in the 2D plot is with respect to a local coordinate system centering on the mass center of the system. Interactions between motors are: (top) 0 kT attraction, (middle) 3.2 kT attraction, and (bottom) 5.3 kT attraction. (B) Transport speed as a function of number of motors and attraction between motors. The dash line is the theoretical maximum transport velocity. (C) The pressure estimated from the integrated active force in 1D radial direction (Eq.(5.11)) for N=90 motor system. Different colors represent motor interactions of: (black) 0 kT attraction, (green) 3.2 kT attraction, and (blue) 5.3 kT attraction. 68

6.1 Reaction coordinates for grain boundary formation and motion can be computed from image analysis of optical microscopy images of electric field mediated colloidal crystallization. (a) Raw images show representative configurations of 210 ~3 μm silica colloids in fluid, bicrystal, and single crystal configurations observed over ~7.5 min following a quench (step voltage change) to V*=0.57 (see main text and Supplementary Methods for definition). Snapshot times are shown by solid black lines in Fig. 1e. Computed reaction coordinates shown by colored particle centers on 8-bit intensity scale for the (b) radius of gyration, R_g, (c) local hexagonal order, $\langle C_6 \rangle$, (d) global hexagonal order, y_6, and time dependent traces for (e) a single voltage quench and (f) ten consecutive cycles (numbered vertical black lines indicate representative images included in Supplementary Fig. 2). 82

6.2 "Two dimensional" trajectories (i.e., two reaction coordinates) capture coalescence of local domains during fast condensation processes to produce bicrystals that relax to single crystals via grain boundary motion over a broad range of timescales. Microscopy images from Figs. 1a with particle centers colored using RGB (Red/Green/Blue) mixing rules for colors represented by two reaction coordinates including (a) ψ6 and C6 and (b) ψ6 and Rg to visualize how global order emerges from local order and during condensation. Ten trajectories following quenches to V*=0.57 with time represented by a 256-color scale (inset scale bar) for (c) (ψ6, C6) and (d) (ψ6, Rg) reaction coordinate pairs with inset plots of single trajectories from Fig. 1e.. 84

6.3 Figure 3. Free energy and friction landscapes obtained by fitting trajectories to Smoluchowski equation (equation 1) that quantitatively capture grain boundary diffusion and migration vs. relative domain sizes and misorientation angles. (a) W(ψ_6, R_g)/kT with inset scale bar and two trajectories obtained from the experiments in Figs. 1 and 2. (b) $D_{\psi_6\psi_6}/(kT\cdot s)$ with inset scale bar with the same trajectories as in (a). (c) Representative configurations from microscopy images and simulated renderings for coordinates marked along trajectories in (a) and (b). Labeled misorientation angles shown by red lines and particle centers are colored according to the RGB composite convention in Fig. 2. First passage time distributions for BD (red) and LDLD (black) trajectories projected onto (d) the ψ_6-axis between 0.47-0.66 (●,●), 0.38-0.56 (▲,▲), 0.28-0.47 (■,■), 0.19-0.38 (◆,◆) and (e) R_g-axis between 1.27-1.25 (●,●),1.25-1.23(▲,▲), 1.23-1.21 (■,■), 1.21-1.19 (◆,◆), 1.21-1.19 (⬢,⬢), 1.19-1.17 (▼,▼), and (f) for trajectories between a sink at (ψ_6=0.8 R_g=1.14) (*i.e.*, global minimum) and sources at (ψ_6=0.38 R_g=1.15) (●,●)......................... 91

6.4 Free energy landscapes based on ψ_6, Rg reaction coordinate pair capture dynamics at all V* to provide quantitative models of grain boundary formation and motion. W(ψ_6, R_g)/kT at (a) V^*=0.31, (b) V^*=0.44, (c) V^*=0.57, and (d) V^*=0.69 with inset renderings of global minimum configuration and representative trajectories from BD simulations that were matched to the experiments (see Supplementary Methods). The free energy scale is indicated by the inset in (a). 96

S6.1 Co-planar thin gold film quadrupole electrode on a cover slip. (a) Top view of device showing connections to function generator. (b) Schematic rendering of device. (c) Nominal 3 μm silica colloids in the quadrupole electrode center at the electric field minimum (particles provide internal scale bar). (d) Contour plot of electric field with linear spectrum scale from E/E0=0-7, where E0 is the nominal electric field magnitude.
Supplementary Figures 1a and b: “Electric field mediated assembly of three dimensional equilibrium colloidal crystals” Juarez, J.J.; Feicht, S; Bevan, M.A. 2012, Soft Matter 8, 94-103. Reproduced by permission of The Royal Society of Chemistry. http://dx.doi.org/10.1039/C1SM06414B
Supplementary Figures 1c and d: “Size dependent thermodynamics and kinetics in electric field mediated colloidal crystal assembly” Edwards, T.D.; Beltran-Villegas, D.J.; Bevan, M.A. 2013, Soft Matter 9, 9208-9218. Adapted by permission of The Royal Society of Chemistry. http://dx.doi.org/10.1039/C3SM50809A 101

S6.2 Representative images and reaction coordinate trajectories for ten consecutive voltage quenches from 0.2 V to 1.2 V. (a) Processed images where particles are painted based on normalized local, $\langle C_6\rangle$, and global, ψ_6, order reaction coordinates. Color scheme is identical to Fig. 2a and Supplementary Videos 1 and 2. (b) $\langle C_6\rangle$ and ψ_6 vs. time, t, with location of extracted images in a. (c) and (d) show same information as a and b except for (ψ_6, R_g) reaction coordinate pair. 102

S6.3 Matching Brownian Dynamics simulations to microscopy experiments. (a) radial distribution function calculated from equilibrium configurations in experiments (●) and simulations (●) at V^*=0.57. (b) Parameterized diffusivities from Eq. (6.16). (c) Mean squared displacement averaged over all particles from experiments and Brownian Dynamic simulations at R_g values of: 1.28 (●), 1.25(■), 1.20(◆), 1.17(⬢), 1.14(▲). (d) Diffusivities at different R_g from the first five points in c (●) and BD (●). 103

S6.4 Matching Brownian Dynamics simulations to microscopy experiments. (a) radial distribution function calculated from equilibrium configurations in experiments (●) and simulations (●) at V^*=0.57. (b) Parameterized diffusivities from Eq. (6.16). (c) Mean squared displacement averaged over all particles from experiments and Brownian Dynamic simulations at R_g values of: 1.28 (●), 1.25(■), 1.20(◆), 1.17(⬢), 1.14(▲). (d) Diffusivities at different R_g from the first five points in c (●) and BD (●).. 110

S6.5 Figure 5. Diffusivity landscape components as a function of R_g and ψ_6 for V^*=0.57. All four diffusivity landscape components: (a) $D_{\psi6\psi6}(kT{\cdot}s)^{-1}$, (b) $D_{\psi6Rg}/(D_{\psi6\psi6}D_{RgRg})^{0.5}$, (c) $D_{Rg\psi6}/(D_{\psi6\psi6}D_{RgRg})^{0.5}$, (d) $D_{RgRg}(kT{\cdot}s)^{-1}$. The inset color scheme is rescaled for each case. The diagonal elements are reported with units, and the cross terms are normalized by the square root of the product of the diagonal terms to check their correlation. 112

7.1 (A) Top view of simulated experiment of quasi-2D configuration of N=210 colloidal particles (2a=3 μm) compressed within a quadrupolar electrode (with electrode gap of dg=100 μm. (B) Electric field magnitude contour plot within quadrupole electrode center (Eq. (7.5)) with arrows indicating relative magnitude and direction of force due to dipole-field interactions (Eqs. (7.2), (7.7)) that concentrates particles in quadrupole center. (C) Typical colloidal assembly trajectories in the order parameter pair (ψ6, Rg) for a system size of N = 210 at voltages of (see definition of nondimensional V* in Eq. (7.21) where V*=1 corresponds to thermodynamic condition for perfect crystal as free energy minimum configuration200): V*=0.42 (blue), V*=0.5 (green), V*=0.57 (black), V*=0.80 (pink), and V*=0.80 (red). Representative states in part C are marked as (rendered in part D with exceptions noted): I (initial fluid state, part A), II (crystal configuration coexisting with peripheral fluid particles), III (low order bicrystal), IV (higher order bicrystal), and V (single crystal with a few particles still experiencing thermal motion at crystal periphery). 118

7.2 (A) Eigenvalue spectrum obtained from diffusion mapping (Eqs. (7.9)) the process of electric field mediated colloidal assembly in a quadrupole electrode (see Fig. 1) for a system size of N=210 and a non-dimensional applied voltage of V^*=0.8. (B) Plot of ~8000 configurations sampled in BD simulations plotted in (ψ_6, R_g) space and colored by values of first non-trivial eigenvector, ν2, shows good sampling of final order parameters. Bottom two plots show points indicating values of the top three non-trivial eigenvector coordinates (ν2, ν3,

ν_4) for the same ~8000 configurations shown in (B) but now colored by their values of (C) the order parameter R_g (Eq. (7.12)) and (D) the order parameter ψ_6 (Eq. (7.15)). 132

7.3 Representative local order parameter trajectories used to obtain Smoluchowski equation coefficients. Results are shown for a system size of N=210. Plots show ensemble average: displacement vs. time for (A) ψ_6 and (B) R_g; displacement variance vs. time in (C) and (F); displacement covariance in (D) and (E). Representative data are shown for several different combinations of starting configurations and applied voltages including: (G) (black circles) (ψ_6, R_g)=(0.1375, 1.146) V^*=0.80; (H) (red triangles) (ψ_6, R_g)=(0.3875, 1.146) V^*=0.57; (I) (cyan squares) (ψ_6, R_g)=(0.7125, 1.125) V^*=0.50. Linear fits to the initial slopes (illustrated by dashed lines) of the data in each plot are used in Eqs. (7.17)-(7.19) to obtain D(x) and W(x) in Figs. 4 and 7. 136

7.4 Free energy and diffusivity landscapes obtained by fitting trajectories to Smoluchowski equation to BD trajectories for N=210 and applied voltages of (top-to-bottom): (A) V^*=0.42, (B) V^*=0.50, (C) V^*=0.57. Plots show (left) free energy landscapes, $W(\psi_6, R_\mathrm{g})/kT$ (Eq. (7.19)), with trajectories, marked coordinates of interest, and inset scale bars, and (middle) four components of diffusivity tensor, D/($kT{\cdot}s$) (Eq. (7.17)), with inset scale bar and same axes as W plots (left-to-right, top-to-bottom): $\mathrm{D}_{\psi6\psi6}$, $\mathrm{D}_{\psi6Rg}$, $\mathrm{D}_{Rg\psi6}$, and D_{RgRg}. T1 and T2 in the left most column of part (C) denote two representative trajectories following different pathways. (D) Renderings in column on far right show representative configurations for coordinates marked on W plots. 138

7.5 Fig. 5. First passage time distributions (FPTD) for BD (black) and LDLD (red) trajectories during processes of condensation and grain boundary migration for system size of N=210 at applied voltage of V*=0.57. (A) Schematics for the process of condensation (vertical arrow along the steep W gradient at Rg direction) and the process of grain boundary migration (horizontal arrow along the W plateau at ψ6 direction). (B) FPTD during the condensation process measured from trajectories from starting points to end points on the Rg-axis between (top to bottom): (1.24, 1.22), (1.22, 1.20), (1.20, 1.18), (1.18, 1.16), and (1.16, 1.14). (C) FPTD during grain boundary migration process measured by tracking trajectories from starting points to end points on the ψ6 -axis between (top to bottom): (0.4, 0.6), (0.3, 0.5), and (0.2, 0.4). (D) FPTD corresponding to T1 and T2 in Fig. 4C between a sink at (ψ6=0.7 Rg=1.18) (i.e., global minimum) and sources at (ψ6=0.15 Rg=1.13) (circles) and (ψ6=0.5 Rg=1.14) (triangles).. 140

7.6 Numerical solution of Smoluchowski equation to compute p(x,t) at observations times of Δt=10s, 50s, 100s, 200s, and 400s for a system size of N=210 at applied voltages of: (A, B) V^*=0.42, (C, D) V^*=0.50, and (E, F) V^*=0.57. The initial condition in all cases is p(x,0)=δ(x-x$_0$) where x$_0$=(ψ_{60}, $R_{\mathrm{g}0}$)=(0.025, 1.22). The left hand plots are two dimensional contour plots of probability density with an inset scale bar in part A. The right hand plots are one dimensional projections of the two dimensional probability density onto the ψ_6 coordinate for: Δt=10s (black), 50s (red), 100s (green), 200s (blue), and 400s (cyan).. 143

7.7 Free energy and diffusivity landscapes with same formatting and procedure to obtain plots in Fig. 4 (see Fig. 4 caption), except results are now shown for different systems sizes (and applied voltages) of (top-to-bottom): (A) N=110 (at V*=0.85), (B) N=210 (at V*=0.80), and (C) N=300 (at V*=0.75). (D) Renderings in column on far right show representative configurations for coordinates marked on W plots. 145

7.8 Numerical solution of Smoluchowski equation to compute $p(x,t)$ at observations times of Δt=10s, 50s, 100s, 200s, and 400s for different systems sizes (and applied voltages) of (top-to-bottom): (A, B) N=110 (at V^*=0.85), (C, D) N=210 (at V^*=0.80), and (D, E) N=300 (at V^*=0.75). The initial condition in all cases is $p(x,0)=\delta(x-x_0)$ where $x_0=(\psi_{60}, R_{g0})=(0.025, 1.18)$. The left hand plots are two dimensional contour plots of probability density with an inset scale bar in part A. The right hand plots are one dimensional projections of the two dimensional probability density onto the ψ_6 coordinate for: Δt=10s (black), 50s (red), 100s (green), 200s (blue), and 400s (cyan). 148

8.1 Quasi-2D colloidal crystal assembly in electric fields. (a) Microfabricated quadrupole electrode. (b) Optical microscopy image of particles within quadrupole. (c) Single particle-field potential (blue-red scale: 0-100 kT). Images of 300 particles with centers colored to visualize reaction coordinates for local hexagonal order, C_6, and global hexagonal order, ψ_6, at electric field amplitudes of λ = (d) 0.2, (e) 0.9, (f) 2.0, and (g, h, i) 19.7. Representative microstructures include bicrystals with (g) large grain boundary (similar sized domains near max misorientation angle), (h) small grain boundary (dissimilar sized domains with smaller misorientation angle), (i) no grain boundary *i.e.*, perfect crystal. 2.8 μm particles provide internal scale bar. 154

8.2 Ramping electric field at different rates without feedback control to understand effect of quench-rate on crystal assembly. Electric field amplitude, (long-dash gray), ramped from 0.2 to 19.7 over (a) 0 s (blue), (b) 1x103 s (cyan), (c) 2x103 s (red), (d) 5x103 s (green), and (e) 104 s (black). Local order, C6 (dotted lines), emerges before global order, ψ6 (solid lines). Equilibrium ψ6 values (open circles) vs. λ approach ψ6 ramp trajectories only for 104 s ramp. 162

8.3 Assembly trajectory on energy landscapes under control (see Movie S1). (a) Free energy landscapes of 300 particles at the four λ's in policy. Example trajectory (black) with coordinates on policy (b) and corresponding images (c-h). (b) Optimal policy calculated using Markov decision process. Images showing representative configurations (same coloring scheme as Figs. 1d-i) at:

(c) $\lambda = 0.2$ before compression, (d) first compression to $\lambda = 19.7$ with grain boundary, (e) relaxation at $\lambda = 0.9$, (f) re-compression at $\lambda = 19.7$ with new grain boundary, (g) relaxation at $\lambda = 2.0$, (h) perfect crystal at $\lambda = 19.7$. 166

8.4 Controlled vs. uncontrolled crystal assembly processes. 100 uncontrolled and 100 controlled trajectories shown as: (a) first 10 cycles with C6 (blue), $\psi 6$ (red), λ (black) vs. time, (b) $\psi 6$ vs. time for 103 s for all experiments colored to indicate ensemble average (bold red), no grain boundary (red: $\psi 6 > 0.7$, C6 > 0.95), small grain boundary (orange: $0.7 > \psi 6 > 0.4$, C6 > 0.95), large grain boundary (peach: $0.4 > \psi 6$, C6 > 0.95), (c) perfect crystals vs. time as cumulative number (dark red) and instantaneous number (bars) with same color scheme as (b). 168

9.1 Equilibrium sedimentation model system at different ε^*: (A) sedimentation equilibrium profile of $\phi(z)$ and $\psi_{4,L}$, and representative equilibrium configuration at four different $\varepsilon^*=0, 0.34, 0.52, 0.69$. (B) Most probable R_z, N_c, $\langle C \rangle$ as a function of $\varepsilon^*$for 9 different ε^* ranging from 0 to 1. N_c ranges from 0 to 8. 189

9.2 Figure 2. Dynamic properties of equilibrium sedimentation model near growth front. (A) L vs. t for particles at different layer positions of below growth front (*gf*-), growth front (*gf*) and above growth front (*gf*+). (B) L_c .vs. ε^* at *gf*-, *gf* and *gf*+ (C) Oblique view and top view rendering of layer structure at *gf*-, *gf* and *gf*+ for $\varepsilon^*=0.34$. 192

9.3 Figure 3. Crystallization *via* direct quench at $\varepsilon^*=1$. (A) R_z and $\langle C \rangle$ as a function of time. (B) profile of $\phi(z)$ and $\psi_{4,L}$, for the final sediment. Renderings of initial configuration, final configuration, and layer structures at $z=4a$, $8a$, $11a$ are shown on the right-hand side. 194

9.4 Schematic of quench-relax controller........ 196

9.5 Results of controlled crystal growth using feed-back controller at (left) $\Delta N_c=1$, (middle) $\Delta N_c=2$, and (right) $\Delta N_c=3$. 198

9.6 Analysis of controller efficiency for $\Delta N_c=1, 2, 3$: average time for building each layer and cumulative time (inset). 199

10.1 Figure 1. Experimental images (A,C,E) and simulation renderings (B,D,F) of charged ~2µm SiO2 colloids at 0.18 area fraction experiencing depletion attraction with each other and a topographically patterned (well depth H=285nm) glass microscope slide surface. The depletion potential is tuned by the depletant size, 2L, at 25C, 2L=113nm (A,B), 35C, 2L=107nm (C,D), 37C, 2L=53nm (E,F). 204

10.2 Schematics of substrate geometry. (A) Snapshot (top views) of simulation rendering and magnified view of particles at pattern edge. (B) Cross sectional view of particles at pattern edge. Green and gray spheres are depletants and colloids. Red band (light) surrounding the gray sphere and the gray substrate is excluded volume (approximated via hard sphere repulsion). 207

10.3 2D Density landscapes from experiments (A,C,E) and simulations (B,D,F) at 25C, 2L=113nm (A,B), 35C, 2L=107nm (C,D), 37C, 2L=53nm(E,F). 212

10.4 2D free energy landscapes from experiments (A,C,E) and simulations (B,D,F) at 25C, 2L=113nm (A,B), 35C, 2L=107nm (C,D), 37C, 2L=53nm(E,F). 215

10.5 1D density profile (A, C, E) and free energy landscapes (B,D,F) from experiments(red line and symbol) and simulations(black line and symbol) at 25C, 2L=113nm (A,B), 35C, 2L=107nm (C,D), 37C, 2L=53nm(E,F). Blue line in (E) is gravitational potential energy landscape. Dash lines show inner (Ri) and outer (Ro) of pattern radius. 218

10.6 Excluded volume difference (A), theoretical potential energy landscape (B), particle pair potential at 25C, 2L=113nm (black), 35C, 2L=107nm (red), 37C, 2L=53nm (green). 220

11.1 Schematics of the sphere-chain model above a planar wall: (A) 3D view (B) side view looking along $n_{\perp 1}$. e_1, e_2 and e_3 are unit vectors of Cartesian coordinate of the lab frame, $n_{\|}$, $n_{\perp 1}$ and $n_{\perp 2}$ are unit vectors of spherical coordinates of the body frame with its origin located at the mass center of the rod. 229

11.2 Diffusivities for sphere-chain rod and cylindrical rod of p=2-30 in bulk: (A) Translational diffusivities in direction $n_{\|}$ (filled black circle), $n_{\perp 1}$ (filled cyan square), for sphere-chain rod from our model and diffusivities in direction $n_{\|}$ (filled green triangle) and $n_{\perp 1}$ (filled pink down triangle) for cylindrical rod from Tirado's model. (B) Rotational diffusivities in direction $n_{\|}$ (filled green down triangle), $n_{\perp 1}$ (filled black circle) for sphere-chain rod and diffusivities in direction $n_{\|}$ (filled pink square) and $n_{\perp 1}$ (filled red up triangle) for cylindrical rod. 243

11.3 Diffusivities for single sphere-chain rods parallel above a wall: (A)(B) height dependent coefficients for translational diffusivities as a function of *h/a* in direction $n_{\|}$, $n_{\perp 1}$, $n_{\perp 2}$ for *p*=7(A), *p*=12(B); (C)(D)) height dependent coefficients for rotational diffusivities as a function of *h/a* in direction $n_{\|}$, $n_{\perp 1}$, $n_{\perp 2}$ for *p*=7(A), *p*=12(B). 247

11.4 Diffusivities for single sphere-chain of aspect ratio 7 oblique to wall (45 degree polar angle): (A)(B) height dependent coefficients for translational and rotational diffusivities as a function of normalized height *h/a* in direction $n_{\|}$,

$n_{\perp 1}$, $n_{\perp 2}$; (C) correlation coefficients Cov_{13}, Cov_{15}, Cov_{24} and Cov_{35} for diffusivity tensor components as a function of normalized height h/a; (D) correlation coefficients Cov_{13}, Cov_{15}, Cov_{24} and Cov_{35} as a function of θ at $h/a=0.05$; Schematics for the correlated motions: (E) translation in $n_{||}$ and translation in $n_{\perp 2}$, (F) translation in $n_{||}$ and rotation in $n_{\perp 1}$, (G) translation in $n_{\perp 1}$ and rotation in $n_{\perp 1}$, (H) translation in $n_{\perp 2}$ and rotation in $n_{\perp 1}$. 249

11.5 Mean squared translational displacement (MSTD) and orientation autocorrelation function for simulation trajectories of single rod $p=5$ in bulk: (A) 3D sequential snapshots of colloidal rod configuration. Displacement vector Δx can be decomposed into components parallel and perpendicular to its axis (in $n_{||}$ direction). $e_1=(1,0,0)$, $e_2=(0,1,0)$ and $e_3=(0,0,1)$ are unit vectors of the lab frame. (B) Simulation extracted and theoretical predicted MSTD curve from Eq.(11.29)(11.30) (black square and solid line) and components in parallel direction (red triangle and solid line) and perpendicular direction (pink circle and solid line). (C) Orientation autocorrelation function from simulation and theoretical prediction from Eq. (11.31) (black triangle and red solid line). 251

11.6 Free energy landscape analysis for single rod electrostatically levitated above wall: (A-F) 2D theoretical FEL from (11.27)(top row,(A)(C)(E)) and simulation extracted via inverse Boltzmann analysis (bottom row,(B)(D)(F))as a function of z/a and θ for rods of aspect ratio 4 7, 12. (G)(H) 1D FEL as a function of z/a and θ for rods of aspect ratio 4, 7 and 12. Symbols are results from inverse Boltzmann analysis, solid lines are theoretical prediction from Eq.(11.28). 253

11.7 Analysis of trajectories for single rod electrostatically levitated above wall: (A) Simulation extracted and theoretical predicted (Eq. (11.32)) MSTD curve and components in parallel direction (black circle and solid line) and perpendicular direction (red circle and solid line) for a rod with p=4. (B) MSTD as a function of lapsed time from simulation and theory on the log-log plot for aspect ratio 4, 7 and 12. Symbols are results from simulation data, solid lines are theoretical predictions(Eq. (11.33)). (C) MSTD curves (from bottom to top) as a function of time at elevation of 2.9a, 3.9a, 4.9a, 5.9a, 6.9a; (D) extracted elevation dependent diffusivity via Eq. (11.35), and theory predicted values via Eq. (11.36) 254

S11.1 The correlation coefficient Cov_{15} (coupling between translation in direction $n_{||}$ rotation and in direction $n_{\perp 1}$) as a function of p and h. (B) The image system for two point forces above the wall. This correlation Cov_{15} is most pronounced at $h/a\sim 1$ and $p=2$(*i.e.* doublet rod). This coupling stems from the fluid velocity field created by the dipoles in image system of an array of point force stokelet that sets the rod to rotate, as showed in the schematics in Fig. S1 (B).[1] For longer rods, the dipole array will cancel each other out in the middle part and decrease the coupling strength. 268

13.1 Optimal control colloidal assembly via reinforcement learning. (A) 100 trajectories starting at (0.05, 20000) under optimal control via reinforcement learning. (B) 100 trajectories starting at (0.05, 20000) under direct deep quench using highest voltages. 278

13.2 Optimal controlled self-propelled colloids for active assembly. (A) Initial configuration of self-propelled colloids. (B) Target sites with hexagonal closed packing order. (C) Trajectories of self-propelled colloids under multiple agent control. (D) Final configuration of self-propelled colloids. 279

1 INTRODUCTION

1.1 Significance and objective

Colloidal systems consisting of nano- or micro-sized particles have been extensively researched in the recent decades. [2,3] [4] Such systems have been used as a model to investigate various fundamental issues in science and emerging technologies: (1) used as 'big atom' system to investigate fundamental structural and dynamical properties during phase transitions such as melting and nucleation;[5-7] (2) used as model system to investigate self-assembly theory and engineering strategies;[8,9] (3) used as the building blocks for colloidal crystals with applications in Photonic bandgap materials due to their lattice parameter being in the length scale of visible light;[10] (4) used to prototype micro-robotics and micro-machine to operate on micro-scale structural microenvironment for chemical, environment, and biomedical applications.[11-16]

This dissertation is devoted to several scientific and engineering aspects of colloidal self-assembly processes that are closed related colloidal crystal fabrication and colloidal robotics and machines. Colloidal self-assembly processes generally refer to the dynamical processes where colloidal particles spontaneously organize into ordered structures. Self-assembly is considered as a key bottom-up approach to fabricate novel micro- and nano-scale materials.[17-19] Currently, however, self-assembly processes have limited applications from several aspects. First, self-assembly processes driven by external force fields, such as gravity field[20], electric field,[21] strong attraction interaction,**[22]** and shear fluids,[23] often resulted in irreversible processes and cannot correct defects. Second, modeling studies of self-assembly generally focus on predicting the thermal equilibrium or steady-state structures as a function of particle interactions, particle shapes, temperature, and concentration;[24,25] while development principled methods to quantify and predict the kinetic processes has rarely been addressed. In addition, there is limited research on conjugating with self-assembly processes with optimal control methodology to engineer the kinetic pathways of self-assembly processes. Moreover, most of self-assembly processes are limited to equilibrium thermodynamic systems, while optimal controlled self-assembly within far-from-equilibrium systems, which might be a potential tools for assembling microscale devices and machines, has rarely been explored.

This dissertation is aimed at addressing these challenges and filling the gaps mentioned above. Our approaches are mainly computational and theoretical, as stated as follows. First, we will develop low dimensional dynamical Smoluchowski equation formulism to model colloidal self-assembly processes, in which thermodynamics and kinetics are being modeled consistently. Colloidal systems consisting of hundreds particles will cause curse of dimensionality in the dynamic model construction; and we will use machine learning algorithms to help reduce the dimensionality and find out order parameters to parameterize the Smoluchowski model. Second, we will conjugate dynamic optimal feedback control methods with the low dimensional dynamical model to design feedback controller for self-assembly systems. From the perspective of material engineering, controlling self-assembly processes with feedback will provide a robust and error-correcting approach to create complicated microstructure. Third, we will explore principles and methods to harness far-from-equilibrium phenomenon and thermodynamics, which enables creation of structures not permitted in equilibrium thermodynamics. In particular, we will use self-propelled colloidal particles system[26] as a model to develop algorithms for optimal positioning and navigation in complex microstructured environments and explore new paradigms for cargo capture and transport. In addition, we will develop advanced computational method to model hydrodynamics and tunable entropy interactions in colloidal systems.

1.2 Background

1.2.1 Self-propelled colloidal systems and optimal control

Bacteria and sperm are examples of natural micro-swimmers that take in environmental energy and turn into mechanical work. Recently, numerous man-made micro-swimmers had been created in various forms, such as bimetal nano-rods and Janus spheres, and function on different mechanism, such as catalysis of chemical fuels[27] and mimicking natural swimmers[28]. A collection of self-propelled colloidal particles is also known as active matter, because of their non-equilibrium thermodynamic nature governing its kinetics.[29] One classic model for a single self-propelled particle is a particle with its orientation undergoes Brownian rotation, and the self-propulsion is restricted to the orientation. Proof-of-concept applications of these man-made swimmers are emerging in a broad range of areas. For example, biomedical applications includes using self-propelled "micro-device" to capture and isolate of cancer cells,[30] navigate and deliver drugs[13,31]; environment applications include polluted water pollution cleaning using self-propelled micro-motors;[12] material engineering applications include fabrication of novel structures based on active interactions.[26,32]

Without strategic control, most of self-propelled system cannot produce useful work in the long run since their propulsion directions are purely random. If we can control the self-propulsion based on the system state, then we can control them to perform tasks by designing control policy on the self-propulsions. For example, self-propelled particles are viewed to possess tremendous potentials of being an intelligent agent[33] to localize and deliver nanoscopic object in complex environments (*e.g.*, tumors, porous media)[14,15,34,35]. A first step to achieve this goal is to establish a principle to reliably and precisely control their positions towards prescribed targets in complex environments.

Controlling multiple self-propelled colloidal particles present both substantial opportunities for potential applications and challenges in control strategy design. Examples of significant biomedical applications include cargo manipulation(e.g. capture and delivery), capture and isolation of cancer cells,[30] targeted drug delivery, and diagnosis. The challenges lying on the computational side include designing efficient algorithms to compute optimal control strategy for this high dimensional nonlinear system.

1.2.2 Low dimensional modeling and control of self-assembly processes

Self-assembly are dynamical processes where multiple predefined components spontaneously organize into ordered structures. Modeling a self-assembly process is inherently challenging because of the high dimensionality of the system and the requirement of the interpretability of the model.

In general, we require dynamic models to contain information about metastable states and the expected times for transitions between these states. Classic modelling tools include master equation,[36] Fokker Planck equation,[37] and Smoluchowski equation,[38] which use partial differential equation to capture the system evolution in the probabilistic point of view. To achieve interpretability and the predictability in the long time scale, the dynamic model is usually parameterized low-dimensional physical meaningful reaction coordinates instead of the full $3N$ particle coordinates.

Another requirement of low dimensional dynamic model is from the optimal control point of view. Even though self-assembly is considered as a fundamental bottom-up approach to fabricate micro- and nano-scale materials, [17-19] most of these processes take place at a fixed thermodynamic condition. As a consequence, these uncontrolled self-assembly processes often end up in undesired metastable states, instead of its global equilibrium state, and impose great limitations on the self-assembly methods for material engineering. Model based optimal control provides a route to overcome the hurdle. One of key challenges in model based optimal control is to construct model with relatively small dimensionality since optimal control algorithms usually have computational costs increase exponentially with the dimensionality of the model. Ideally, construction of such dynamic models at different thermodynamic conditions can enable designing control strategies of temporal switching thermodynamic conditions during the processes to achieve desired states.[9,39,40]

A typical feedback control system usually consists of functionalities of: (1) sensing the system state, (2) actuating particle via change thermodynamic conditions; and (3) closing the loop to assign actuator settings based on sensor readings (*via* an optimal policy). This approach adds robustness and self-correction machinery into the self-assembly process, therefore can be used to correct defects in real-time to produce perfect crystals.

1.2.3 Depletion in colloidal systems

Depletion interactions are ubiquitous in colloidal mixture systems. They arise when species of smaller particles excluded from gaps between larger colloid particles and surfaces. The exclusion creates the concentration difference of smaller particles inside the gap and outside the gap, thus causing an effective attraction among larger colloidal particles or surfaces. Typical colloidal mixture systems are monodisperse colloidal particle mixed with smaller particles from polymers, micelles, hydrogel particles, and nanoparticles.[41]

With an understanding of the mechanism of depletion attraction, we can engineer such potentials by manipulating either the osmotic pressure or the excluded volume. For example, using thermosensitive micelles,[42] hydrogel particles,[43,44] and polymer chains[45] as depletants enables changing the osmotic pressure and the excluded volume via temperature. For another example, by designing surface features,[46] researcher have created templates for crystallization,[47,48] and lock-and-key colloids (*i.e.*, local curvature).[49]

1.2.4 Hydrodynamics in colloidal rod systems

Hydrodynamic interaction are long range interactions between colloidal particles suspended in liquids. They arise either when the motion of one particle generates a velocity field in the fluid affecting the motion of nearby particles or when the velocity field is near a general no-slip boundary surface[50]. Hydrodynamics is essential in mediating the hindered diffusion when particle approaching no-slip surface[51] and generating couplings in some self-assembly systems consisting of self-spinning particles.[52] Even though the hydrodynamics of spherical system has been extensively researched in the past decades,[53] there is still limited understanding on how hydrodynamics affects rod motion near a planar substrate. We are particularly interested in the hydrodynamics of colloidal rods, because they appear in a wide variety of areas, ranging from biological macromolecules[54] to novel building blocks in materials engineering.[55]

The diffusion behavior of individual rod in the suspension is fully determined by its 6 by 6 diffusivity tensor, **D**. A colloidal rod in the bulk will have different translational and rotational diffusion coefficients in directions along and perpendicular to its long axis;[56] its diffusivity tensor **D** will only have diagonal terms in its own body frame(i.e., no couplings between different modes of motion). However, when a colloidal rod is near a no-slip planar wall, the bounding surface will make self-diffusion coefficients (*i.e.*, diagonal terms in **D**) of the rod be a function of its intrinsic geometry(i.e. length and aspect ratio), and other external parameters (*e.g.*, elevation and orientation). Moreover, additional couplings among translations and rotations appear; the off-diagonal terms in **D** will contain non-zero entries.

1.3 Summary and dissertation outline

This dissertation is organized as follows: *Chapter 2* describes general theory for (i) colloid and surface interactions, (ii) order parameters for colloidal assembly, (iii) stochastic process theory, and (iv) optimal control theory for stochastic systems. *Chapter 3* describes common methods used in the dissertation, including parameter estimations in stochastic systems, and computational methods for stochastic optimal control. *Chapters 4-10* describes the major results of the PhD research. *Chapter 4* develops the single agent stochastic optimal algorithm for single colloidal self-propelled rod and its direct application in maze navigation. This algorithm enables calculation of optimal strategy of applying self-propulsion velocity given real-time system states such that the rod can arrive prescribed target in minimum time. *Chapter* 5 extends the single agent stochastic optimal control to multiple agent stochastic optimal algorithm, which enables optimal control of multiple agents, i.e., self-propelled colloids, to multiple prescribed targets. This multiple agent optimal control algorithm is used as the building blocks for constructing cargo capture and transport algorithms. The working mechanism of cargo capture and transport is analyzed in details to reveal the fundamental design principles for micro-machines. *Chapter 6-8* combines low dimensional modeling method and optimal control theory to examines issues: (1) grain boundary formation and dynamics using low dimensional model; (2) optimal strategy to assemble perfect colloidal crystal using electric field mediated interactions. The low dimensional model describes the system's evolution of crystallization microstructures in terms of global ordering and condensation. *Chapter 9* describes a method to continuously grow ordered colloidal crystal using feedback controller, which is an extension of chapter 9 to scalable fabrication of colloidal crystals. *Chapter 10* describes a generic computational modeling approach for depletion mediated colloidal assembly on topographic patterns. *Chapter 11* investigate the colloidal rod motion near a planar wall. Using a modified Stokesian dynamic simulation method, the diffusivity tensor of a colloid rod as a function of its configuration is obtained. A set of trajectory analysis methods were developed to extract dynamical and equilibrium properties from rod motion trajectories. *Chapter 12* summarizes the conclusions from these chapters. Finally, *Chapter 13* presents some preliminary results on ongoing research projects and author's views on future directions related to this dissertation.

2 THEORY

2.1 Colloidal and surface interactions

2.1.1 Net potential energy interactions

Throughout this dissertation, we usually consider a system of N spherical particles experiencing forces due to interaction from different sources, including gravity, electric field, electrostatic repulsion with underlying substrate, depletion interactions and electrostatic repulsion with nearby particles. The net potential u_i of a single particle i can be written as the sum of potentials from individual sources, given as

$$u_i = u_G^{pf} + u_{DE}^{pf} + u_E^{pw} + \sum_{j \neq i} u_{E,ij}^{pp} + \sum_{j \neq i} u_{DD,ij}^{pp} + \sum_{j \neq i} u_{D,ij}^{pp} \tag{2.1}$$

where the subscripts refer to interactions of: (G) gravitational, (DE) induced-dipole-electric field, (E) electrostatic repulsion, (D) depletion, and (DD) induced-dipole-induced-dipole; superscripts refer to interactions of: (pf) particle-field, (pw) particle-wall, and (pp) particle-particle. u_i will usually be a function of positions of all the particles. The resulting force acting on the particle i is simply given as

$$F_i = -\nabla u_i \tag{2.2}$$

where the gradient is taken with respect to the position of particle i.

2.1.2 Gravitational interactions

The gravitational potential energy for each colloidal particle is given as

$$u_G^{pf}(z) = Gh = mg\left(z-a\right) = \left(4/3\right)\pi a^3(\rho_p - \rho_f)g\left(z-a\right) \tag{2.3}$$

where G is the buoyant weight, g is the gravitational acceleration, a is the radius of the particle, ρ_p and ρ_f are the particle and fluid densities, respectively.

2.1.3 Electrostatic interactions

When suspended in an aqueous solution, a charged surface will induced a cloud of counterions, whose density distribution is governed by Poisson-Boltzmann equation. The density profile of the counterions will be a function of distance to surface and will decay exponentially with characteristic length κ^{-1}, given as

$$\kappa = \left(2e^2Z^2n_b / \varepsilon_m kT\right)^{1/2} \tag{2.4}$$

where Z is the electrolyte valence, ε_m is the solvent dielectric constant, k is Boltzmann's constant, T is absolute temperature, e is the elemental charge and n_b is the bulk number concentration of ions. For a 1:1 monovalent electrolyte, $n_b = N_A C$, where C is the electrolyte molarity and N_A is Avogadro's number. When two surfaces with the same charge approach each other, the overlapping the counterions will induce a repulsive force, known as double layer electrostatic repulsion. When $\kappa a << 1$, the electrostatic repulsion between a colloidal spherical particle and its underlying charged planar substrate is given as

$$\begin{gathered} u_E^{pw}(z) = 2B\exp\left[-\kappa(z-a)\right] \\ B = 32\pi\varepsilon_m a\left(\frac{kT}{e}\right)^2 \tanh\left(\frac{e\psi_1}{4kT}\right)\tanh\left(\frac{e\psi_2}{4kT}\right) \end{gathered} \tag{2.5}$$

where ψ_1 and ψ_2 are surface potentials on the two interacting surfaces and z is the distance between the center of sphere to the planar wall. Similarly, the electrostatic repulsion between two colloidal particles i and j is given as

$$u_{E,ij}^{pp}\left(r_{ij}\right) = B\exp\left[-\kappa\left(r_{ij}-2a\right)\right] \tag{2.6}$$

where r_{ij} is the distances between the centers of the particles i and j.

2.1.4 Depletion potentials

In a binary mixture of colloidal particles of two different sizes, there exists an entropy effect that induce an attraction between the large particles and between large particle and the underlying planar substrate. When two large particles are approaching each other such that the gap in between cannot fit the small particles, the osmotic pressure of small particles has a larger value outside the gap (i.e., the bulk solution) than inside gap. As a consequence of this imbalance, the osmotic pressure will push the two large particle to get closer, appearing as an attraction, known as depletion attraction, between the large particles. Such depletion attraction was first modeled by Asakura and Oosawa (AO), and further improved as,[57]

$$\begin{aligned} u_D^{pp}(r) &= -V^{pp}\left(r\right)\Pi \\ u_D^{pw}(z) &= -V^{pw}\left(z\right)\Pi \end{aligned} \tag{2.7}$$

where V^{pp} and V^{pw}.are the excluded volume(the volume between the gap where the depletent cannot fit in), and Π is the osmotic pressure of the depletants. The excluded volume terms is a function of separation, which can be obtained from geometric considerations given by,[2,58,59]

$$\begin{aligned} V^{pp}\left(r\right) &= \pi\left[\left(4/3\right)\left(a+L\right)^3\left(1-\left(3/4\right)r\left(a+L\right)^{-1}+\left(1/16\right)r^3\left(a+L\right)^{-3}\right)\right] \\ V^{pw}\left(z\right) &= \pi\begin{bmatrix}\left(4/3\right)L^3+4L^2a-4La\left(z-a\right) \\ +a\left(z-a\right)^2-L\left(z-a\right)^2+\left(1/3\right)\left(z-a\right)^3\end{bmatrix} \end{aligned} \tag{2.8}$$

where L is the depletant radius, p is the center-center distance, and z is the center to surface distance.

2.1.5 Induced-dipole interactions

In a non-uniform AC electric field, a colloidal particle will be induced an effective dipole due to the distortion of counterions distribution surrounding the particle by the electric field. The induced effective dipole will have the general form as

$$p = \alpha E \tag{2.9}$$

where α is the effective permittivity and E is the electric field vector. This induced effective dipole will contribute two additional interactions to the system: the particle-field interaction known as induced-dipole-electric-field interaction and the particle-particle interaction known as induced-dipole-induced-dipole interactions. The induced-dipole-electric-field interaction with a potential given by,[60]

$$u_{DE}^{pf}\left(r_i\right) = -2kT\lambda_E f_{cm}^{-1} E^*\left(r_i\right)^2 \tag{2.10}$$

where r_i is the position vector for particle *i*, E* is the normalized electridc field magnitude profile function, E_0 is the characteristic electric field magnitude used as the normalizing constant, the non-dimensional parameter λ_E is given as

$$\lambda_E = \pi\varepsilon_m a^3 \left(f_{cm}E_0\right)^2 / kT \tag{2.11}$$

and f_{cm} is the Clausius-Mosotti factor given as,

$$f_{cm} = \mathrm{Re}\Big[\Big(\tilde{\varepsilon} \qquad \tilde{} \qquad \tilde{} \qquad \tilde{} \qquad \_ \tag{2.12}$$

Here $\tilde{\varepsilon}_m$ and $\tilde{\varepsilon}_p$ are complex medium and particle permitivities of the form, $\tilde{\varepsilon} = \varepsilon - \mathrm{i}\sigma/\omega$, where σ is the conductivity, and ω is the angular frequency.

Similarly, the induced-dipole-induced-dipole interaction potential is given as

$$u_{DD,ij}^{pp}\left(r_{ij}, \theta_{ij}, R\right) = -kT\lambda_E P_2\left(\cos\theta_{ij}\right)\left(2a/r_{ij}\right)^3 E^*\left(R\right)^2 \tag{2.13}$$

where r_{ij} is the center-to-center distance between particles i and j, θ_{ij} is the angle formed between induced dipole direction of particles i and j, and $P_2(\cos\ \theta_{ij})$ is the second order Legendre polynomial.

2.2 Common order parameters for colloidal assembly

To monitor the structural evolution of the colloidal assembly process, it is important to define some order parameters, which are the functions of the particle configuration, to characterize the structural properties of the particle configurations.

2.2.1 Radius of gyration

The degree of condensation of a set of n colloidal particles is captured using the radius of gyration, R_g, which is defined as,

$$R_g = 0.5n^{-1}\left[\sum\left\|r_i - r_j\right\|^2\right]^{0.5} \tag{2.14}$$

where r_i is the position vector of particle i. R_g will take larger values for configurations that are less compact.

2.2.2 Global and local order parameters

The degree of global order in particle configurations is defined as,[61-63]

$$\psi_6 = \frac{1}{j}\sum_j \psi_{6,j} \tag{2.15}$$

where $\psi_{6,j}$ is the six-fold bond orientational order parameter of particle j, defined as

$$\psi_{6,j} = \frac{1}{n_{C,j}}\sum_{k=1}^{n_{C,j}} e^{i6\theta_{jk}} \tag{2.16}$$

where $n_{C,j}$ is the number of neighbors within the first coordinate shell of particle j, θ_{jk} is the angle of the vector joining particle i and j. ψ_6 produces values between 0 and 1, with 0 indicates 0 crystallinity and 1 indicate perfect crystal crystalline.

The degree of local order of a given particle configuration can be defined as

$$C_6 = \frac{1}{n}\sum_{i=1}^{n} C_{6,i} \tag{2.17}$$

where the local crystallinity $C_{6,j}$, for particle j, counting the number of crystalline nearest neighbors, is defined as

$$C_{6,j} = \sum_{k=1}^{nc_j}\begin{bmatrix}\begin{vmatrix}1 & \chi_{6,j} \geq 0.32 \\ 0 & \chi_{6,j} < 0.32\end{vmatrix}\end{bmatrix} \tag{2.18}$$

where $\chi_{6,j}$ is known as the connectivity between crystalline particles, given by,

$$\chi_{6,j} = \frac{\left|\operatorname{Re}\left[\psi_{6,j}\psi_{6,k}^{*}\right]\right|}{\left|\psi_{6,j}\psi_{6,k}^{*}\right|} \tag{2.19}$$

2.3 Stochastic process theory

2.3.1 Ito stochastic differential equation

Colloidal particles experience Brownian motion due to imbalanced molecular collision and drift due to potential energy gradients. Let $x(t)$ be the 1D position of a colloidal particle, then $x(t)$ is stochastic process, and it is governed by the Ito stochastic differential equation given as

$$dx(t) = m(x(t),t)dt + \sigma(x(t),t)dw(t) \tag{2.20}$$

where m is the drift coefficient, σ is the variance coefficient, and w(t) is the standard Wiener process satisfying[64]

$$\langle w(t)\rangle = 0, \langle w(t)w(s)\rangle = t\delta(t-s) \tag{2.21}$$

To simulate a stochastic process governed by Eq. (2.20), we can use the following discretized form as

$$x(t+\Delta t) = x(t) + m(x(t),t)\Delta t + \sigma(x(t),t)\varepsilon \tag{2.22}$$

where Δt is the integration time step, and ε is the normal random variable with zero mean and variance Δt.

The drift coefficient m and the variance coefficient σ are related to the physical property of the system as

$$m = -\frac{D}{kT}\frac{dW}{dx} + \frac{dD}{dx}, \sigma = \sqrt{2D(x)} \tag{2.23}$$

where D(x) is the diffusivity landscape (DL), W(x) is the free energy landscape (FEL), k is the Boltzmann's constant and T is the absolute temperature. The gradient term dD/dx is known as spurious drift.[65]

Similarly, a colloidal particle undergoing multiple dimensional drift and diffusion can be modeled by multiple dimension Ito stochastic differential equation, given as

$$d\mathbf{x}(t) = (-\frac{\mathbf{D}}{kT}\cdot\nabla W + \nabla\cdot\mathbf{D})dt + \sqrt{2\mathbf{D}}\cdot d\mathbf{w}(t) \tag{2.24}$$

where $\mathbf{x} \in R^3$, **D**(x) is the 3×3 diffusivity landscape, and $W(\mathbf{x})$ is the 3D free energy landscape, and **w**(t) is the 3D wiener process satisfying

$$\langle w_i(t)\rangle = 0, \langle w_i(t)w_j(s)\rangle = t\delta_{ij}\delta(t-s), i,j = 1,2,3 \tag{2.25}$$

where the subscript denote the component of wiener process.

2.3.2 Fokker-planck equation

The Fokker-Planck equation is a partial differential equation governing the evolution the probability density of a stochastic process. Formally, let $x(t)$ be the stochastic process governed by Ito stochastic differential equation(Eq. (2.24)) given by

$$d\mathbf{x}(t) = (-\frac{\mathbf{D}}{kT}\cdot\nabla W + \nabla\cdot\mathbf{D})dt + \sqrt{2\mathbf{D}}\cdot d\mathbf{w}(t) \tag{2.26}$$

Then the corresponding Fokker-Planck equation is given as[37]

$$\frac{\partial p(\mathbf{x}(t),t)}{\partial t} = \nabla\cdot(p(\frac{\mathbf{D}}{kT}\cdot\nabla W - \nabla\cdot\mathbf{D})) + \sum_{i,j}^{3}\frac{\partial^2}{\partial x_i \partial x_j}D_{ij}p \tag{2.27}$$

where $p(\boldsymbol{x}(t),t)$ is the probability density function for the random variable $\mathbf{x}(t)$ at time t.

2.3.3 Smoluchowski equation

The Smoluchowski equation is a special form of the Fokker-Planck equation, usually, it is written as

$$\frac{\partial p(\mathbf{x}(t),t)}{\partial t} = \nabla\cdot(p\frac{\mathbf{D}}{kT}\cdot\nabla W) + \sum_{i,j}^{3}\frac{\partial}{\partial x_i}D_{ij}\frac{\partial}{\partial x_j}p \tag{2.28}$$

which can be obtained by directly expand the second term of the right-hand side of Eq. (2.27). We can also write Eq. (2.28) in a more compact vector form as

$$\frac{\partial p(\mathbf{x}(t),t)}{\partial t} = \nabla\cdot(p\frac{\mathbf{D}}{kT}\cdot\nabla W) + \nabla\cdot(\mathbf{D}\cdot\nabla p) \tag{2.29}$$

The equilibrium solution to Eq. (2.28) as $t\rightarrow\infty$ is given as

$$p^{eq}(\mathbf{x}) \propto \exp(-\frac{W(\mathbf{x})}{kT}) \qquad (2.30)$$

which can be obtained from Eq. (2.29) by setting the left-hand side to be zero.

2.4 Stochastic optimal control theory

Consider a dynamic model represented by a set of finite state Markov chains parameterized by finite actions *a* from action space *A* on state space S, given as

$$p(s_{n+1}) = P(s_{n+1} \mid s_n, a) p(s_n), a \in A \qquad (2.31)$$

We can further associate with each state with a cost, *i.e.*, via a cost function *C*: *S*→*R*. The optimal control problem can be formulated as the optimization as

$$\min_{\pi} \mathbb{E}\left[{}_{n=0} \qquad (s_n) \right] \qquad (2.32)$$

where π: S → A is a function, known as the control policy, we are optimizing over, and γ∈[0,1) is the discount factor with larger value putting larger weights on future cost. The cost function can associate large cost with the undesired state and smaller cost with desired state such that the optimal policy π* will try to avoid undesired states and prefer to stay in desired state.

The optimization problem in Eq. (2.32) can be solved using dynamic programming principles, as we will discuss in the next chapter.

With a control policy π (optimal or non-optimal), the probability evolution of the system state can be obtained by iterating the Markov chain, given as

$$
\begin{aligned}
P(s_n \mid s_0) &= [\prod_{i=0,\ldots,n-1} P(s_{i+1} \mid s_i, \pi(s_i))]P(s_0) \\
P(s_0) &= I_{s_{init}}(s_0)
\end{aligned}
\tag{2.33}
$$

where s_{init} is the system’s initial state, $I_x(y)$ is the indicator function that equals 1 only if $x=y$.

3 METHODS

3.1 Parameter estimation in multi-dimensional smoluchcowski equation

Consider an *m* dimensional Smoluchowski equation given as

$$\frac{\partial p(\mathbf{x}(t),t)}{\partial t} = \nabla\cdot(p\frac{\mathbf{D}}{kT}\cdot\nabla W) + \nabla\cdot(\mathbf{D}\cdot\nabla p) \tag{3.1}$$

where $\mathbf{x} \in R^{m}$ and $\mathbf{D} \in R^{mm}$. Our goal is to estimate the parameter **D** and *W* from the trajectories. This Smoluchowski equation has the associated Fokker-Planck equation and Ito stochastic differential equation given as

$$\frac{\partial p(\mathbf{x}(t),t)}{\partial t} = \nabla\cdot(p(\frac{\mathbf{D}}{kT}\cdot\nabla W - \nabla\cdot\mathbf{D})) + \sum_{i,j}^{3}\frac{\partial^2}{\partial x_i \partial x_j}D_{ij}p \tag{3.2}$$

$$d\mathbf{x}(t) = (-\frac{\mathbf{D}}{kT}\cdot\nabla W + \nabla\cdot\mathbf{D})dt + \sqrt{2\mathbf{D}}\cdot d\mathbf{w}(t) \tag{3.3}$$

We can define drift coefficient and diffusion coefficient in terms of the trajectory statistics as

$$\mathbf{D}_i^{(1)}(\mathbf{x}) = \lim_{\tau\to 0}\frac{1}{\tau}\left\langle x_i(t+\tau) - x_i(t)\right\rangle\Big|_{x(t)=\mathbf{x}} \tag{3.4}$$

$$\mathbf{D}_{ij}^{(2)}(\mathbf{x}) = \lim_{\tau\to 0}\frac{1}{2\tau}\left\langle \left[x_i(t+\tau) - x_i(t)\right]\left[x_j(t+\tau) - x_j(t)\right]\right\rangle\Big|_{\mathbf{x}(t)=\mathbf{x}} \tag{3.5}$$

where $\mathbf{D}^{(1)}$ is the drift vector field, $\mathbf{D}^{(2)}$ is the diffusivity tensor, the brackets represent an ensemble average. Then from Eq. (3.3), we have

$$\mathbf{D}_i^{(1)}(\mathbf{x}) = (-\frac{\mathbf{D}}{kT}\cdot\nabla W + \nabla\cdot\mathbf{D}) \tag{3.6}$$

$$\mathbf{D}_{ij}^{(2)}(\mathbf{x}) = \mathbf{D} \tag{3.7}$$

The free energy landscape, $W(\mathbf{x})$, can be obtained from $\mathbf{D}^{(1)}$ and $\mathbf{D}^{(2)}$ *via* integration as,

$$\frac{W(\mathbf{x}_2)-W(\mathbf{x}_1)}{kT}=-\int_{\mathbf{x}_1}^{\mathbf{x}_2}(\mathbf{D}^{(2)})^{-1}\cdot(\mathbf{D}^{(1)}-\nabla\cdot\mathbf{D}^{(2)})d\mathbf{x} \tag{3.8}$$

where the integral can be evaluated from an arbitrary path from $\mathbf{x}_1$ to $\mathbf{x}_2$.

3.2 Value iteration method for infinite horizon optimal control

In the stochastic optimal control using Markov decision process framework for infinite horizon, we usually need to solve the following optimization problem

$$\begin{gathered}\min_{\pi}\mathbf{E}[\sum_{n=0}^{\infty}\gamma^n C(s_n)]\\ P(s_n)=P(s_n\,|\,s_{n-1},a)P(s_{n-1})\end{gathered} \tag{3.9}$$

where $\gamma\in[0,1)$ is the discount factor, C is the cost function depend on the system state $s_n\in S$ (n is the time step, S is the state space), and the system model is descriped by a finite state Markov chain parameterized by the finite actions $a\in A$ (A is the action space) as $P(s_n|s_{n-1},a)$, and the goal is to seek an policy π: S→A such that the objective function is minimized.

To solve this optimization problem, we can define a cost-to-go function under policy π as

$$J^{\pi}(s_0)=\mathbf{E}[\sum_{n=0}^{\infty}\gamma^n C(s_n)] \tag{3.10}$$

where the cost-to-go function J only depends the control policy π and the initial state s_0. We can defined value function as

$$V(s_0)=\min_{\pi}J^{\pi}(s_0) \tag{3.11}$$

Using the dynamical programming principle, we have the following relationship,[66]

$$V(s_0) = C(s_0) + \min_a \sum_{s_1 \in S} \gamma P(s_1 \mid s_0, a) V(s_1) \tag{3.12}$$

Furthermore, (1) we can equip the space of all value function with an 2-norm and therefore convert the space of all value function into a normed vector space ; (2) we define an normed vector space an operator *T* map from the value function space to the value function space as

$$TV = C + \min_\pi \gamma VP \tag{3.13}$$

It can be showed that the operator *T* is a contraction mapping; therefore, there exists an unique value function *V** as the fixed point of the operator (which is also the minimum value of objective function in (3.9)).[66,67] As a consequence, we can start with an initial guess of V^0 and iterate until convergence using the following iteration formula, given as

$$V^{n+1} = TV^n \tag{3.14}$$

4 OPTIMAL NAVIGATION OF SELF-PROPELLED COLLOIDAL RODS IN MAZES

4.1 Abstract

Controlling navigation of self-propelled microscopic ‘robots’ subject to random Brownian motion in complex microstructured environments (*e.g.*, porous media, tumor vasculature) is important to many emerging applications (*e.g.*, enhanced oil recovery, drug delivery). In this work, we design an optimal feedback policy to navigate an activatible self-propelled colloidal rod in complex mazes. Actuation of the rods is modeled based on a light-controlled osmotic flow mechanism, which produces different propulsion velocities along the rod’s long axis. Actuation-parameterized Langevin equations, with soft rod-obstacle repulsive interactions, are developed to describe the system dynamics. A Markov decision process (MDP) framework is used for optimal policy calculations with design goals of colloidal rods reaching target end points in minimum time. Simulations show that optimal MDP-based policies are able to control rod trajectories to target regions successively in mazes with increasing complexities. The structure of the optimal control policy demonstrates the general principle of navigation: globally following the geometric paths and locally utilizing Maxwell’s demon-like strategy.

4.2 Introduction

Inspired by the natural micro-swimmers, such as bacteria and sperm, numerous man-made micro-swimmers/robotics has been created in the most recently years.[27] These swimmers take various forms, such as bimetal nano-rods and Janus spheres, and function on different strategies, such as catalysis of chemical fuels[27] and mimicking natural swimmers[28]. Proof-of-concept applications of these man-made swimmers have been investigated in a broad range of areas. For example, biomedical applications includes using self-propelled "micro-device" to capture and isolate of cancer cells,[30] navigate and deliver drugs[13,31]; environment applications include using self-propelled micro-motors to clean polluted water.[12] In particular, it is anticipated that such micro-swimmers possess tremendous potentials of being an intelligent agent[33] to localize and deliver nanoscopic object in complex environments (*e.g.*, tumors, porous media) , and further being the building blocks of nano and micro functional machines[14,15,34,35]. Broadly relevant research includes the behavior of micro-swimmer in homogenous and inhomogeneous environments with random or patterned obstacles,[68] thermodynamics of active matter system[69], and assembly of cluster and crystalline structures with self-propelled particles. [26,32]

Consider a self-propelled colloidal rod (Fig. 1A) as a representative model for a broad range of micron sized devices, particles, and objects that can make fast deterministic movements along its axis *via* propulsion. A first step towards fully unleash the potential of these self-propelled rods is to establish a principle to reliably and precisely control the rod's position towards prescribed targets in complex environments. More precisely, navigation of a self-propelled rod involves guiding it to follow a certain geometric path towards the target and then maintains it around the target. The navigation process is against the Brownian motion of the rod itself, which drives the rod to uniformly sample all possible positions and orientations available to the system as required by entropy maximization. Therefore, to fight against Brownian motion, an effective navigation usually requires actuators, such as tunable propulsion, to make the system controllable. Recently, simple feedback control rule to position a self-propelled particle to prescribed location in free space has been investigated experimentally using photo nudging.[70,71] However, considering complex environment containing obstacles and dead-ends, the principle for optimal navigation remains unclear. Moreover, questions like the minimal requirement and the limitation for optimal navigation, which will be ultimately connected to the design the self-propelled systems, have not been addressed. The goal of this work is to study the principle of optimal navigation, and its generalizations and limitations. Ultimately, understanding the optimal control principle for the single rod task will provide insight to solving more challenging control tasks, such as multi-agent control. From a more general perspective, the controlled navigation of self-propelled rods can also be viewed as navigation the system through an entropy landscapes parameterized by the positions. Relevant theoretical and practical aspects of modeling and navigation through landscapes have been investigated extensively in our previous research.[9,72]

Here we use computer simulation and optimal control algorithms to study the optimal navigation of the self-propelled micro-motors in mazes of increasing complexity and the underlying principles for optimal navigation. We consider a simple binary actuation system with feedback control (Fig. 1). This feedback control system consists of: (1) a sensor (e.g. microscope) sensing the system state, *i.e.*, the rod's position and orientation, (2) a actuator (e.g. a tunable lighting device) actuating ON or OFF of the propulsion, and (3) closing the loop to assign actuation based on system state sensor readings (*via* an optimal policy). A discrete Markov chain model is used to obtain a probabilistic description of the system evolution under different actuations. A Markov decision process framework, using the Markov chain model as an input, is used to calculate the optimal control strategy under various circumstances ranging from free space, simple mazes to complex mazes. We first consider concrete examples of optimal navigation, and then we generalize our optimal navigation principle to various settings. The ultimate goal of this research is to apply such feedback control scheme into real-time experiments, in which the theoretical and practical aspects have been addressed in our previous feedback controlled colloidal crystallization studies. [9,73,74]

4.3 Methods

4.3.1 Equation of motion

The equation of motion of a self-propelled rod subject to Brownian motion in 2D can be modeled as

$$\begin{aligned} \mathbf{r}(t+\Delta t) &= \mathbf{r}(t) + \frac{\mathbf{D}_t}{kT}\cdot\mathbf{F}\Delta t + \Delta\mathbf{r}^B + v\cos(\varphi)\mathbf{e}_1 + v\sin(\varphi)\mathbf{e}_2 \\ \varphi(t+\Delta t) &= \varphi(t) + \frac{D_r}{kT}\mathbf{T}\cdot\mathbf{e}_3\Delta t + \Delta\varphi^B \end{aligned} \tag{4.1}$$

where v is the propulsion speed as the control input (concrete realization of the propulsion velocity might depend on the specific mechanism and application, here we assume it is using light activation mechanism[75]), $\mathbf{r}$ is the position vector of the rod, Δt is the integration time step, k is the Boltzmann's constant, T is the temperature. $\mathbf{D}_t$ is the diffusivity tensor (in the lab frame), which can be obtained *via* $\mathbf{D}_t = \mathbf{nn}D_{t,\parallel} + (\mathbf{I}-\mathbf{nn})D_{t,\perp}$, where $\mathbf{I}$ is the indentity tensor, $\mathbf{n}$ is the orientation vector $\mathbf{n}$ = (cos(φ),sin(φ)), $D_{t,\parallel}$ and $D_{t,\perp}$ are the translational diffusivity coefficients parallel and perpendicular to its long axis, and dyadic product is applied on product $\mathbf{nn}$. D_r is the rotation diffusion coefficient. Brownian translational and rotational displacement vectors $\Delta\mathbf{r}^B$ and $\Delta\mathbf{r}^R$ obey

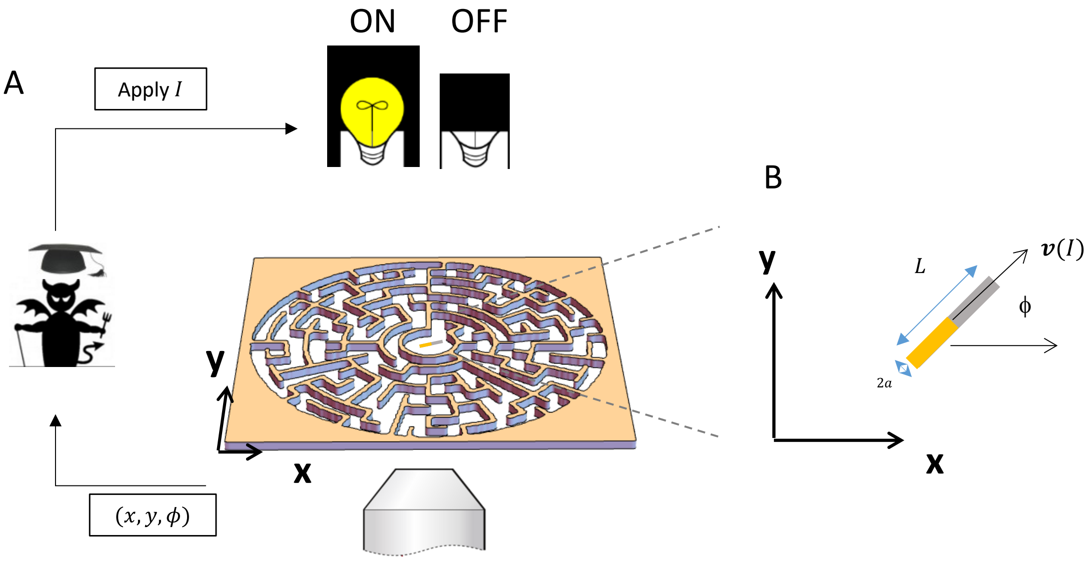

Figure 1 | Schematics of navigating self-propelled rod in a maze with feedback control. (A) The imaging system feed the state information (x, y, ϕ) into the controller (here represented by a Maxwell demon), which decides turning on or off the stimulating light. The stimulating light will enable the rod to generate self-propulsion along its long axis. (B) The coordinate system used to measure the position and orientation of the rod. The self-propelled rod has a length of L, and diameter of $2a$, and it will propel itself along its long axis with speed v as function of light intensity I.

$$\begin{aligned} \left\langle \Delta\mathbf{r}^B \right\rangle = 0, \left\langle \Delta\mathbf{r}^B (\Delta\mathbf{r}^B)' \right\rangle = 2\mathbf{D}_t \Delta t \\ \left\langle \Delta\varphi^B \right\rangle = 0, \left\langle \Delta\varphi^B \Delta\varphi^B \right\rangle = 2D_r \Delta t \end{aligned} \tag{4.2}$$

where the superscript ‘’’ denotes transpose operation. The force **F** and torque **T** resulting from interactions between the rod and the obstacles are documented in Methods.

One important characteristic of this model is that the orientation, *i.e.*, the direction of the propulsion, cannot be directly controlled. When there is nonzero propulsion velocity, i.e., $v > 0$, directed motion can be observed in the short time scale(observation time $t \ll 1/D_r$), whereas random motion will be observed on a longer time scale(observation time $t \gg 1/D_r$).

4.3.2 Optimal control framework & probability evolution

With a set of realizable propulsion speeds, an optimal control policy in the navigation task is a set of rules specifying which velocity to use when given the instantaneous system state characterized by (x, y, ϕ) such that the rod can reach prescribed target at some minimum cost (*e.g.*, time, energy consumption *etc.*). We use Markov decision process framework(MDP) to calculate the optimal control policy. [76] This framework has greater generalization and flexibility to deal with stochastic nonlinear effect due to the nonlinear coupling of Brownian rotation to the self-propulsion compared to classical linear Gaussian controllers.[77] In this framework, a discrete-time Markov chain model is first built to model the probability transition under propulsions, and then an optimal control policy is obtained that minimize the custom defined cost function associated with a Markov process characterized by the Markov chain model.

As showed in Fig. 2A, an MDP is characterized by parameters (S, P, A, C): (1) S, known as state space, is a finite set consisting of elements s that describe possible states the system; (2) A, known as action space, is a small set of possible actions or decisions allowed to control the system; (3) C is one-discrete-time-step, or simply one-step, cost function that specifies the cost of being in a state (and possibly performing some action); (4) $P(s_{n+1}|s_n,a_n)$ is the one-step transition probability specifying the probability of its next state $s_{n+1} \in S$ if the rod is starting at state $s_n \in S$ and taking action $a_n \in A$ during this time step(Here the subscript n is used to index the time step). Note that in our current study of rod navigation in different environments, S is simply the collection of discretized states (x, y, ϕ) excluding those overlapping with obstacles; P is essentially a Markov chain model that describes the system dynamics using transition probabilities, which can usually be estimated from the simulated or experimental data; *A* will only have two elements ON and OFF, representing propulsion is on or off. In general, *A* might depend on the state the system (in cases where some action is restricted), and can be written as *A*(*s*).

We formulate the optimal navigation policy as a policy enable the system to reach our prescribed target state with minimum (time) cost starting from arbitrary initial state s_0 as:[76]

$$\begin{aligned} &\pi^* = \arg\min_{\pi} \mathbf{E}[\sum_{n=0}^{T} \gamma^n C(s_n)], \\ &C(s_n) = \begin{cases} 0, \text{if } s_n \in S^{target} \\ 1, \text{otherwise} \end{cases} \\ &P(s_n) = P(s_n \mid s_{n-1}, a) P(s_{n-1}) \end{aligned} \tag{4.3}$$

where $\mathbb{E}$ is the expectation with respect to probability distribution of the trajectories under control policy, $\pi{:}S \rightarrow A$ that maps a state to an action, s_n is the system state at time step *n*, *T* is the time horizon (*i.e.*, number of steps) for the planning, and the cost function *C* essentially says a cost of 1 will be incurred if the system is not reside in the target states S^{target}, a subset of *S*. Note: the cost value 1 can be other positive scalar and will not affecting the solution; such formulation is commonly used in motion planning of robotic system; [78] the argument π of the objective function is implicitly included in the expectation operator since π affects the future state probability distribution (See Eq. (4.3) third line). We put the details of numerical solution of Eq. (4.3) in *methods*. The feedback control system used throughout this manuscript is showed in Fig. 2B: a sensor(*i.e.*, a microscope) that reads the the state $s=(x, y, \phi)$ of the system; then the policy π will map the state s to certain action, *i.e.*, propulsion speed; then the corresponding propulsion speed is appied onto the system for a period of update time Δt_c.

With a control policy π (optimal or non-optimal), the probability evolution of the system state under the action of the optimal control can be obtained by iterating the Markov chain, given as

$$\begin{aligned} &P(s_n \mid s_0) = [\prod_{i=0,\ldots,n-1} P(s_{i+1} \mid s_i, \pi(s_i))]P(s_0) \\ &P(s_0) = I_{s_{init}}(s_0) \end{aligned} \tag{4.4}$$

where s_{init} is the system's initial state, $I_x(y)$ is the indicator function that equals 1 only if $x=y$.

Based on Eq. (4.4), mean first passage time distribution predicted from the Markov chain model can be calculated as

$$P(n\Delta t) \approx \sum_{s_n \in S^{\text{target}}} P(s_n \mid s_0) - \sum_{s_{n-1} \in S^{\text{target}}} P(s_{n-1} \mid s_0) \tag{4.5}$$

where Eq.(4.5) is a discrete time version of $\rho(\tau) = \frac{d}{d\tau}\int_0^\tau \mathrm{d}t \int_{s \in S^{target}} P(s(t) \mid s_0)\,\mathrm{d}s$ in continuous system.[37]

4.4 Results & discussion

4.4.1 Transition probability in free space

As a demonstration of optimal control principle, we first consider concrete examples of optimal navigation and then generalize the principle later. We select a rod of length 1um, the available control contains an OFF mode with propulsion speed 0um/s and an ON mode with propulsion speed 4.5um/s, and the control update time Δt_c = 1s. Other details related to the simulation are included in *Methods*. The MDP framework requires a Markov chain model to approximate the system dynamics, which is described by the transition probability $P(s_{n+1} \mid s_n, a)$ (each time step is Δt_c = 1s). Fig. 2 shows the transition probability of the rod under different actuations *a* for one discrete time step Δt_c = 1s with starting state (x, y, ϕ)=(0, 0, 0). The position (x, y) distribution after one Δt under OFF mode (v=0um/s) gives a Gaussian shape with mean position located at (0, 0) (Fig. 2A), whereas the distribution becomes a strong distorted 'Gaussian' with mean position located at ~(4.5

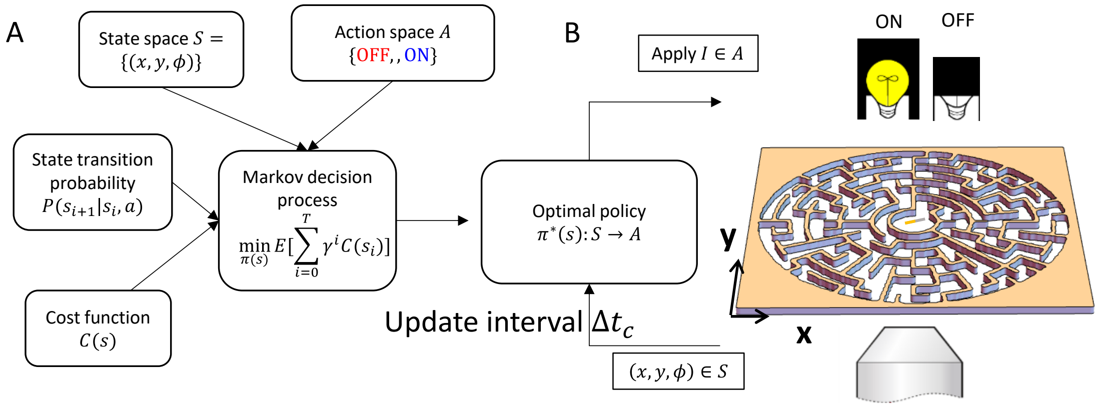
A
State space $S = \{(x, y, \phi)\}$
Action space A $\{OFF, , ON\}$
State transition probability $P(s_{i+1}|s_i, a)$
Markov decision process
$\min_{\pi(s)} E[\sum_{i=0}^{T} \gamma^i C(s_i)]$
Cost function $C(s)$
B
Apply $I \in A$
ON
OFF
Optimal policy $\pi^*(s): S \to A$
Update interval Δt_c
$(x, y, \phi) \in S$
y
x

Figure 2 | Schematics of calculating optimal control policy using Markov decision process framework offline and execute optimal control plan online. (A) Markov decision process framework takes state space S, action space A, state transition probability P and a cost function C as input, and produce an optimal control policy. (B) Execute the optimal policy using feedback loop with every 1s control interval. The current state (x, y, ϕ) is feed back to update the current control action.

um, 0) under the ON mode (v=4.5um/s) as a result of the propulsion (Fig. 2B). The angular

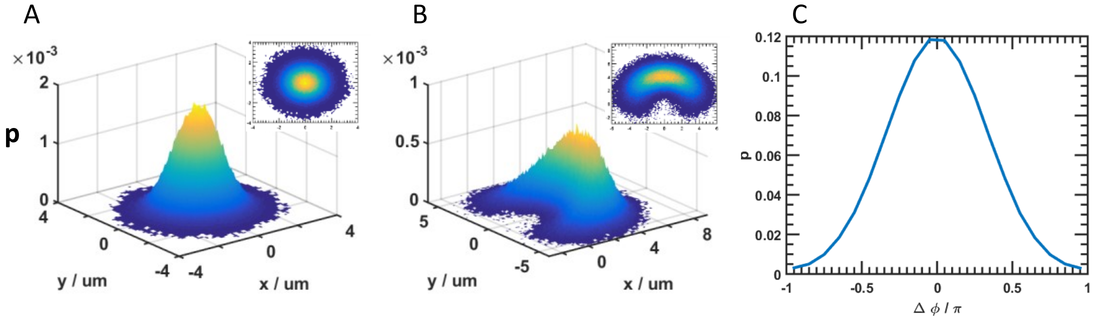

Figure 3 | Plot of transition probability $p(s_{n+1}|s_n,a)$ under different actions a with discrete time step 1s starting from initial state (0, 0, 0). (A)(B) Probability distribution of position (x, y) after one discrete time step under actions of off mode (A) and on mode(C). (D) Probability distribution of angular displacement after one discrete time step. Note that the choice of action will not affect this angular distribution.

displacement distribution (Fig. 2C) is Gaussian with zero mean and standard deviation of $\sqrt{\langle \Delta\phi^2 \rangle} = \sqrt{2D_r \Delta t}$ ~60 degrees and does not depend on the propulsion velocity. This relatively large standard deviation in angular displacement is consistent with the large spread in the position probability distribution in the ON mode (Fig. 2B).

4.4.2 Rod navigation in free space

Using the transition probability as input, we can numerically calculate optimal control policy for different navigation task. The optimal navigation of self-propelled rods in free space towards a specified target is showed in Fig. 4. Fig. 4A shows a representative optimally navigated trajectory starting with initial state (x, y, ϕ) = (30,30,0) and the target position (x, y) = (0,0). The optimal control policy as a function of state (x, y, ϕ) specifies which propulsion speed v to use when the system is at state (x, y, ϕ) (Fig. 4B). The policies at different orientations are differed simply by a rotation around the target position (in here, the origin) due to the symmetry of free space. The optimal control policy is to minimize the mean deviation of position to the target at the next time step with given choices of velocities. The intuition picture underlying the control policy is that when the target is in the front and relatively far away, propulsion will be turned ON to reduce the mean distance to the target, whereas if the target is in the back or nearby, OFF mode with zero propulsion should be used, since using faster propulsion will tend to overshoot rather than decrease the mean distance to the target. If we denote the projection of target-rod distance vector onto the long axis of the rod as d_n, then the policy can be more compactly expressed as:

$$a = \begin{cases} \text{ON}, & d_n > 2.3um \\ \text{OFF,otherwise} & \end{cases} \tag{4.6}$$

Note that this policy resembles with Maxwell's demon[79] that only acts when the proper system state appears due to thermal fluctuations, or more generally uses information to drive an entropy-decreasing process.

We use the first passage time distribution of rod to the target (here we define arrival at target position as the distance to the target smaller than 2um) to evaluate the performance of using control vs. without control (*i.e.* using a single speed constantly). The first passage time is defined as the time taken by the rod to reach the target position from the initial position. The key result for free space navigation is that optimal control case can achieve finite first passage time with the mean of ~60s, whereas the mean first passage time for random walker (in the long time scale, uncontrolled fast, slow and diffusion mode can be all treated as random walker with effective diffusivity[80] given as $D_{eff} = D_t + v^2 / 4Dr$) to is unbounded.[81,82] The asymptotic distribution of the first passage time[82] (*i.e.* the distribution as *t* goes to infinity) goes like $1/t\ln^2(t)$, which agrees with our simulation results.

The evolution of probability distribution of the rod’s position under optimal control can be obtained by iterating Eq.(4.4). The resulting probability evolution (in Fig. 4D) provides the statistical viewpoint of how a rod is optimally navigated to the specified target as a function of time. The probability distribution maintains a compact shape towards to targeted origin at around 60s following a straight line (*i.e.,* the shortest geometric path); in contrast, the evolution probability distribution of a random walker will be a spreading Gaussian shape.

4.4.3 Rod navigation in simple mazes

Fig. 5 shows the result of the optimal navigation towards target position (x, y)=(2, 25) in a simple maze. Fig. 5A displays a typical trajectory navigating towards target under optimal control with starting state (x, y, ϕ)=(3, 3, 0). The optimal control policy (Fig. 5B)

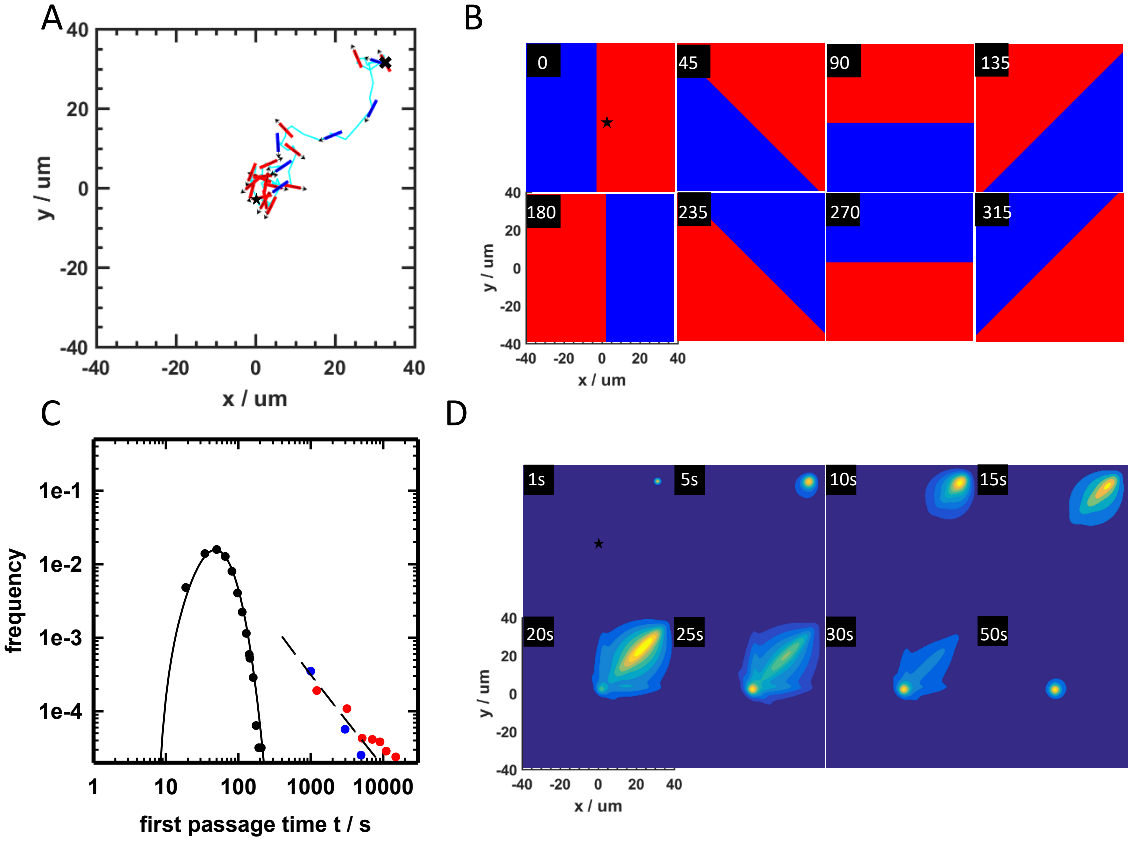

Figure 4 | Optimal navigation of self-propelled rod in free space. (A) Simulated optimally controlled trajectory of 200s with starting state (x, y, ϕ)=(30, 30, 0) and target position (x, y) = (0, 0) (B) Optimal control policy calculated using Eq. (4.3) as a function of discretized state (x, y, ϕ). 8 subplots corresponds to states with angles falling into 8 different angular intervals [-π/8, π/8], [π/8, 3π/8], [3π/8, 5π/8], [5π/8, 7π/8], [7π/8, 9π/8], [9π/8, 11π/8], [11π/8, 13π/8], [13π/8, 15π/8]. (C) First passage time distribution obtained from simulation trajectory statistics (symbols) and theoretical predictions from Eq. (4.5) (solid lines): optimal control (black), off mode (red), and on mode (blue). Dash line is the asymptotic distribution of $1/t\ln^2(t)$ (D) Theoretical probability evolution from Eq. (4.4) under optimal control as function of time.

essentially has a global structure and a local structure. Globally, the control policy is trying to steer the rod to follow the shortest geometry path from an arbitrary initial state towards the target; locally, the control policy is seeking to actuate the rod with different propulsion in order to follow such a path based on a Maxwell demon-like strategy: Turn ON to follow a "path" leading to the target if the rod's orientation is "correct"; otherwise, turn OFF to wait for the "correct" orientation to appear in the Brownian rotation process.

Fig. 5C shows the first passage time distribution of navigating the rod using optimal control vs. uncontrolled. The distributions generated from simulation and theoretical prediction agree well, and they indicate that optimal control can achieve target ~10X faster than OFF mode control, *i.e.*, diffusion. The ON mode is comparable to optimal control due to the simple geometry of the maze, *i.e.*, fast random exploration can enable the rod to arrive the target fast. However, the optimal navigation policy will maintain the rod's position close to the target, whereas the constant ON mode fails to do so.

The probability evolution of position at different time steps under the optimal is shown in Fig. 5D. Compared to optimal navigation in free space, one interesting feature is that during the probability evolution process, some fraction of the probability will accumulate near the inlet(not the outlet) of the long and narrow channel; this is, an barrier is imposed near the inlet. The physical interpretation is that rate of rod leaving the channel is faster than rate entering the channel. The wide opening allows the Brownian rotation to deviate the direct motion due to fast motion, slowing the rate of passing the channel, while inside the channel, the confinement will help the rod maintain the directed motion and thus leave the channel with fast propulsion.

4.4.4 Rod navigation in complex mazes

We can extend similar approach for more complex mazes, as showed in Fig. 6A, which can be viewed as enlarged mazes with repeating of local geometry patterns of the simple maze (Figure 5A). A representative trajectory shown in Figure 6A starting with (4, 4, 0) navigated towards target position (67,5). Locally, the optimal control policy (Fig 6B) shows similar patterns with the policy in the simple maze (Fig. 6B), whereas globally

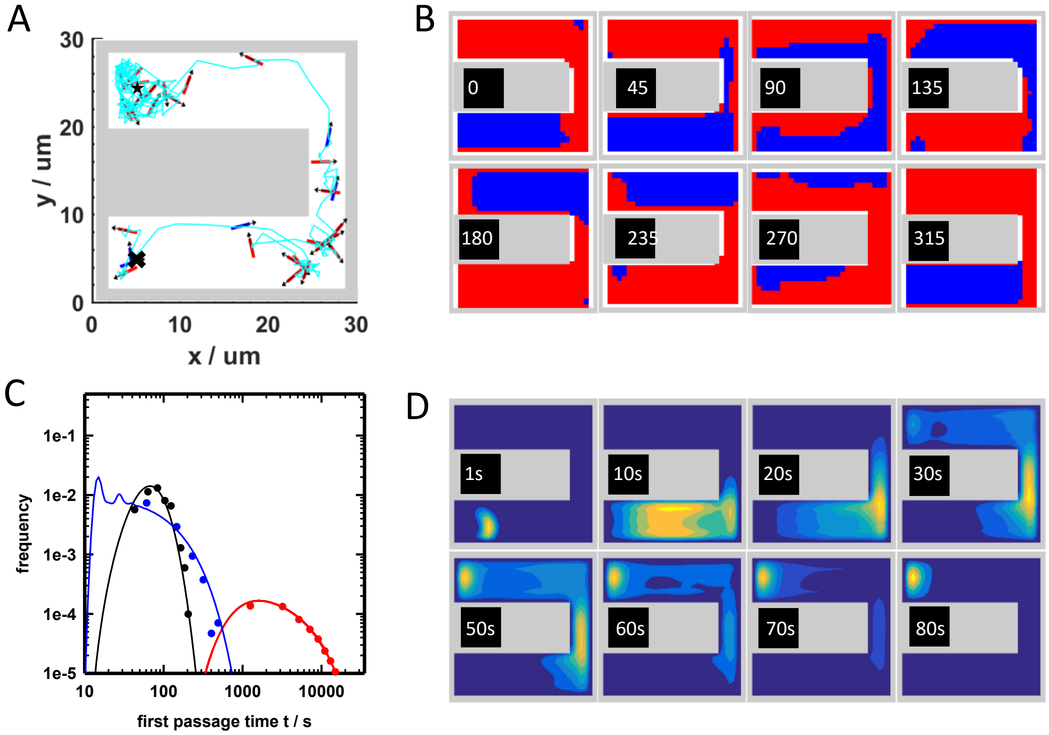

Figure 5 | Optimal navigation of self-propelled rod in a simple maze. (A) Simulated optimally controlled trajectory of 200s with starting state (x, y, ϕ)=(3, 3, 0) and target position (x, y) = (3, 25) (B) Optimal control policy calculated using Eq. (4.3) as a function of discretized state (x, y, ϕ). 8 subplots corresponds to angles falling into 8 different angular intervals [-π/8, π/8], [π/8, 3π/8], [3π/8, 5π/8], [5π/8, 7π/8], [7π/8, 9π/8], [9π/8, 11π/8], [11π/8, 13π/8], [13π/8, 15π/8]. (C) First passage time distribution obtained from simulation trajectory statistics (symbols) and theoretical predictions from Eq. (4.5) (solid lines): optimal control (black), off mode (red), and on mode (blue). (D) Theoretical probability evolution from Eq. (4.4) under optimal control as function of time.

following geometry path that depends on the maze global geometry. In the first passage time analysis, the optimal control can now achieve 3X faster than the ON mode of fast random exploration, and ~100X faster than the OFF mode diffusion. The probability evolution further demonstrates the success and effectives of optimal control; and note that the accumulation of probability in the inlet of channels appears as the simple maze example.

The above analysis procedure can be applied in the most complex maze, as showed in Fig. 6(C)(D)(E)(F). Built on the previous basic cases, the result is straightforward understood. As the maze become larger and complex, the advantages of the optimal control compared to fast random exploration will be more pronounced. The optimal control outperforms the ON mode about 80X and OFF mode diffusion about 8000X.

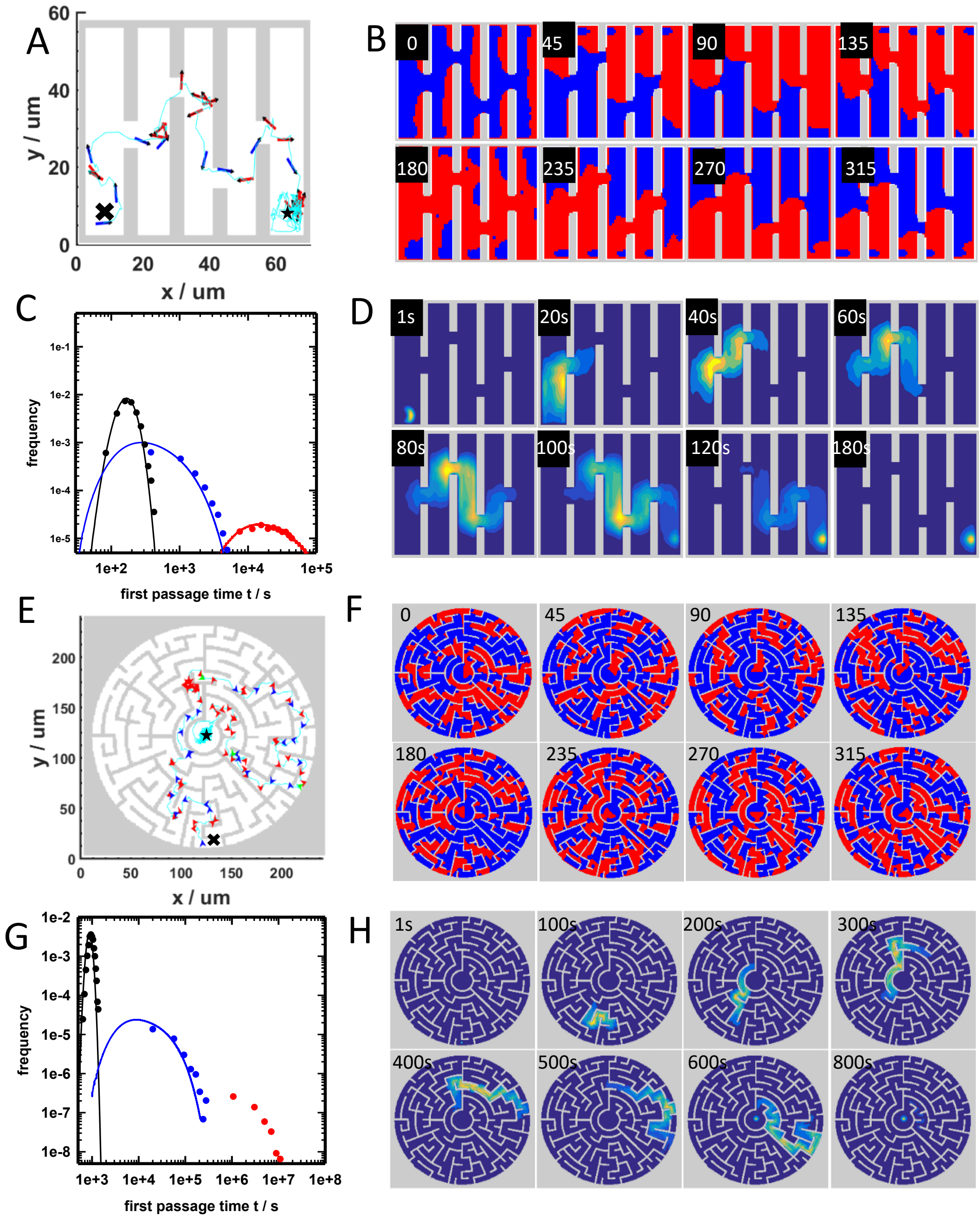

Figure 6 | Optimal navigation of self-propelled rod in a complex mazes (A)(B)(C)(D) and (E)(F)(G)(H), with the same descriptions as in Figure 5.

4.4.5 Scaling of performance

Practical application usually involves navigation task of large scales, therefore it is important to investigate how the optimal navigation performance changes with traveling distance in navigation tasks. We consider the scaling in two types of navigations: (1) navigations in free space with increasing Euclidian distance between the target and starting point in free space; (2) navigations in mazes with similar local geometry patterns and increasing travel distance (in terms of shortest geometry path, shown in Fig. 7A). Fig. 7B shows the mean first passage time under optimal control varies linearly with the path length in both free space and mazes. The free space optimal navigation is more time costly because the existence of regular geometry obstacles (lines) can enhance the directed motion, *i.e.*, increasing the persistence length of propulsion motion. As a comparison, the mean first passage time for the uncontrolled cases either remains infinitely large in free space travel, or increase dramatically as the maze size increases in mazes.

We found that the dramatic improvement in navigation performance in optimal control compared with uncontrolled can be summarized by power law given as: $t \sim L_{\mathrm{M}}$ for optimal control, and $t \sim L_{\mathrm{M}}^{2.8}$ for uncontrolled case. The power law is obtained using the following arguments: For optimal control case, we approximate as $d \sim L_M$, which gives optimal control scaling of $t \sim L_M$; For uncontrolled case, we use the result characterizing the scaling of mean first passage time via random exploration between two points in bounded porous media environment with Euclidian distance Δr given by[83],

$$t \propto A_{free} \Delta r^{d_w/d_f} \tag{4.7}$$

where d_f is the fractal dimension of free space of porous media, d_w is the fractal dimension the random walk, the A_{free} is the free space in the bounded mazes. Let $\Delta r \sim L_M$, $A_{\text{free}} \sim L_M^{df}$ (d_f <=2), we obtain an approximate model as t $t \propto L_M^{\beta}$ by lumping all the exponents together to β, where β is fitted to be ~2.8.

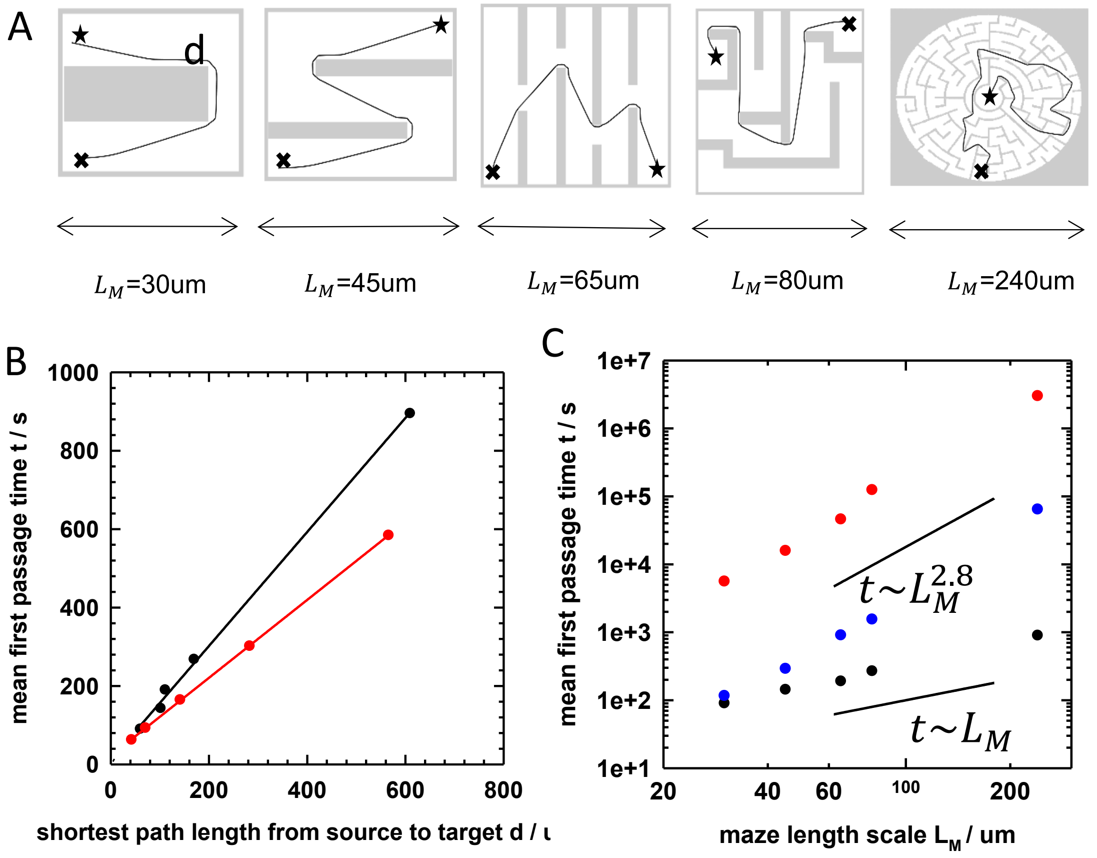

Figure 7 | Scaling analysis for mean first passage time for rod navigation under different strategies in mazes of increasing length scales. (A) Mazes of increasing sizes, starting point and ending points are marked by cross symbol and pentagram. Shortest geometric path are plotted as solid lines. (B) The mean first passage for rod under optimal control is linear with the shortest path length. (C) Approximate scaling relationship between mean first passage time and maze length scale for rod under different control strategies.

4.4.6 Generalization of optimal control principle

Our previous concrete example demonstrate the superior navigation performance of the optimal navigation in free space and mazes. Now we are in the position to generalize the optimal navigation and investigate the limitation of this optimal navigation principle. We address these issue by investigating how positioning accuracy and arrival time performance depends on control parameters. We first introduce revolution number[71] and Peclet number[84] as

$$\lambda = \frac{\Delta t_c}{\tau} = D_r \Delta t_c, \mathrm{Pe} = \frac{\mathrm{v}\tau}{\sqrt{2D_t\tau}} = \frac{\mathrm{v}}{\sqrt{2D_t D_r}} \tag{4.8}$$

where revolution number characterize the amount of the rotation within a time interval Δt_c, Peclet number characterize the ratio of persistence length over the diffusion distance on the characteristic time scale τ. We characterize the positioning accuracy using positioning error defined as

$$\sigma(\lambda, \mathrm{Pe}) = \sqrt{\int_{\mathbf{R}^2} ((x - x_{\mathrm{target}})^2 + (y - y_{\mathrm{target}})^2) p^{\pi^*(\mathrm{Pe},\lambda)}(x, y) dxdy} \tag{4.9}$$

where $p^{\pi^*(\mathrm{Pe},\lambda)}$ is the steady state distribution of the positions resulting from using optimal policy $\pi^*(\lambda,\mathrm{Pe})$. A typical distribution is showed in SI Fig. 1(A).

Fig. 8(A) show the positioning error as a function of parameter λ and Pe. It is generally beneficial to use smaller λ since more frequent feedback will not decrease positioning accuracy(if the system is deviating from the target, faster feedback rate will enable earlier correction). It is also found that the positioning error will continuously decrease as we increase and Pe while decrease λ cooperatively in the same time. The interpretation is that faster speed with faster control update will reduce the position error, *i.e.* better control of its position; however, simply varying λ or Pe while keeps the other fixed will increase the position error. It should be note that continuously decreasing λ while increasing Pe, cannot completely eliminate the position error. This uneliminable position error is intrinsic, and can be mathematically defined as

$$\sigma_{in} = \min_{\lambda, Pe} \sigma(\lambda, Pe) = \lim_{\substack{Pe \to \infty \\ \lambda \to 0}} \sigma(\lambda, Pe) \tag{4.10}$$

Note that the intrinsic error should only depends on the intrinsic properties of the system, *i.e.* D_t and D_r. Fig. 8(C) shows the intrinsic position error as a function of D_r and D_t. Note that we found that $\sigma_{in} \sim \sqrt{D_t / D_r}$.

As for the influence of control parameter on the arrival time performance, we consider different navigation tasks to examine how the navigation performance depends on λ and Pe. The navigation tasks are navigation in free space and navigation around different sizes of obstacles (Fig. 8(C)), which is a generation of various scenarios common in navigation in complex environments. We can further define a geometric constant $\eta = L_{obs} / L$, which is the characteristic length scale for the maze over the length of the rod. For free space navigation, we define $\eta = \infty$.

The performance plot in Fig. 8D show the influence of λ and Pe on mean first passage time in navigation tasks characterized by various η. Similar to the positioning accuracy, it is generally beneficial to use smaller λ since more frequent feedback will not decrease performance(if the system is doing good, then just maintain the previous decision;

if the system is doing bad, faster feedback rate will enable earlier correction). In actual experiments, the choice of λ is dependent on the imaging system, memory requirement of the algorithm. Smaller time will require higher spatial resolution.

Similar to the positioning accuracy, with a fixedλ, there is an optimal Pe; and the optimal Pe will increase as λ decreases. An analog to understand this is a driver drive in higher speed requires faster reaction time, otherwise too large speed (*i.e.* large Pe) will tend to overshoot and too small speed simply reduce the performance. The optimal Pe at fixed λ also slightly increase with geometric constant η of the task. This is because smaller η requires finer control on the distance, therefore small Pe is preferred. Note that Pe = 0 or $\lambda = \infty$ will reduce the system to a purely diffusion or an unattended random walker, which will lead to unbounded in the mean first passage time, as we investigated previously.[82]

We can conclude from above observation that positioning accuracy and arrival performance are closed connected, since navigation through a path can be viewed be a series of positioning subtasks along the path. The position error further reflects the uncontrollable components in the feedback control system, which gives insight on the limitation of our control algorithm: a system with larger intrinsic positioning error, characterized by $\sigma_{in} \sim \sqrt{D_t / D_r}$ can not be efficiently navigated. This insight will enable us to make better design on the geometry and mechanism of self-propelled system, which will ultimately affect D_t and D_r.

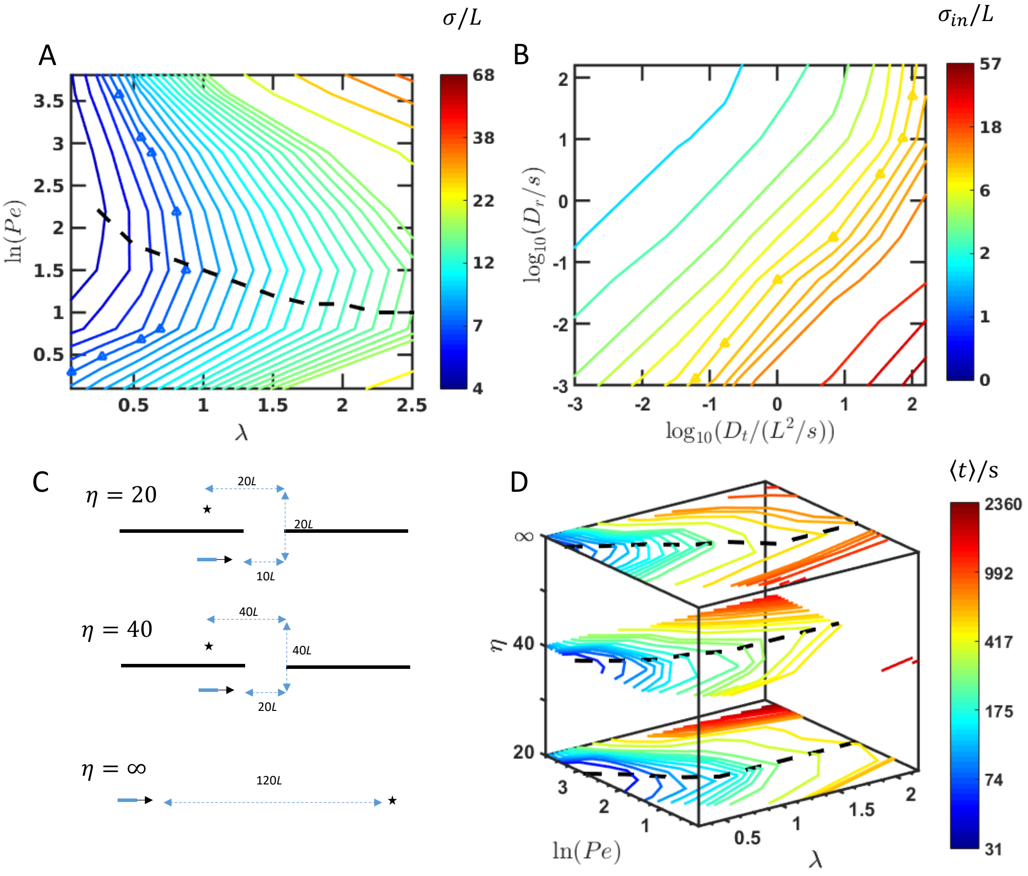

Figure 8 | Generalization of optimal control. (A) Positioning error (σ/*L*) as a function of λ and Pe. The contour line with triangle symbols denotes the isoline with σ/*L*=10. The black dash line passes through the minimum point on each contour line, indicating the optimal choice of Pe (in terms of minimizing positioning error) at different value of λ. (B) Intrinsic position error as a function of D_r and D_t. The contour line with triangle symbols denotes the isoline with σ/*L*=10. (A) Schematics for different navigation tasks characterized by geometric parameter η. (B) Summary of mean first passage time under optimal strategies in different navigation tasks as a function of control system setting Pe and λ. The black dash line passes through the minimum point on each contour line, indicating the optimal choice of Pe (in terms of minimizing navigation time cost) at different value of λ.

4.5 Conclusion & outlook

We have demonstrated the application of Markov decision framework to construct an optimal control policy in navigation task in free space and complex mazes. The optimal control policy can achieve orders-of-magnitude faster in first passage time in navigation tasks compared to uncontrolled random explorations. The performance under optimal control can linearly scale up with length of the shortest path connecting the initial position and final position. We identify non-dimension parameters in the control system, and we generalize the optimal control by investigating how these non-dimensional parameters affect the positioning error and first passage time performance. The optimal control framework will find potential application in employing self-propelled devices performing tasks, such as cargo transport in complex environments. Generalization the optimal control framework to 3D is straightforward. The MDP framework remains the same except that the system state is defined as $s=(x, y, z, \theta, \phi)$, where θ is the polar angle and ϕ is the azimuth angle.

5 CARGO CAPTURE AND TRANSPORT VIA OPTIMALLY CONTROLLED SELF-PROPELLED COLLOIDAL MOTORS

5.1 Abstract

Using strategic control, stochastic systems consisting of a group of self-propelled microscopic 'robots' with Brownian motion can be harnessed to perform work not allowed in equilibrium thermodynamics. Using self-propelled Janus motors as the model system, we demonstrate a new paradigm for cargo capture and transport based on multiple-agent feedback control. The control algorithm is able to coordinate multiple motors to cooperate on forming a reconfigurable vehicle for cargo transport with Pareto optimality. The underlying physical principles on structure control and momentum transfer of this system are investigated. The design space on how to improve device efficiency are explored.

5.2 Introduction

The last decade has witnessed an emergence of research interests in self-propelled microscopic systems, which consist of micro-scaled natural or man-made objects that are able to propel themselves by consuming external environmental energy. Examples include bacterial[85] and chemical catalytic systems.[27] Such system is also known as active matter, for their contrasting differences in the non-equilibrium nature and the underlying physical laws governing its kinetics. The research focus on its scientific principles covers thermodynamics,[29,86] emerging macroscopic motion[87], stress distribution,[88] hydrodynamics,[89] and ultimately their connections to the physics of life.[90] The understanding of its scientific principles are motivating various engineering applications to harness the non-equilibrium properties to perform tasks not permitted in scenarios governed by equilibrium thermodynamics. Proof-of-concept applications of these systems are spaning a broad range of areas. For example, using self-propelled "micro-device" navigate and deliver drugs[13,31] in biomedical applications; water pollution cleaning in environmental applications[12]; mechanical device can perform work via rotating gears in the active bath; and creation of novel structures based on active interactions.[26,32] Conjugating active systems with strategic control can enable more efficient and broad applications. Successful examples include: colloid delivery via constant feedback control enabled by properly designed three-dimensional microstructures,[11] the formation of active rectification devices by controlling spatial light intensity on a light-activated active system,[15] and feedback Light-activated navigation on free spaces and complex mazes.

Among all these potential applications, cargo manipulation(e.g. capture and delivery) are of particular interest as motivated by their potential significance to biomedical applications; for example, capture and isolation of cancer cells,[30] targeted drug delivery, and diagnosis. These cargo related tasks have been accomplished via man-made micro-machines by attaching cargo via magnetic, electrostatic interactions, and bio-chemical interactions.[30] These designs might have the drawbacks of: (1) the limited interactions can be exploited; and (2) not being robust due to the lack of error-correcting machinery. To overcome these inherent limitations, here we demonstrate a new paradigm for cargo capture and transport based on multi-agent feedback control of active system. Our design consists of a number of self-propelled Janus motors conjugated with a feedback control system. The strategy for cargo capture and transport process are summarized as (Fig. 1B) steering each motors to form a stable packing structure around the cargo and then move the 'locked' cargo by properly transporting momentums. The realization of such strategy relies on the feedback control system to have real-time capabilities of: (1) sensing the system state, i.e., the positions and orientations of motors and the position of the cargo; (2) a decision making module that calculating optimal actuation strategy based on the system state; (3) actuation module that actuates each motor individually. Compared to conventional cargo delivery strategies, such design offers the following advantages: (1) large design space to perform different types of cargo capture and transport task (2) robust via feedback control; (3) real-time programming and multitask all-in-one.

Our study is structured as follows. We first illustrate an optimal control algorithm in steering multiple motors to arrive at multiple assigned targets. The application of this algorithm to cargo capture, isolation, and transport are then illustrated. We explore the design space and investigate the underlying physical principles on structure control and momentum transport during capturing and transporting process. Ultimately, even though our demonstration is limited to cargo manipulation, our strategy and method in navigation, structure control, and momentum transport can be generalize to applications of active system in different domains, such as self-organizing reconfigurable machines and devices, active assembly of topological structure, etc.. Finally, because of the advancement of optical manipulation techniques enable fine control on the spatial lightning.[91], such multi-agent control system will hold promise in the future.

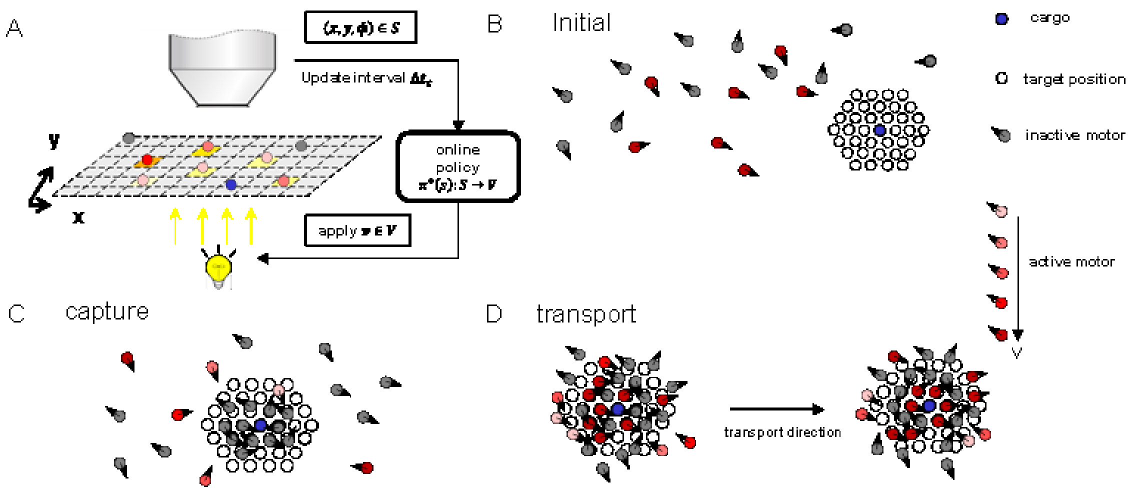

Figure. 1. Schematics of navigating self-propelled rod in a maze with feedback control. (A) The imaging system feed the information of system state $S=(x, y, \phi)$ containing positions and orientation of the motor and the positions of the target into the online control policy module, which outputs velocities to use for the motors. The control policy is executed by the actuator module containing the illuminator(light bulb) and a selective phone mask such that each motor can be tuned to desired velocities. This feedback control procedure will loop at every interval of Δt_c. (B) Schemes of using optimal controlled colloidal motors to perform cargo capture and transport. Targets are designed to dynamically located around the cargo. And optimally controlled motors are controlled using feedback system in (A) to track these targets. When motors are localized to their target sites via optimal controlled, the cargo will be caged, and hence captured. After the cargo are captured, the controller will maintain the motor to the target sites and selectively activate motors in the transport direction (the dash black arrow) such that the motors will move with the cargo in the transport direction.

5.3 Theory

5.3.1 Equation of motion for motors

We model the equation of motions of our self-propelled micro-motors indexed by $I_M=\{1,2,\ldots,p\}$ as

$$\begin{aligned} r_i(t+\Delta t) &= r_i(t) + \frac{D_t}{kT}\cdot F_i\Delta t + \Delta r_i^B + v_i(t)\mathbf{n}_i \\ \phi_i(t+\Delta t) &= \phi_i(t) + \Delta\varphi_i^B \end{aligned} \tag{5.1}$$

where $i \in I_M$, v_i is the propulsion speed of the motor i as the control input (concrete realization of the propulsion velocity might depend on the specific mechanism and application, here we assume it is using light activation mechanism[75]), $r_i = (x, y)$ is the position vector of the motor i, $\mathbf{n}_i$ is the orientation of motor i, given as $\mathbf{n}_i = (\cos(\phi_i), \sin(\phi_i))$, Δt is the integration time step, k is the Boltzmann's constant, and T is the temperature. $D_t = kT/6\pi\mu a$ is the translation diffusivity, with μ as the visocity, and $D_r = kT/6\pi\mu a^3$ is the rotational diffusivity. The Brownian translational and rotational displacement $\Delta\mathbf{r}_i^B$ and $\Delta\varphi_i^B$ both have mean 0 and variances of $2D_t\Delta t$ and $2D_r\Delta t$ respectively. F_i is the forces due to interactions of electrostatic repulsion[2] and depletion attractions[92] between motors, given as

$$\begin{aligned} \mathbf{F}_i &= -\sum_{j\neq i} \nabla u_{i,j}^{pp}\left(r_{ij}\right) \\ u_{i,j}^{pp}\left(r\right) &= B_{pp}\exp\left[-\kappa\left(r-2a\right)\right] + \Pi V_{ex}(r) \\ V_{ex}(\mathrm{r}) &= \pi\left(\frac{4}{3}(a+L)^3\left(1-\frac{3}{4}\frac{r}{a+L}+\frac{1}{16}\left(\frac{r}{a+L}\right)^3\right)\right) \end{aligned} \tag{5.2}$$

where B_{pp} is the pre-factor for electrostatic interactions, κ^{-1} is the Debye length, L is the depletant radius. The depletion attraction is written as the product of osmotic pressure, Π, and excluded volume, V_{ex}.

5.3.2 Optimal multi-agent control framework

The central optimal control task throughout this work is to optimally control a set of motors to track a set of moving targets. More specifically, we are seeking an optimal control policy, or a set of rules, specifying which self-propulsion velocity to use when given the instantaneous system state characterized by motors' position and orientation (x, y, ϕ) and targets' position (x, y) such that the distances between motors and targets are minimized as the system evolves. We first define notations to formalize our methods of obtaining optimal control policy. Let I_M=1,2,…,p index motors and let I_T=1,2,3,…p index the targets. A system state *s* is defined as the concatenation of state vector of each individual motor as $s = (s_1,s_2,\ldots,s_p)$,$s_i = (r_i, \phi_i)$, $r_i=(x, y)$, $i \in I_M$. The state space S is the set containing all possible value of s. The state space S can be viewed as the product of state spaces of individual motors, i.e., $S=S_1\times S_2\times\ldots\times S_p$. An action *u* is defined as the concatenation of individual velocity as $u=(v_1, v_2,\ldots,v_p)$. The action space *U* is the set containing all admissible value of *u*. The action space U can be viewed as the product of action spaces of individual motors, *i.e.*, $U=U_1\times U_2\times\ldots\times U_p$, with $U_i=\{v: 0\leq v \leq v_{max}\}$.

In the multi-agent control framework, we will *assign* different motors to track different target. Because IM and IT are of the same size, an assignment from I_M to I_T is a permutation on the set IM. We further define *G* as the set of all admissible assignment, then G contains q! all possible permutations of IM. Finally, we defined a control policy π is a mapping from S to V. A policy π can also be viewed as the concatenation of individual policies, $\pi = (\pi_1, \pi_2,\ldots, \pi_p)$, $\pi_i: S_i\rightarrow U_i$, in which each π_i specifies v_i to use when motor *i* is at state s_i .

The objective of finding an optimal *instantaneous* policy at time t with system state s (*i.e.* propulsion velocities) to track targets can be mathematically formulated as:

$$\pi^*(s,t) = \arg \min_{\substack{g\in G \\ \pi(s)\in U}} \sum_{i\in I_M} \left\langle (r_i(t+\Delta t_c) - r_{t,\mathrm{g(i)}}(t+\Delta t_c))^2 \right\rangle \tag{5.3}$$

where Δt_c is the control update interval, $r_{t,g(i)}(t)$,$g(i)\in I_T$ is the position vector of target assigned to motor *i*(represented by g(*i*)), < > is taking expectation with respect to joint probability distribution of ri and rt at time $t + \Delta t_c$. Essentially, we are optimizing over all possible admissible assignments and velocity specification such that we can steer our motors to their assigned targets closer in future time $t + \Delta t_c$ such that the mean squared error is minimized. However, the above optimization problem is difficult to solve since it is a mixed programming involves integer programming and continuous programming under constraints. We approximate the optimal solution using the following two sub-steps: solve g^* first and then solve π whiling fixing g^*. The procedure can be formulated as

$$g^* = \arg\min_{g \in G} \sum_{i \in I_M} (r_i(\mathrm{t}) - \mathrm{r}_{t,g(i)}(\mathrm{t}))^2 \tag{5.4}$$

$$\begin{aligned} \pi^*(s,t) &= \arg \min_{\pi(s,t) \in U} \sum_{i \in I_M} \left\langle (r_i(t+\Delta t) - r_{t,g^*(\mathrm{i})}(t))^2 \right\rangle \\ \Leftrightarrow \pi_i^*(s_i,t) &= \arg \min_{\pi_i(s_i,t) \in U_i} \left\langle (r_i(t+\Delta t) - r_{t,g^*(\mathrm{i})}(t))^2 \right\rangle, i \in I_M \end{aligned} \tag{5.5}$$

The optimization of Eq. (5.37) can be solved using Hungarian algorithm in combinatory optimization.[93] The optimization of Eq. (5.5)can be decomposed into optimization problem for each motor, which is also trackable.

5.3.3 The cargo capture and transport algorithm

We list the cargo capture and transport algorithm as follows. The cargo capture algorithm can be viewed as a special case of multiple motors to multiple targets algorithm, in which the target sites are prescribed to surround the moving cargo. The cargo transport algorithm will select a subset of motors as transporters satisfying a distance criterion and orientation criterion. These transporters will turn on their maximum speed to contribute momentum to the system. The rest of the motors will execute speed to steer themselves to the target sites, thus maintaining the caging structure.

Cargo capture algorithm

```
Construct the lattice target sites around the cargo
Loop with frequency $\Delta t_c$:
    Calculate the optimal velocities from Eq. (5.37).
    Update the position of motors and cargo within $\Delta t_c$ using Equations of motion.
    Reconstruct the target sites around the cargo.
End Loop
```

Cargo transport in θ direction algorithm

```
Construct the target sites around the cargo
Loop with frequency $\Delta t_c$:
    Calculate the optimal velocities for all motors from Eq. (5.37).
    For each motor $i$:
        If $|\phi_i - \theta| < \theta_c$ and $\|r_i - r_{t,g(i)}\| < a$
            Set the self-propulsion velocity for motor $i$ to be maximum velocity.
        End If
    End For
    Update the position of motors and cargo within $\Delta t_c$ using Equations of motion.
    Reconstruct the target sites around the cargo.
End Loop
```

5.3.4 Measuring tracking performance

We measure the performance of motors tracking targets by first passage time. We first define the first passage time for a motor *i* to reach a target *j* as

$$\tau_{m,i} = \min\{t : r_i(t) \in S_i^{t\arg et}\}, S_i^{t\arg et} = \{s_i : \left\| r_i - r_{t,\mathrm{j}} \right\| \le a\} \tag{5.6}$$

Then the definition of first passage time for *p* motors to *p* targets can be defined as

$$\tau_m = \max_{i \in I_M} \tau_{m,i} \tag{5.7}$$

which is the last first passage time of all the motors.

5.3.5 *Capture characterization*

The dynamical process of cargo capture can be monitored by the mean deviation of motors from their assigned targets, defined as

$$d_M = \frac{1}{Na}\sum_{i=1}^{N}\left\| r_i - r_{t,g(i)} \right\| \tag{5.8}$$

and the deviation of the cargo to the mass center of the motors, defined as

$$d_C = \left\| \sum_{i=1}^{N}\frac{1}{N} r_i(t) - r_{cargo}(t) \right\| \tag{5.9}$$

We further assess the capture quality via the normalized deviation of the cargo by the capture span S_T associated with targets sites, given as

$$\varepsilon = \frac{d_C}{S_T}, S_T = \frac{1}{2}\max_{i\neq j}\left\| r_{t,i} - r_{t,j} \right\| \tag{5.10}$$

The normalized deviation ε quantifies how tight the cargo is being caged by the motors. ε greater than 1 suggests that motors fails to maintain the cargo inside their capture span; ε much smaller than 1 suggests that cargo is being tightly captured. Intuitively, the more motor we have, the larger S_T, and the easier the cargo being expected to be captured.

5.3.6 *Governing equation on steady state structures*

In the steady state during the capture and transport processes, the steady state structure should satisfy the force balance between the osmotic pressure and the active force generated by propulsion. By assuming the equilibrium structure is close to circular shape, we have force balance in the radial direction given as[88]

$$\frac{dP_{os}}{dR} = -\rho(R)F_{act}(R) \tag{5.11}$$

where $P_{os}(R)$ is the pressure at distance R from the mass center of the configuration, and $\rho(R)$ is the density profile at distance R from the mass center. The macroscopic balance equation will generally hold for length scales larger than radius a.[94] By assuming the system reach thermodynamic equilibrium, the pressure can be expanded as $P_{\mathrm{os}}(R)= \rho(R)kTZ$, where Z is the compressibility factor. $F_{act}(R)$ is the mean active forces in the radial direction, which can be written as

$$F_{act}(R) = \frac{6\pi\mu a}{N}\left\langle \sum_{i=1}^{N} \delta(r_i(t) - r_c(t) - R)(v_i(t)\mathbf{n}_i - \overline{v}_c)\cdot d_i \right\rangle, d_i = \frac{-(r_i(t) - r_c(t))}{\left\| r_i(t) - r_c \right\|}$$

(5.12)

where the <> means time average in the steady state process, d_i is the unit vector of the inward radial direction, $r_c(t)$is the instantaneous average position(mass center) of all motors, $\overline{v}_c$ is the average velocity of the whole cluster system, δ is the Dirac delta function, and N is the number of motors.

5.3.7 Conservation of momentum and transport speed

When all the cargo, including the cargo, (N+1 particles) are moving collectively with average velocity $\overline{v}_c$, the whole cluster will experience a total hydrodynamic friction force F_{fri}, given as,

$$F_{fri} = (N+1)6\pi\mu a\overline{v}_c \tag{5.13}$$

Then, the balance (in the steady state sense) of the total friction force F_{fri} and total active forces given by $6\pi\mu a v_i \mathbf{n}_i$ enable us to establish an equality between transport velocity of the cluster as a whole as

$$(N+1)6\pi\mu a\overline{v}_c = \sum_{i=1}^{N} 6\pi\mu a \left\langle v_i \mathbf{n}_i \right\rangle \tag{5.14}$$

where the <> means time average in the steady state process. By arranging terms we have the average transport velocity given as

$$\overline{v}_c = \frac{1}{N+1}\sum_{i=1}^{N} \left\langle v_i \mathbf{n}_i \right\rangle \tag{5.15}$$

5.3.8 Theoretical maximum velocity

Consider N motors transporting a single spherical cargo, the theoretical maximum velocity $\overline{v}_{c,\max}$ from (5.15) using equilibrium uniform probability distribution on $\mathbf{n}$ is given as

$$\overline{v}_{c,\max} = \frac{N}{N+1}\int_{-\phi_c}^{\phi_c} \frac{\cos(\phi)}{2\pi} d\phi = \frac{N\sin(\phi_c)}{\pi(N+1)} \tag{5.16}$$

where ϕ_c is the threshold angle for transport activation in the cargo transport algorithm.

5.4 Methods

5.4.1 Simulated experiments

In this work, we perform BD simulations to verify the efficacy of optimal control policy. The integration time step is 0.1ms. The simulation parameters used are listed in table 1. The control update interval Δt_c is 0.1s. Parameters used in the simulation are listed in the following table.

Table 1

Parameter	Equation	value
a(nm)^a	(5.2)	1000
B_{pp} (a/kT)	(5.2)	2.2974
κ^{-1} (nm)^c	(5.2)	10
D_t(m^2/s)	(5.1)	5.13e-13
D_r(rad^2/s)	(5.1)	0.55
v(m/s)	(5.1)	[0,5e-6]

All the optimal control simulations except for transport in this manuscript are performed using the following procedure repeated with interval Δt_c: first sense the state of all motor and positions of targets, and then calculate the optimal control policy using Eq. (5.3) and execute the policy $v_i = \pi^*_i(s_i)$.

5.4.2 Construction of first passage time from simulation

In construction of first passage time distribution on different control strategies, we run our simulation with specified initial state and calculate the first passage time as defined in Eq.(5.7). About 1000 trajectories are used to construct the first passage time distribution. Usually, the wider the distribution, the more trajectories are needed.

5.4.3 Transport speed measurement

During the cargo transport process, the average transport speed is obtained by dividing the horizontal traveling distance by the time interval during a 2000s transport process.

5.4.4 Statistics for active velocity, density, and area fraction

The spatial distribution of active velocities, density, and area fraction is obtained from simulation data using histogram method averaged over snapshots as the system reach steady state. The snapshots are taken very 0.5s and usually 10000 snapshots are used for constructing statistics. The spatial resolutions are $0.25a\times0.25a$ for 2D space, and $2a$ for 1D space.

5.5 Results & discussion

5.5.1 Capture time characterization

We start with the case of single motor tracking single target subject to Brownian motion. Fig. 2A shows the optimal control policy that specifies the choice of propulsion speed given the target's position respective to the motor's position and orientation. The optimal control policy is obtained as the approximate solution to the one-step look-ahead optimization problem given as

$$\pi^*(s,t) = \arg \min_{\pi(s,t)\in U} \left\| \overline{r_1}(t+\Delta t_c) - \overline{r_{t,1}}(t+\Delta t_c) \right\|^2 \tag{5.17}$$

where the bar means expectation. The optimization can be intuitively interpreted as seeking the optimal speed such that we have the minimum distance between the mean position of the motor and the target in the next time step. The details about solving this problem are documented in *supporting information.* The optimal control policy can also be written compactly as

$$v^* = \begin{cases} \min(\frac{d}{\Delta t_c}, v_{\max}), d > 0 \\ 0 \end{cases} \tag{5.18}$$

where *d* is the projection the vector connecting motor center onto the direction vector $\mathbf{n}_1$, and Δt_c is the control time interval.

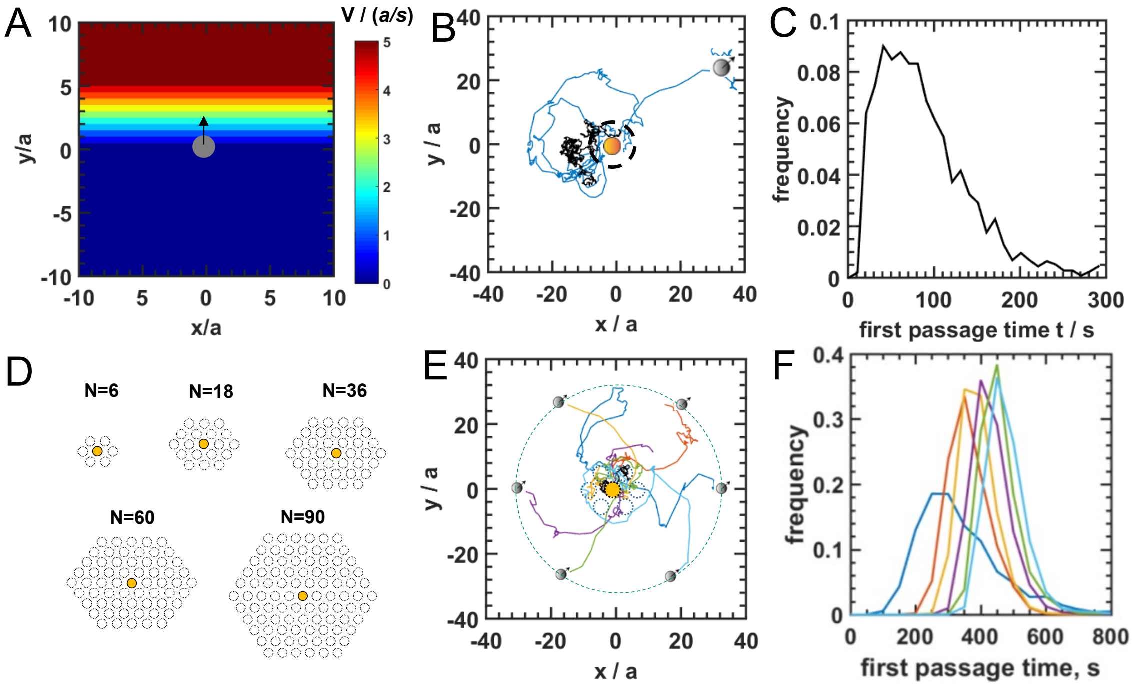

Figure. 2. (A) Optimal control policy for motors under speed constraint $v \in [0, 5\ a/s]$. The optimal control policy specifies the self-propulsion speed v to be used given target position (x, y) with respect to the local coordinate system, which is centered on the motor center and has its y axis aligning with the motor's orientation vector **n** (the arrow). (B) Representative trajectory (blue solid line) of an optimally controlled motor (starting with initial state (x, y, ϕ)=(30,30,0)) tracking a target (initially located at position (0,0)) undergoing Brownian motion with the black solid line as the trajectory. The black dashed line around the target represents the target region used to calculate first passage time. (C) The distribution of first passage time τ for an optimally controlled single motor tracking a Brownian moving target as described in (B). (D) Design of target sites (dashed circles) for multiple motors to capture and transport cargo. Five different design schemes for different number of motors are demonstrated. Target sites are dynamically placed around the cargo such that when motors are perfectly localized at the target sites, cargo will be caged, therefore captured. (E) The representative trajectories of 6 optimally controlled motors tracking 6 dynamic targets moving simultaneous with the Brownian cargo. The cargo (yellow circle) is initially located at position (0, 0). The motors are initially equally spaced on a circle (dash blue) with radial distance $30a$ to the cargo. The targets are drawn as dashed circles around the cargo. Solid lines are trajectories of motors and the cargo. (F) The distribution of first passage time τ for a N motor tracking N dynamic targets (initially located at position (0,0)) with initial distance of $300a$. From left to right are N=1, 6, 18, 36, 60, 90.

A typical trajectory of the motor under such control strategy is showed in Fig 2B. The efficiency of the target tracking process can be characterized by the first passage time distribution. The significance of the optimal control can also be viewed from the fact that the any uncontrolled system tracking a target requires an infinite mean time to get to the target. [82]

5.5.2 Multiple particle tracking multiple targets

In the experiment of multiple particle tracking multiple targets, by design surrounding target sites dynamically surrounding (the target sites will move around with the cargo) the cargo(Fig. 2D), such that when motors arriving at the target sites, they will form a 'cage' to capture cargo. The target sites are designed to have multiple shells such that the cargo will be more stably caged inside. Fig. 2E show the trajectories of controlling 6 particle to track the 6 targets surrounding a Brownian cargo particle. Fig. 2F shows the first passage time distribution of control 6, 18, 36, 60, and 90 motors to track the 6,18,36,60, and 90 targets around the cargo respectively. The first passage time of all the motors arriving at their assigned targets is simply the time cost for a cargo to be captured. Note that the mean first passage time will increase as the number of motors increase since it require more time to put more particles into their target sites.

5.5.3 Transient process in capture

Figure 3 shows the trajectories of 90 motors executing the algorithms cargo capture(0~300s) and transport (300s~1300s), as Fig. 1. BCD schematics shows. During capture process 0~300s, all motors are approaching their optimally assigned target sites quickly under optimal control. As a consequence, the distance of each motor to its optimally assigned target decrease dramatically initially (Fig. 3B). Similarly, the distance between the mass center of motor and the cargo also decrease dramatically initially (Fig. 3C). During the later stage of the capture process (200s~300s), the system enter into the steady state with the values of these two distance metrics remaining relatively constant.

The transport process starts from 300s to 1500s, where all motors with the caged cargo move collectively horizontally to the right with constant speed of 0.7um/s, as showed in Fig. 3D. Note that the transport process does not experience any noticeable initial transient stage and quickly enter into a steady state. During the whole transport process, the deviation of the motors and cargo will remain at the relatively larger values than in the steady state of the capture process.

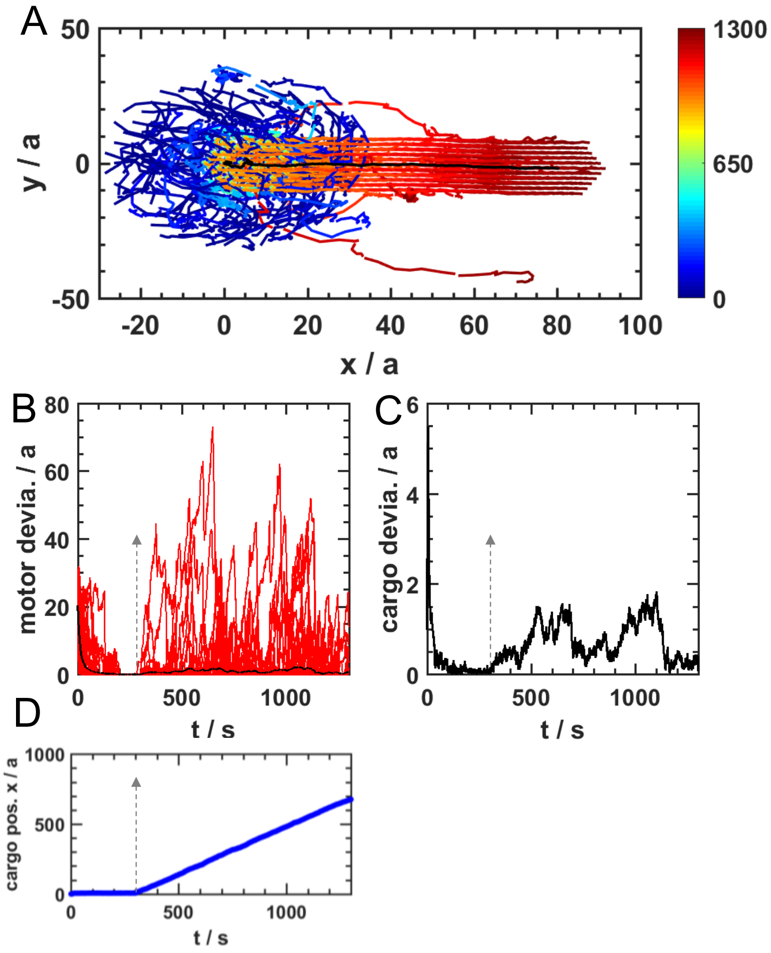

Figure. 3. Trajectory for capture and transport process. Cargo initially located at (0,0), after 1300s, cargo is transported to position at (90,0) (A) The black solid line represents the cargo. The color spectrum from blue to red represents the time scale. Other solid lines denote the trajectories of the motors. (B) The distance of each motor to its optimally assigned target position surrounding the cargo as a function of time. Each red line represents one motor. The black denotes the mean value. 0 to 300 s is the capture process, and 300s – 1500s is the transport process. The left part of the arrow is capture process and the right part is the transport process. (C) The distance of cargo to the mass center of all motors as a function of time. (D) The cargo's position in the x axis as a function of time.

5.5.4 Steady state structure during capture

The resulting steady state structure from capture process will depend on the motor number and the interactions between motors. As a coarse first-step analysis, we assess how the capture quality will depend on the motor number and the motor interactions. The capture quality is characterized by the normalized cargo deviation (Eq. (5.10)). It is found that increasing motor number and attraction strength will reduce the normalized deviation, indicating more stable and robust capture. For the case of cargo capture using only 6 motors, these motors fail to maintain the cargo around their center of mass. The steady state structures can be more accurately characterized by the 2d motor position distribution with respect to the cargo position, as showed in Figure 4B. As the attractions between motors increase, the steady state structure will become more and more condensed and compact. In particular, at zero attraction case, the position distribution profile can spread out to $20a$, with large amount of fluid-like motors in the periphery. As we increase the attraction strength to 5.3kT, the steady state structure is similar to crystalline lattice structure, with lattice point coincide with the target sites. The active forces exerted by the optimally controlled motors play a fundamental role in determining the steady structure. To illustrate this, we decompose the active forces acting on every particle into the radial direction (with the mass center being the origin) and tangential direction (*i.e.* perpendicular to radial direction). The radial active forces for N=90 system with different motor attractions are showed in the Fig. 4B. In all attraction strengths, there are always positive radial forces acting inward directions, thus balancing the osmotic pressure that drives the system to expand outward. Moreover, the radial active forces resulting from the optimal controller is behaving adaptively. That is, the radial active forces will decrease as attraction increase, because stronger attractions between motors will help hold the dense structure; as a consequence, smaller radial active forces are needed to maintain the structure. It is also found that the active forces in the tangent direction are order-of-magnitude smaller than the radial forces. The balance between the osmotic pressure and active forces can be more accurately described as Eq. (5.11). Note that we can use sedimentation method to estimate the equation of the state used for calculate the osmotic pressure. Fig. 3C shows the comparison of osmotic pressure in the radial direction vs. the integrated active forces in the radial direction.

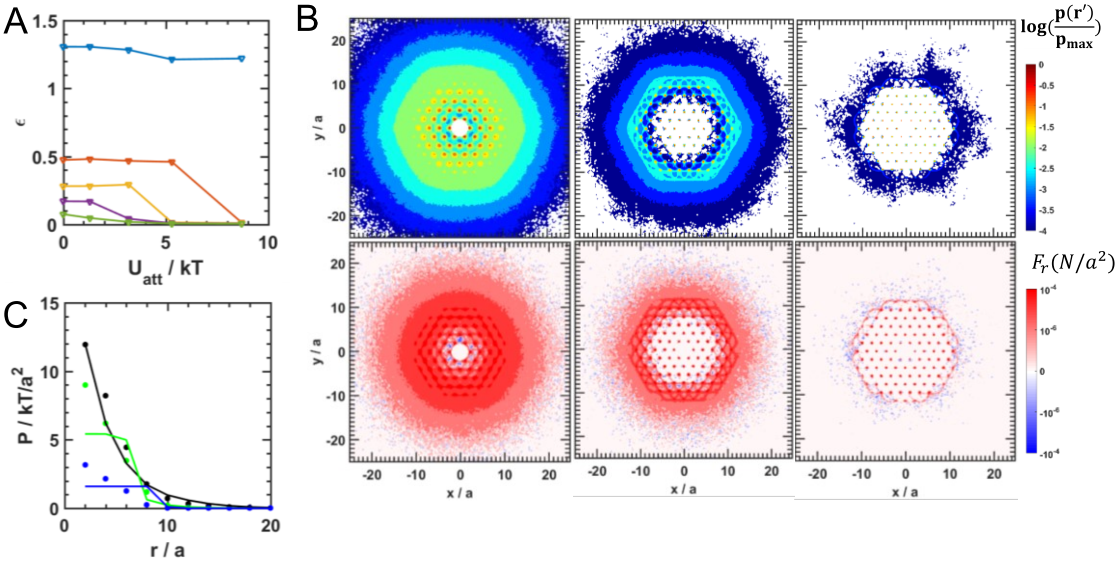

Figure. 4. (A) The normalized mean deviation of cargo to the mass center of motor as a number of number of motors N (from top to bottom: N=6, 18, 36, 60, 90) and attraction strength U_{att} between motors. (B) (upper row)2D steady state position distribution of 90 motors tracking 90 targets sites surrounding a Brownian moving cargo and (lower row) the steady state active force distribution in radial direction distribution. The coordinate in the 2D plot is with respect to a local coordinate system centering on the mass center of the system. Interactions between motors are: (left) 0 kT attraction, (middle) 3.2 kT attraction, and (right) 5.3 kT attraction. (C) The pressure estimated from the integrated active force in 1D radial direction (Eq. (5.11)) for N=90 motor system. Different colors represent motor interactions of: (black) 0 kT attraction, (red) 1.8 kT attraction, (green) 3.2 kT attraction, and (blue) 5.3 kT attraction.

5.5.5 Steady state structure during transport

Fig. 5A (first column) show the 2D density profile of 90 motors with different attraction strength respect to a moving cargo center in the steady state of the transport process. Similar to the steady state structure in capture process, the stronger the attraction, the more compact it will be. Compared with capture process, there are two contrasting characteristics of the steady state structure density profiles in the transport process: (1) the structure is relatively more expanded, especially at low attraction cases; (2) the resulting density profile is asymmetric 2D.

During transport process, the active forces play two essential roles: providing the momentum for transport and balancing the osmotic pressure to maintain the caging structure. The active forces acting on each motor in the horizontal direction is showed in Fig. 5A(second column). For the zero attraction case, the 2D horizontal forces distribution resembles a bi-polar structure, with the left part being dominantly positive and the right part dominantly negative. Note that the appearance of the bipolar force distribution is due to the transport algorithm's requirement to maintain the caging structure during the whole transport process *via* the active forces. As a consequence, the overall structure is squeezed by the active forces to maintain the caging structure. Moreover, the negative and positive forces are not perfectly cancelled out, with the positives forces exceeds the negative forces (note that there are some positive forces sparsely distributed on the right). The summation of the horizontal forces gives a positive value, indicating that there is a net total force in the horizontal direction to provide the momentum to move. As we increase the attraction strength to 3.2kT, the horizontal force distribution is similar to 0kT case, except that the positive-direction forces dominates more the negative-direction forces, giving a more positive net total force. When the attraction strength is 5.3kT, the force distribution is dominantly positive, thus providing the strongest driving force for the caging structure to collectively translate. Note that the net total active forces in the vertical direction are found to be order-of-magnitude smaller than the horizontal forces. In the 5.3kT attraction case, the attraction itself is able to maintain the structure; therefore, active forces are mainly contribute the momentum.

To clearly demonstrate the role played by active forces in maintaining the structure, we first obtain the net forces used to maintain the structure by subtracting the original active forces by the frictional forces experienced due to the translation. The projection of these net structure maintaining forces onto the radial direction is showed in Fig. 5A(third column). The distribution profile is similar to the cases in capture steady state. There exist active forces in the radial direction to maintain the structure by balancing with the osmotic pressure. Similar to steady state structure during capture, such balance can be approximated described by Eq.(5.11). And the comparison of the osmotic pressure and active forces suggests the existence of such balance, as showed in Fig. 5B.

The amount of momentums transfer from the active forces to the caging structure is reflected on the difference in the transport speeds. Fig 5C shows the transport speeds as a functions of motor numbers and attraction strength between motors. The average transport speed is measured from simulation using travel distance divided by travel time interval. The measured speeds agree with the prediction from Eq. (5.15) based on momentum conservation. It is found that stronger the attraction and larger number of motors, the faster of the transport. This is because when motors have stronger attractions, more active forces are used in the transport to generate faster speeds, as we discuss in the analysis of horizontal active forces. Note that the maximum transport speed can be reached is nearly independent of the motor number at large N, as showed in Eq. (5.16).

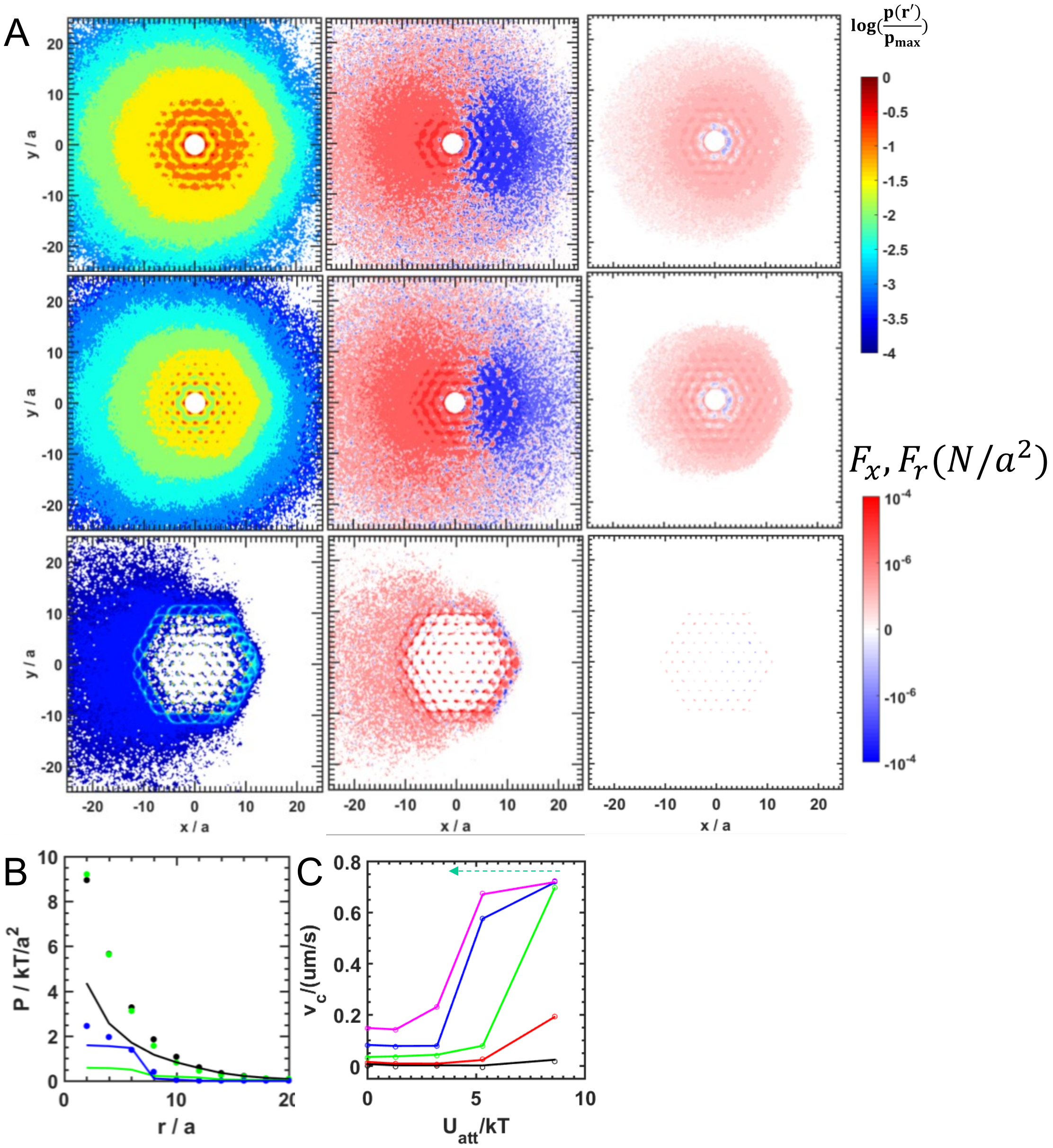

Figure. 5. (A) 2D steady state position distribution of 90 motors tracking 90 targets sites surrounding a Brownian moving cargo, (middle column) the steady state active force distribution in positive horizontal direction distribution, and (right column) the steady state residual active force distribution in radial direction distribution. The coordinate in the 2D plot is with respect to a local coordinate system centering on the mass center of the system. Interactions between motors are: (top) 0 *kT* attraction, (middle) 3.2 *kT* attraction, and (bottom) 5.3 *kT* attraction. (B) The pressure estimated from the integrated active force in 1D radial direction (Eq.(5.11)) for N=90 motor system. Different colors represent motor interactions of: (black) 0 *kT* attraction, (green) 3.2 *kT* attraction, and (blue) 5.3 *kT* attraction. (C) Transport speed as a function of number of motors and attraction between motors. The dash line is the theoretical maximum transport velocity.

5.6 Conclusion

In this paper, we developed the optimal control algorithm can steer multiple motors to multiple targets. This algorithm was then used to implement a new paradigm design for cargo capture and transport. The steady structures during the capture and transport process are found to depend on the pair attraction between motors and number of motors. We found that active forces resulting from self-propulsion is essential in maintaining the caging structure during the cargo capture, and play two roles during the cargo transport: both maintaining the structure by balancing the osmotic pressure and providing the transport momentum for the system. The interplay of these two roles can be affected by the interactions between the motors and the number of motors; further, it determines the amount of the active forces used to transport the cargo, and thus affecting the transport speed.

5.7 Supplemental methods & theory

5.7.1 Brownian dynamics of colloidal motors and cargos

We model the equation of motions of the self-propelled colloidal motors indexed by $I_M=\{1,2,\ldots,N\}$ as

$$\begin{aligned} r_i(t+\Delta t) &= r_i(t) + \frac{D_t}{kT}\cdot F_i\Delta t + \Delta r_i^B + v_i(t)\mathbf{n}_i \\ \phi_i(t+\Delta t) &= \phi_i(t) + \Delta\varphi_i^B \end{aligned} \tag{5.19}$$

where i $\in I_M$, v_i is the propulsion speed as the control input (concrete realization of the propulsion velocity might depend on the specific mechanism and application, here we assume it is using light activation mechanism[75]), $r_i=(x, y)$ is the position vector of the motor, **n**$_i$ is the orientation of motor *i*, given as **n**$_i$ =(cos(ϕ_i),sin(ϕ_i)), Δt is the integration time step, *k* is the Boltzmann's constant, *T* is the temperature. $D_t = kT/6\pi\mu a$ is the translation diffusivity, with μ as the visocity, and D_r = kT/6πμa^3 is the rotational diffusivity. The Brownian translational and rotational displacement Δr_i^B and $\Delta\varphi_i^B$ both have mean 0 and variances of $2D_t\Delta t$ and $2D_r\Delta t$ respectively. F_i is the forces due to interactions (details in the following section) with motors and the cargo.

We model the equation of motion of the cargo as

$$r_c(t+\Delta t) = r_c(t) + \frac{D_t}{kT} \cdot F_c \Delta t + \Delta r_i^B \tag{5.20}$$

where parameters D_t, *k*, *T*, Δr_i^B and Δt are the same as the parameters in the motor's simulations, and F_c is the force due to interactions with motors.

We model the equation of motion of a Brownian target as

$$r_t(t+\Delta t) = r_t(t) + \Delta r_i^B \tag{5.21}$$

where same parameter of Δr_i^B and Δt are used. Note that the Brownian target will not interact with any other objects.

5.7.1.1 Colloidal interactions

The motors' interactions consist of electrostatic repulsion[2] and depletion attractions[92] between motor *i* and motor *j*, given as

$$
\begin{aligned}
u_{i,j}\left(r_{ij}\right) &= B_{pp}\exp\left[-\kappa\left(r_{ij}-2a\right)\right]+\Pi V_{ex}(r_{ij}) \\
V_{ex}(r_{ij}) &= \pi\left(\frac{4}{3}(a+L)^3\left(1-\frac{3}{4}\frac{r_{ij}}{a+L}+\frac{1}{16}\left(\frac{r_{ij}}{a+L}\right)^3\right)\right)
\end{aligned}
\tag{5.22}
$$

where B_{pp} is the pre-factor for electrostatic interactions, κ^{-1} is the Debye length, L is the depletant radius, r_{ij} is the distance between centers of motor i and j. The depletion attraction is written as the product of osmotic pressure, Π, and excluded volume, V_{ex}.

The interaction between motors and the cargo only include electrostatic interactions given as

$$
u_{c,i}\left(r_{c,i}\right) = B_{pp}\exp\left[-\kappa\left(r_{c,i}-2a\right)\right] \tag{5.23}
$$

where the parameters B_{pp} and κ^{-1} are the same as parameters in motors' interactions, and $r_{c,i}$ is the distance between the centers of the cargo and the motor i.

With these interaction potentials, we can calculate the force terms in Eq. (4.1) (5.20) as

$$
\begin{aligned}
F_i &= -\left(\nabla u_{c,i}\left(r_{ij}\right)+\sum_{j\neq i, j\in I_M}\nabla u_{i,j}\left(r_{ij}\right)\right) \\
F_c &= \sum_{j\in I_M}\nabla u_{c,j}\left(r_{c,j}\right)
\end{aligned}
\tag{5.24}
$$

5.7.2 Calculation of optimal control policy

With a set of realizable propulsion speeds, an optimal control policy in the cargo capture and transport tasks is a set of rules specifying which velocity to use when given the instantaneous system state characterized by motors' position and orientation (x, y, ϕ) and assigned targets' position in order to accomplish specific task under optimality criterion.

The central optimal control task throughout this work is to optimally control a set of motors to track a set of moving targets. We first define notations to formalize our methods of obtaining optimal control policy. Let $I_M=\{1,2,\ldots,N\}$ index motors and let $I_T=\{1,2,3,\ldots,N\}$ index the targets, where N is the number of motors and targets. A system state s is defined as the concatenation of state vector of each individual motor as $s = (s_1,s_2,\ldots,s_N)$,$s_i = (r_i, \phi_i)$, $r_i=(x, y)$, $i \in I_M$. The state space S is the set containing all possible value of s. The state space S can be viewed as the product of state spaces of individual motors, i.e., $S=S_1\times S_2\times\ldots\times S_N$. An action u is defined as the concatenation of individual velocity as $u=(v_1, v_2,\ldots,v_N)$. The action space U is the set containing all admissible value of u. The action space U can be viewed as the product of action spaces of individual motors, *i.e.*, $U=U_1\times U_2\times\ldots\times U_N$, with $U_i=\{v: 0\leq v \leq v_{max}\}$.

5.7.2.1 Single motor optimal control to track Brownian target

The single motor optimal control problem is the special case of N=1. The objective of finding an optimal *instantaneous* policy (*i.e.* propulsion speed) for the motor such that the motor can get to the target in minimum time formulated as:

$$\pi^*(s,t) = \arg \min_{\pi(s,t)\in U} \left\langle \left\| r_1(t+\Delta t_c) - r_{t,1}(t) \right\|^2 \right\rangle \tag{5.25}$$

where Δt_c is the control update interval, $r_{t,1}(t)$ is the position vector of target, $r_1(t)$ is the position vector of motor i, < > is taking expectation with respect to joint probability distribution of $r_1(t+\Delta t_c)$ and $r_{t,1}(t)$. And the $r_1(t+\Delta t_c)$ under velocity v is given by integration of (4.1) from t to $t+\Delta t_c$ as

$$r_1(t+\Delta t_c) = r_i(t) + \int_0^{\Delta t_c} (\Delta r_i^B + v\mathbf{n}_1)dt \qquad (5.26)$$

In the short time scale tc << 1/Dr, the probability density of $r_1(t+\Delta t_c)$ and $r_{t,1}(t+\Delta t_c)$ will highly concentrated around their mean value. And we will seek an approximate solution to (5.25) as

$$\pi^*(s,t) = \arg \min_{\pi(s,t)\in U} \left\| \overline{r_1}(t+\Delta t_c) - \overline{r_{t,1}}(t+\Delta t_c) \right\|^2 \qquad (5.27)$$

where the bar over $r_1(t+\Delta t_c)$ and $r_{t,1}(t+\Delta t_c)$ denotes the mean values. Note that such approximation is *well-grounded* because short t_c is used throughout this paper and *necessary* since fast calculation is required for both on-line policy calculation and multi-motor control.

The mean position of $r_{t,1}(t+\Delta t_c)$ is simply $r_{t,1}(t)$ from basic property of Brownian motion. The mean position can be showed to be

$$\overline{r_1}(t+\Delta t_c) = r_1(t+\Delta t_c) + v\mathbf{n}_1\Delta t_c \qquad (5.28)$$

using tools from stochastic process on Lie group. We document the procedures in the next section since this part is highly technical, and reader can skip it without losing continuity.

With the mean position formulated, the optimal speed as the solution to Eq. (5.27) can be written as

$$v^* = \begin{cases} \min(\dfrac{d}{\Delta t_c}, v_{\max}), d > 0 \\ 0 \end{cases} \qquad (5.29)$$

5.7.2.2 Probability distribution using Lie group theory

(This section closely follows the reference.[95])The equation of motion of a single self-propelled motor is given by the following Ito stochastic differential equation as

$$\begin{pmatrix} dx \\ dy \\ d\phi \end{pmatrix} = \begin{pmatrix} v\cos\phi \\ v\sin\phi \\ 0 \end{pmatrix} dt + \begin{pmatrix} \sqrt{2D_t}\cos\phi & -\sqrt{2D_t}\sin\phi & 0 \\ \sqrt{2D_t}\sin\phi & \sqrt{2D_t}\cos\phi & 0 \\ 0 & 0 & 1 \end{pmatrix} \begin{pmatrix} dw_1 \\ dw_2 \\ dw_3 \end{pmatrix}$$

Consider an element in lie algebra se(2) given by **x**=(v1, v2, *ϕ*), it has an equivalent matrix form given by

$$\mathbf{x} = (\mathrm{v}_1, \mathrm{v}_2, \phi), \mathbf{X} = \mathbf{x}^{\vee} = \begin{pmatrix} 0 & -\phi & v_1 \\ \phi & 0 & v_2 \\ 0 & 0 & 0 \end{pmatrix} \in se(2) \qquad (5.30)$$

where we used the wedge operator to convert a vector to associated matrix form. The elements in lie algebra se(2) is associated to elements in the Lie group SO(2) via matrix exponential, given as

$$g = \exp(\mathbf{X}) = \begin{pmatrix} \cos\phi & -\sin\phi & t_1 \\ \sin\phi & \cos\phi & t_2 \\ 0 & 0 & 1 \end{pmatrix} = \begin{pmatrix} R & t \\ 0 & 1 \end{pmatrix} \qquad (5.31)$$

where

$$\begin{aligned} t_1 &= [v_2(\cos(\phi)-1) + v_1\sin(\phi)]/\phi \\ t_2 &= [v_1(1-\cos(\phi)) + v_2\sin(\phi)]/\phi \end{aligned} \qquad (5.32)$$

Consider a rigid body whose position and orientation given by g(t), the spatial velocity in the body frame is given as

$$g^{-1}g' = \begin{pmatrix} R^T R' & Rt' \\ 0^{1\times 2} & 0 \end{pmatrix}, \tag{5.33}$$

where

$$R = \begin{pmatrix} \cos\phi & -\sin\phi \\ \sin\phi & \cos\phi \end{pmatrix}, R' = \begin{pmatrix} -\sin\phi & -\cos\phi \\ \cos\phi & -\sin\phi \end{pmatrix}\phi', R^T R' = \begin{pmatrix} 0 & -1 \\ 1 & 0 \end{pmatrix}\phi', Rt' = \begin{pmatrix} \cos\phi v_1 + \sin\phi v_2 \\ -\sin\phi v_1 + \cos\phi v_2 \end{pmatrix}$$

$$(5.34)$$

Converting matrix form to vector form, we have

$$(g^{-1}g')^{\vee}\, dt = \begin{pmatrix} \cos\phi dx + \sin\phi dy \\ -\sin\phi dx + \cos\phi dy \\ d\phi \end{pmatrix} = \begin{pmatrix} v \\ 0 \\ 0 \end{pmatrix} dt + \begin{pmatrix} \sqrt{2D_t} & 0 & 0 \\ 0 & \sqrt{2D_t} & 0 \\ 0 & 0 & \sqrt{2D_r} \end{pmatrix} \begin{pmatrix} dw_1 \\ dw_2 \\ dw_3 \end{pmatrix} = h dt + H dw$$

This linear constant coefficient stochastic differential equation will have a Gaussian distribution, with mean value given as

$$\mu(t) = \exp(\int_0^t h^\wedge d\tau) = \exp(\begin{pmatrix} 0 & 0 & \int_0^t v d\tau \\ 0 & 0 & 0 \\ 0 & 0 & 0 \end{pmatrix}) = \begin{pmatrix} 1 & 0 & vt \\ 0 & 1 & 0 \\ 0 & 0 & 1 \end{pmatrix}$$

and covariance matrix given as

$$\Sigma(t) = \int_0^t Ad(\mu^{-1}(\tau))\,\mathrm{HH}^T\, Ad^T(\mu^{-1}(\tau))d\tau$$

$$Ad(\mu^{-1}(\tau)) = \begin{pmatrix} 1 & 0 & 0 \\ 0 & 1 & -vt \\ 0 & 0 & 1 \end{pmatrix}, \Sigma(t) = \int_0^t \begin{pmatrix} 1 & 0 & 0 \\ 0 & v^2t^2 & vt \\ 0 & -vt & 1 \end{pmatrix} d\tau = \begin{pmatrix} D_t^2 t & 0 & 0 \\ 0 & v^2t^3/3 + D_t^2 t & -vt^2\,\mathrm{D}_r/2 \\ 0 & -vt^2\,\mathrm{D}_r/2 & \mathrm{D}_r^2\, t \end{pmatrix}$$

In other words, the distribution of g at time t has the following density function

$$f(g \mid \mu, \Sigma) \propto \exp(-\frac{1}{2}(\log(\mu^{-1}\cdot \mathrm{g})^{\vee})^T \Sigma^{-1}(\log(\mu^{-1}\cdot \mathrm{g})^{\vee})) \qquad (5.35)$$

where

$$\mu(t) = \begin{pmatrix} 1 & 0 & vt \\ 0 & 1 & 0 \\ 0 & 0 & 1 \end{pmatrix}$$

$$\Sigma(t) = \begin{pmatrix} D_t^2 t & 0 & 0 \\ 0 & v^2t^3/3 + D_t^2 t & -vt^2\,\mathrm{D}_r/2 \\ 0 & -vt^2\,\mathrm{D}_r/2 & \mathrm{D}_r^2\, t \end{pmatrix}$$

The interpretation of the μ gives that mean position is vt.

5.7.2.3 *Multiple motor optimal control*

In the multi-agent control framework, we will *assign* different motors to track different target. We define an assignment as a mapping *g* from I_M to I_T. Such assignment can be mathematically defined as a mapping *g* from I_M to I_T. We further define *G* as the set of all admissible mappings. The constraints on *G* will depend on specific tasks, *e.g.*, if p=q, we will restrict *G* as the all possible bijective mapping from I_M to I_T, indicating that each motor will trace a distinct target. Finally, we defined a control policy π is a mapping from

S to V. A policy π can also be viewed as the concatenation of individual policies, $\pi = (\pi_1, \pi_2, \ldots, \pi_p)$, π_i: $S_i \rightarrow U_i$, in which each π_i specifies v_i to use when motor *i* is at state s_i .

The objective of finding an optimal *instantaneous* policy (*i.e.* propulsion velocities) to track targets can be mathematically formulated as:

$$\pi^*(s,t) = \arg \min_{\substack{g \in G \\ \pi(s) \in U}} \sum_{i \in I_M} \left\langle (r_i(t+\Delta t_c) - r_{t,\mathrm{g(i)}}(t))^2 \right\rangle \tag{5.36}$$

where Δt_c is the control update interval, $r_{\mathrm{t,g(i)}}(\mathrm{t}), \mathrm{g(i)} \in \mathrm{I_T}$ is the position vector of target assigned to motor *i*(represented by g(*i*)), < > is taking expectation with respect to probability distribution of ri at time $t + \Delta t_c$. Essentially, we are optimizing over all possible admissible assignments and velocity specification such that we can steer our motors to their assigned targets closer in future time $t + \Delta t_c$ in the mean squared error sense. However, the above optimization problem is difficult to solve since it is a mixed programming involves integer programming and continuous programming under constraints. We approximate the optimal solution using the following two sub-steps: solve *g* first and then solve π whiling fixing *g*. The procedure can be formulated as

$$g^* = \arg \min_{g \in G} \sum_{i \in I_M} (r_i(\mathrm{t}) - \mathrm{r}_{t,g(i)}(\mathrm{t}))^2 \tag{5.37}$$

$$\begin{aligned} \pi^*(s,t) &= \arg \min_{\pi(s,t) \in U} \sum_{i \in I_M} \left\langle (r_i(t+\Delta t) - r_{t,g^*\mathrm{(i)}}(t))^2 \right\rangle \Leftrightarrow \\ \pi_i^*(s_i,t) &= \arg \min_{\pi_i(s_i,t) \in U_i} \left\langle (r_i(t+\Delta t) - r_{t,g^*\mathrm{(i)}}(t))^2 \right\rangle, i \in I_M \end{aligned} \tag{5.38}$$

The optimization of Eq. (5.37) can be solved using Hungarian algorithm in combinatory optimization.[93] The optimization of Eq. (5.38) can be decomposed into optimization problem for each motor, which is also trackable.

5.7.3 Sedimentation equilibrium

In order the estimate the equation of state for 2D colloidal system with various interactions, we design sedimentation equilibrium method to construct the equation of state. Similar approach has also been applied in elsewhere.[96]

The simulation box has periodic boundary condition in the horizontal direction(x direction). Monte carlo simulation using Metropolis algorithm was used. The system is initialized from a perfect lattice state and let it melt to equilibrium. When the system reaches equilibrium, particle coordinates are collected every 1000 steps and total 10000 samples are collected.

The density profile $\rho(h)$ in the vertical direction (h direction) is estimated by constructing a normalized histogram on the h coordinates of each particle. The local area fraction ϕ is calculated as $\phi=\rho\pi a^2$.

Assuming force balance hold locally, then we have pressure at specified h, denoted as p(h), is balanced with weight above, mathematically, we have

$$p(h)L = \int_h^\infty \rho(h) G dh \tag{39}$$

In addition, the pressure is connected to the equation of state as

$$p(\phi(\mathrm{h})) = \rho(h) kTZ(\phi(\mathrm{h})) = \frac{\phi(h)}{\pi a^2} kTZ(\phi(\mathrm{h})) \tag{40}$$

where Z is the compressibility as a function of area fraction. From Eq.(39)(40), we are able to calculate p(ϕ) as a function of local area fraction for systems of different colloidal interactions.

6 COLLOIDAL CRYSTAL GRAIN BOUNDARY FORMATION AND MOTION*

6.1 Abstract

The ability to assemble nano- and micro- sized colloidal components into highly ordered configurations is often cited as the basis for developing advanced materials. However, the dynamics of stochastic grain boundary formation and motion have not been quantified, which limits the ability to control and anneal polycrystallinity in colloidal based materials. Here we use optical microscopy, Brownian Dynamic simulations, and a new dynamic analysis to study grain boundary motion in quasi-2D colloidal bicrystals formed within inhomogeneous AC electric fields. We introduce "low-dimensional" models using reaction coordinates for condensation and global order that capture first passage times between critical configurations at each applied voltage. The resulting models reveal that equal sized domains at a maximum misorientation angle show relaxation dominated by friction limited grain boundary diffusion; and in contrast, asymmetrically sized domains with less misorientation display much faster grain boundary migration due to significant thermodynamic driving forces. By quantifying such dynamics vs. compression (voltage), kinetic bottlenecks associated with slow grain boundary relaxation are understood, which can be used to guide the temporal assembly of defect-free single domain colloidal crystals.

---

* Reprinted with permission from “"Colloidal crystal grain boundary formation and motion." *Scientific reports* 4 (2014). By Edwards, Tara D., Yuguang Yang, Daniel J. Beltran-Villegas, and Michael A. Bevan. Copyright © 2014 Nature Publisher Group

6.2 Introduction

Photonic and meta- materials provide examples where ordered particles on length scales comparable to electromagnetic wavelengths produce exotic emergent properties[97]. Colloidal crystallization provides a potential route to self-assemble such materials *via* processes amenable to scalable manufacturing; however, robust schemes have yet to be identified to obtain the necessary low defect densities. From a broader perspective, obtaining perfect crystals on any length scale remains more art than science (*e.g.*, atoms, molecules, macromolecules)[98,99]. To design robust crystal growth, recrystallization, and annealing schemes to minimize defects, it is necessary to know the basic mechanisms of defect formation and motion.

Although three-dimensional configurations of complex particles are the ultimate goal of self-assembly schemes[17,24], here we investigate a relatively simple problem that is still not well understood: how grain boundaries form and move during quasi two-dimensional (2D) crystallization of spherical colloids. Quasi-2D colloidal crystals have been used in studies of melting[100], nucleation[42], point defect diffusion[101], and grain boundary fluctuations[102]. Other relevant studies include 2D analyses of colloidal crystals to investigate impurity mediated growth[103], particle motion within grain boundaries[104], and grain boundary pre-melting[105]. Despite these extensive studies, fundamental understanding of grain boundary formation and motion remains rudimentary[106] in all but the most model simulation studies[107]. 2D crystals are also of interest based on their relevance to thin films[108], bubble rafts[109], and graphene[110]. Understanding how grain boundary motion enables relaxation of multi-domain crystals into defect-free crystals is therefore scientifically and technologically interesting.

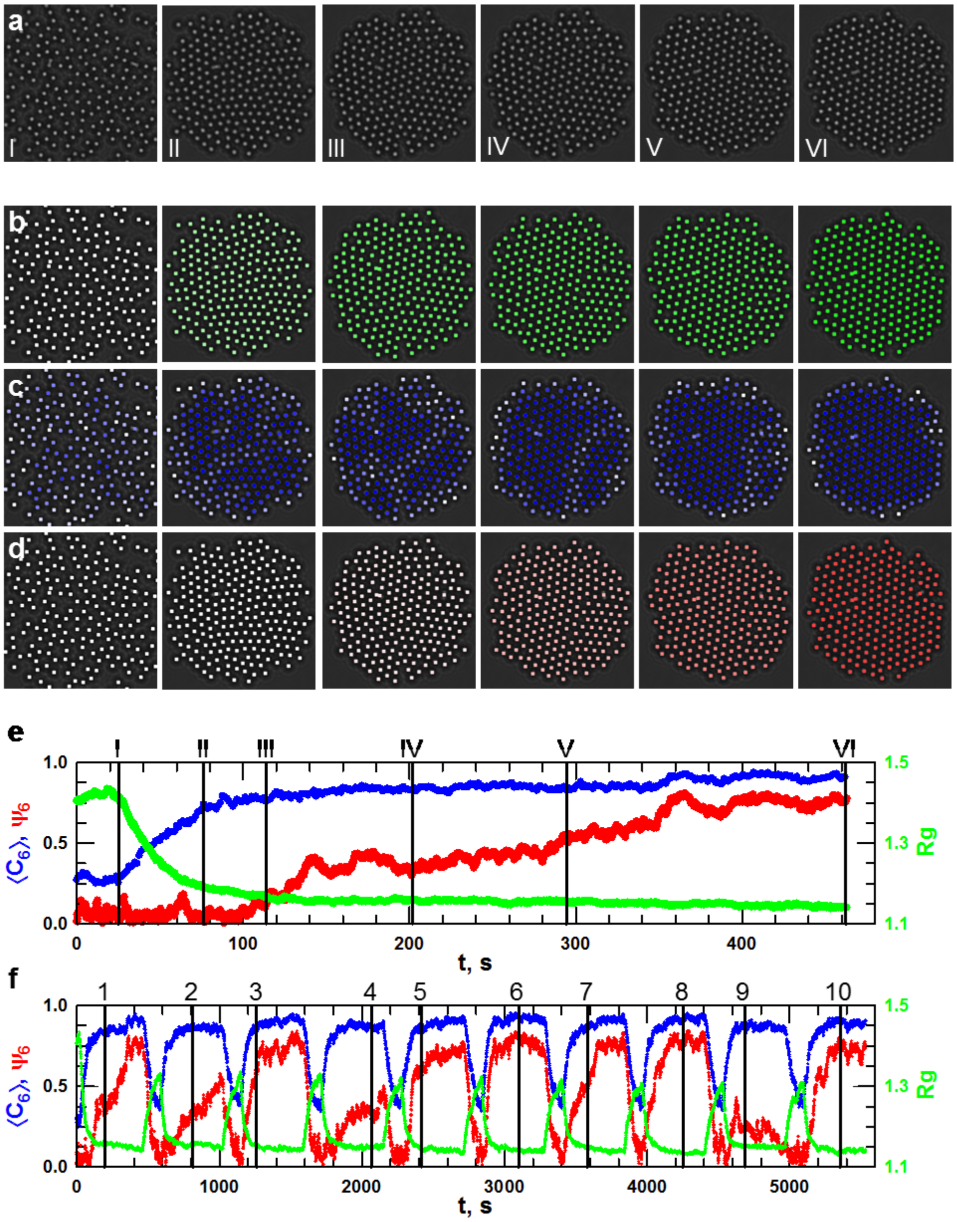

Figure 1. Reaction coordinates for grain boundary formation and motion can be computed from image analysis of optical microscopy images of electric field mediated colloidal crystallization. (**a**) Raw images show representative configurations of 210 ~3 μm silica colloids in fluid, bicrystal, and single crystal configurations observed over ~7.5 min following a quench (step voltage change) to V^*=0.57 (see main text and Supplementary Methods for definition). Snapshot times are shown by solid black lines in Fig. 1e. Computed reaction coordinates shown by colored particle centers on 8-bit intensity scale for the (**b**) radius of gyration, R_g, (**c**) local hexagonal order, $\langle C_6 \rangle$, (**d**) global hexagonal order, ψ_6, and time dependent traces for (**e**) a single voltage quench and (**f**) ten consecutive cycles (numbered vertical black lines indicate representative images included in Supplementary Fig. 2).

6.3 Results

In this work, we employ real-time microscopy to observe grain boundary formation and motion in a quasi-2D colloidal crystal containing ~200 colloidal particles (Fig. 1a, Supplementary Videos 1-4). Aqueous ~3 micron SiO_2 charged colloids crystallize in a quadrupole electrode in MHz AC electric fields (see Methods, Supplementary Information)[111], where field-mediated compression of induced dipoles is balanced by the quasi-2D colloid osmotic pressure (*i.e.*, effective hard disk). The electric field amplitude (*i.e.*, applied voltage) is effectively a surrogate for pressure and hence acts as a global thermodynamic variable that determines the relative free energy of all particle configurations for fixed voltage, number, and temperature. In the following, we report non-dimensional voltages, where $V^*=1$ is the voltage required for N particles to produce a hexagonal close packed crystal with hexagonal morphology (as demonstrated in previous work with agreement between microscopy experiments, MC simulations, and perturbation theory[112], see Supplemental Information for additional details).

Our previous characterization of electric field mediated colloidal interactions and assembly has yielded kT-scale potentials[113,114], feedback control over system size[111], and conditions to crystallize N particles[112]. Based on these findings, we set $N=210$ in Fig. 1, which routinely forms bicrystals (*i.e.*, 1 grain boundary between 2 domains) in contrast to single domains in smaller systems and >2 domains in larger systems. As shown in Fig. 1, step-quenches to $V^*=0.57$ cause an initially dilute fluid phase to first rapidly condense, then form grain boundaries *via* coalescence of local domains, and finally display grain boundary motion as bicrystals relax to single crystals. Reversibility allows repeated quenches between fluid and crystal states to probe the stochastic dynamics of grain boundary formation, diffusion (*i.e.*, random motion), and migration (*i.e.*, drift). We first focus on the V^*=0.57 case, but later (in Fig. 4) investigate step-changes to both lower and higher values of V^*.

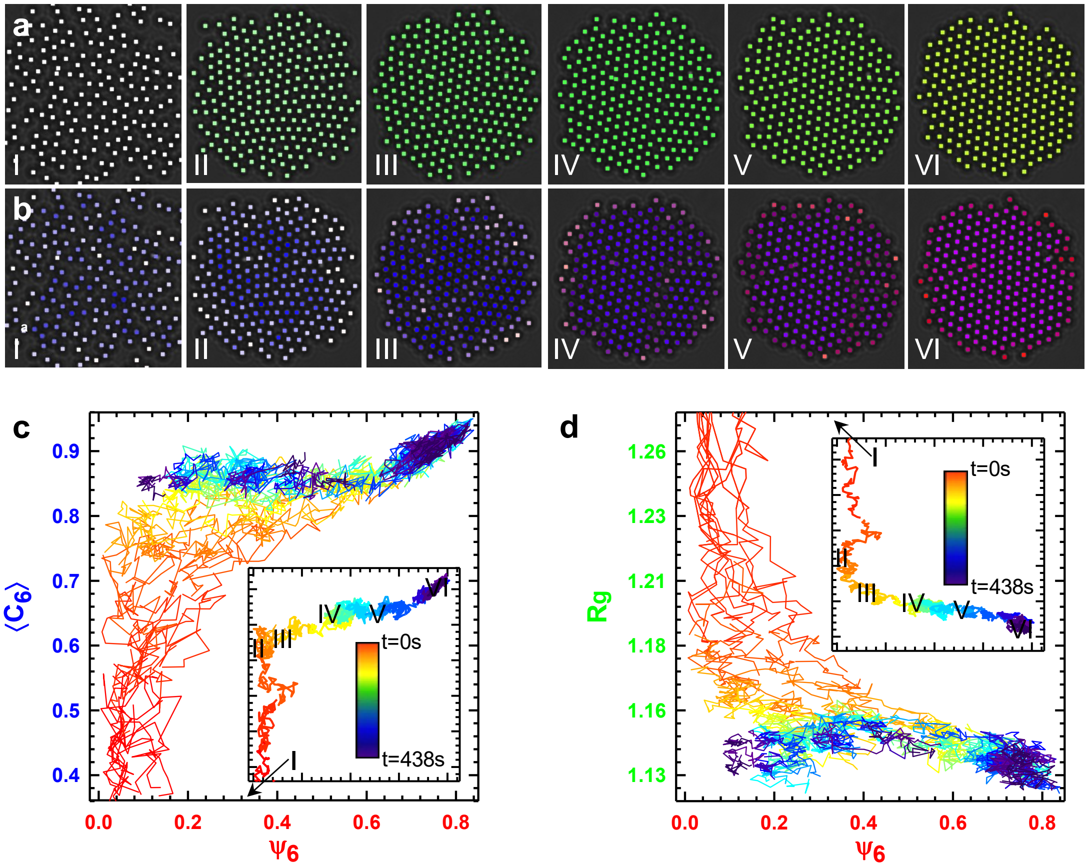

Figure 2. "Two dimensional" trajectories (*i.e.*, two reaction coordinates) capture coalescence of local domains during fast condensation processes to produce bicrystals that relax to single crystals via grain boundary motion over a broad range of timescales. Microscopy images from Figs. 1a with particle centers colored using RGB (Red/Green/Blue) mixing rules for colors represented by two reaction coordinates including (**a**) ψ_6 and C_6 and (**b**) ψ_6 and R_g to visualize how global order emerges from local order and during condensation. Ten trajectories following quenches to V^*=0.57 with time represented by a 256-color scale (inset scale bar) for (**c**) (ψ_6, $\langle C_6 \rangle$) and (**d**) (ψ_6, R_g) reaction coordinate pairs with inset plots of single trajectories from Fig. 1e.

To interpret and model these measurements, we aim to develop a "low-dimensional model" that quantitatively captures the observed dynamics using "reaction coordinates"[115] (rather than enumerating all $2N$ translational degrees of freedom)[38,116]. The use of the term "low-dimensional" here does not refer to the Euclidian spatial dimension (*i.e.*, x and y particle center coordinates), which is effectively quasi-two dimensional, but rather, "dimensionality" refers to the number of reaction coordinates necessary to capture the stochastic dynamics of grain boundary formation. It is "low dimensional" because we expect the number of reaction coordinates to be considerably less than the $2 \times (N=210) = 420$ dimensions that would be necessary to uniquely specific all possible two-dimensional configurations of 210 particles. Although the term "low-dimensional" may be unfamiliar to some readers, other synonymous terms such as "coarse-grained models" could also be confusing based on an unfortunate overlap of terms relevant to the application of interest in this work.

Candidate reaction coordinates are computed from particle centers and used to color code images (Figs. 1b-f) including: the radius of gyration, R_g[111], to capture condensation from fluid to crystal states, average local hexagonal order, $\langle C_6 \rangle$[43], to capture the onset of crystallization, and global hexagonal order, ψ_6[117], to capture the degree of polycrystallinity. R_g and $\langle C_6 \rangle$ are normalized by their N particle single crystal values (see Supplementary Methods), so that $\langle C_6 \rangle$ goes from 0-1 for fluids to complete locally ordered states, and R_g decreases from arbitrarily high numbers to 1 for complete condensation[112]. ψ_6 is 0 for fluids and 1 for single-domain crystals like $\langle C_6 \rangle$, but in contrast, depends strongly on relative domain size and misorientation (*e.g.*, $\psi_6=0$ for bicrystals of identically sized 111 domains with 30° misorientation).

The reaction coordinates trajectories following a single voltage quench (Fig. 1e) show initially decreasing R_g and increasing $\langle C_6 \rangle$ occur in unison (*i.e.*, $R_g^{-1} \approx \langle C_6 \rangle$), which demonstrates a close coupling between condensation and local ordering. As R_g and $\langle C_6 \rangle$ plateau, indicating an overall condensed configuration with all particles contained in locally crystalline domains, $\psi_6 \approx 0$, indicating a bicrystal. For t>100 s, R_g and $\langle C_6 \rangle$ remain essentially unchanged while ψ_6 rises from 0 to ~0.8, which clearly corresponds to grain boundary motion from the bicrystal interior to the periphery where it vanishes (Fig. 1c, Supplementary Video 1).

Ten successive voltage quenches from initial fluid states (Fig. 1f) demonstrate the stochastic nature of the grain boundary dynamics, which is expected from the underlying probabilistic colloidal motion. While R_g and $\langle C_6 \rangle$ reveal condensation and local order emerge in a similar manner for each cycle, the ψ_6 trajectories can be categorized into several cases: (1) ψ_6 tracks $\langle C_6 \rangle$ indicating the simultaneous emergence of local and global order, (2) ψ_6 becomes localized at intermediate values for varying time periods before again increasing, (3) ψ_6 becomes arrested for the duration of the observation time, and (4) in one case, ψ_6 initially increases but then vanishes. The stochastic nature of the observed grain boundary dynamics apparent in an ensemble of trajectories is an important aspect to capture in a quantitative model.

To develop a low-dimensional model of grain boundary formation and motion, it is necessary to determine the number and type of reaction coordinates. For example, it could be speculated that ψ_6 is all that is required to track grain boundaries since it visually tracks polycrystallinity in Fig. 1. However, simply tracking ψ_6 does not capture how parallel processes of local condensation and crystallization determine the formation and motion of grains of different sizes, shapes, and orientations, which ultimately determine the mechanisms of polycrystals relaxing to single crystals. In addition, ψ_6 does not uniquely identify some configurations; for example, fluid configurations and maximally misaligned bicrystals both have ψ_6=0.

To illustrate how reaction coordinate pairs capture additional information, experimental configurations are colored using two coordinates (Figs. 2a, b) and 2D trajectories of (ψ_6, $\langle C_6\rangle$) (Fig. 2c) or (ψ_6, R_g) (Fig. 2d) vs. time, where time is indicated by a 256-color scale. We do not plot (R_g, $\langle C_6\rangle$) since these coordinates are highly correlated in Fig. 1, although such a pair could be useful to distinguish condensed amorphous microstructures (*i.e.*, glasses/gels). Such 2D plots immediately address one issue; plotting ψ_6 against either R_g or $\langle C_6\rangle$ distinguishes fluid and bicrystal configurations (*e.g.*, high R_g, low ψ_6 vs. low R_g, low ψ_6). These trajectories also show how local ordering (*i.e.*, increasing $\langle C_6\rangle$) and condensation (*i.e.*, decreasing R_g) influence the emergence of polycrystallinity and subsequent grain boundary motion. Trajectories starting at lower ψ_6 tend to become localized at lower ψ_6 after condensation, whereas trajectories with initially higher ψ_6 tend to rapidly form single crystals.

Although tools exist to identify the minimum dimensionality (*i.e.*, number of reaction coordinates) from observed dynamics (*e.g.*, diffusion mapping[118-120]), such methods are not currently able to predict physically meaningful reaction coordinates[115]. Ultimately, the number and types of reaction coordinates can be determined empirically by finding what is necessary to produce a quantitative stochastic dynamic model. Because the measured trajectories display both drift and diffusion along reaction coordinates, which appear to be mediated by free energy gradients (*i.e.*, driving forces) and fluctuations/friction (*i.e.*, randomness/resistance), it is assumed that such processes can be captured by a low-dimensional Smoluchowski equation given by[121],

$$\frac{\partial p(\mathbf{x},t)}{\partial t} = \nabla \mathbf{D}(\mathbf{x})\left[\nabla + \frac{1}{kT}\frac{dW(\mathbf{x})}{d\mathbf{x}}\right]p(\mathbf{x},t) \tag{6.1}$$

where $p(\mathbf{x}, t)$ is the probability density of finding the system at coordinate $\mathbf{x}$ at time, t, $W(\mathbf{x})$ is the free energy landscape, kT is thermal energy, and $\mathbf{D}(\mathbf{x})$ is the diffusivity landscape, which can be related in the usual way to mobility, $\mathbf{m}(\mathbf{x})$, and friction, $\boldsymbol{\zeta}(\mathbf{x})$, landscapes as $\mathbf{D}(\mathbf{x}) = \mathbf{m}(\mathbf{x})kT = \boldsymbol{\zeta}(\mathbf{x})^{-1}kT$. The variable $\mathbf{x}$ is a vector of reaction coordinates where the number of coordinates is the model "dimension." The Smoluchowski equation is a special case of the Fokker-Planck equation that also satisfies the fluctuation-dissipation theorem and leads to Boltzmann sampling at equilibrium (*i.e.*, $p(\mathbf{x})=\exp[-W(\mathbf{x})/kT]$)[38,121]. In more descriptive terms, $W(\mathbf{x})$ is the free energy change associated with moving from one particle configuration to another (or one reaction coordinate to another; (*e.g.*, $\mathbf{x}_1=(\psi_{6,1}, R_{g,1})$ to $\mathbf{x}_2=(\psi_{6,2}, R_{g,2})$), and $\mathbf{D}(\mathbf{x})$ captures the associated configuration dependent changes in diffusion and friction (*i.e.*, fluctuations and dissipation).

To obtain $W(\mathbf{x})$ and $\mathbf{D}(\mathbf{x})$ in Eq. (6.1) from trajectories like those in Figs. 1 and 2, we analyzed Brownian Dynamic (BD) simulations that were matched to experiments (by capturing all equilibrium and dynamic properties of the quadrupole experiment on the particle scale[112-114], see Supplementary Methods). This approach was used because statistics on the particle scale are easily obtained to match experiments and simulations, but BD simulations are better suited to generating large numbers of grain boundary trajectories (*e.g.*, each experimental grain boundary trajectory in Fig. 1 is acquired for ~10 min.).

To provide more details of the matching process and trajectory analysis, inverse Monte Carlo was used to obtain interaction potentials that capture all equilibrium properties (*i.e.*, radial distribution functions), which were then employed in BD simulations that captured all dynamic properties (*i.e.*, particle scale diffusion, reaction coordinate trajectories). It is important to note that it was necessary to include concentration dependent hydrodynamic interactions in the BD simulations to produce agreement with experiments. Statistical methods reported in the literature[38], and further developed by us for application to colloidal assembly[122], were used to analyze large numbers of BD simulated trajectories to construct $W(\mathbf{x})$ and $\mathbf{D}(\mathbf{x})$ (see more details in Supplementary Methods and our previous work[120,122]). In brief, the displacement and mean squared displacement of reaction coordinate vs. time trajectories can be used to measure drift and diffusion at each value of $\mathbf{x}$, which ultimately yield $W(\mathbf{x})$ and $\mathbf{D}(\mathbf{x})$.

To assess the quantitative accuracy of candidate low-dimensional dynamic models, we compared first passage time distributions for ensembles of trajectories between different starting and ending states from particle-scale BD simulations and low-dimensional Langevin dynamic (LDLD) simulations. The LDLD simulations are based on a Langevin equation given as,

$$\mathbf{x}(t+\Delta t)=\mathbf{x}(t)-\mathbf{D}\left[\mathbf{x}(t)\right]\cdot(kT)^{-1}\nabla W\left[\mathbf{x}(t)\right]\Delta t+\nabla\cdot\mathbf{D}\left[\mathbf{x}(t)\right]+\left[2\mathbf{D}\left[\mathbf{x}(t)\right]\Delta t\right]^{1/2}\mathbf{\Gamma}(t) \tag{6.2}$$

where the coefficients are the same as in Eq. (6.1), Δt is the integration time step, and $\mathbf{\Gamma}(t)$ is a noise variable. A successful LDLD model will accurately reproduce first passage time distributions obtained from high $2N$-dimensional particle-scale BD simulations, and hence the experimental trajectories that were quantitatively matched to the BD simulations. The only quantitatively accurate model to emerge from candidate 1D and 2D models was one based on (ψ_6, R_g) (so higher dimensional models were not considered). Fig. 3a shows the $W(\mathbf{x})$ that quantifies the relative free energy of every configuration and the free energy gradients that drive motion. The global free energy minimum at $\mathbf{x}=(\psi_6, R_g)\approx(0.8, 1.14)$ indicates a single domain crystal (with a thin fluid envelope at its periphery) is the thermodynamically favored configuration (image VI in Fig. 3c).

The diffusivity landscape, $\mathbf{D}(\mathbf{x})$, in Eqs. (6.1) and (2) is a 2×2 tensor; it has diagonal components that capture how friction/mobility in each reaction coordinate mediate drift due to free energy gradients in the same coordinate ($D_{\psi6\psi6}$, D_{RgRg}), and cross-terms that capture how friction/mobility mediate drift due to free energy gradients in orthogonal coordinates ($D_{\psi6Rg}$, $D_{Rg\psi6}$). Fig. 3b shows $D_{\psi6\psi6}/kT$, which captures how friction mediates drift and diffusion in ψ_6 due to free energy gradients in ψ_6. The other components of $\mathbf{D}(\mathbf{x})$ are reported in Supplementary Fig. 5. D_{RgRg} shares similar features with $D_{\psi6\psi6}$. The cross-terms ($D_{\psi6Rg}$, $D_{Rg\psi6}$) indicate a weak coupling between driving forces and drift/diffusion (*i.e.*, friction increases as free energy increases) along orthogonal coordinates for $\psi_6 \gtrsim 0.5$, although this is relatively minor compared to the diagonal terms.

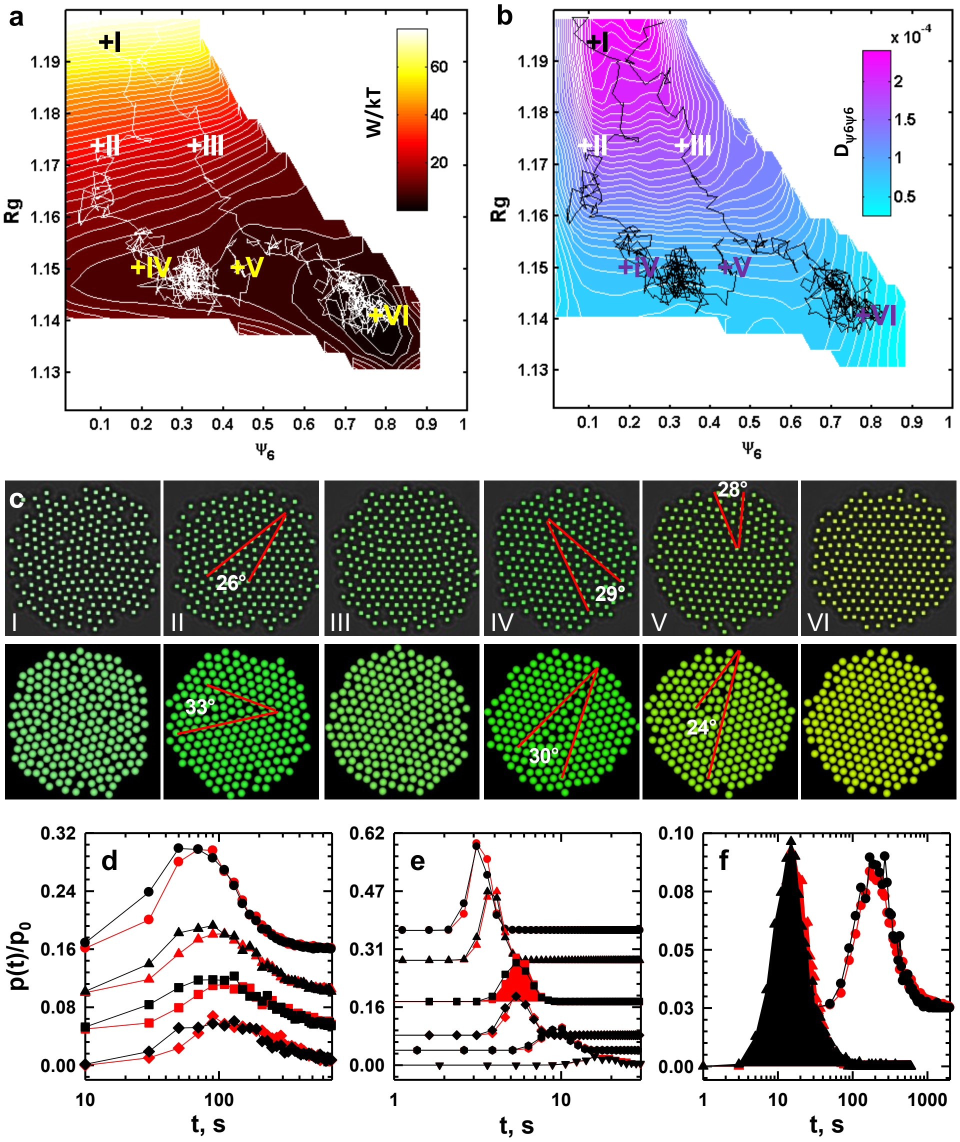

Figure 3. Free energy and friction landscapes obtained by fitting trajectories to Smoluchowski equation (equation 1) that quantitatively capture grain boundary diffusion and migration vs. relative domain sizes and misorientation angles. (**a**) $W(\psi_6, R_g)/kT$ with inset scale bar and two trajectories obtained from the experiments in Figs. 1 and 2. (**b**) $D_{\psi6\psi6}/(kT \cdot s)$ with inset scale bar with the same trajectories as in (a). (**c**) Representative configurations from microscopy images and simulated renderings for coordinates marked along trajectories in (a) and (b). Labeled misorientation angles shown by red lines and particle centers are colored according to the RGB composite convention in Fig. 2. First passage time distributions for BD (red) and LDLD (black) trajectories projected onto (**d**) the ψ_6-axis between 0.47-0.66 (●,●), 0.38-0.56 (▲,▲), 0.28-0.47 (■,■), 0.19-0.38 (◆,◆) and (**e**) R_g-axis between 1.27-1.25 (●,●),1.25-1.23(▲,▲), 1.23-1.21 (■,■), 1.21-1.19 (◆,◆), 1.21-1.19 (⬢,⬢), 1.19-1.17 (▼,▼), and (**f**) for trajectories between a sink at (ψ_6=0.8 R_g=1.14) (*i.e.*, global minimum) and sources at (ψ_6=0.38 R_g=1.15) (●,●). and (ψ_6=0.65 R_g=1.16) (▲,▲).

Representative configurations (Fig. 3c) and first passage time distributions (Fig. 3d-f) show the resulting low dimensional ψ_6, R_g model quantitatively captures the measured grain boundary dynamics. The agreement between the BD and LDLD simulations is excellent (Fig. 3d-f), demonstrating that Eqs. (6.1) and (6.2) with the $W(\psi_6, R_g)$ and $\mathbf{D}(\psi_6, R_g)$ in Fig. 3 provide accurate low dimensional dynamic models of the experiments in Figs. 1 and 2.

6.4 Discussion

To aid discussion of how features on $W(\psi_6, R_g)$ and $\mathbf{D}(\psi_6, R_g)$ are connected to microscopic mechanisms, two limiting trajectories are shown on these landscapes; one where a grain boundary forms between two domains and does not move out of the crystal on the ~10 min observation time [trajectory 1 (T1): I-II-IV-V], and one where two domains form but the grain boundary quickly moves to the crystal periphery in <1 min to produce a single domain crystal [trajectory (T2): I-III-VI]. Both trajectories are consistent with expectations by showing drift (*i.e.*, migration) along free energy gradients and superimposed stochastic motion (*i.e.*, diffusion) that is most evident where free energy gradients are minimal. The dramatic difference between these two trajectories is most evident as they approach the global minimum (Fig. 3f) (as quantified between "sources" at III and IV and a "sink" at VI). An order of magnitude difference is observed in the most probable first passage times with ~20 s for III-VI and ~200 s for IV-VI; the latter distribution also shows a much longer asymmetric tail with some trajectories taking >1,000 s to traverse the $W(\psi_6, R_g)$ plateau at low R_g.

The T1 trajectory corresponds to rapid condensation along a steep free energy gradient where two locally ordered domains coalesce into a bicrystal with a near maximum 30° misorientation angle. At point IV on T1, the grain boundary randomly diffuses on a free energy plateau with a minimal free-energy gradient (*i.e.*, driving force) to drive migration of the grain boundary to the crystal edge; the trajectory is localized between IV-V for ~10 min. In addition to vanishing free energy gradients, the friction in the vicinity of IV-V is increased ~6× compared to uncondensed states. Multi-body hydrodynamic interactions (*i.e.*, near-field lubrication and far-field flow within the particle structure[123]) increase particle-scale friction during condensation, which is consistent with the increased friction for trajectories at low R_g on $\mathbf{D}(\psi_6, R_g)$ (Fig. 3b). Although first passage times vary linearly with frictional changes compared to an exponential dependence for free energy changes[124,125], diffusion mediated by friction is the rate determining process in the presence of vanishing free energy gradients (plateau of Fig. 3a).

In contrast to T1, the T2 trajectory is initiated with higher global order before moving down the free energy gradient and rapidly continuing towards the global free energy minimum single crystal. Although T2 passes close to T1, low friction at high R_g allows sufficient diffusion towards higher ψ_6, As a result, T2 bypasses the free energy plateau region at low R_g to avoid slow diffusion like T1, and instead shows much faster grain boundary migration. Friction uniformly increases with decreasing R_g (due to hydrodynamic interactions), and has almost no dependence on ψ_6, so there is no path of least resistance on $\mathbf{D}(\psi_6, R_g)$. In short, the fastest trajectories are ones that bypass the free energy plateau region.

The microscopic mechanisms associated with these different trajectories can be understood from the images/renderings (Fig 3c) and the physical meaning of the reaction coordinates. R_g clearly captures condensation as shown by large free-energy gradients on $W(\psi_6, R_g)$ and increasing resistance to configurational changes on $\mathbf{D}(\psi_6, Rg)$ as the result of multi-body hydrodynamic interactions. At this point, we can speculate why $\langle C_6 \rangle$ was not part of a successful dynamic model; it is an indirect measure of condensation, and thus not as good as R_g, and it is the emergence of global order, captured by ψ_6, that is most important to track grain boundaries.

The ψ_6 dependence of $W(\psi_6, R_g)$ indicates that domains coalescing with minimal misorientation produce higher global order from the outset, which also translates to faster grain boundary migration (*via* free-energy gradients) from the crystal interior to the periphery. Practically, low misorientation angles produce smaller energy barriers to particle-scale motion (in full $2N$-dimensional particle-scale space) within (*e.g.*, string-like motion) and across (*e.g.*, cooperative motion) grain boundaries[126]. In contrast, domains that coalesce near the maximum 30° misorientation display low initial global order that translates into slow grain boundary diffusion on a $W(\psi_6, R_g)$ plateau. Such bicrystals represent an unstable equilibrium where the energy (*e.g.*, energy/atom, interfacial energies)[108] of the two sides balance, however, the lower free energy state single crystal ($\sim 10kT$) is achieved by fluctuations that eventually allow one grain to increase at the expense of the other grain decreasing.

Because ψ_6 does not resolve different combinations of domain size and misorientation, but accurately captures the dynamics, it appears that all such configurations relax in an indistinguishable manner. In particular, greater misorientations between dissimilar sized grains produces relaxation rates equivalent to cases where domains have less misorientation but are of similar size. This finding shows how using ψ_6 as a reaction coordinate indicates an aspect of grain boundary motion that would not be easily discovered from tracking particle-scale motion alone. Because grain boundary motion involves many particles rearranging in a cooperative fashion based on relative domain sizes and orientations, it is useful to have a global parameter that captures configurational changes of the entire particle ensemble, and therefore naturally captures cooperative phenomena.

The approaches used to measure and model grain boundary motion for V^*=0.57 in Figs. 1-3 can be applied at other V^*. Using the same BD simulations and non-equilibrium analyses, $W(\psi_6, R_g)$ were constructed in the range V^*=0.31-0.69 (Fig. 4a-d) along with representative trajectories and global minimum configurations. At the lowest V^*, particles are weakly confined in concentrated fluid configurations without crystal grains or boundaries, which produces a relatively featureless $W(\psi_6, R_g)$. At the highest V^*, $W(\psi_6, R_g)$ is qualitatively similar to Fig. 3a, but the plateau stretches from very low to high ψ_6 with an even shallower gradient and deeper global minimum at $\psi_6 \rightarrow 1$. At intermediate V^*, the $W(\psi_6, R_g)$ show a continuously shifting global minimum towards lower R_g and higher ψ_6 and a stretching plateau corresponding to slower grain boundary migration. $\mathbf{D}(\mathbf{x})$ vs. V^* are not reported here, but the general trend with increasing voltage is a decreasing magnitude (*i.e.*, decreasing mobility, increasing friction), which is consistent with more condensed configurations hindering particle motion and hence motion along both reaction coordinates. In short, with increasing compression, once grain boundaries form, they experience slower migration and diffusion, and the single perfect crystal clearly emerges as the global free energy minimum configuration.

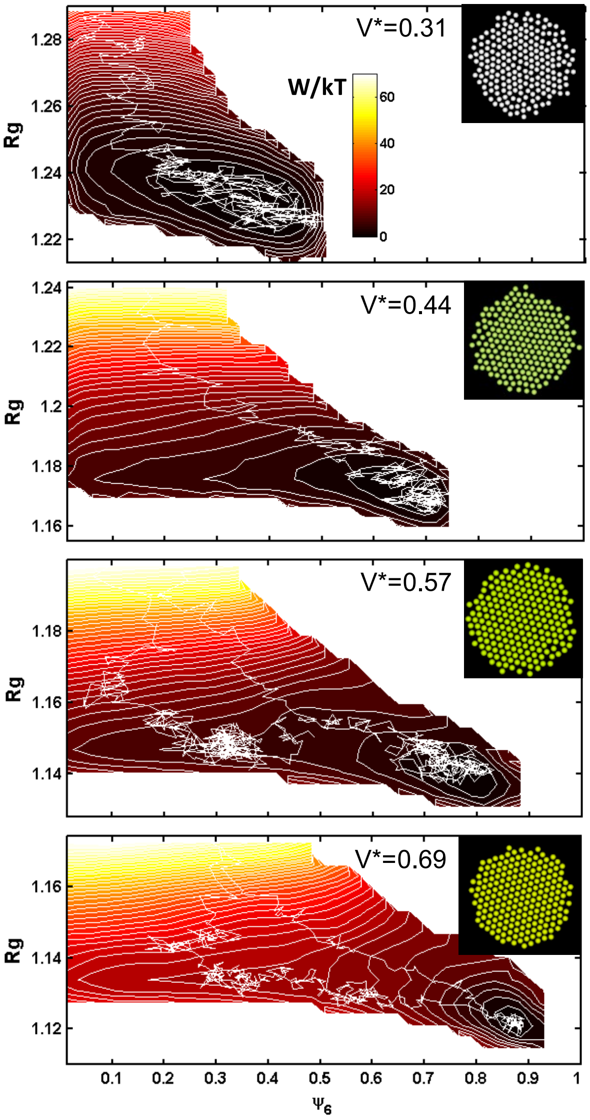

Figure 4. Free energy landscapes based on ψ_6, *Rg* reaction coordinate pair capture dynamics at all V* to provide quantitative models of grain boundary formation and motion. W(ψ_6, R_g)/*kT* at (**a**) *V**=0.31, (**b**) *V**=0.44, (**c**) *V**=0.57, and (**d**) *V**=0.69 with inset renderings of global minimum configuration and representative trajectories from BD simulations that were matched to the experiments (see Supplementary Methods). The free energy scale is indicated by the inset in (a).

The results show voltage cannot simply be increased to increase order, since in general this produces increasingly arrested polycrystalline states. It is interesting to consider how grain boundary formation and motion might be manipulated by "switching" between $W(\psi_6, R_g)$ at different V^*. If V^* is increased very slowly, it would be possible to remain in the global free energy minimum configuration at all voltages; this is the thermodynamic equilibrium limit and a known strategy to make single crystals. However, faster schemes are generally desirable. The optimal control policy[127] to achieve a single perfect crystal in minimal time could employ the quantitative non-equilibrium dynamic models in Eqs. (6.1) and (6.2) to switch between $W(\psi_6, R_g)$ at different V^* in an automated, informed manner using feedback control[73]. In particular, monitoring reaction coordinates in real-time could identify slowly relaxing polycrystalline configurations (*i.e.*, due to vanishing free-energy gradients and high friction), and then V^* could be tuned to "land" on another $W(\psi_6, R_g)$ at the same coordinates where faster relaxation occurs.

In summary, we report agreement between optical microscopy measurements, Brownian Dynamic simulations, and low-dimensional models of stochastic grain boundary formation and motion in quasi-2D colloidal bicrystals. Our results show that two reaction coordinates, one for condensation and one for global order, are sufficient to quantitatively capture first passage times between critical configurations at each applied voltage. Free energy and diffusivity landscapes show that the relative misorientation angles and domain sizes formed during condensation determine the subsequent grain boundary motion. Bicrystals with similar sized domains and a near 30° maximum misorientation angle relax *via* slow grain boundary diffusion mediated by high friction and vanishing free energy gradients, whereas bicrystals with asymmetrically sized and/or less misoriented domains relax *via* much faster grain boundary migration due to greater thermodynamic driving forces. By quantifying such dynamics as a function of voltage, ongoing work is developing optimal control algorithms to dynamically tune voltages to avoid kinetic bottlenecks associated with slow grain boundary dynamics. Future work will extend the approaches reported here for bicrystals to many-domain crystals, where different reaction coordinates might be required to track the how polycrystallinity evolves at stages well before a single domain emerges.

6.5 Methods

Coplanar gold thin film quadrupole electrodes were patterned on glass microscope coverslips by spin coating photoresist and physical vapor deposition of a 15 nm chromium layer and a 35 nm gold layer. Nominal 3.13 μm diameter SiO_2 colloids with ~50 mV zeta potentials were fractionated in DI water and centrifuged/redispersed five times in 0.1 mM NaOH. PDMS o-rings were coated with vacuum grease and sealed between a coverslip with the patterned quadrupole electrode before it was connected in series with a function generator. Microscopy was performed on an inverted optical microscope with a 63× objective and a 12-bit CCD camera that captured 336 pixel × 256 pixel (81 μm × 62 μm) digital images at rate of 8 frames/s. Video capture and image manipulation were performed using algorithms in MATLAB.

BD simulations in the canonical ensemble were performed for 210 colloidal particles at constant voltage using numerical methods described in previous papers[122,128-131]. A 0.1 ms time step was used for at least 2×10^7 steps, and reaction coordinates were stored every 1250 steps for subsequent analysis. Particles in simulations were confined within 2D planes. Inverse Monte Carlo methods (including image resolution limiting effects)[132-134] were used to match measured and simulated radial distribution functions to determine parameters in interactions potentials. The diffusivity was matched by comparing measured and simulated mean square displacements. Parameters used in the BD simulations are reported in the Supplementary Information.

6.6 Supplementary materials

Materials: Coplanar quadrupole gold thin film electrodes were patterned on glass microscope coverslips (Corning) that were sonicated in acetone for 30 min, sonicated in isopropanol (IPA) for 30 min, rinsed with copious amounts of deionized (DI) water, soaked in Nochromix (Godax) for 1 h, again rinsed with copious amounts of DI water, sonicated in 0.1 M KOH for 30 min, again rinsed with copious amounts of DI water, and dried with N_2 prior to patterning. The quadrupole electrodes were fabricated by spin coating photoresist (S1813, Shipley) onto microscope cover slips, UV exposure through a chrome photomask, and physical vapor deposition of a 10 nm chromium adhesive layer and a 40 nm gold layer. The photoresist liftoff was accomplished with agitation in 1165 Remover (Shipley). The electrode tips are separated by ~100 μm. Prior to experimentation, the coverslips with patterned quadrupole electrodes were again sonicated in acetone for 15 min, sonicated in IPA for 15 min, rinsed with copious amounts of DI water, and dried with N_2.

Sedimentation Fractionation of SiO_2 Colloids: Nominal 3.13 μm diameter SiO_2 colloids (Bangs Laboratories) were fractionated in DI water to minimize colloidal particle size polydispersity in experiments. One mL of as-received stock SiO_2 particles was added to a glass test tube containing ~33 mL of DI water. The test tube was sealed and sonicated for 10 min to disperse and suspend the colloidal particles. Particles were then allowed to sediment ~6 h until the colloidal sedimentation line fell approximately half way down the test tube. One aliquot of the sedimented particle dispersion was then removed using a 9" glass Pasteur pipette (Fisher Scientific) approximately one third of the distance from the top of the colloidal sedimentation line. The removed particle dispersion aliquot was dispensed into and stored in a second glass test tube. The removed volume of sedimented particle dispersion was replaced with DI water. Unless all the particles in the colloidal dispersion are of identical size, it is possible to obtain a monodisperse colloidal dispersion by repeating this procedure and removing an aliquot of sedimented particles from the same location each time. This procedure was repeated until the second test tube was approximately half full with the colloidal dispersion removed from the first test tube. At this point, the remaining volume of the second test tube was topped off with DI water. The procedure used for the first and second test tubes was repeated using the second and a third test tubes. The fractionated 3.13 μm SiO_2 particles were stored at 2-8 °C. Prior to each experiment, the fractionated colloidal particles in DI water were centrifuged and redispersed in 0.1 mM NaOH five times.

Quadrupole Electrode: Supplementary Fig. 1 displays the quadrupole electrode device set-up. Experiments were performed in batch cells consisting of Sylgard polydimethylsiloxane (PDMS, Dow Corning). Prior to experimentation the o-rings were sonicated in IPA for 15 min, rinsed with IPA, and dried with lens paper (Fisher Scientific). To construct batch cells, PDMS o-rings were coated with vacuum grease (Dow Corning) and sealed between the coverslip with the patterned quadrupole electrode and a glass coverslip (Corning). 90 μL of the colloidal particle dispersion was dispensed into the batch cell and allowed to sediment for 5 min prior to sealing to obtain approximately 210 particles in the quadrupole. 22 gauge magnet wires were attached to the coplanar electrode using conductive carbon tape (Ted Pella). The coplanar electrode was then connected in series with a function generator (Agilent) with one lead attached to the north-south poles and

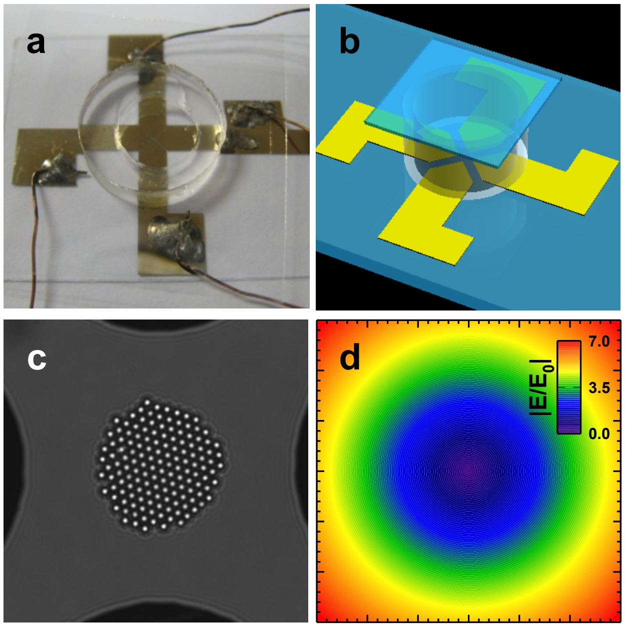

Supplementary Figure 1. Co-planar thin gold film quadrupole electrode on a cover slip. (**a**) Top view of device showing connections to function generator. (**b**) Schematic rendering of device. (**c**) Nominal 3 μm silica colloids in the quadrupole electrode center at the electric field minimum (particles provide internal scale bar). (**d**) Contour plot of electric field with linear spectrum scale from E/E_0=0-7, where E_0 is the nominal electric field magnitude.

Supplementary Figures 1a and b: “Electric field mediated assembly of three dimensional equilibrium colloidal crystals” Juarez, J.J.; Feicht, S; Bevan, M.A. 2012, *Soft Matter* 8, 94-103. Reproduced by permission of The Royal Society of Chemistry. http://dx.doi.org/10.1039/C1SM06414B

Supplementary Figures 1c and d: “Size dependent thermodynamics and kinetics in electric field mediated colloidal crystal assembly” Edwards, T.D.; Beltran-Villegas, D.J.; Bevan, M.A. 2013, *Soft Matter* 9, 9208-9218. Adapted by permission of The Royal Society of Chemistry. http://dx.doi.org/10.1039/C3SM50809A

another to the east-west poles.

Microscopy: Microscopy was performed on an inverted optical microscope (Axio Observer A1, Zeiss) with a 63× Zeiss air objective lens (0.6 numerical aperture) at 1.6 magnification. A 12-bit CCD camera (ORCA-ER, Hamamatsu) captured 336 pixel × 256 pixel (81 μm × 62 μm) digital images at rate of 8 frames/s. Video capture and image manipulation were performed using the MATLAB Image Processing and Image Acquisition Toolboxes. Image analysis algorithms coded in MATLAB were used to simultaneously locate and track particle centers, as well as, compute local and global order parameters in real time[73,111]. Instantaneous values of voltage, frequency, and order

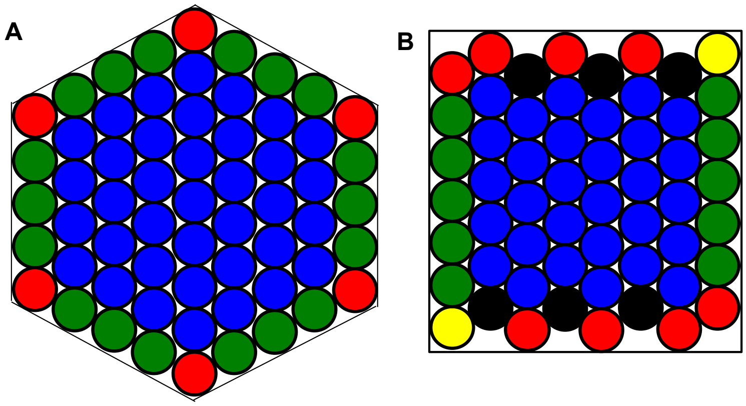

Supplementary Figure 2. Hexagonally closed packed array of particles confined to (A) hexagon and (B) square morphologies with colors indicating the number of hexagonal close packed neighbors as $C_6 = 6$, blue; $C_6 = 5$, black; $C_6 = 4$, green; $C_6 = 3$, red; $C_6 = 2$, yellow.

“Multiple electrokinetic actuators for feedback control of colloidal crystal size” Juarez, J.J.; Mathai, P.P.; Liddle, A.J.; Bevan, M.A. 2012, *Lab on a Chip* 12, 4063-4070. Reproduced by permission of The Royal Society of Chemistry. http://dx.doi.org/10.1039/C2LC40692F

parameter values were written to ASCII text files, and images were written to TIFF stacks for creating movies.

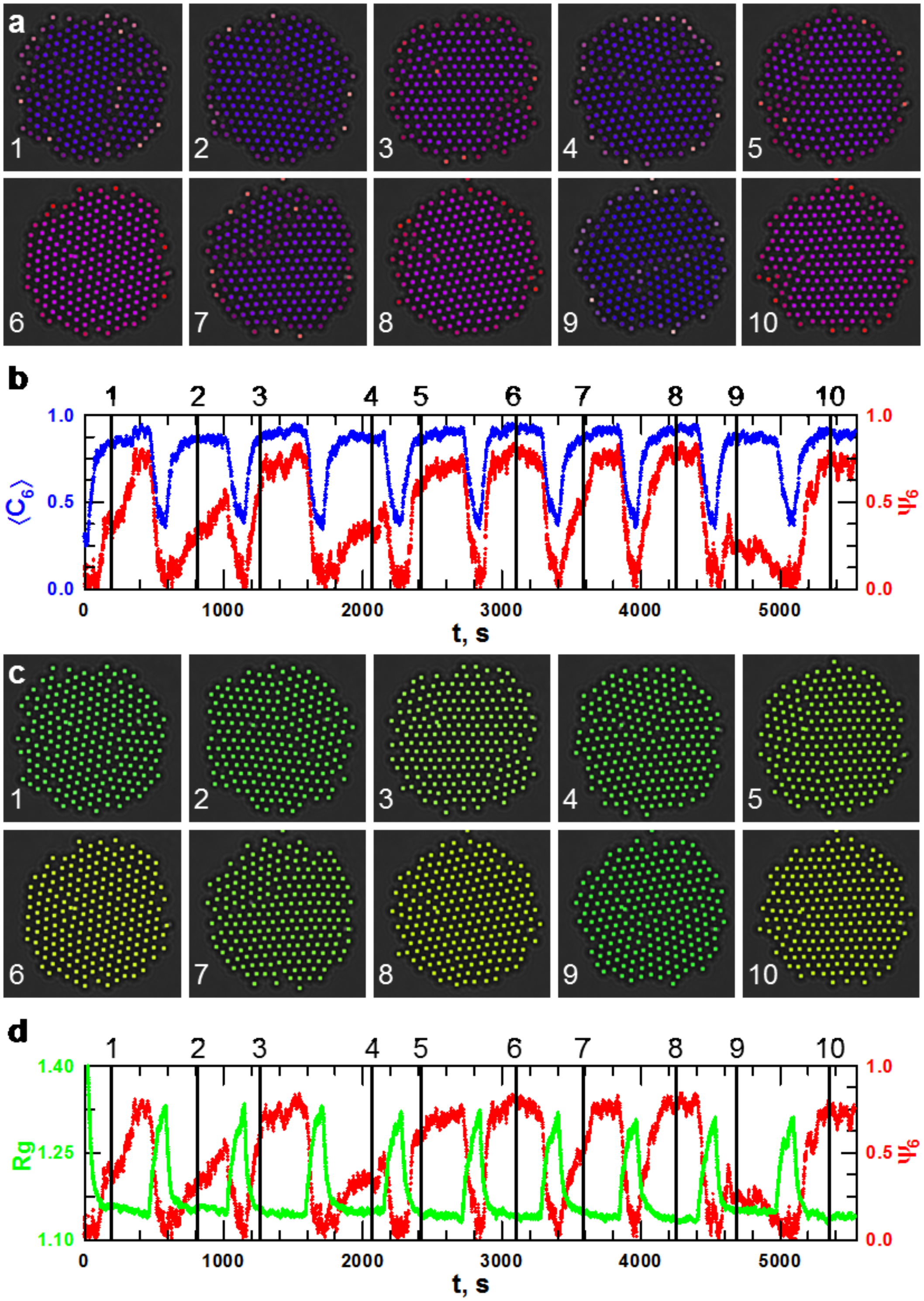

Supplementary Figure 3. Representative images and reaction coordinate trajectories for ten consecutive voltage quenches from 0.2 V to 1.2 V. (**a**) Processed images where particles are painted based on normalized local, $\langle C_6 \rangle$, and global, ψ_6, order reaction coordinates. Color scheme is identical to Fig. 2a and Supplementary Videos 1 and 2. (**b**) $\langle C_6 \rangle$ and ψ_6 vs. time, t, with location of extracted images in **a**. (**c**) and (**d**) show same information as **a** and **b** except for (ψ_6, R_g) reaction coordinate pair.

The electric field amplitude and frequency were controlled *via* the function generator using a device driver written in the MATLAB Instrument Control Toolbox. A sinusoidal voltage with a 1 MHz frequency was cycled ten times (see Supplementary Fig. 3) between 0.2 V and 1.2 V every 1,000 frames. From our previous work,[112] $V(N, \kappa^{-1})$ is the voltage at which all particles crystallize in a system of N particles and is dependent upon the electrostatic repulsion between particles as given by[112],

$$\begin{aligned} V\left(N,\kappa^{1}\right) &= a_0\left(\kappa^{-1}\right)\cdot N^{-b_0\left(\kappa^{-1}\right)} \\ a_0\left(\kappa^{-1}\right) &= 7.15+4.10\cdot 10^{-3}\kappa^{-1} \\ b_0\left(\kappa^{-1}\right) &= 0.219+4.24\cdot 10^{-4}\kappa^{-1} \end{aligned} \tag{6.3}$$

where κ^{-1} is the Debye length. The value of $V^{*}=V/V(N, \kappa^{-1})$, is the experimental applied voltage, V, normalized by the expression in equation (8.2).

Reaction Coordinates: Supplementary Fig. 2 shows how reaction coordinates are computed for different system sizes to include edge effects, and Supplementary Fig. 3 shows reaction coordinate computed from particle centers in real-time for ten voltage cycles. The degree of condensation of our colloidal particles was captured using a normalized radius of gyration, R_g, given as,

$$R_g = 0.5N^{-1}\left[\sum\left|r_i - r_j\right|^2\right]^{0.5} \Big/ R_{g,HEX} \tag{6.4}$$

where $R_{g,HEX}$, the radius of gyration for two dimensional (2D) hexagonally close packed (hcp) particles within regular polygon morphologies given by[111],

$$R_{g,HEX} = 5^{0.5}3^{-1}aN^{0.5} \tag{6.5}$$

where a is the particle radius.

The global six-fold bond orientational order, ψ_6, of particle configurations is given by[43,44,117],

$$\psi_6 = \left| \frac{1}{N} \sum_{j=1}^{N} \psi_{6,j} \right| \tag{6.6}$$

where N is the total number of particles in the ensemble, and $\psi_{6,j}$ is the local six-fold bond orientation order of particle j given as[43,44,117],

$$\psi_{6,j} = \frac{1}{N_{C,j}} \sum_{k=1}^{N_{C,j}} e^{i6\theta_{jk}} \tag{6.7}$$

where $\psi_{6,j}$ is the six-fold bond orientation order parameter of particle j, $N_{\mathrm{C,j}}$ is the number of neighbors within the first $g(r)$ peak (coordination radius) of particle j, and θ_{jk} is the angle between particle j and each neighboring particle k with an arbitrary reference direction. Connectivity between crystalline particles, $\chi_{6,jk}$, is given by,

$$\chi_{6,jk} = \frac{\left| \mathrm{Re}\left[\psi_{6,j} \psi_{6,k}^{*} \right] \right|}{\left| \psi_{6,j} \psi_{6,k}^{*} \right|} \tag{6.8}$$

where $\psi_{6,j}^{*}$ is the complex conjugate of $\psi_{6,j}$. This is used to compute the local order parameter for six-fold connectivity, $C_{6,j}$, which produces integer values between zero and six. The number of crystalline nearest neighbors, $C_{6,j}$, for particle j is determined using the criterion[135],

$$C_{6,j} = \sum_{k=1}^{N_C(j)} \left[\begin{vmatrix} 1 & \chi_{6,j} \geq 0.32 \\ 0 & \chi_{6,j} < 0.32 \end{vmatrix} \right] \tag{6.9}$$

$$\langle C_6 \rangle = \frac{1}{N}\sum_{i=1}^{N} C_6(i) \Big/ \langle C_6 \rangle_{HEX} \tag{6.10}$$

where $\langle C_6 \rangle$ is the average normalized local six-fold connectivity order, normalized by $\langle C_6 \rangle_{\mathrm{HEX}}$, the six-fold connectivity order for 2D hcp particles with a hexagonal morphology given by[111],

$$\langle C_6 \rangle_{HEX} = N^{-1} 6\left(3S^2 + S\right) \tag{6.11}$$

$$S = -\left(1/2\right) + \left[\left(1/3\right)\left(N-1\right) + \left(1/4\right)\right]^{1/2} \tag{6.12}$$

Particle Scale Brownian Dynamics Simulations: Brownian Dynamics (BD) simulations in the canonical ensemble were performed for 210 colloidal particles at constant voltage using numerical methods described in our previous papers[122,128-131]. A 0.1 ms time step was used for at least 2×10^7 steps, and reaction coordinates were stored every 1250 steps for subsequent analysis. Particles in simulations were confined within 2D planes. In the following sections, we provide additional details of the BD simulations, as well as, the models for the conservative forces based on potentials measured in our previous work[113,114,136]. All parameters used in the BD simulations are reported in Table 1.

Supplementary Table 1. Parameters for BD simulations and experiments. a, colloidal particle size[137], **b**, Debye screening length, **c**, particle and wall Stern potential[137], **d** peak voltage applied to electrodes, **e**, Clausius-Mosotti factor for an AC field frequency at 1 MHz[114], **f**, medium dielectric permittivity, **h** electrode spacing[138].

Variable	**Theory/Simulation**	**Experiment**
$2a$/nm[a]	2,870	2,800-2,900

T/K	293	293
κ^{-1}/nm[b]	30	30
ψ/mV[c]	-50.0	-50.0
V_{pp}/V[d]	0.65,0.92,1.2,1.45	1.2
V^*	0.31, 0.44, 0.57, 0.69	0.57
f_{cm}[e]	-0.4667	-0.4667
ε_m[f]	78	78
d_g/µm[h]	91	~100

The BD simulations were based on a Langevin equation as,

$$m\frac{d\mathbf{U}}{dt}=\mathbf{F}^{H}+\mathbf{F}^{P}+\mathbf{F}^{B} \quad (6.13)$$

where m is the particle buoyant mass, $\mathbf{U}$ is a velocity vector, and the force vector has three parts including dissipative hydrodynamic forces, $\mathbf{F}^H$, conservative forces due to potential fields, $\mathbf{F}^P$, and stochastic Brownian forces, $\mathbf{F}^B$. By letting $\mathbf{F}^H=-kT(\mathbf{D}^{-1})\cdot\mathbf{U}$, integrating Eq. (6.13) and using the mid-point algorithm, an equation of motion for particle displacements is obtained as[139,140],

$$\mathbf{r}=\mathbf{r}^{0}+\left(\nabla\cdot\mathbf{D}^{0}\right)\Delta t+\left(kT\right)^{-1}\mathbf{D}^{0}\cdot\left(\mathbf{F}^{P,0}+\mathbf{F}^{B,0}\right)\Delta t \tag{6.14}$$

where the superscript "0" indicates quantities computed at the beginning of the time interval. Specific details of implementing Eq. (6.14) in dynamic simulations are described in previous publications[128,129]. The Brownian force $\mathbf{F}^B$ is characterized by a mean and variance given by,

$$\begin{gathered}\left\langle\mathbf{F}^{B}\right\rangle=\mathbf{0}\\ \left\langle\mathbf{F}^{B}(0)\mathbf{F}^{B}(t)\right\rangle=2(kT)^{2}\left(\mathbf{D}^{-1}\right)\delta(t)\end{gathered} \tag{6.15}$$

D in Eqs. (6.14) and (6.15) was computed using the methods for finite numbers of particles above a no-slip plane using the methods of Brady and co-workers. **D** is related to the resistance tensor, **R**, through the generalized Stokes-Einstein relation, $\mathbf{D}=kT\mathbf{R}^{-1}$. Here **R** is computed to include hydrodynamic interactions, which are separated into far-field, multi-body and a near-field, lubrication contributions as[141-146],

$$\mathbf{R}=\left(\mathbf{M}^{\infty}\right)^{-1}+\mathbf{R}_{2B}-\mathbf{R}_{2B}^{\infty} \tag{6.16}$$

where $\mathbf{M}^{\infty}$ is the far-field mobility tensor constructed in a pairwise manner. The inverse of $\mathbf{M}^{\infty}$ is a true multi-body, far-field approximation to the resistance tensor. Lubrication is included by adding the exact two-body resistance tensor [142,145,146], $\mathbf{R}_{2B}$, and subtracting the two-body, far-field resistance tensor, $\mathbf{R}_{2B}^{\infty}$, to avoid double counting. To specify an approximate configuration-dependent **D** to reduce computational cost, the diagonal elements of **D** (without cross terms) are parameterized in a look up table as a function of the ensemble R_g and the distance, R_i, of particle i from the configuration center of mass (Supplementary Fig. 3b).

The interaction energy between colloids within the quadrupole electrode is modeled as the superposition of electrostatic double layer repulsion, dipole-field interactions, and dipole-dipole interactions. The net conservative forces, $\mathbf{F}^{P}$, in Eq. (6.14) are calculated based on the total conservative force acting on particle i as,

$$\mathbf{F}_{i}^{P}=-\nabla_{r_i}\left[u_{de,i}^{pf}+\sum_{j\neq i}\left(u_{e,i,j}^{pp}+u_{dd,i,j}^{pp}\right)\right] \tag{6.17}$$

where the electrostatic potential between particles i and j, $u^{pp}_{e,i,j}(\mathbf{r})$, is given by[2],

$$u^{pp}_{e,i,j}\left(r_{ij}\right)=32\pi\varepsilon_m a\left(\frac{kT}{e}\right)^2\tanh^2\left(\frac{e\psi}{4kT}\right)\exp\left[-\kappa\left(r_{ij}-2a\right)\right] \tag{6.18}$$

where κ^{-1} is the Debye screening length, where r_{ij} is the center-to-center distance between particles, ε_{m} is the medium dielectric constant, k is Boltzmann's constant, T is absolute temperature, e is the elemental charge, and ψ is the colloid surface potential. Dipole-field interactions can be described by,[113]

$$u^{pf}_{de,i}\left(\mathbf{r}_i\right)=-2kT\lambda f_{cm}^{-1}\left(\frac{E\left(\mathbf{r}_i\right)}{E_0}\right)^2 \tag{6.19}$$

where $\mathbf{r}_i$ is the position of particle i relative to the center of the quadrupole electrode, f_{cm} is the Clausius-Mosotti factor, $\lambda=\pi\varepsilon_m a^3(f_{cm}E_0)^2/kT$, $E(\boldsymbol{r}_i)$ is the electric field, and $E_0=8^{-0.5}V_{pp}/d_g$, where V_{pp} is the peak-to-peak AC voltage and d_g is the gap width between opposite electrodes. Dipolar interactions between particles i and j are given by[114],

$$u^{pp}_{dd,i,j}\left(\mathbf{r}\right)=-kT\lambda P_2\left(\cos\theta_{ij}\right)\left(\frac{2a}{r_{ij}}\right)^3\left(\frac{E\left(\mathbf{r}_i\right)}{E_0}\right)^2 \tag{6.20}$$

where $P_2(\cos\theta_{\mathrm{ij}})$ is the second Legendre polynomial and θ_{ij} is the angle between the line that connects the two particle centers and the electric field. The quadrupole electric field is given by an approximate expression[147] corrected to fit numerical COMSOL results as,

$$\left|\frac{E\left(L\right)}{E_0}\right|=\frac{4L}{d_g}\begin{bmatrix}2.081\times10^{-7}L^4-1.539\times10^{-9}L^3+\\8.341\times10^{-5}L^2+1.961\times10^{-5}L+1.028\end{bmatrix} \tag{6.21}$$

where x and y are Cartesian coordinates with origin at the quadrupole center, and $L=(x^2+y^2)^{0.5}$.

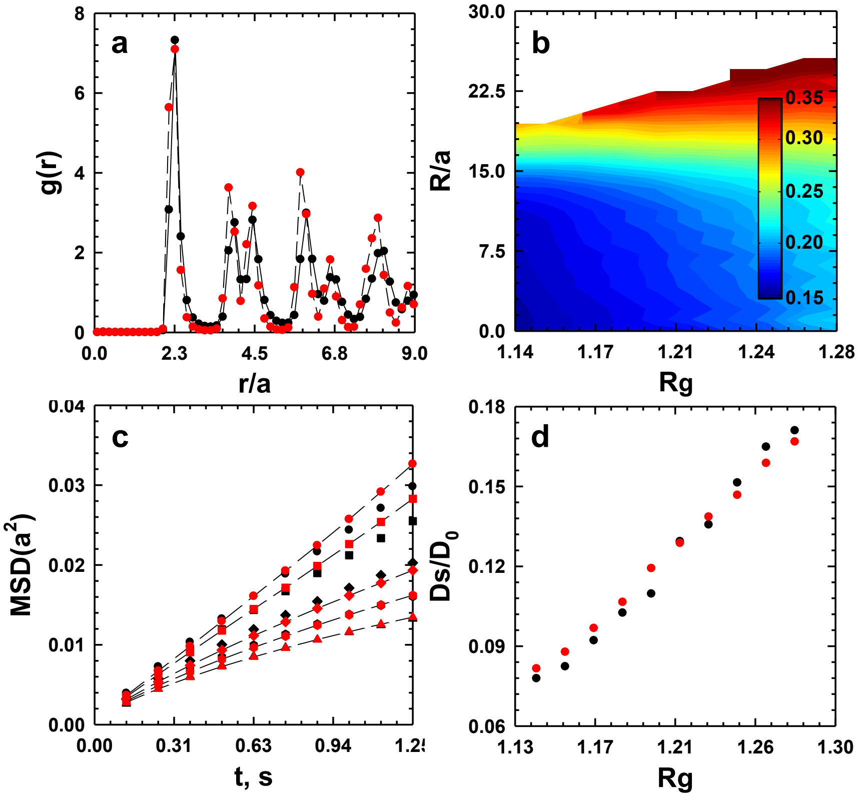

Supplementary Figure 4. Matching Brownian Dynamics simulations to microscopy experiments. (**a**) radial distribution function calculated from equilibrium configurations in experiments (●) and simulations (●) at *V**=0.57. (**b**) Parameterized diffusivities from Eq. (6.16). (**c**) Mean squared displacement averaged over all particles from **experiments** and **Brownian Dynamic simulations** at R_g values of: 1.28 (●), 1.25(■), 1.20(◆), 1.17(⬢), 1.14(▲). (**d**) Diffusivities at different R_g from the first five points in **c** (●) and BD (●).

Matching Microscopy Experiments and Brownian Dynamics Simulations: Inverse Monte Carlo methods (including image resolution limiting effects)[132-134] were used to match measured and simulated radial distribution functions to determine parameters in interactions potentials (Supplementary Fig. 4a). The particle radius and electrode gap were adjusted in Eqs. (6.18)-(6.21) from initial estimates based on independent characterization. The diffusivity in Eqs. (6.14)-(6.15) was matched by comparing measured and BD simulated mean square displacements (Supplementary Figs. 4c, 4d) (using the potentials from the inverse MC analysis) and adjusting the distance between the underlying substrate and the 2D plane containing the particles when computing **D** *via* Eq. (6.16). The final values of $\mathbf{D}(R_\mathrm{g}, R_i)$ are shown in Fig. 4b.

Analysis to obtain Smoluchowski equation coefficients: Methods to fit the Smoluchowski equation coefficients are described in detail in our previous manuscripts[120,122,131]. Here we describe in brief the linear fitting method. The local drift and diffusion coefficients can be obtained through the formulas[121],

$$\mathbf{D}_i^{(1)}(\mathbf{x}) = \lim_{\tau \to 0} \frac{1}{\tau} \left\langle \chi_i(t+\tau) - \chi_i(t) \right\rangle \Big|_{\chi(t)=\mathbf{x}} = \frac{\partial \mu_i}{\partial t} \tag{6.22}$$

$$\mathbf{D}_{ij}^{(2)}(\mathbf{x}) = \lim_{\tau \to 0} \frac{1}{2\tau} \left\langle \left[\chi_i(t+\tau) - \chi_i(t)\right]\left[\chi_j(t+\tau) - \chi_j(t)\right] \right\rangle \Big|_{\chi(t)=\mathbf{x}} = \frac{1}{2} \frac{\partial \sigma_{ij}^2}{\partial t} \tag{6.23}$$

where $\mathbf{D}^{(1)}$ is the drift vector field, $\mathbf{D}^{(2)}$ is the diffusivity tensor, $\boldsymbol{\chi}$ is a particular realization of $\mathbf{x}$, the brackets represent an ensemble average, and the right hand side provides compact notation based on the definition of a derivative and traditional symbols of statistics (*i.e.*, mean, variance, covariance). $\mathbf{D}^{(2)}$ is the same as $\mathbf{D}(\mathbf{x})$ in Eqs. (1) and (2) in the manuscript text, where we drop the superscript '(2)' for convenience. The free energy landscape, $W(\mathbf{x})$, can be obtained from $\mathbf{D}^{(1)}$ and $\mathbf{D}^{(2)}$ *via* integration as,

$$\frac{W(\mathbf{x}_2)-W(\mathbf{x}_1)}{kT} = -\int_{\mathbf{x}_1}^{\mathbf{x}_2} (\mathbf{D}^{(2)})^{-1}\cdot(\mathbf{D}^{(1)}-\nabla\cdot\mathbf{D}^{(2)}) \qquad (6.24)$$

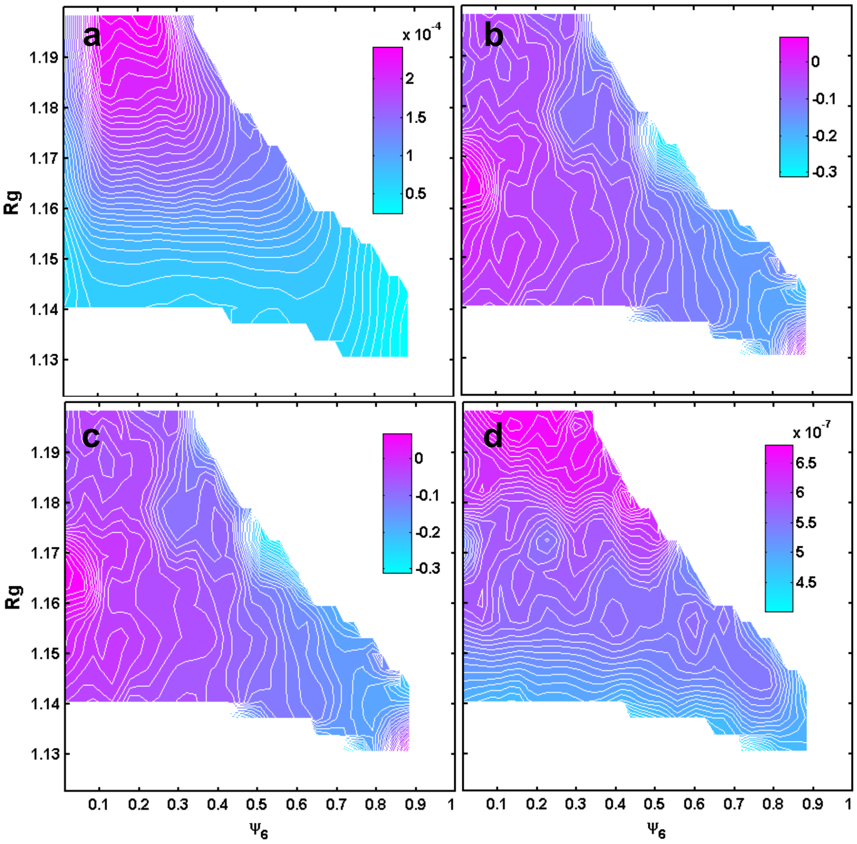

Supplementary Figure 5. Diffusivity landscape components as a function of R_g and ψ_6 for V^*=0.57. All four diffusivity landscape components: (**a**) $D_{\psi6\psi6}(kT\cdot s)^{-1}$, (**b**) $D_{\psi6Rg}/(D_{\psi6\psi6}D_{RgRg})^{0.5}$, (**c**) $D_{Rg\psi6}/(D_{\psi6\psi6}D_{RgRg})^{0.5}$, (**d**) $D_{RgRg}(kT\cdot s)^{-1}$. The inset color scheme is rescaled for each case. The diagonal elements are reported with units, and the cross terms are normalized by the square root of the product of the diagonal terms to check their correlation.

In the present study, $\mathbf{x}=(\psi_6, R_g)$ trajectories for input into Eqs. (6.22) and (6.23) were generated from a total of 6535 BD simulations initiated from a library of experimental fluid and polycrystalline configurations. Trajectories were analyzed based on 839 different (ψ_6, R_g) grid points with at least 400 trajectories passing through each grid point. The resolution for the R_g and ψ_6 coordinates were 0.0032 and 0.025. All $W(\mathbf{x})$ are reported in the main text, and all components of $\mathbf{D}(\mathbf{x})$ for $V^*=0.57$ are shown in Supplementary Fig. 5.

Low Dimensional Langevin Dynamics (LDLD) simulations: In order to verify the low-dimensional model based on $\mathbf{D}(\mathbf{x})$ and $W(\mathbf{x})$ obtained from Eqs. (6.23) and (6.24), LDLD simulations were performed based on an equation of motion (also reported as Eq. (2) in the main text),

$$\mathbf{x}(t+\Delta t)=\mathbf{x}(t)-\mathbf{D}\left[\mathbf{x}(t)\right]\cdot(kT)^{-1}\nabla W\left[\mathbf{x}(t)\right]\Delta t+\nabla\cdot\mathbf{D}\left[\mathbf{x}(t)\right]+\left[2\mathbf{D}\left[\mathbf{x}(t)\right]\Delta t\right]^{1/2}\mathbf{\Gamma}(t) \tag{6.25}$$

where Δt=0.125 s is the integration time step, and $\mathbf{\Gamma}(t)$ is a noise variable with zero mean and unity variance based on the Ito convention[148].

BD and LDLD simulations were compared based on first passage time distributions reported in Fig. 3 of the main text. The same BD trajectory data used to obtain the Smoluchowski coefficients was used to construct first passage time distributions. For LDLD simulation results, statistics were first collected from 4,000 trajectories initiated in fluid and polycrystalline states (from 40 grid points with 100 different random number generator seeds). After initial sampling, another 4,000 simulations were performed for states with insufficient sampling. These 8,000 dynamic trajectories were used to construct first passage time distributions between different states.

7 DYNAMIC COLLOIDAL ASSEMBLY PATHWAYS VIA LOW DIMENSIONAL MODELS†

7.1 Abstract

Here we construct a low-dimensional Smoluchowski model for electric field mediated colloidal crystallization using Brownian Dynamic simulations, which were previously matched to experiments. Diffusion mapping is used to infer dimensionality and confirm the use of two order parameters, once for degree of condensation and one for global crystallinity. Free energy and diffusivity landscapes are obtained as the coefficients of a low-dimensional Smoluchowski equation to capture the thermodynamics and kinetics of microstructure evolution. The resulting low-dimensional model quantitatively captures the dynamics of different assembly pathways between fluid, polycrystal, and single crystals states, in agreement with the full *N*-dimensional data as characterized by first passage time distributions. Numerical solution of the low-dimensional Smoluchowski equation reveal statistical properties of the dynamic evolution of states vs. applied field amplitude and system size. The low-dimensional Smoluchowski equation and associated landscapes calculated here can serve as models for predictive control of electric field mediated assembly of colloidal ensembles into two-dimensional crystalline objects.

7.2 Introduction

Self-assembly refers to dynamical processes where predefined components spontaneously organize into ordered structures. Self-assembly is considered as a key bottom-up approach to fabricate novel nano- and micro- and nano-scale materials.[17-19] Modeling studies of self-assembly generally focus on predicting the resulting equilibrium or steady-state structures as a function of particle interactions, particle shapes, temperature, and concentration.[24,25] Such equilibrium information is important for yielding design rules for building blocks capable of assembling into complex structures. However, the existence of metastable states, kinetic bottlenecks, and competing pathways during dynamical assembly processes can prevent self-assembling systems from reaching thermodynamically stable states on experimentally accessible time scales.[149,150]

---

† Reprinted with permission from "Dynamic colloidal assembly pathways via low dimensional models." *The Journal of chemical physics* 20 (2016): 204904. by Yang, Yuguang, Raghuram Thyagarajan, David M. Ford, and Michael A. Bevan. © 2016 American Institute of Physics.

In addition to understanding the thermodynamics of self-assembly, it is beneficial to uncover the underlying driving forces and dynamics governing self-assembly processes. In general, dynamic models should contain information about the existence of metastable states as well as the expected times for transitions between states. Ideally, construction of such dynamic models at different thermodynamic conditions can enable the rational design of optimal kinetic pathways to achieve desired states by performing state-dependent temporal actuation of the system.[9,39,40] The evolution of stochastic dynamical self-assembling systems can be formulated using for example a master equation,[36] Fokker Planck equation,[37] or Smoluchowski equation.[38]

The Smoluchowski equation (SE) is suitable to describe Markovian stochastic processes for thermally equilibrated systems. The SE contains thermodynamic and kinetic information in its coefficients and has been applied to complex systems involving protein folding,[151] colloidal assembly,[122] and micellization.[38] In such complex systems, the SE is usually not parameterized by $3N$ particle coordinates, but instead by low-dimensional coordinates capturing the collective behavior of the system. The procedure to obtain a suitable SE can be briefly described as: (1) identifying the dimensionality of the dynamics (*i.e.*, number of slow modes of collective motion) via trajectory analysis (*e.g.*, principal component analysis,[152] diffusion mapping[153,154]), (2) finding a suitable set of coordinates, which are often scalar functions of the $3N$ particle coordinates, to capture the slow modes (usually heuristically chosen based on coarse grained physics), and (3) obtaining coefficients for the SE in the low dimensional coordinates via fitting schemes (e.g., local linear fitting,[155] global Bayesian inference[120]). The SE coefficients include the free energy landscape, W, which reflects free energy differences between different configurations, and the diffusivity landscape, D, which captures the mobility of trajectories in configuration space. The SE solution describes the probability distribution of states as a function of time, thus providing a dynamic statistical model for assembly processes. We have previously applied these tools to develop dynamic models of depletion attraction mediated colloidal cluster crystallization,[120,122] which we applied in subsequent studies focused on optimal control of such systems.[9,40]

In this work, we present a systematic framework for building a low-dimensional model to capture the assembly of finite sized quasi-2D colloidal crystals using Brownian Dynamic (BD) simulations matched to our previous experiments.[112] The experiment involves using an electric field to compress colloids in the center of a quadrupole (Fig. 1). This simple assembly problem demonstrates the basic features of competing pathways, metastable states, and relaxation from metastable state, and we have quantified the interactions potentials,[113,114,136] system size dependent thermodynamics and kinetics,[112] and grain boundary formation.[150] As such, it serves as a well characterized and understood test case for a general low-dimensional modeling method. From an application standpoint, it is interesting in its own right for reconfigurable colloidal materials and devices,[156,157] which we have demonstrated in circuit elements,[158] feedback controlled colloidal crystal assembly,[39,111] and in the formation of three dimensional crystals.[138] Assembly trajectories in candidate order parameters (Fig. 1C) help to show the general approach investigated in this work, where parameters that quantify condensation and order together capture the relevant states and dynamics as particles moves from fluid to polycrystal to single crystal states (Fig. 1D). Our results demonstrate the ability to fit a low-dimensional SE to a large number of BD simulations to obtain the W and D coefficients, which we relate to physical states and dynamic processes associated with colloidal crystal assembly vs. applied field amplitude and system size (number of particles). Our modeling efforts in this work include dimensionality reduction, order parameter estimation, model validation, and physical interpretation of the dynamic model.

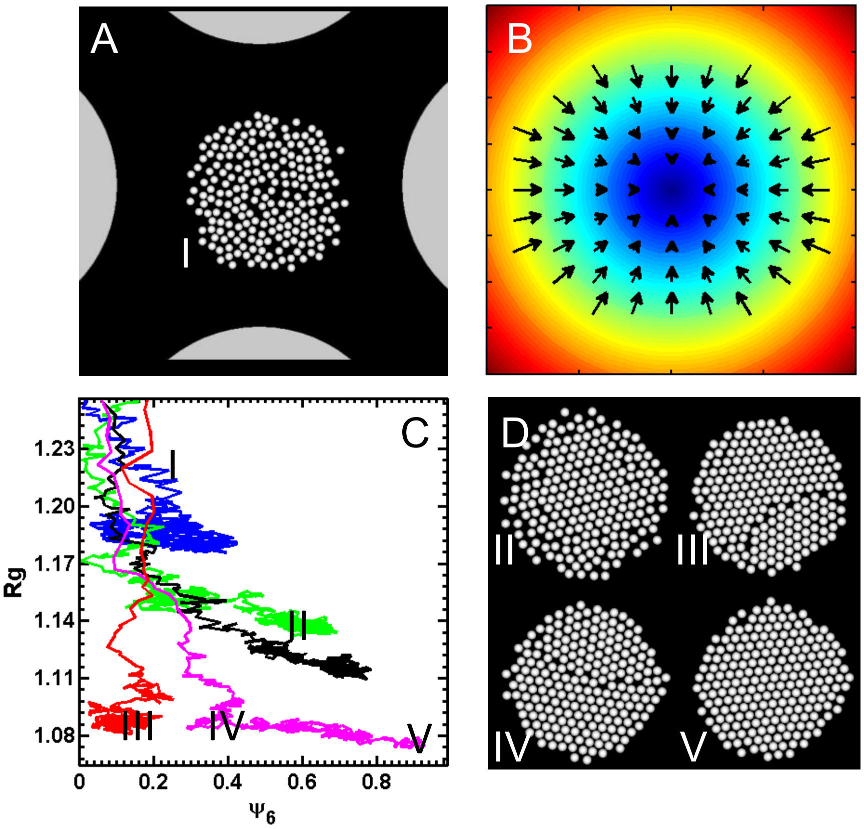

Figure. 1. (A) Top view of simulated experiment of quasi-2D configuration of N=210 colloidal particles ($2a$=3 μm) compressed within a quadrupolar electrode (with electrode gap of d_g=100 μm. (B) Electric field magnitude contour plot within quadrupole electrode center with arrows indicating relative magnitude and direction of force due to dipole-field interactions (Eqs. (7.2), (7.7)) that concentrates particles in quadrupole center. (C) Typical colloidal assembly trajectories in the order parameter pair (ψ_6, R_g) for a system size of N = 210 at voltages of (see definition of nondimensional V^* in Eq. (7.21) where V^*=1 corresponds to thermodynamic condition for perfect crystal as free energy minimum configuration[112]): V^*=0.42 (blue), V^*=0.5 (green), V^*=0.57 (black), V^*=0.80 (pink), and V^*=0.80 (red). Representative states in part C are marked as (rendered in part D with exceptions noted): I (initial fluid state, part A), II (crystal configuration coexisting with peripheral fluid particles), III (low order bicrystal), IV (higher order bicrystal), and V (single crystal with a few particles still experiencing thermal motion at crystal periphery).

7.3 Theory

7.3.1 Interaction potentials

In this paper, we model electric field mediated quasi-2D colloidal assembly in a quadrupole electrode using previously measured potentials.[113,114,136] In brief, colloidal particles interact via electrostatic double layer repulsion, dipole-field potentials, and dipole-dipole potentials. The electrostatic repulsion between particle i and j is given as,[159]

$$u_{e,i,j}^{pp}\left(r_{ij}\right)=B^{pp}\exp\left[-\kappa\left(r_{ij}-2a\right)\right] \tag{7.1}$$

where r_{ij} is center-to-center distance between particles, a is particle radius, and B^{pp} is the pre-factor for pair electrostatic repulsion between colloidal particles.[159] The dipole-field potential for particle i in a spatially varying electric field is given as,[113]

$$u_{de,i}^{pf}\left(\mathbf{r}\right)=-2kT\lambda f_{cm}^{-1}\left[E\left(\mathbf{r}_i\right)/E_0\right]^2, \quad \lambda=\frac{\pi\varepsilon_m a^3\left(f_{cm}E_0\right)^2}{kT} \tag{7.2}$$

where $\mathbf{r}_i$ is the position of particle i, k is Boltzmann's constant, T is temperature, f_{cm} is the Clausius-Mossotti factor, λ is a non-dimensional amplitude, ε_m is the medium dielectric constant, $E(\mathbf{r}_i)$ is the local electric field peak magnitude at the particle position, and E_0 is given by,

$$E_0=8^{-0.5}\left(V_{pp}/d_g\right) \tag{7.3}$$

where V_{pp} is the peak-to-peak voltage and d_{g} is the electrode gap. The dipole-dipole interaction potential between particles i and j is given by,[114]

$$u_{dd,i,j}^{pp}\left(\mathbf{r}_{ij}\right)=-kT\lambda P_2\left(\cos\theta_{ij}\right)\left(2a/r_{ij}\right)^3\left[E\left(\mathbf{r}_i\right)/E_0\right]^2 \tag{7.4}$$

where $P_2(\cos\theta_{\mathrm{ij}})$ is the second Legendre polynomial and θ_{ij} is the angle between the line connecting particle centers and the electric field line direction. The electric field in the quadrupole center is approximated as,[39,111,138]

$$\left|\frac{E\left(\mathbf{r}_i\right)}{E_0}\right|=\frac{4r}{d_g} \tag{7.5}$$

where $r=(x^2+y^2)^{0.5}$, and x and y are Cartesian coordinates with origin at the quadrupole center.

7.3.2 Colloidal particle dynamics

Particle dynamics in quasi-2D configurations near a planar surface are modelled using previously reported methods[129] with several modifications. The equation of motion for Brownian particles is given as,[139]

$$\begin{gathered}\mathbf{r}(t+\Delta t)=\mathbf{r}(t)+\frac{\mathbf{D}^{P}}{kT}(\mathbf{F}^{P}+\mathbf{F}^{B})\Delta t+\nabla\cdot\mathbf{D}^{P}\Delta t\\ \left\langle\mathbf{F}^{B}\right\rangle=0,\qquad\left\langle\mathbf{F}^{B}(t_1)(\mathbf{F}^{B}(t_2))^{T}\right\rangle=2(kT)^{2}\left(\mathbf{D}^{P}\right)^{-1}\delta(t_1-t_2)\end{gathered}\tag{7.6}$$

where $\mathbf{r}$ is the $2N$ dimensional position vector, $\mathbf{F}^B$ is the Brownian force vector, and $\mathbf{F}^P$ is the total conservative force vector, and the superscript T denotes transpose. The components of $\mathbf{F}^P$ describing the conservative force acting on particle i are given as,

$$\mathbf{F}_i^P=-\nabla_{r_i}\left[u_{de,i}^{pf}+\sum_{j\neq i}\left(u_{e,i,j}^{pp}+u_{dd,i,j}^{pp}\right)\right]\tag{7.7}$$

and $\mathbf{D}^P$ is the diffusivity tensor, related to grand resistance tensor $\mathbf{R}^P$ via Stokes-Einstein relation $\mathbf{D}^P=kT(\mathbf{R}^P)^{-1}$, where $\mathbf{R}^P$ is given by,[141]

$$\mathbf{R}^P=\left(\mathbf{M}^{\infty}\right)^{-1}+\mathbf{R}_{2B}-\mathbf{R}_{2B}^{\infty}\tag{7.8}$$

which includes pair-wise lubrication interactions, $\mathbf{R}_{2B}$, and many-bodied far-field interactions, $(\mathbf{M}^{\infty})^{-1}-\mathbf{R}_{2B}^{\infty}$, above a no-slip plane.[160,161]

7.3.3 Diffusion mapping

From a set of particle configurations (*i.e.*, snapshots), we compute a Markov probability matrix, $\mathbf{M}$, whose elements $\mathbf{M}_{ij}$ are a measure of the probability of hopping between the snapshots i and j. We denote each snapshot as a set X composed of the coordinate vectors of all particles (*i.e.*, $X = (\mathbf{x}_1, \mathbf{x}_2, \ldots, \mathbf{x}_N)$). To construct **M**, a measure of the distance between snapshots is required that resides in a $2N$ dimensional space. First, it is necessary to calculate a distance matrix, $\boldsymbol{\Delta}$, whose elements $\boldsymbol{\Delta}_{ij}$ are the distance metric between two snapshots X_i and X_j. In this work, the distance metric is a weighted combination of the Hausdorff distance matrix, **H**,[120] and a local orientation distance matrix, **O**, given as,

$$\begin{aligned} \Delta_{ij} &= \left[\left(\mathbf{H}_{ij} / \lVert \mathbf{H} \rVert_F \right)^2 + \left(\mathbf{O}_{ij} / \lVert \mathbf{O} \rVert_F \right)^2 \right]^{0.5} \\ \mathbf{H}_{ij} &= \max_{\mathbf{x}_m \in X_i} \min_{x_n \in X_j} \lVert \mathbf{x}_m - \mathbf{x}_n \rVert_2 \\ \mathbf{O}_{ij} &= \min_{\theta_t} \lVert h_i(\theta) - h_j(\theta + \theta_t) \rVert_2 \end{aligned} \tag{7.9}$$

where $\lVert\cdot\rVert_F$ denotes the Frobenius norm, and $h_i(\theta)$ is the normalized bonding angle histogram for snapshot i, where θ_t is the offset in order to achieve the global optimal alignment. The geometric average of H and O is motivated by considering the norm of a two-component vector. Hausdorff distance is the greatest of all distances from a particle in one snapshot to the closest particle in another snapshot and has been used previously in systems of unlabeled particles.[120,154] The bonding angle is the angle of the vector $(\mathbf{x}_i - \mathbf{x}_j)$ joining neighboring particles i, j with respect to the x-axis. We then define the kernel matrix using $\mathbf{K}_{ij} = \exp(-\Delta_{ij}^2/2\varepsilon^2)$, with ε being the parameter that sets the correlation length in the system. The parameter ε is chosen using a technique outlined elsewhere.[162,163] Each row of the kernel matrix **K** is normalized to obtain **M** as,

$$\mathbf{M}_{ij} = \frac{\mathbf{K}_{ij}}{\sum_j \mathbf{K}_{ij}} \tag{7.10}$$

where the solution of the right eigenvalue problem,

$$\mathbf{M}\nu = \lambda\nu \tag{7.11}$$

produces an eigenvalue spectrum, λ_n, and corresponding set of eigenvectors, ν. The eigenvalue spectrum provides insight on the number of dimensions required to describe the process dynamics. The corresponding eigenvectors provide a low dimensional embedding of the $2N$ dimensional configurations in the data set. In this work, the eigenvectors are not used directly as order parameters but are correlated against candidate coarse variables to identify a suitable set of order parameters.

7.3.4 Order parameters

Following procedures similar to our previous study,[120] here we define two order parameters, R_g and ψ_6, as order parameters ultimately to be employed in a low-dimensional dynamic model (in the results and discussion section we provide justification for their use based on diffusion mapping). The degree of condensation of colloidal particles is captured using the radius of gyration, R_g, which is given as,

$$R_g = 0.5N^{-1}\left[\sum\left|r_i - r_j\right|^2\right]^{0.5} / R_{g,HEX} \tag{7.12}$$

which is a measure of the root mean square distance between particles within an ensemble normalized by a factor $R_\text{g,HEX}$. This factor is the radius of gyration for 2D HCP particles within regular polygon morphologies given by,[39]

$$R_{g,HEX} = 5^{0.5}3^{-1}aN^{0.5} \tag{7.13}$$

where a is the particle radius and N is the particle number in the system. The degree of global orientational order in particle configurations obtained from particle coordinates using,[164]

$$\psi_{6,j} = \frac{1}{N_{C,j}} \sum_{k=1}^{N_{C,j}} e^{i6\theta_{jk}} \tag{7.14}$$

$$\psi_6 = \frac{1}{N} \left| \sum_{j}^{N} \psi_{6,j} \right| \tag{7.15}$$

where $\psi_{6,j}$ is the local six-fold bond orientation order parameter of particle j, $N_{\mathrm{C,j}}$ is the number of neighbors within the first $g(r)$ peak (coordination radius) of particle j, θ_{jk} is the angle between particle j and each neighboring particle with an arbitrary reference direction, and ψ_6 is the global bond orientation order determined by averaging over all particles, which produces values between 0 for disordered fluids and perfect bicrystals (*i.e.*, crystal with equal sized domains misoriented by 30 degrees) and 1 for defect-free, single domain hexagonal packed lattices.

7.3.5 Low-dimensional smoluchowski & langevin equations

Colloidal assembly trajectories are modeled using a low-dimensional Smoluchowski Equation (SE) parameterized by order parameter coordinates given as,[120,122,150]

$$\frac{\partial p(\mathbf{x},t)}{\partial t} = \nabla \cdot \mathbf{D}(\mathbf{x}) \cdot \left[(kT)^{-1} \nabla W(\mathbf{x}) + \nabla \right] p(\mathbf{x},t) \tag{7.16}$$

where $p(\mathbf{x}, t| \mathbf{x}_0, 0)$ is the probability density for system to be at a state characterized by the coordinate $\mathbf{x}=(\psi_6, R_g)$ at time t given that the system starts at $\mathbf{x}_0$ at t=0. The coefficient, $\mathbf{D}(\mathbf{x})$, which is a symmetric tensor, is the diffusivity landscape (DL) consisting of two diagonal terms $D_{\psi6\psi6}$, D_{RgRg}, and two off-diagonal terms $D_{\psi6Rg}$ and $D_{Rg\psi6}$. The coefficient

$W(\mathbf{x})$ is the free energy landscape (W), which captures the free energy of every configuration based on its coordinate $\mathbf{x}=(\psi_6, R_\mathrm{g})$. The SE describes the probability density evolution in the order parameter space given the initial probability distribution. The evolution is determined by the right hand side propagator, which contains $\mathbf{D}(\mathbf{x})$ and $W(\mathbf{x})$ that dictate the kinetic and thermodynamic aspects of the system. Our assumption implies that the stationary distribution from Eq. (7.16) is the thermodynamic equilibrium probability distribution $p(\mathbf{x})=\exp[-W(\mathbf{x})/kT]$, which can be obtained by setting the right-hand-side to be zero.

The coefficients $\mathbf{D}(\mathbf{x})$ and $W(\mathbf{x})$ in Eq. (7.16) can be extracted from assembly trajectories using a linear fitting procedure.[120,122,150] In brief, the initial slope of the mean displacement vs. time and mean displacement variance vs. time (*i.e.*, mean squared displacement, covariance matrix) at each local coordinate can be used to evaluate drift, $\mathbf{v}(\mathbf{x})$, and diffusivity tensor, $\mathbf{D}(\mathbf{x})$, as,

$$\mathbf{v}_i(\mathbf{x}) = \frac{\partial \mu_i}{\partial \Delta t} = \lim_{\Delta t \to 0} \frac{1}{\Delta t} \left\langle (\boldsymbol{\chi}(t+\Delta t) - \boldsymbol{\chi}(t))_i \right\rangle_{\boldsymbol{\chi}(t)=\mathbf{x}}$$

$$\mathbf{D}_{ij}(\mathbf{x}) = \frac{1}{2}\frac{\partial \sigma_{ij}^2}{\partial \Delta t} = \lim_{\tau \to 0} \frac{1}{2\Delta t} \left\langle (\boldsymbol{\chi}(t+\Delta t) - \boldsymbol{\chi}(t))_i (\boldsymbol{\chi}(t+\Delta t) - \boldsymbol{\chi}(t))_j \right\rangle_{\boldsymbol{\chi}(t)=\mathbf{x}}$$

(7.17)

where $\boldsymbol{\chi}$ is the instantaneous order parameter coordinate $\mathbf{x}$, and the bracket indicates the average of all trajectories sampling each coordinate. The free energy landscape, $W(\mathbf{x})$, is related to the drift as (by expanding the derivative of Eq. (7.16) and comparing with the Fokker-Planck equation[37]),

$$\frac{\mathbf{D}}{k_B T} \cdot \nabla W + \nabla \cdot \mathbf{D} = \mathbf{v} \tag{7.18}$$

where the first term on the left has the typical form of mobility coefficient multiplied by the gradient of the energy, and the second term is the noise-induced drift.[37,165] This expression can be integrated to obtain,

$$W(\mathbf{x}_2) - W(\mathbf{x}_1) = -\int_{\mathbf{x}_1}^{\mathbf{x}_2} (\mathbf{D})^{-1} \cdot (\mathbf{v} - \nabla \cdot \mathbf{D}) \tag{7.19}$$

The coefficients **D**(**x**) and W(**x**) can also be used to produce a low dimensional Langevin dynamic (LDLD) equation given by,

$$\mathbf{x}(t+\Delta t) = \mathbf{x}(t) - \frac{\mathbf{D}}{k_B T} \cdot \nabla W \Delta t + \nabla \cdot \mathbf{D} \Delta t + \sqrt{2\mathbf{D}\Delta t} \cdot \boldsymbol{\zeta} \tag{7.20}$$

where $\boldsymbol{\zeta}$ is a vector of Gaussian random numbers with zero mean and unity variance based on the Ito convention.[148] The LDLD equation can be used to directly generate trajectories in the low-dimensional order parameter space.

7.4 Methods

7.4.1 Brownian & langevin dynamic simulations

Particle scale dynamics were simulated in the canonical ensemble using Brownian Dynamics (BD) via Eq. (7.6). In particular, ~2000-4000 BD simulations were performed for different system sizes (N=110, 210, 300), different applied electric fields, and from many different initial configurations spanning dilute fluid to crystalline states. The initial configurations used to launch simulations were chosen adaptively to ensure every point in the order parameter space has ~200 samplings to reduce variance in subsequent analyses. This This single large set of BD simulations was used for extracting SE coefficients (Figs. 3, 4, 7) and first passage time characterization (Fig. 5). Simulation parameters are reported in Table 1. The electric field in each simulation is normalized as,

$$V^* = V_{\mathrm{pp}} / V_{\mathrm{xtal}} \tag{7.21}$$

$$\begin{aligned} V_{xtal} &= a_0 N^{-b_0} \\ a_0 &= 7.15 + 4.10 \cdot 10^{-3} \kappa^{-1} \\ b_0 &= 0.219 + 4.24 \cdot 10^{-4} \kappa^{-1} \end{aligned} \tag{7.22}$$

where V_{pp} is the peak-to-peak applied voltage, and V_{xtal} is the lowest voltage to crystalize all particles based on system size and Debye length, κ^{-1}, as reported in our previous work.[112] For each simulation, a 0.1 ms integration time step was used for at least 1.5×10^7 steps (so that each simulation reaches equilibrium). Particle coordinates were stored every 125 ms for calculation of ψ_6 and R_{g}. Particles in BD simulations were fixed within a 2D plane. To reduce computational cost in the BD simulations, hydrodynamic interactions were approximated by the diagonal elements of $\mathbf{D}^P$ computed using Eq. (7.8), which were parameterized in a look-up table vs. the configuration R_g and the distance of particle i to the configuration center of mass (see previous work for details[150]). Low Dimensional Langevin Dynamics (LDLD) for the first passage time characterization (Fig. 5) were simulated via the equation of motion in Eq. (7.20) using the $W(\mathbf{x})$ and $\mathbf{D}(\mathbf{x})$ obtained from Eqs. (7.17) and (7.19) using an integration time step of Δt=0.125 s.

7.4.2 Diffusion mapping

For the diffusion mapping analysis, a large number of configurations (snapshots) were generated using BD simulations for a system size of N=210 with V^*=0.80. The data set contained ~8000 configurations covering all of configuration space including fluid, polycrystalline, and crystalline states. Each configuration snapshot in the data set was processed to remove the translational degrees of freedom by setting the configuration origin as the center-of-mass as,

$$x_i^{'} = x_i - \bar{x}, \quad \bar{x} = \frac{1}{N}\sum_{i=1}^{N} x_i, \quad i = 1, 2, ..., N \tag{7.23}$$

where the translated coordinates form a data matrix, X=[x'_1,x'_2,…x'_N], which can be used to find the eigenvector n_1 of matrix XX^T as principle angle with the x-axis as, $\theta=\cos^{-1}(\mathbf{n}_1\cdot\mathbf{e}_1)$. This angle is used to remove rotational degrees of freedom using a rotational transformation given as,

$$x_i^{''} = \begin{pmatrix} \cos(\theta) & \sin(\theta) \\ -\sin(\theta) & \cos(\theta) \end{pmatrix} x_i^{'} \tag{7.24}$$

where the position vectors x" is used as the input to the diffusion mapping analysis, so as to not include dynamics in these additional degrees of freedom, but instead capture microstructural dynamic processes. The bonding angle histogram is discretized into 128 bins from $-\pi$ to π.

7.4.3 Smoluchowski equation solution

The coefficients $\mathbf{D}(\mathbf{x})$ and $W(\mathbf{x})$ in Eq. (7.16) can be extracted from assembly trajectories using the linear fitting procedure[120,122,150] described in Eqs. (7.17)-(7.19). In this work, R_g and ψ_6 coordinates are discretized with a resolution of 0.0032 and 0.025. After the coefficients are obtained, the resulting SE (Eq. (7.16)) can be numerically solved to obtain the probability evolution $p(\mathbf{x}, \Delta t \mid \mathbf{x}_0, 0)$ at different observation times, Δt, for given initial conditions. In this work, the SE is solved using explicit upwind differentiation for parabolic partial differential equations with reflective boundary conditions.[166] The discrete version of Eq. (7.16) is given as,

$$
\begin{aligned}
p_{i,j}^{n+1} - p_{i,j}^{n} \approx{} & \frac{D_{i+1,j}^{\psi_6} p_{i+1,j}^{n} - 2D_{i,j}^{\psi_6} p_{i,j}^{n} + D_{i-1,j}^{\psi_6} p_{i-1,j}^{n}}{(\Delta\psi_6)^2}\Delta t + \\
& \frac{D_{i,j+1}^{R_g} p_{i,j+1}^{n} - 2D_{i,j+1}^{R_g} p_{i,j+1}^{n} + D_{i,j-1}^{R_g} p_{i,j-1}^{n}}{(\Delta R_g)^2}\Delta t + \\
& \frac{\mathbf{max}(v_{i-1,j}^{\psi_6} p_{i-1,j}^{n},0) + \mathbf{min}(v_{i+1,j}^{\psi_6} p_{i+1,j}^{n},0) - v_{i,j}^{\psi_6} p_{i,j}^{n}}{\Delta\psi_6}\Delta t + \\
& \frac{\mathbf{max}(v_{i,j-1}^{R_g} p_{i,j-1}^{n},0) + \mathbf{min}(v_{i,j+1}^{R_g} p_{i,j+1}^{n},0) - v_{i,j}^{R_g} p_{i,j}^{n}}{\Delta R_g}\Delta t
\end{aligned}
\tag{7.25}
$$

where the subscripts indicate order parameter grid points, the superscript, *n*, on *p* denotes the time step, the superscript order parameter on *v* denotes the drift component from Eq. (7.17), and the superscripts in *D* denotes the diagonal components in **D** from Eq. (7.17). The off-diagonal components of **D** are ignored in this work for simplicity and because they are relatively small compared to the diagonal terms. One constraint on the set of equations given by Eq. (7.25) is that the sum of the right-hand-side of all equations must be zero via the conservation of probability. Eq. (7.25) is discretized with a resolution of $\Delta\psi_6 = 0.032$, $\Delta R_g = 0.0025$, and $\Delta t = 0.01$s.

7.4.4 First passage time distributions

To verify the extracted coefficients in Eq. (7.17), we compare BD (Eq. (7.6)) and LDLD (Eq. (7.20)) simulations based on first passage time distributions between different states. These different states are chosen to capture the condensation process (fluid to polycrystal), grain boundary migration process (polycrystal to single domain crystal), as well as the combination of the two (fluid to single domain crystal). The first passage time distributions are constructed by counting the arrival time to specified ending states of trajectories starting from the same initial state. The same BD trajectory data used to obtain the SE coefficients was used to construct first passage time distributions. For LDLD simulation results, statistics were first collected from 4,000 trajectories initiated in fluid and polycrystalline states (from 40 grid points with 100 different random number generator seeds). After initial sampling, another 4,000 simulations were performed for states with insufficient sampling. These 8,000 dynamic trajectories in low dimensional space via LDLD were used to construct first passage time distributions between different states.

7.5 Results & discussion

7.5.1 Dimensionality from diffusion mapping

The first step towards building a low dimensional Smoluchowski model is to identify the number and the appropriate choice of order parameters. To this end, we have used a machine learning technique, called diffusion mapping, which identifies the intrinsic manifold of a large data set and provides a suitable low dimensional representation.[154] We have applied the diffusion maps technique to smaller systems in our earlier work to build low dimensional models.[120] In the current implementation of diffusion mapping, we use a new composite distance metric ($\boldsymbol{\Delta}$) based in complementary metrics for both condensation (**H**) and ordering (**O**) processes important to colloidal crystallization. We apply to the analysis to simulation data that was previously matched to experiments, which enables high spatial and temporal resolution and statistical sampling to avoid some issues[133,167] when working directly with experimental microscopy data (which can be overcome when treated carefully[168]).

Fig. 2 shows results of a diffusion mapping[118] analysis of a large number of

Brownian Dynamic (BD) simulations of the assembly of N=210 particles into quasi-2D colloidal crystals in a quadrupolar electric field. The BD simulations were matched to experiments in previous work.[113,114,136,150] Fig. 2A shows the eigenvalue spectrum obtained from the diffusion mapping analysis. A large spectral gap after the first non-trivial eigenvalue, λ_2, and smaller gaps after the third and fourth eigenvalues, λ_3 and λ_4, suggest a one-dimensional nature to the data but two additional dimensions need to be considered. When plotting the data in the space of the first three eigenvectors (ν_2, ν_3, and ν_4) (Figs. 2C, D), the data points are seen to lie on a 2D surface in the 3D space, indicating that the dynamical system is effectively two-dimensional and described primarily by the coordinates ν_2 and ν_3. The ν_4 values are highly correlated with the values of ν_2; such dependencies indicate multiple eigenvectors characterizing the same dynamic pathway.[163]

We also studied how the eigenvectors correlate with physically meaningful candidate order parameters[40,43,44,112,120,122,150,169] by coloring the data in Fig. 2. Although eigenvectors from diffusion mapping can be used directly as order parameters[170] or for high-throughput screening of candidate order parameters,[171,172] such methods are computationally expensive and were not explored in this work. Fig. 2C shows the data colored by values of R_g. R_g is highly correlated with ν_2, as indicated by the continuous spectrum of color vs. that coordinate. Fig. 2D shows the data colored by values of ψ_6. It is found that ψ_6 is highly correlated with a combination of ν_2 and ν_3. The data points plotted in (ψ_6, R_g) space in Fig. 2B shows that the data span the regions of interest in the configuration space (based on the candidate order parameters) and is well correlated with the top non-trivial eigenvector, ν_2. Therefore, it appears that R_g and ψ_6 are able to parameterize data embedded in the 2 significant coordinates identified by the diffusion mapping analysis. We will use these variables to build a low dimensional model of quasi-2D colloidal crystallization in electric fields.

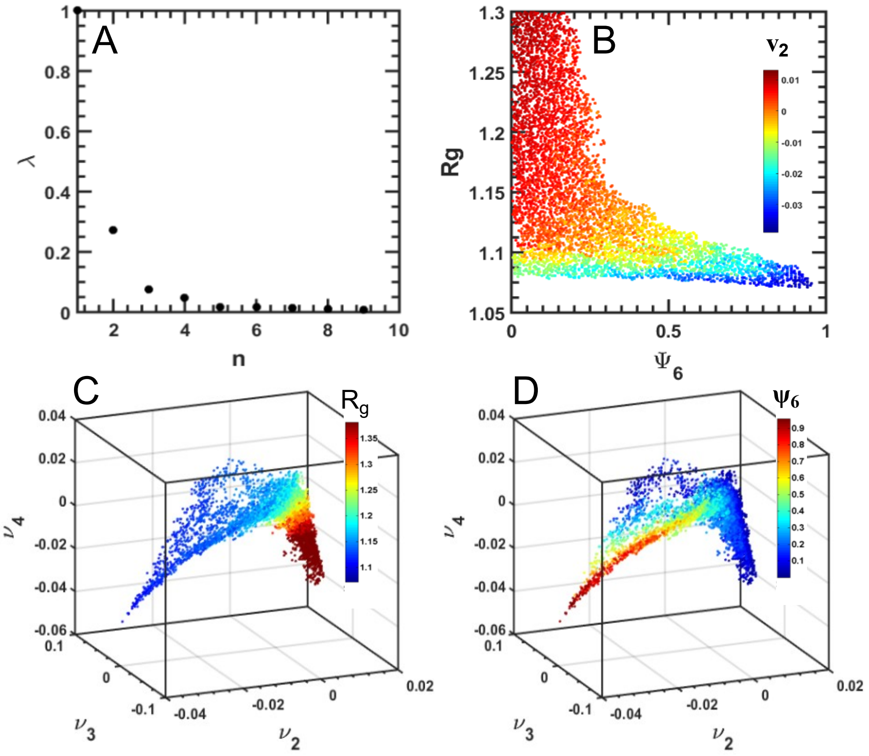

Figure. 2. (A) Eigenvalue spectrum obtained from diffusion mapping (Eqs. (7.9)) the process of electric field mediated colloidal assembly in a quadrupole electrode (see Fig. 1) for a system size of N=210 and a non-dimensional applied voltage of V^*=0.8. (B) Plot of ~8000 configurations sampled in BD simulations plotted in (ψ_6, R_g) space and colored by values of first non-trivial eigenvector, ν_2, shows good sampling of final order parameters. Bottom two plots show points indicating values of the top three non-trivial eigenvector coordinates (ν_2, ν_3, ν_4) for the same ~8000 configurations shown in (B) but now colored by their values of (C) the order parameter R_g (Eq. (7.12)) and (D) the order parameter ψ_6 (Eq. (7.15)).

7.5.2 Smoluchowski analysis of assembly trajectories

Fig. 3 shows examples of dynamic quantities obtained by analyzing a large set of ψ_6, R_g coordinates generated from BD simulated trajectories. Results in Fig. 3 are for

N=210 particles with the following combinations of starting coordinates and applied non-dimensional voltages: (ψ_6, R_g) = (0.138, 1.15), V^* =0.80 (example of fluid condensation); (ψ_6, R_g) = (0.3875, 1.146), V^* = 0.57, (example of grain boundary motion); and (ψ_6, R_g) = (0.7125, 1.125), V^* = 0.5 (example of melting). Figs. 3A, B show the ensemble average of displacement vs. time for each starting coordinate. Positive slopes indicate the existence of driving force to increase ψ_6 (*i.e.* ordering) or R_g (*i.e.* expansion), whereas negative slopes indicate driving forces to decrease these quantities. The steepness of the slope characterizes the magnitude of the driving force (*i.e.*, Eqs. (7.17)-(7.19)). The slopes of each curve are qualitatively consistent with expectations for condensation ($\Delta\psi_6\uparrow$, $\Delta R_g\downarrow$) and melting ($\Delta\psi_6\downarrow$, $\Delta R_g\uparrow$), and the shallow slope associated with grain boundary motion shows the weak driving force for this process.

Figs. 3C-F show the ensemble average of the four components in covariance matrix as a function of time for the same initial coordinates and applied voltage as in Figs. 3A,B. As shown in the theory section (Eq. (7.17)), the initial slopes are proportional to the magnitude of the four components of the diffusivity tensor of the low-dimensional Smoluchowski equation (Eq. (7.16)). The cross terms in the diffusivities tensor reflect the coupling between both drift and diffusion along the ψ_6 and R_g coordinates. Deviations of slopes at longer times from the initial short time slopes indicate effects of drift due to the underlying landscape (that can either produce migration or localization of trajectories). Most of the fitted initial slopes via Eq. (7.17) have relative uncertainties (i.e. the standard value of the fitted value divided by the value itself) on the order of ~2% or smaller, which cause the resulting free energy landscape via Eq. (7.19) and propagation of error to have relative uncertainties of ~4%.

7.5.3 Field dependent landscapes (for fixed system size)

By performing the analysis illustrated in Fig. 3 at many grid points in the order parameter space, it is possible to construct coordinate dependent W and $\mathbf{D}$ (*i.e.*, "landscapes") for fixed thermodynamic conditions. For the example in the present study, the voltage, V, determines the magnitude of the electric field compressing induced dipoles, and therefore acts as a global thermodynamic variable. As such, for each V^*, the relative free energy and diffusivity of each configuration can be determined to construct W and $\mathbf{D}$ for all possible configurations. Fig. 4 shows the landscapes of W and $\mathbf{D}$ for several values of increasing V^* for a system size of N=210.

At the lowest voltage, V^*=0.42 (Fig. 4A), the global minimum of W is located at ψ_6, $R_g \approx$ 0.25, 1.18; the structure is a dense fluid consisting of several small ordered clusters (rendering I) but lacks global orientational order due to minimal coalescence in the presence of weak compression of dipoles. Fig. 4A shows a single example trajectory plotted on W, which illustrates compression of an expanded fluid configuration (*i.e.* low ψ_6, high R_g) towards the global minimum with a relatively small free energy change (~15 kT) where it then diffuses locally.

The four diffusivity components are shown in middle column of Fig. 4A. The $\mathbf{D}_{\psi 6 \psi 6}$ component (upper left) has relatively larger values in the vicinity of $\psi_6 \approx$0.2-0.3, which is consistent with grain boundary motion in polycrystalline structures that produces larger fluctuations in ψ_6. $\mathbf{D}_{\psi 6 \psi 6}$ decreases only slightly as R_g decreases due to hydrodynamic hindrance in compact configurations. Large regions of the diffusivity landscape cross-terms, $\mathbf{D}_{\psi 6 Rg}$ and $\mathbf{D}_{Rg \psi 6}$, have values near zero, except for slightly negative values encountered in the vicinity of ψ_6, $R_g \approx (0.4, 1.18)$. These negative values in the cross-terms indicate a weak correlation between decreasing R_g and increasing ψ_6, which is consistent with condensation being correlated with ordering. Given the different relative magnitudes of ψ_6 and R_g, the relative importance of the cross terms can also be interpreted using a correlation coefficients defined as, $\rho = D_{\psi 6\mathrm{Rg}}/(D_{\psi 6\psi 6}D_{\mathrm{RgRg}})^{0.5}$. In all cases, this correlation coefficients is less than 5%, suggesting very little correlation between R_g and ψ_6 such that the cross terms are negligible. This finding is supported by comparing BD and LDLD simulations with and without the cross terms, which are quantitatively indistinguishable.

As V^* increases to 0.5, the global minimum in W (Fig. 4B) shifts to ψ_6, $R_g \approx (0.6, 1.14)$, indicating both increased condensation and global ordering compared to V^*=0.42. The equilibrium structure (rendering III) is characterized has a single central hexagonal close packed core with small number of peripheral fluid-like particles. While the free energy gradient in the R_g coordinate increases when increasing V^* from 0.42 to 0.5, the free energy gradient in the ψ_6 direction is shallow. For example, bi-domain crystals formed in the vicinity of $R_g \approx$1.14-1.16, $\psi_6\approx$0-0.3 (*i.e.* low ψ_6, low R_g) (rendering II) have misorientation angles close to 30 degrees, which are metastable structures with minimal driving force for grain boundary migration. As for the diffusivity landscape at V^*=0.5, $\mathbf{D}_{\psi 6\psi 6}$ and $\mathbf{D}_{RgRg}$ decreases as R_g become smaller, which is due to the increased hindrance at denser configuration slows down the particle arrangement behavior. At V^*=0.57 (Fig. 4C), the global minimum in W now shifts to ψ_6, $R_g\approx(0.6, 1.14)$, with more ordered and condensed equilibrium structure (rendering VI). The diffusivity landscape components share similar features with the other voltages. At this voltage, the free energy plateau region on W (with a minimal free energy gradient) shifts and stretches to coordinates in the range

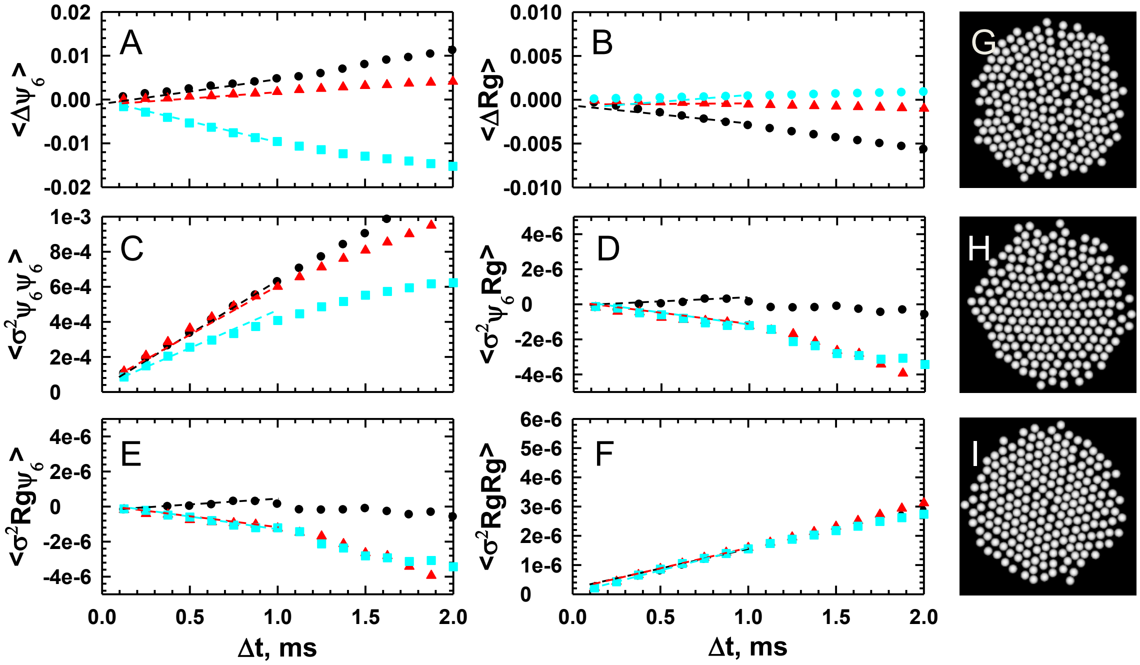

Figure. 3. Representative local order parameter trajectories used to obtain Smoluchowski equation coefficients. Results are shown for a system size of N=210. Plots show ensemble average: displacement vs. time for (A) ψ_6 and (B) R_g; displacement variance vs. time in (C) and (F); displacement covariance in (D) and (E). Representative data are shown for several different combinations of starting configurations and applied voltages including: (G) (black circles) (ψ_6, R_g)=(0.1375, 1.146) V^*=0.80; (H) (red triangles) (ψ_6, R_g)=(0.3875, 1.146) V^*=0.57; (I) (cyan squares) (ψ_6, R_g)=(0.7125, 1.125) V^*=0.50. Linear fits to the initial slopes (illustrated by dashed lines) of the data in each plot are used in Eqs. (7.17)-(7.19) to obtain **D**(**x**) and W(**x**) in Figs. 4 and 7.

around $R_g \approx$ 1.12-1.13, ψ_6≈0-0.5.

7.5.4 Field dependent assembly pathways

On the landscapes in Fig. 4C, there are two typical assembly kinetic pathways, as exemplified by the trajectories T1 and T2 plotted on W. The T1 trajectory corresponds to rapid condensation along a steep free energy gradient where two locally ordered domains coalesce into a bi-crystal with a near maximum 30° misorientation angle. From V to VI, the bi-crystal relaxes into a single domain as one grain grows at the expense of the other.

In contrast to T1, the T2 trajectory develops higher global order via initial stochastic motion before it moves down the free energy gradient and is rapidly funneled towards the global free energy minimum. The intermediate microstructure (rendering IV) is typically characterized by domains with similar orientation (*i.e.* small misorientation angle). Domains with small misorientation angles easily relax during coalescence and condensation, which is consistent with a smaller free energy barrier to grain boundary motion. As a result, T2 is able to bypass the free energy plateau at low R_g to avoid the slow diffusion process encountered in the T1 trajectory, which results in much faster equilibration the global free energy minimum single crystal. For all voltages, all diffusivity components uniformly decreases with decreasing R_g, so that paths T1 and T2 do not experience significantly different levels of friction as part of determining the total time to produce single perfect crystals.

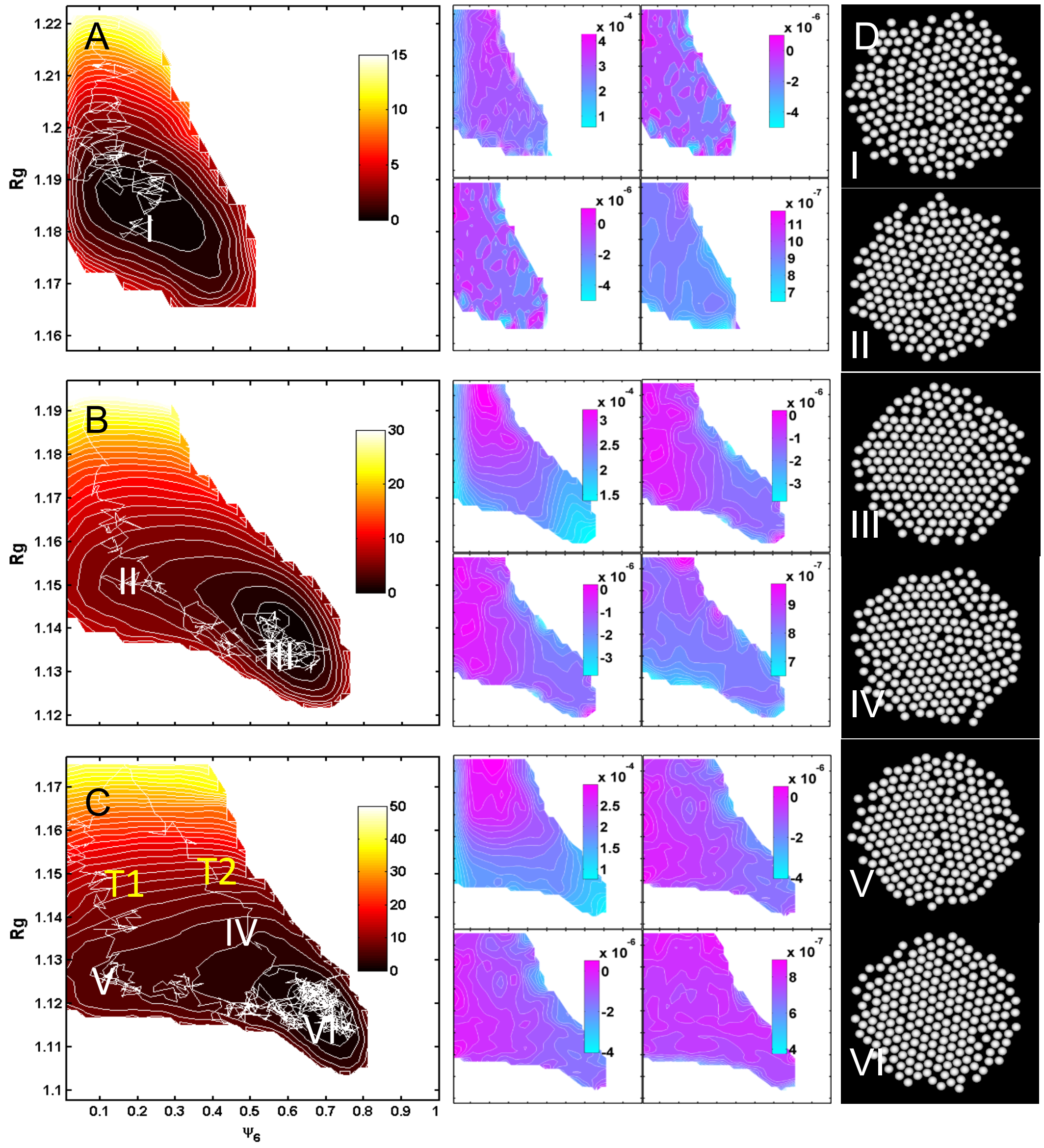

Figure. 4. Free energy and diffusivity landscapes obtained by fitting trajectories to Smoluchowski equation to BD trajectories for N=210 and applied voltages of (top-to-bottom): (A) V*=0.42, (B) V*=0.50, (C) V*=0.57. Plots show (left) free energy landscapes, $W(\psi_6, R_g)/kT$ (Eq. (7.19)), with trajectories, marked coordinates of interest, and inset scale bars, and (middle) four components of diffusivity tensor, $\mathbf{D}/(kT{\cdot}s)$ (Eq. (7.17)), with inset scale bar and same axes as W plots (left-to-right, top-to-bottom): $D_{\psi6\psi6}$, $D_{\psi6Rg}$, $D_{Rg\psi6}$, and D_{RgRg}. T1 and T2 in the left most column of part (C) denote two representative trajectories following different pathways. (D) Renderings in column on far right show representative configurations for coordinates marked on W plots.

7.5.4.1 Assembly Pathway Times

The low dimensional models based on the landscapes shown in Fig. 4 not only provide qualitative information about the assembly process but also quantitatively capture assembly dynamics. By evaluating statistical properties of trajectories from the full *N*-dimensional BD simulations and low-dimensional Langevin dynamic (LDLD) simulations, such as the first passage times for transitions from one state to another state, it is possible to evaluate the accuracy of the LDLD model.[120,150] Fig 5 compares first passage time distributions from BD and LDLD simulations at $V^*=0.57$ for $N=210$. First passage time distributions show histograms of the times it takes to pass for the first time between initial states end states characterized by (ψ_6, R_g) coordinates on the W. The first passage time is a distribution due to the stochastic nature of the assembly dynamics.

As depicted in Fig. 5A, we simplify the presentation of first passage time distributions by comparing assembly processes characterized by either (1) condensation along the steep W gradient parallel to the R_g axis (plotted in Fig. 5B), or (2) grain boundary relaxation along the W plateau parallel to the ψ_6 axis (plotted in Fig. 5C). For predominantly condensation processes, Fig. 5B shows a set of first passage time distributions for assembly trajectories between initial and final R_g coordinates specified in the figure caption. These distributions are obtained by averaging over all ψ_6 coordinates sampled during condensation. In the case of trajectories dominated by grain boundary relaxation, Fig. 5C shows first passage time distributions for trajectories between initial and final ψ_6 coordinates, which are averaged over all R_g coordinates. It is interesting to note the order of magnitude greater first passage time for grain boundary motion compared to condensation. Good agreement between *N*-dimensional BD simulations and the LDLD simulations is observed, indicating the accuracy of the *W* and **D** from the Smoluchowski analysis.

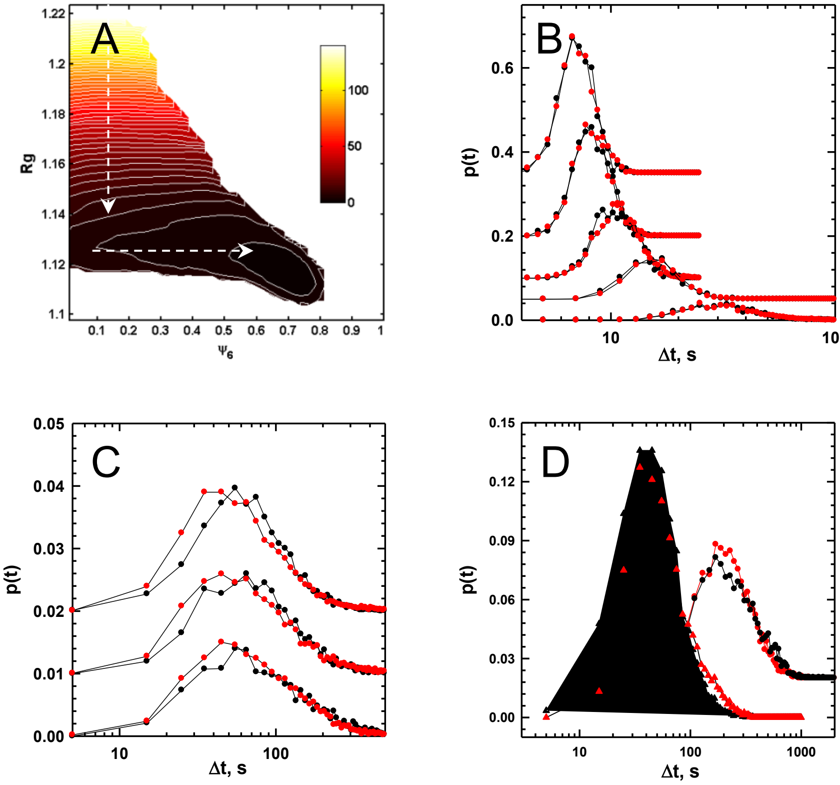

Figure. 5. First passage time distributions (FPTD) for BD (black) and LDLD (red) trajectories during processes of condensation and grain boundary migration for system size of *N*=210 at applied voltage of *V**=0.57. (A) Schematics for the process of condensation (vertical arrow along the steep W gradient at R_g direction) and the process of grain boundary migration (horizontal arrow along the W plateau at ψ_6 direction). (B) FPTD during the condensation process measured from trajectories from starting points to end points on the R_g-axis between (top to bottom): (1.24, 1.22), (1.22, 1.20), (1.20, 1.18), (1.18, 1.16), and (1.16, 1.14). (C) FPTD during grain boundary migration process measured by tracking trajectories from starting points to end points on the ψ_6-axis between (top to bottom): (0.4, 0.6), (0.3, 0.5), and (0.2, 0.4). (D) FPTD corresponding to T1 and T2 in Fig. 4C between a sink at (ψ_6=0.7 R_g=1.18) (*i.e.*, global minimum) and sources at (ψ_6=0.15 R_g=1.13) (circles) and (ψ_6=0.5 R_g=1.14) (triangles).

Although the first passage time distributions projected onto the R_g and ψ_6 axes show the full *N*-dimensional BD and LDLD models agree quantitatively, they don't tell the whole story in terms of the assembly dynamics. It is still essential to use the two dimensions to characterize first passage times for different assembly pathways. For example, Fig. 5D shows first passage time distributions roughly corresponding to trajectories T1 and T2 in Fig. 4C (*i.e.*, one starts at (ψ_6=0.38 R_g=1.15) and the other one starts at (ψ_6=0.65 R_g=1.16); both terminate at the global minimum). The fast T2 trajectory makes it to the global free energy minimum single crystal nearly two orders of magnitude faster than the slow T2 trajectory that is detained on the free energy plateau corresponding to grain boundary diffusion. This large difference in first passage times is not capture by projecting to the 2D trajectories to onto either the ψ_6 or R_g axes as shown by the first passage times in Figs. 5B,C.

After showing the accuracy of the LDLD model via first passage time distributions, it is possible to more completely explore the dynamic evolution of the system using the low dimensional W and $\mathbf{D}$ in Fig. 4 to numerically solve the SE (Eq.(7.16)). This provides more complete information on the time evolution of states during stochastic assembly processes (e.g., compared to first passage times alone). Fig. 6 shows the solution of SE (*i.e.* $p(\mathbf{x},t)$) for N=210 at different voltages and observation times, Δt, with given initial conditions, $p(\mathbf{x},0)=\delta(\mathbf{x}-\mathbf{x}_0)$, $\mathbf{x}_0$=(0.025, 1.22), which corresponds to a starting fluid configuration.

At the lowest V^*, Figs. 6A,B show the evolution of $p(\mathbf{x}, \Delta t)$ is characterized by slow drift and diffusion of the initial delta function towards the new equilibrium state, which is a broader distribution of configurations centered on a more condensed fluid state. Convergence to the equilibrium Boltzmann distribution is observed to occur within ~200s (most easily seen from blue and cyan curves in Fig. 6B). At the intermediate V^*, Figs. 6C,D show how $p(\mathbf{x}, \Delta t)$ more rapidly drifts towards more condensed and ordered states before a new most probable loosely packed crystal state emerges between 100-200s and the equilibrium distribution is reached within ~400s. At the highest V^*, which corresponds to conditions when a single crystal is expected as the global free energy minimum configuration, Figs. 6E,F show how $p(\mathbf{x}, \Delta t)$ drifts even more rapidly toward evolving ordered configurations that once again reach the equilibrium distribution in ~400s. The results in Fig. 6 show how the low dimensional model captures the stochastic evolution of the probability density of states at different thermodynamic conditions, which captures all dynamic information necessary to design, control, and optimize colloidal assembly schemes in this system.

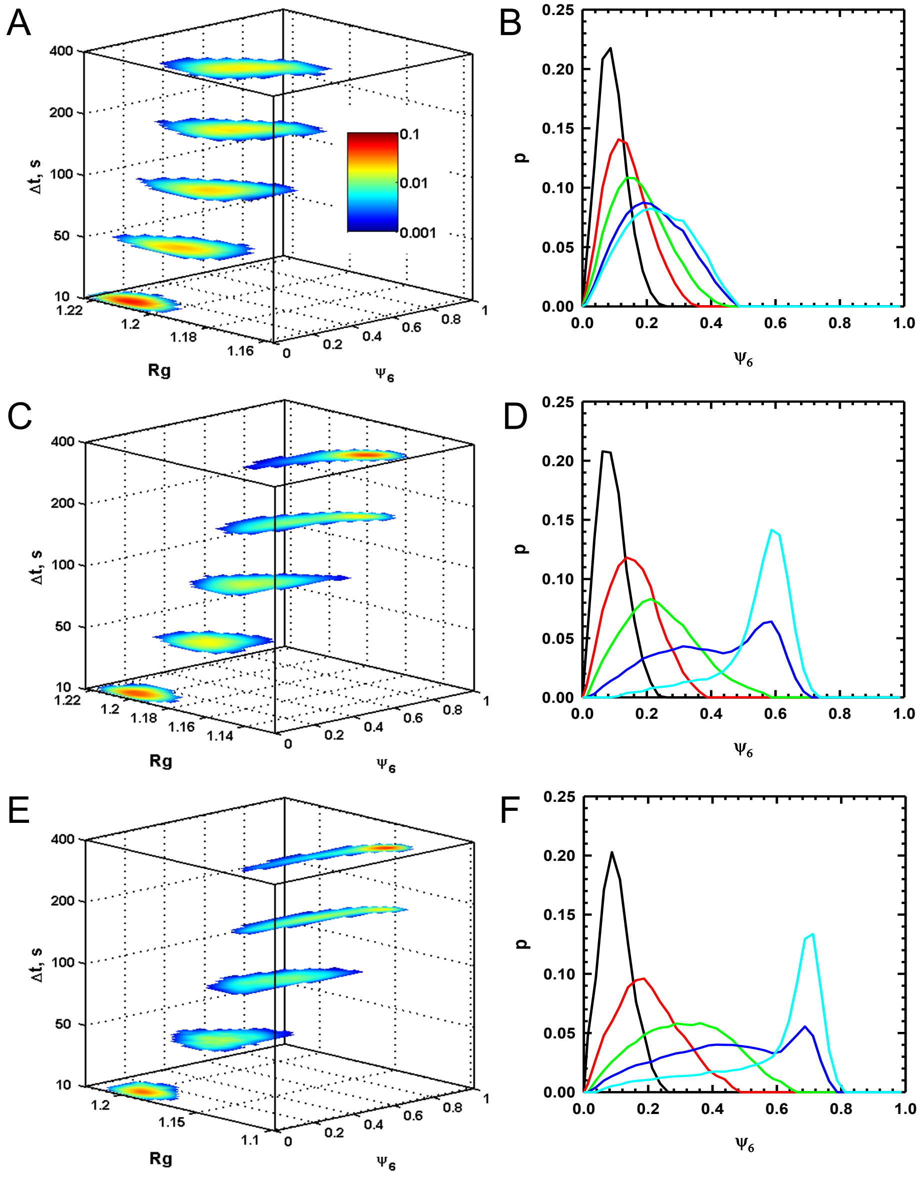

Figure. 6. Numerical solution of Smoluchowski equation to compute $p(\mathbf{x},t)$ at observations times of Δt=10s, 50s, 100s, 200s, and 400s for a system size of N=210 at applied voltages of: (A, B) V^*=0.42, (C, D) V^*=0.50, and (E, F) V^*=0.57. The initial condition in all cases is $p(\mathbf{x},0)=\delta(\mathbf{x}-\mathbf{x}_0)$ where $\mathbf{x}_0=(\psi_{60}, R_{g0})=(0.025, 1.22)$. The left hand plots are two dimensional contour plots of probability density with an inset scale bar in part A. The right hand plots are one dimensional projections of the two dimensional probability density onto the ψ_6 coordinate for: Δt=10s (black), 50s (red), 100s (green), 200s (blue), and 400s (cyan).

7.5.5 System size dependent assembly pathways

Because the results in Figs. 1-6 are for a single system size of N=210, we now explore different systems sizes and voltages to see how the low dimensional model and assembly behavior changes. Fig. 7 shows W and $\mathbf{D}$ for N=110, 210, and 300 at voltages that produce equilibrium structures of comparable global order and degree of condensation (*i.e.* similar equilibrium ψ_6 and R_g; see Fig. 7 caption for details). All W and $\mathbf{D}$ share similar qualitative features (*e.g.*, a steep free energy gradient followed by a plateau) and corresponding microstructures at the plateau region (*i.e.*, bicrystals at low ψ_6 and single crystals at high ψ_6) marked on the landscapes and shown in the right column of Fig. 7. Quantitative differences with increasing system size include a shift of the global minimum on each W towards somewhat higher R_g and lower ψ_6, which is due to the smaller number of particles packing more densely and being more easily ordered. Increasing system size also produces a systematic decrease in the diagonal terms of $\mathbf{D}$ (*i.e.*, $\mathbf{D}_{\psi6\psi6}$, $\mathbf{D}_{\mathrm{RgRg}}$), which is most likely due to increasing hydrodynamics hindrance and associated resistance to rearrangement with increasing crowding.

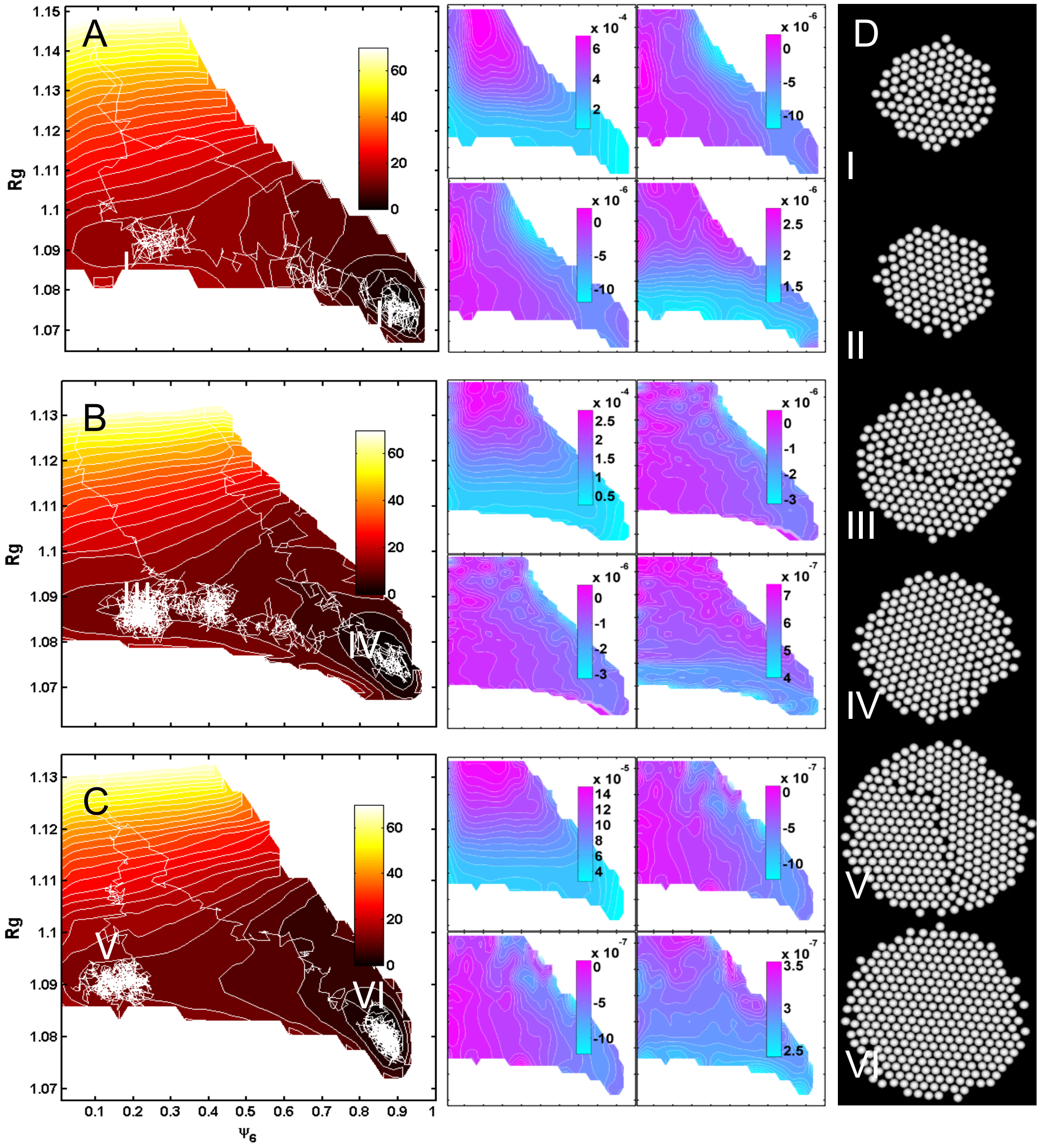

Figure. 7. Free energy and diffusivity landscapes with same formatting and procedure to obtain plots in Fig. 4 (see Fig. 4 caption), except results are now shown for different systems sizes (and applied voltages) of (top-to-bottom): (A) N=110 (at V^*=0.85), (B) N=210 (at V^*=0.80), and (C) N=300 (at V^*=0.75). (D) Renderings in column on far right show representative configurations for coordinates marked on W plots.

Using the W and **D** from Fig. 7, quantitative differences in the assembly kinetics can be examined by numerically solving the SEs for the three system sizes in Fig. 8 (using the same procedure and formatting as Fig. 6). Fig. 8 shows the solution of SE from initial conditions of $p(\mathbf{x},0)=\delta(\mathbf{x}-\mathbf{x}_0)$, $\mathbf{x}_0=(0.025, 1.18)$ for N=110, 210, and 300 for Δt=10s, 50s, 100s, 200s, and 400s. Within the first ~100s, the distributions in all cases show rapid condensation along the R_g direction (*i.e.* R_g decreases) towards the W plateau near $R_g\approx1.09$ with $p(\mathbf{x}, t)$ spanning all ψ_6 coordinates. At longer times, the probability density is depleted at the low ψ_6 region and simultaneously accumulates towards the high ψ_6 region.

The general trend in these data vs. system size is that smaller systems more rapidly approach the global free energy minimum ordered state compared to larger systems sizes. Specifically, for the N=110 system at Δt=100s, around half of all trajectories have already reached the general vicinity of equilibrium (i.e., area under the curve at high ψ_6) whereas the rest are trapped in the plateau regions of the Ws shown in Fig. 7. From Δt>100s, most trajectories relax towards the equilibrium ordered state except for a small persistent portion in the vicinity of $\psi_6\approx0.1$. The microstructures in the region of low R_g and $\psi_6\approx0.1$ correspond to nearly perfect bi-crystals, which are metastable with essentially no free energy gradient to drive relaxation (which only occurs when stochastic fluctuations initiate an imbalance that causes one domain to grow at the expense of the other[150]).

With increasing system size, and particularly for the largest system here of N=300, at Δt=100-200s, nearly all the trajectories are trapped on the W plateau, and their subsequent relaxation towards the perfect crystal state are significantly slowed compared to the N=110 system. This slowing down with increasing system size can be attributed to the differences in the absolute values of the diffusivity landscapes in the region of configuration space corresponding to polycrystal relaxation towards single crystals states. Because all system sizes have plateaus on W in this region, there is little to no thermodynamic driving force all cases, so the kinetics is governed by diffusion and resistance in the ψ_6 direction. The relatively larger diffusivities in the ψ_6 coordinate for smaller systems allow trajectories to 'fluctuate' more as part of relaxing towards the single crystal in the global free energy well. This system size dependent behavior has been observed in our previous experiments,[112] which indicates the validity of the low dimensional models developed in this work. Extension of the approach here to larger system sizes could eventually slow dynamics to the point that assumptions underlying the analysis and interpretation in the present study (*i.e.*, ergodicity, detailed balance, thermodynamic equilibrium) could eventually be called into question. There are no signatures of non-Markovian behavior to indicate any issues with the validity of these assumptions in the present work (all properties are independent of path and initial conditions in order parameter space).

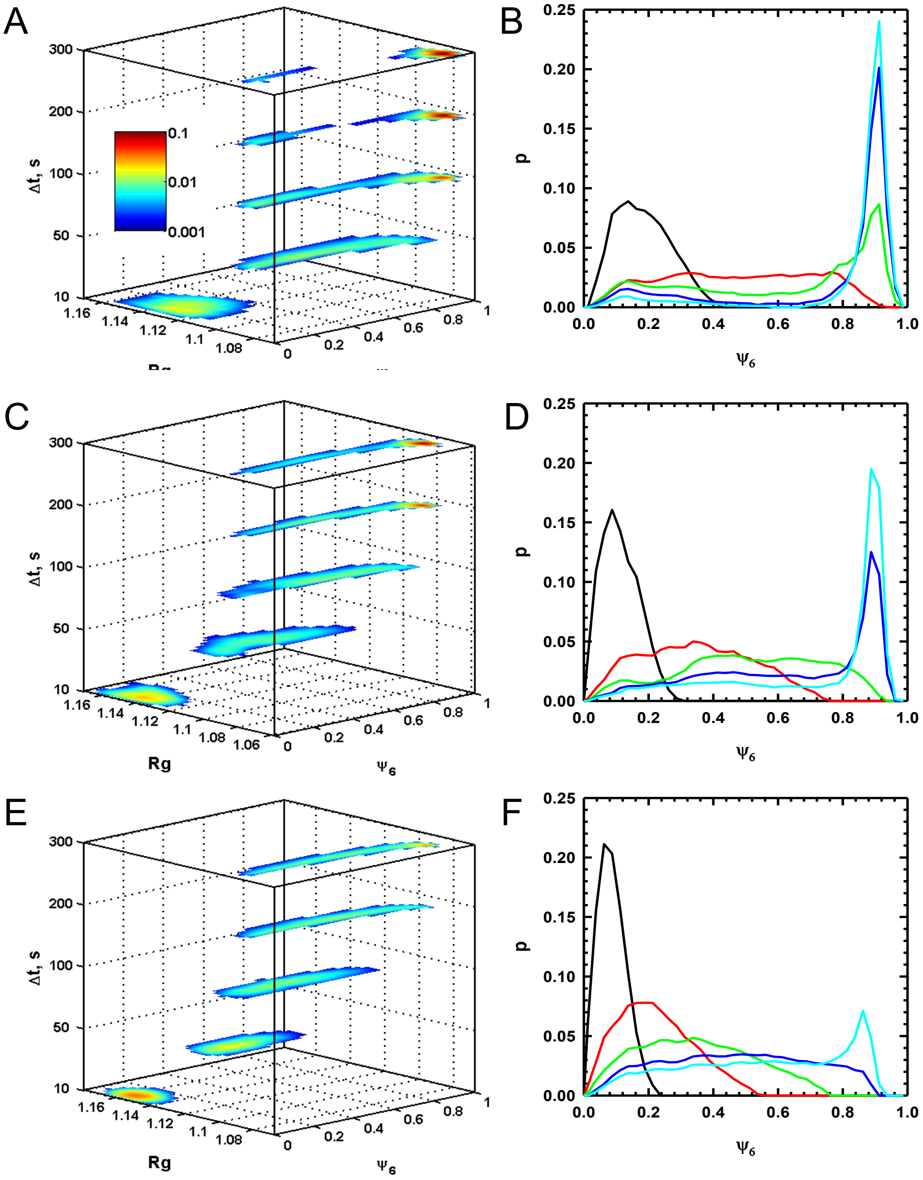

Figure. 8. Numerical solution of Smoluchowski equation to compute $p(\mathbf{x},t)$ at observations times of Δt=10s, 50s, 100s, 200s, and 400s for different systems sizes (and applied voltages) of (top-to-bottom): (A, B) N=110 (at V^*=0.85), (C, D) N=210 (at V^*=0.80), and (D, E) N=300 (at V^*=0.75). The initial condition in all cases is $p(\mathbf{x},0)=\delta(\mathbf{x}-\mathbf{x}_0)$ where $\mathbf{x}_0=(\psi_{60}, R_{g0})=(0.025, 1.18)$. The left hand plots are two dimensional contour plots of probability density with an inset scale bar in part A. The right hand plots are one dimensional projections of the two dimensional probability density onto the ψ_6 coordinate for: Δt=10s (black), 50s (red), 100s (green), 200s (blue), and 400s (cyan).

7.6 Conclusions

We reported the development of a low-dimensional Smoluchowski equation to quantify the thermodynamics and kinetics of colloidal crystal assembly in electric fields. The dimensionality and order parameter choice was supported by a diffusion mapping analysis. Order parameters describing global order, ψ_6, and degree of condensation, R_g, were found to yield a low-dimensional model that quantitatively captured assembly dynamics as determined by first passage times in agreement with N-dimensional dynamic data. The free energy and diffusivity landscapes from the Smoluchowski model revealed two types of kinetic pathways; one where condensation and global order emerge simultaneously to rapidly yield single domain crystals, and another one where fast condensation with local ordering, but not global ordering, results in polycrystal formation. Numerical solution of the low-dimensional Smoluchowski equation shows the temporal evolution of the probability of states for different voltages and system sizes, which quantifies how these two variables determine the evolution of order in electric field mediated quasi-2D crystallization. Ultimately, the low dimensional model quantitatively captures slow grain boundary dynamics in the presence of vanishing free energy gradients, where friction associated with configurational rearrangements determines the relaxation rate for polycrystals to form single crystals via grain boundary motion. These low-dimensional models are currently being used to design optimal control policies for closed loop and open loop control of colloidal assembly processes designed to form single crystal structures.

Tables

Table 1. Parameters for simulations of colloidal particles in a quadrupole electrode: (a) number of particles, (b) particle size, (c) Debye screening length, (d) electrostatic potential pre-factor, (e) Clausius-Mossotti factor for 1 MHz AC field, (f) medium permittivity, (g)

electrode spacing, (h) temperature, (i) radius of gyration for 2D HCP particles within regular hexagon morphologies, (j) lowest voltage to crystallize system, (k) applied voltage, (l) normalized voltage, (m) non-dimensional field strength.

Variable	Value
N^a	110,210,300
a (nm)[b]	1400
κ^{-1} (nm)[c]	10
$B^{pp}(kT)$[d]	3206
f_{cm}[e]	-0.4667
$\varepsilon_m/\varepsilon_0$[f]	78
d_g (μm)[g]	100
T (°C)[h]	20
$R_{g,HEX}$(nm)[i]	15122(N=210); 10944(N=110); 18074(N=300)
V_{xtal}(volt)[j]	1.89(N=210); 2.71(N=110); 1.43(N=300)
V(Volts)[k]	0.8, 0.94, 1.07, 1.51(N=210); 2.3(N=110); 1.07 (N=300)
V^*(Volts)[l]	(0.42, 0.5, 0.57, 0.80) (N=210); 0.85(N=110); 0.75(N=300)
λ^m	2.5, 3.5, 4.5, 9(N=210); 21 (N=110); 4.5(N=300)

8 OPTIMAL FEEDBACK CONTROLLED ASSEMBLY OF PERFECT CRYSTALS‡

8.1 Abstract

Perfectly ordered states are targets in diverse molecular to microscale systems involving for example atomic clusters, protein folding, protein crystallization, nanoparticle superlattices, colloidal crystals, *etc*. However, there is no obvious approach to control the assembly of perfectly ordered global free energy minimum structures; near-equilibrium assembly is impractically slow, and faster out-of-equilibrium processes generally terminate in defective states. Here, we demonstrate the rapid and robust assembly of perfect crystals by navigating kinetic bottlenecks using closed-loop control of electric field mediated crystallization of colloidal particles. An optimal policy is computed with dynamic programming using a reaction coordinate based dynamic model. By tracking real-time stochastic particle configurations and adjusting applied fields *via* feedback, the evolution of unassembled particles is guided through polycrystalline states into single domain crystals. This approach to controlling the assembly of a target structure is based on general principles that make it applicable to a broad range of processes from nano- to micro- scales (where tuning a global thermodynamic variable yields temporal control over thermal sampling of different states *via* their relative free energies).

---

‡ Reprinted with permission from "Optimal Feedback Controlled Assembly of Perfect Crystals." *ACS nano* 7 (2016): 6791-6798 by Tang, Xun, Bradley Rupp, Yuguang Yang, Tara D. Edwards, Martha A. Grover, and Michael A. Bevan. Copyright © 2016 American Chemical Society.

8.2 Introduction

Assembling colloidal nano- and micro- particle components into perfectly ordered configurations could enable metamaterials with exotic properties that are otherwise unattainable.[97,173-175] Obtaining perfect structures is non-trivial at any scale (*e.g.*, atomic clusters, nanoparticle superlattices, folded proteins). Limited successful examples of perfect crystals on molecular scales include monocrystalline silicon for microelectronics *via* near-equilibrium directional growth from a seed crystal, and single small protein crystals for x-ray crystallography *via* combinatorial screening. Such perfect atomic and molecular crystals are often obtained using open-loop control at near equilibrium conditions; *i.e.*, recipes based on slow nucleation, growth, and annealing to allow constituents to gradually assemble and relax into global free energy minimum perfect crystals. Like molecular crystallization, the capability to tune colloidal nano- and micro-particle crystallization has been shown in a number of studies;[42,176-187] however, the controlled assembly of perfect thermodynamically stable colloidal crystals has not yet been demonstrated.

Crystallization kinetics depend on how constituents collectively assemble *via* diffusion. Molecular diffusion rates allow crystal growth near equilibrium to occur on timescales that are economically viable for manufacturing of high value-added materials. Colloidal nano- to micro- scale components, by virtue of their size, diffuse orders of magnitude more slowly than molecules, and hence colloidal assembly at near equilibrium conditions is impractical. The alternative, rapid out-of-equilibrium assembly, leads to defects (*e.g.*, polycrystals) and often arrested amorphous states. There appears to be an insurmountable gap between the limits of assembling perfect crystals *via* excessively long equilibrium processes and rapidly producing defective structures.

Here, we overcome the inherent drawbacks of open-loop controlled colloidal particle assembly processes by demonstrating rapid assembly of perfect crystals with closed-loop ("feedback") control based on a microscopic dynamic model. Practically, the experiment involves compressing charged colloids within a quadrupolar electric field (Fig. 1). This is a self-assembly process in which a global thermodynamic variable (*i.e.*, electric field) changes the relative free energy of all configurations, causing particles to assemble *via* thermal motion to minimize their free energy. To enable feedback control, essential real-time capabilities require: (1) sensing the system state (*via* image analysis), (2) actuating particle interactions to navigate energy landscapes (*via* field mediated potentials), and (3) closing the loop to assign actuator settings based on sensor readings (*via* an optimal policy). This approach corrects defects in real-time to produce perfect crystals. While feedback control has been explored in microscopic systems including single particles,[188] colloidal assembly,[39] shear induced transitions,[189] nanostructure morphology,[190] and maximizing crystallinity,[191] none have produced perfect crystals using real-time defect correction.

Ultimately, this study is a proof-of-principle demonstration of controlling the navigation between two states in free energy space,[192] which we practically implement to create perfect 2D colloidal crystals. However, this approach could be used to navigate between any states including other colloidal microstructures (*e.g.*, gels, glasses, chains, clusters *etc*.) Because colloidal particles thermally sample different configurations *via* diffusion based on their relative free energies, and as such are often considered as models of atoms[193-195] (often in connection to the thermodynamics and kinetics of crystallization),[101,105,196-198] the physics underlying our approach is general across a range of length scales including molecular and nano- scales. As such, if correctly adapted (including appropriate methods to tune interactions[176-180] and to sense states, *e.g.*, *via* diffraction,[199,200] optical Fourier transforms,[201] super-resolution microscopy,[202,203] liquid cell electron microscopy[204]), the approach outlined in this work could be used to control states in systems of atoms, molecules, macromolecules, and nanoparticles. In addition to enabling the assembly of static, equilibrium target states, the ability to actively control particle ensembles between different non-equilibrium states could enable reconfigurable metamaterials (*i.e.*, metadevices).[205]

8.3 Methods

Sample preparation. Coplanar quadrupole Au thin film electrodes were patterned on glass microscope coverslips that were sonicated in acetone for 30 min, sonicated in isopropanol (IPA) for 30 min, rinsed with deionized (DI) water, soaked in Nochromix (Godax) for 1 h, rinsed with DI water, sonicated in 0.1 M KOH for 30 min, rinsed with DI water, and dried with N_2. The electrodes were fabricated by spin coating photoresist (S1813, Shipley) onto microscope cover slips, UV exposure through a chrome photomask, and physical vapor deposition of a 15 nm chromium adhesive layer and a 35 nm gold layer. The photoresist liftoff was accomplished with agitation in 1165 Remover (Shipley). The electrode tips are separated by ~100 μm. Prior to experimentation, the coverslips with patterned quadrupole electrodes were sonicated in IPA for 30 min, acetone for 30 min, IPA for 30 min, rinsed in DI water, then suspended in Nochromix for 20 min, rinsed with DI water, and dried with N_2.

Experiments were performed in batch cells consisting of Viton O-rings. To construct batch cells, O-rings were coated with vacuum grease and sealed between the coverslip with the electrode and a glass coverslip. 100 μL of the colloidal particle dispersion was dispensed into the batch cell and allowed to sediment for 5 min prior to sealing with a coverslip to obtain approximately 300 particles in the quadrupole. 22 gauge copper wires were attached to the electrode using conductive carbon tape. The electrode was then connected in series with a function generator (Agilent 33220a) with one lead attached to the north-south poles and another to the east-west poles.

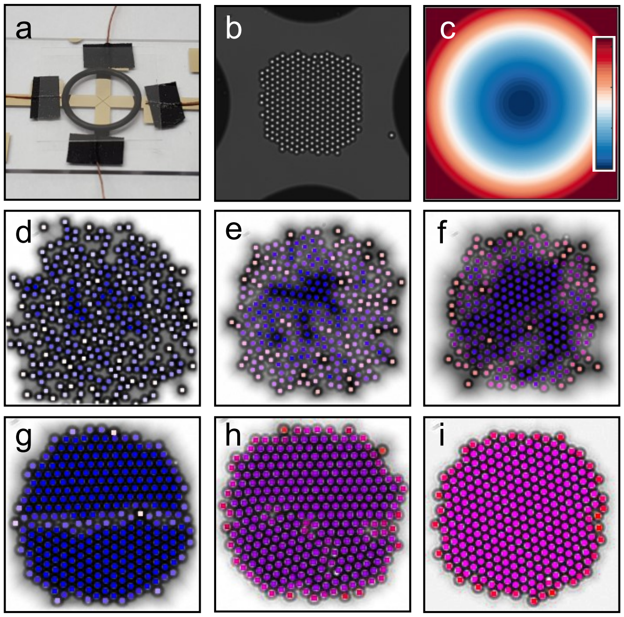

Figure 1 | Quasi-2D colloidal crystal assembly in electric fields. (**a**) Microfabricated quadrupole electrode. (**b**) Optical microscopy image of particles within quadrupole. (**c**) Single particle-field potential (blue-red scale: 0-100 *kT*). Images of 300 particles with centers colored to visualize reaction coordinates for local hexagonal order, **C_6**, and global hexagonal order, ψ_6, at electric field amplitudes of λ = (**d**) 0.2, (**e**) 0.9, (**f**) 2.0, and (**g, h, i**) 19.7. Representative microstructures include bicrystals with (**g**) large grain boundary (similar sized domains near max misorientation angle), (**h**) small grain boundary (dissimilar sized domains with smaller misorientation angle), (**i**) no grain boundary *i.e.*, perfect crystal. 2.8 μm particles provide internal scale bar.

Microscopy. Microscopy was performed on an inverted optical microscope with a 63× Zeiss air objective lens (0.6 numerical aperture) at 1.25 magnification. A 12-bit CCD camera captured 336 pixel × 256 pixel (104 μm × 79 μm) digital images at rate of 10 frames/s. Image capture and analysis were performed using MATLAB Image Processing and Image Acquisition Toolboxes. Image analysis algorithms coded in MATLAB were used to simultaneously locate and track particle centers, as well as, compute local and global order parameters in real time,[39] Experimental values of ψ_6 and C_6 were normalized by constants $\psi_{6,\max} = 0.8$ and $C_{6,\max} = 0.95$ to account for particle tracking errors.

Feedback Control. The electric field amplitude and frequency were controlled *via* the function generator using a device driver written in the MATLAB Instrument Control Toolbox. A sinusoidal voltage with a 1 MHz frequency was varied between $\lambda = 0.2$, 0.9, 2.0, and 19.7 for controlled cycles and held at a constant $\lambda = 19.7$ for uncontrolled cycles. The value of λ is related to the electric field and peak to peak voltage as,

$$\begin{aligned} \lambda &= \pi\varepsilon_{\mathrm{m}} a^3 \left(f_{\mathrm{CM}} E_0\right)^2 / kT \\ E_0 &= 8^{-0.5} V_{\mathrm{pp}} / d_{\mathrm{g}} \end{aligned} \tag{8.1}$$

where λ has the same definition as the main manuscript, d_{g} is the electrode gap, and V_{pp} is the peak-to-peak voltage set in the function generator. For $d_{\mathrm{g}} = 100$ μm in this and previous work, the value of V_{pp} at which all particles crystallize in a system of N particles was determined to be,

$$\begin{aligned} V_{pp} &= a_0 N^{-b_0} \\ a_0 &= 7.15 + 4.10 \cdot 10^{-3} \kappa^{-1} \\ b_0 &= 0.219 + 4.24 \cdot 10^{-4} \kappa^{-1} \end{aligned} \tag{8.2}$$

where κ^{-1} is the Debye length. Values of V_{pp} and λ used in this work are reported in

Supplementary Table 1.

Several properties could change in the course of a ~31 hour experiment, such as particle stability, solvent conditions, and evaporation, *etc*. However, there is no evidence that any of these factors changed the experimental conditions by plotting any measured quantity vs. time. This is shown by the fact that the probability that an uncontrolled cycle would form a perfect crystal remains for all practical purposes constant for the experiment duration.

The radius of gyration, R_g, was used to measure the degree of melting between individual cycles. After a perfect crystal was obtained or 1000s had elapsed, the system was melted at $\lambda = 0.2$ until $R_g = 25.5\mu\text{m}$, at which point the next crystallization cycle was started. R_g is given by,

$$R_g = 0.5N^{-1}\left[\sum \left|r_i - r_j\right|^2\right]^{0.5} \Big/ R_{g,HEX} \tag{8.3}$$

where $R_{g,HEX}$ is the radius of gyration for two dimensional hexagonally close packed particles with regular polygon morphologies given by,

$$R_{g,HEX} = 5^{0.5}3^{-1}aN^{0.5} \tag{8.4}$$

Reaction Coordinates: Reaction coordinates are computed for different system sizes to include edge effects. The global six-fold bond orientational order, ψ_6, is given by,[43,44,117]

$$\psi_6 = \left|\frac{1}{N}\sum_{j=1}^{N}\psi_{6,j}\right| \tag{8.5}$$

where N is the total number of particles in the ensemble, and $\psi_{6,j}$ is the local six-fold bond orientation order of particle j given as,

$$\psi_{6,j} = \frac{1}{N_{C,j}}\sum_{k=1}^{N_{C,j}} e^{i6\theta_{jk}} \tag{8.6}$$

where $N_{C,j}$ is the number of neighbors within the first $g(r)$ peak (coordination radius) of particle j, and θ_{jk} is the angle between particle j and each neighboring particle k with an arbitrary reference direction. Connectivity between crystalline particles, $\chi_{6,jk}$, is given by,

$$\chi_{6,jk} = \frac{\left|\mathrm{Re}\left[\psi_{6,j}\psi_{6,k}^{*}\right]\right|}{\left|\psi_{6,j}\psi_{6,k}^{*}\right|} \tag{8.7}$$

where $\psi^{*}_{6,j}$ is the complex conjugate of $\psi_{6,j}$. This is used to compute the local order parameter for six-fold connectivity, $C_{6,j}$, which produces integer values between zero and six. The number of crystalline nearest neighbors, $C_{6,j}$, for particle j is determined using the criterion,[135]

$$C_{6,j} = \sum_{k=1}^{N_{C,j}} \left[\begin{vmatrix} 1 & \chi_{6,jk} \geq 0.32 \\ 0 & \chi_{6,jk} < 0.32 \end{vmatrix}\right] \tag{8.8}$$

$$C_6 = \frac{1}{N}\sum_{i=1}^{N} C_{6,i} \Big/ \left\langle C_6 \right\rangle_{HEX} \tag{8.9}$$

where C_6 is the average normalized local six-fold connectivity, normalized by $\langle C_6 \rangle_{HEX}$, the C_6 value for 2D hexagonal close packed particles with a hexagonal morphology given by,[39]

$$\left\langle C_6 \right\rangle_{HEX} = N^{-1} 6\left(3S^2 + S\right) \tag{8.10}$$

$$S = -\left(1/2\right) + \left[\left(1/3\right)\left(N-1\right) + \left(1/4\right)\right]^{1/2} \tag{8.11}$$

Markov State Model Construction: A Markov state model (MSM)[206] is characterized by a set of discretized states S, and a probability transition matrix $P(\lambda)$ for each input λ. $P(\lambda)$ is composed of transition probability $P(\lambda)_{ij}$, which denotes the probability of the system to be in state j, after a transition time of Δt, given the current state as i, under an input λ. The state space is defined by the reaction coordinates (ψ_6, C_6). The discretization is fine enough to distinguish configurations that lead to different dynamics, but not too fine to lead to sampling issues in building the transition matrix and computational issues in solving for the control policy.[207] We discretized the reaction coordinate ψ_6 into 50 intervals and C_6 into 120 intervals after trial-and-error inspection. A total of 6000 discrete states were defined.

We generated sample data from the BD simulations to build four MSM for each of our four input levels: $\lambda = 0.2, 0.9, 2.0, 19.7$. For each model, BD simulations are initialized in different discrete states to cover a commonly visited region of the state space. The simulations were repeated to ensure the important states have enough samples to account for stochastic effects. Simulations were conducted under both constant and time-varying inputs to enrich sampling, with voltage switching at intervals of $\Delta t = 100$ s, corresponding to the transition time used in the MSM. To preserve the Markovity of the system, a large transition time Δt is desired for better accuracy,[207-209] but at the cost of intermediate information loss. After an investigation over a range of transition times on the model accuracy, the transition time $\Delta t = 100$s was chosen to balance the MSM accuracy with the ability to actuate at useful time intervals (see main text for discussion of inherent system response time).

Markov Decision Process Based Optimal Control Policy Calculation: A Markov decision process (MDP) is composed of a MSM, a set t of discrete time epoch i, and a set A of discrete actions λ.[210,211] If t is a finite set, the MDP is called finite-horizon MDP, and it is called infinite-horizon MDP if t is an infinite set. An optimal control policy associated with an infinite-horizon MDP is a time-independent policy, *i.e.*, the control policy is stationary at each update interval. Considering the convenience in practical use as well as its ability for visualization and understanding, we investigated the infinite-horizon MDP based optimization problem to solve for a stationary optimal control policy. In the infinite-horizon MDP, the optimization is achieved over an infinite number of time steps, i, and the objective function is defined as,

$$J^{\pi}(\mathbf{x}) = X\left\{\sum_{i=0}^{\infty}\gamma^{i}R(\mathbf{x}_{i},\lambda_{i})\right\} \tag{8.12}$$

where X is the expectation operator, $\pi : S \rightarrow A$, is a feasible policy composed of control actions $\lambda_i \in A$, $\boldsymbol{x}_i \in S$ is the discrete state, i is the discrete time instant, and $\gamma \in (0,1)$ is the discount factor introduced to ensure the convergence to optimality in dynamic programming. $R(\mathbf{x}_i, \lambda_i) : S \times A \rightarrow \mathbf{R}$ is the one-stage reward function obtained when the system is in state $\mathbf{x}$, and a control action λ is taken. The optimal value function J^* and the optimal policy π^* are defined in Equation (13), where "sup" indicates the supremum, and Π^s is the set of all feasible control policies,

$$\begin{aligned} J^{*}(\mathbf{x}) &= \sup_{\pi\in\Pi^{s}} J^{\pi}(\mathbf{x}) \\ \pi^{*}(\mathbf{x}) &= \arg\left\{\sup_{\pi\in\Pi^{s}} J^{\pi}(\mathbf{x})\right\} = \arg J^{*}(\mathbf{x}) \end{aligned} \tag{8.13}$$

In our particular calculation, the one-stage reward function is defined as $R(\mathbf{x}_i, \lambda_i) = \psi_6^2$, with a discount factor of $\gamma = 0.99$. With a discount factor so close to 1, the future values of the reward are nearly as important as the initial reward, over the ten control intervals considered here. The objective function was selected to achieve the highest possible ψ_6 value, which corresponds to a highly ordered, single domain crystalline state of the system. C_6 is not included explicitly in the objective function, but a high ψ_6 value state automatically requires a high C_6 value due to physical constraints. The optimal control policy was solved with dynamic programming in the MDP framework, using a policy iteration algorithm embedded in the MDP Toolbox from MATLAB central distribution.[212]

8.4 Results and discussion

8.4.1 Stochastic polycrystal assembly

Assembly is performed with 300 SiO_2 colloids (radius, a = 1.4 μm) confined by gravity into a quasi-2D layer within a quadrupole electrode (Fig. 1a, see *Methods* & *Supplementary Information* (*SI*)). A function generator controls the amplitude of a 1 MHz AC field, which determines the degree of localization of colloids at the field minimum in the quadrupole center (Figs. 1b). The dipole-field potential characterizing the potential energy associated with confining particles is (Fig. 1c),[114]

$$u(\mathbf{r}) = -\lambda f_{\mathrm{CM}}^{-1}\left[E(\mathbf{r})/E_0\right]^2 \qquad (8.14)$$

where $\lambda = \pi_m a^3 (f_{CM} E_0)^2/kT$ characterizes how strongly the radially varying field, $E(r)/E_0$, confines particles relative to thermal energy, kT, and f_{CM} depends on the particle, ε_p, and medium, ε_m, dielectric properties (see *Methods* & *SI*).[213] A balance of the field confinement against the quasi-2D dispersion osmotic pressure determines, for a given particle number, whether a fluid or solid phase will form *versus* λ (Fig. 1d-i).[112] As system size increases, polycrystallinity (*i.e.*, misoriented crystal domains with grain boundaries, Fig. 1g,h) becomes increasingly prevalent; this is the defect we aim to repair *via* feedback control.

To develop a sensor and model for grain boundary formation and motion, we employ a reaction coordinate based dynamic model.[214] Two reaction coordinates are necessary to quantify polycrystallinity: the degrees of global order, ψ_6, and local order, C_6. Values of ψ_6 and C_6 are computed in real-time from particle centers obtained *via* microscopy and image analysis (see *Methods* & *SI*). To briefly describe how reaction coordinates capture different states, $\psi_6 \approx 0$ for amorphous states (Fig. 1d) and polycrystals (Fig. 1g), whereas $\psi_6 \approx 1$ for perfect crystals (Fig. 1h). C_6 captures emergence of crystallinity during condensation and distinguishes amorphous (low C_6) and polycrystalline (high C_6) states (that both have $\psi_6 \approx 0$).

8.4.2 Polycrystallinity versus uncontrolled ramp rate

We illustrate the need for feedback control by first showing examples without feedback control that demonstrate the trade-off between generating perfect crystals *via* slow, near-equilibrium ramps *versus* polycrystals *via* ramps too fast for relaxation into single crystals (Fig. 2). Assembly trajectories are reported for *N*=300 particles in Brownian Dynamic (BD) simulations matched to experiments[214] for several orders of magnitude in field ramp time. Non-equilibrium ψ_6 and C_6 trajectories averaged over 100 simulations for ramp times of 0, 1×10^3, 2×10^3, 5×10^3, and 10^4 s are shown alongside equilibrium ψ_6 (*i.e.*, free energy minima values at each λ, see *SI*). As expected, local ordering always precedes global ordering. The key result is that a > 10^4 s ramp is required to achieve 100% perfect crystals in the near-equilibrium limit (*i.e.*, ramped ψ_6 passes through equilibrium ψ_6 values at long times). Faster ramps produce non-equilibrium polycrystals that do not relax to single crystals in the allotted times.

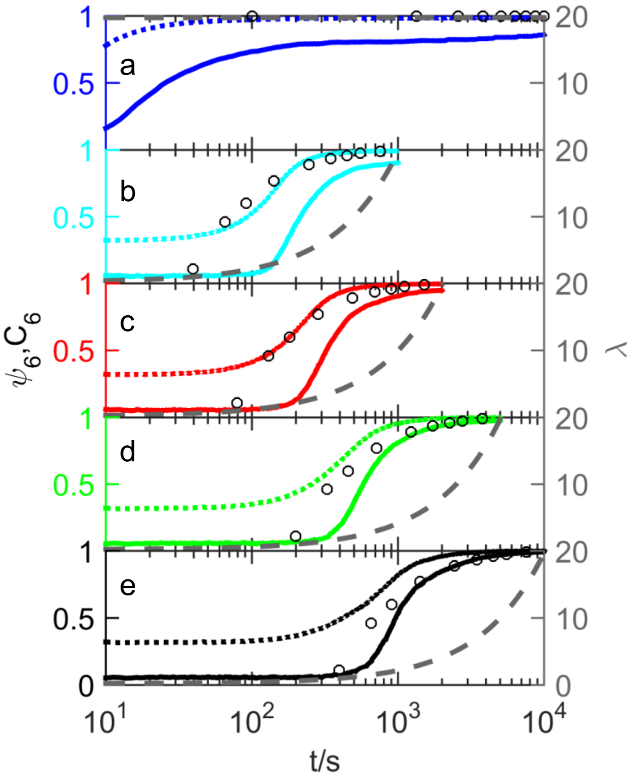

Figure 2 | Ramping electric field at different rates without feedback control to understand effect of quench-rate on crystal assembly. Electric field amplitude, λ (long-dash gray), ramped from 0.2 to 19.7 over (**a**) 0 s (blue), (**b**) 1x10^3 s (cyan), (**c**) 2x10^3 s (red), (**d**) 5x10^3 s (green), and (**e**) 10^4 s (black). Local order, C_6 (dotted lines), emerges before global order, ψ_6 (solid lines). Equilibrium ψ_6 values (open circles) vs. λ approach ψ_6 ramp trajectories only for 10^4 s ramp.

8.4.3 Feedback controlled navigation of energy landscapes

The (ψ_6, C_6) coordinates quantitatively capture non-equilibrium stochastic trajectories between states, which provides a dynamic model to *close the loop* between *sensing* (determining the current state) and *actuation* (specifying λ to achieve a new state). A (ψ_6, C_6) based model quantifies field mediated crystallization dynamics *via* a Smoluchowski equation given as,[214]

$$\frac{\partial p(\mathbf{x},\lambda,t)}{\partial t} = \nabla \cdot \mathbf{D}(\mathbf{x},\lambda) \cdot \left[\nabla + \frac{1}{kT} \nabla W(\mathbf{x},\lambda) \right] p(\mathbf{x},\lambda,t) \tag{8.15}$$

where p is probability, $\mathbf{x} = (\psi_6, C_6)$, $\mathbf{D}$ is a diffusivity landscape, and W is a free energy landscape. The dynamic model encapsulated in Eq. (6.1) enables formulating an optimal control scheme based on free energy gradients in W and hydrodynamic mediated friction in $\mathbf{D}$.[214]

Controlling crystallization is conceptually the navigation of free energy landscapes, W, at each electric field amplitude, λ (Fig. 3a). The equilibrium ramp (Fig. 2e) corresponds to slowly increasing $\lambda(t)$ so the configuration resides near the free energy minimum on each W. Faster ramps (Fig. 2a-d) in $\lambda(t)$ cause sampling of non-equilibrium polycrystalline states on each W where vanishing gradients provide minimal driving force for relaxation.[214] The more sophisticated approach here is to determine the optimal $\lambda(t)$ based on current (ψ_6, C_6) coordinates to maximize the probability of moving from the initial fluid to the perfect crystal. Because the particle and grain boundary motion are stochastic, each process is unique, so no one $\lambda(t)$ is best every time; instead closed-loop control is required to obtain the optimal actuation.

To determine how to change the electric field *versus* time (*i.e.*, $\lambda(t)$) to best navigate the free energy landscapes, W, we use a Markov decision process based policy using dynamic programming.[210] This framework requires a discretized version of Eq. (6.1), known as a Markov state model,[206] which consists of a "probability transition matrix" to quantify the transition probability between all states during a time step, Δt, at each λ. The resulting policy, π, provides a mapping from the current measured state, $\mathbf{x}$, to the next action, λ, to be taken. Mathematically, $\lambda_{i+1} = \pi(\mathbf{x}_i)$, where i is the time step. The optimal policy at each state $\mathbf{x}$ maximizes the objective function J^{π},[215]

$$J^{\pi}(\mathbf{x}) = X\left\{\sum_{i=0}^{\infty}\gamma^{i}R(\mathbf{x}_{i},\lambda_{i})\right\} \tag{8.16}$$

where X is the expectation operator and $R(\mathbf{x}_i, \lambda_i)$ is the reward function at time step i. In this work $R = \psi_6^2$, such that a high global crystallinity is "rewarded." The discount factor γ ensures convergence of the policy calculation, and here is set to 0.99 (see *Methods* for details). The Markov decision process calculation provides the optimal policy (Fig. 3b) in the form of a look-up table, indicating the λ to use when assembly trajectories pass through each (ψ_6, C_6) coordinate.

A typical single experimental trajectory (Fig. 3a,b) illustrates how the control policy is implemented. Practically, the feedback control is achieved in real-time *via* the followings steps: (1) image analysis is used to locate particle centers and compute updated (ψ_6, C_6) coordinates every 100 ms, which are plotted as trajectories on the W at each λ (Fig. 3a); (2) the current values of the (ψ_6, C_6) coordinates are found in the optimal control policy look-up table (Fig. 3b); and (3) the new value of the quadrupole voltage (λ) found in the look-up table is updated every 100 s, which is shown by the trajectories jumping between the W in Fig. 3a every time the λ value is changed. The policy update time of Δt = 100 s was determined by considering actuation times comparable to the inherent system response time.

The policy update time and inherent system response time depends on the cooperative short-range motion of particles necessary for grain boundary motion,[216,217] which can be estimated from the long time self-diffusivity as, $D_S^L = D_S^S[1+2\phi g(2a)]^{-1}$, where D_S^S is the short time self-diffusivity, ϕ is the particle area fraction, and $g(2a)$ is the radial distribution function contact value within the quasi-2D colloidal monolayer.[129]

Using D_S^S =0.5D_0 (D_0 is the Stokes-Einstein value) to account for particle-wall hydrodynamics,[146] and the hard disk fluid radial distribution function for g(2a),[218] the time for particles to diffuse over a distance comparable to their own radius is, $\tau = a^2/D_S^L \approx 100$s at low concentrations. By considering how the soft electrostatic repulsion between particles significantly decrease g(2a),[129] D_S^L becomes a weak function of ϕ, and as such, $\tau \approx 100$s captures the characteristic structure relaxation time scale for all configurations and λ. Estimating D_S^L based on dense fluid properties can be rationalized since motion within grain boundaries has been compared to concentrated melt dynamics.[105,219,220] In addition, the different λ values in conjunction with the inhomogeneous field cause the dynamics to vary significantly from the concentrated interior of the particle ensemble to the vanishing density at its periphery.[112] Practically, the 100s update time worked better than faster or slower times, consistent with the above analysis.

Movies (Movie S1) and images of particle configurations (Figs. 3c-h) at start, end, and policy update points (Fig 3b) show the policy uses: (1) the highest field (λ = 19.7) for rapid initial assembly and to quench the final perfect crystal, (2) the lowest field (λ = 0.2) to partially disassemble large grain boundaries, and (3) intermediate field amplitudes (λ = 0.9, λ = 2.0) to assist relaxation of smaller grain boundaries. The control policy at most times drives rapid assembly at the highest field setting and is only reduced occasionally to eliminate defects without completely disassembling structures and restarting assembly.

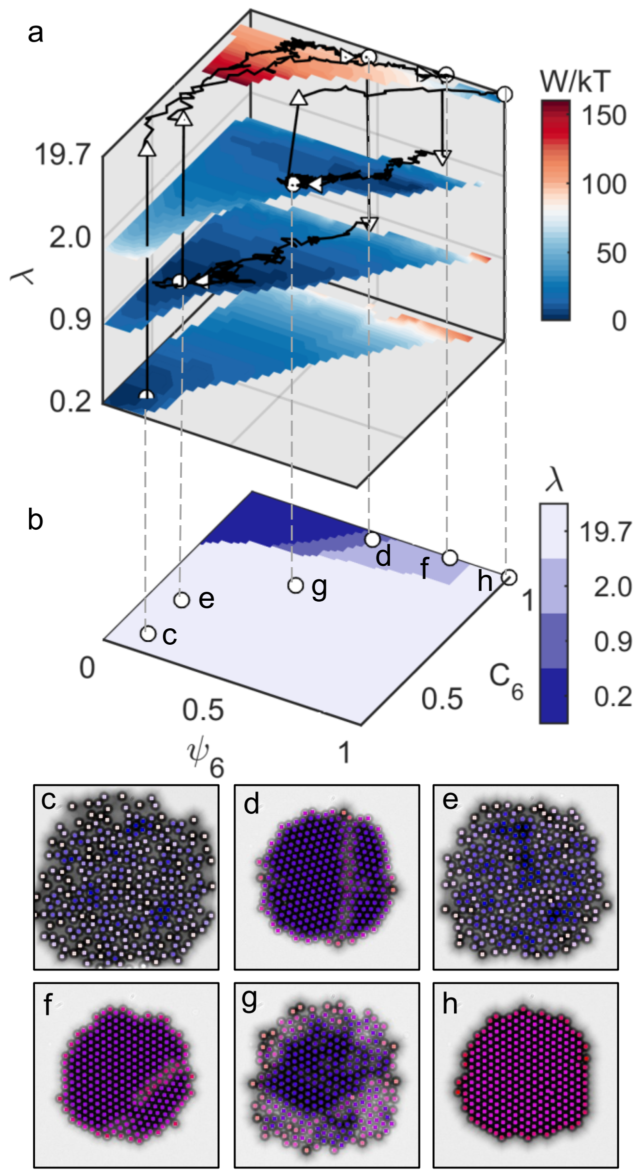

Figure 3 | Assembly trajectory on energy landscapes under control (see Movie S1). (**a**) Free energy landscapes of 300 particles at the four λ's in policy. Example trajectory (black) with coordinates on policy (b) and corresponding images (c-h). (**b**) Optimal policy calculated using Markov decision process. Images showing representative configurations (same coloring scheme as Figs. 1d-i) at: (**c**) λ = 0.2 before compression, (**d**) first compression to λ = 19.7 with grain boundary, (**e**) relaxation at λ = 0.9, (**f**) re-compression at λ = 19.7 with new grain boundary, (**g**) relaxation at λ = 2.0, (**h**) perfect crystal at λ = 19.7.

8.4.4 Controlled versus uncontrolled assembly

Because colloidal assembly trajectories are stochastic, it is essential to collect sufficient statistics for a fair comparison of uncontrolled and controlled processes; to address this issue, 200 alternating uncontrolled and controlled cycles were obtained in a fully automated experiment over > 31 hr (see *Methods* & *SI*, Fig. 4). Each cycle used feedback control to: (1) ensure initial disassembly, (2) followed by either a step-quench without intervention or 100 s control updates, and (3) termination after either obtaining a perfect crystal or 10^3 s. The first 10 cycles illustrate several scenarios (Movie S2, Fig. 4a) including trajectories that: (1) quickly relax for small grain boundaries (#3, #7, #9); (2) slowly relax to form a perfect crystal < 1000 s (#1); (3) form metastable crystals that never relax (#5); (4) always form perfect crystals either without (#4, #10) or with (#2, #6, #8) several feedback corrections.

Analysis of all 200 ψ_6 *versus* time trajectories (Fig. 4b) and # of perfect crystals *versus* time (Fig. 4c) show key quantities to assess the controller's success at producing perfect crystals. A handful of perfect crystals form immediately during coalescence without grain boundaries (17 uncontrolled vs. 19 controlled) by bypassing slow grain boundary motion on free energy plateaus (W at $\lambda = 19.7$ in Fig. 3a).[214] The remaining ~160 trajectories illustrate how control removes grain boundaries by choosing lower λ. When removing small grain boundaries, perfect crystals are obtained in 100% (52/52) of trajectories after 1-2 corrective steps, whereas 78% (37/47) of small grain boundary bicrystals relax to perfect crystals without control. The ultimate test of the controller is for large grain boundaries; 93% (27/29) of controlled trajectories produce perfect crystals after 3-4 corrective steps vs. 18% (6/34) of uncontrolled processes. In the final accounting, controlled processes produced perfect crystals 98% of the time while uncontrolled processes were 60% successful.

8.5 Conclusions & outlook

Our results demonstrate optimal feedback control to robustly assemble perfect colloidal crystals orders of magnitude faster than a slow quasi-equilibrium ramp and much more reliably than rapid quenches. An optimal policy is computed with dynamic programming based on a low-dimensional reaction coordinate dynamic model. By tracking real-time stochastic particle configurations and employing the optimal policy to adjust

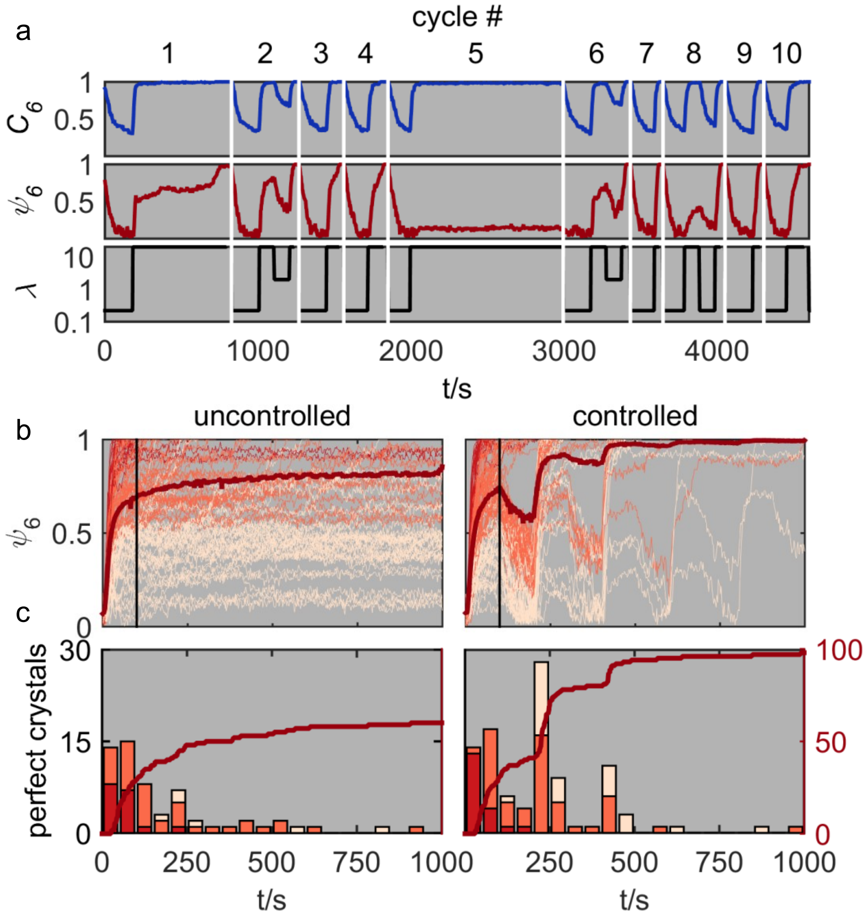

Figure 4 | Controlled vs. uncontrolled crystal assembly processes. 100 uncontrolled and 100 controlled trajectories shown as: (**a**) first 10 cycles with C_6 (blue), ψ_6 (red), λ (black) vs. time, (**b**) ψ_6 vs. time for 10^3 s for all experiments colored to indicate ensemble average (bold red), no grain boundary (red: $\psi_6 > 0.7$, $C_6 > 0.95$), small grain boundary (orange: $0.7 > \psi_6 > 0.4$, $C_6 > 0.95$), large grain boundary (peach: $0.4 > \psi_6$, $C_6 > 0.95$), (**c**) perfect crystals vs. time as cumulative number (dark red) and instantaneous number (bars) with same color scheme as (b).

applied electric fields *via* feedback, the evolution of unassembled particles is guided through polycrystal states into single domain crystals.

There are a number of ways this approach could be adapted and extended. For example, our approach could be implemented to constructively employ multiple complementary actuators (*e.g.*, magnetic fields to exert torques,[221] tunable depletion attraction to quench final states)[43] or be combined with other methods such as templated self-assembly (either unactuated[48,222] or actuatable[223]). Based on our prior work on nanoparticle assembly,[158] system size effects,[112] and three dimensional assembly in electric[138] and gravitational fields,[224] our approach can also be adapted to: (1) smaller nanoparticles (with different sensors; *e.g.*, attenuation based imaging,[158,224] scattering/diffraction),[199] (2) larger systems either through continuous processing (rather than batch processing; *e.g.*, a microfluidic device), parallelization (*e.g.*, electrode arrays),[225] or informing open-loop schemes (*e.g.*, toggling),[186] and (3) 3d crystals in thin films and possibly bulk crystals.

Further extensions of the methods and analyses developed in this work could be applied to other nano- and micro- scale processes involving: anisotropic particles or multi-component mixtures (with more states and bottlenecks), dynamical steady-states and out-of-equilibrium end points (where a Fokker-Planck equation describes the dynamics rather than a Smoluchowski equation), active micromachines and reconfigurable device elements (rather than static targets), and even synthetic materials systems that mimic basic control elements in biological systems (*e.g.*, chaperone control of protein folding and aggregation).[226] Our approach is based on first-principle concepts that are general to any molecular, nano-, or micro- scale assembly process where components thermally sample different configurations based on their relative free energies, states can be measured in real-time, an actuation mechanism exists to alter driving forces, and a dynamic model connects system responses to actuator settings.

8.6 Supplementary materials

Materials: Coplanar quadrupole Au thin film electrodes were patterned on glass microscope coverslips (Corning) that were sonicated in acetone for 30 min, sonicated in isopropanol (IPA) for 30 min, rinsed with deionized (DI) water, soaked in Nochromix (Godax) for 1 h, rinsed with DI water, sonicated in 0.1 M KOH for 30 min, rinsed with DI water, and dried with N_2. The electrodes were fabricated by spin coating photoresist (S1813, Shipley) onto microscope cover slips, UV exposure through a chrome photomask, and physical vapor deposition of a 15 nm chromium adhesive layer and a 35 nm gold layer. The photoresist liftoff was accomplished with agitation in 1165 Remover (Shipley). The electrode tips are separated by ~100 μm. Prior to experimentation, the coverslips with patterned quadrupole electrodes were sonicated in IPA for 30 min, acetone for 30 min, IPA for 30 min, rinsed in DI water, then suspended in Nochromix for 20 min, rinsed with DI water, and dried with N_2.

Quadrupole Electrode: Experiments were performed in batch cells consisting of Viton O-rings. To construct batch cells, O-rings were coated with vacuum grease (Dow Corning) and sealed between the coverslip with the electrode and a glass coverslip (Corning). 100 μL of the colloidal particle dispersion was dispensed into the batch cell and allowed to sediment for 5 min prior to sealing with a coverslip to obtain approximately 300 particles in the quadrupole. 22 gauge magnet wires were attached to the electrode using conductive carbon tape (Ted Pella). The electrode was then connected in series with a function generator (Agilent 33220a) with one lead attached to the north-south poles and another to the east-west poles.

Microscopy: Microscopy was performed on an inverted optical microscope (Axio Observer A1, Zeiss) with a 63× Zeiss air objective lens (0.6 numerical aperture) at 1.25 magnification. A 12-bit CCD camera (ORCA-ER, Hamamatsu) captured 336 pixel × 256 pixel (104 μm × 79 μm) digital images at rate of 10 frames/s. Image capture and analysis were performed using MATLAB Image Processing and Image Acquisition Toolboxes. Image analysis algorithms coded in MATLAB were used to simultaneously locate and track particle centers, as well as, compute local and global order parameters in real time.[39,111] Experimental values of ψ_6 and C_6 were normalized by constants $\psi_{6,\max} = 0.8$ and $C_{6,\max} = 0.95$ to account for particle tracking errors.

Feedback Control: The electric field amplitude and frequency were controlled via the function generator using a device driver written in the MATLAB Instrument Control Toolbox. A sinusoidal voltage with a 1 MHz frequency was varied between $\lambda = 0.2$, 0.9, 2.0, and 19.7 for controlled cycles and held at a constant $\lambda = 19.7$ for uncontrolled cycles. The value of λ is related to the electric field and peak to peak voltage as,

$$\begin{aligned} \lambda &= \pi \varepsilon_{\mathrm{m}} a^3 \left(f_{\mathrm{CM}} E_0 \right)^2 / kT \\ E_0 &= 8^{-0.5} V_{\mathrm{pp}} / d_{\mathrm{g}} \end{aligned} \tag{8.17}$$

where λ has the same definition as the main manuscript, d_{g} is the electrode gap, and V_{pp} is the peak-to-peak voltage set in the function generator. For $d_{\mathrm{g}} = 100$ μm in this and previous work, the value of V_{pp} at which all particles crystallize in a system of N particles was determined to be,

$$
\begin{aligned}
V_{pp} &= a_0 N^{-b_0} \\
a_0 &= 7.15 + 4.10 \cdot 10^{-3} \kappa^{-1} \\
b_0 &= 0.219 + 4.24 \cdot 10^{-4} \kappa^{-1}
\end{aligned}
\tag{8.18}
$$

where κ^{-1} is the Debye length. Values of V_{pp} and λ used in this work are reported in Supplementary Table 1.

Several properties could change in the course of a ~31 hour experiment, such as particle stability, solvent conditions, and evaporation, etc. However, there is no evidence that any of these factors changed the experimental conditions by plotting any measured quantity vs. time. This is shown by the fact that the probability that an uncontrolled cycle would form a perfect crystal remains for all practical purposes constant for the experiment duration.

Supplementary Table 1. Parameters for experiments and simulations. **a**. particle diameter,[137] **b**. Debye screening length, **c**. particle and wall Stern potential[137], **d**. applied peak-to-peak voltage, **e**. dimensionless electric field strengths used for policy control, **f**. Clausius-Mossotti factor for an AC field frequency at 1 MHz,[114] **g**. medium dielectric permittivity, **h**. electrode spacing.[138]

Variable	Theory/Simulation	Experiment
$2a$/nm[a]	2870	2870
T/K	293	293
κ^{-1}/nm[b]	10	10
ψ/mV[c]	-50.0	-50.0
V_{pp}/V[d]	0.2, 0.4, 0.6, 1.9	0.2, 0.4, 0.6, 1.9
λ[e]	0.2, 0.9, 2.0, 19.7	0.2, 0.9, 2.0, 19.7
f_{CM}[f]	-0.4667	-0.4667

ε_{m}[g]	78	78
d_g/μm[h]	96	96

The radius of gyration, R_g, was used to measure the degree of melting between individual cycles. After a perfect crystal was obtained or 1000s had elapsed, the system was melted at $\lambda = 0.2$ until $R_g = 25.5\mu\text{m}$, at which point the next crystallization cycle was started. R_g is given by,

$$R_g = 0.5N^{-1}\left[\sum \left|r_i - r_j\right|^2\right]^{0.5} \Big/ R_{g,HEX} \tag{8.19}$$

where $R_{g,HEX}$ is the radius of gyration for two dimensional hexagonally close packed particles with regular polygon morphologies given by,

$$R_{g,HEX} = 5^{0.5}3^{-1}aN^{0.5} \tag{8.20}$$

Reaction Coordinates: Reaction coordinates are computed for different system sizes to include edge effects. The global six-fold bond orientational order, ψ_6, is given by,[43,44,117]

$$\psi_6 = \left|\frac{1}{N}\sum_{j=1}^{N}\psi_{6,j}\right| \tag{8.21}$$

where N is the total number of particles in the ensemble, and $\psi_{6,j}$ is the local six-fold bond orientation order of particle j given as,

$$\psi_{6,j} = \frac{1}{N_{C,j}}\sum_{k=1}^{N_{C,j}} e^{i6\theta_{jk}} \tag{8.22}$$

where $N_{\mathrm{C,j}}$ is the number of neighbors within the first $g(r)$ peak (coordination radius) of particle j, and θ_{jk} is the angle between particle j and each neighboring particle k with an arbitrary reference direction. Connectivity between crystalline particles, $\chi_{6,\mathrm{jk}}$, is given by,

$$\chi_{6,jk} = \frac{\left|\mathrm{Re}\left[\psi_{6,j}\psi_{6,k}^{*}\right]\right|}{\left|\psi_{6,j}\psi_{6,k}^{*}\right|} \tag{8.23}$$

where $\psi^{*}_{6,j}$ is the complex conjugate of $\psi_{6,j}$. This is used to compute the local order parameter for six-fold connectivity, $C_{6,j}$, which produces integer values between zero and six. The number of crystalline nearest neighbors, $C_{6,j}$, for particle j is determined using the criterion,[135]

$$C_{6,j} = \sum_{k=1}^{N_{C,j}} \left[\begin{vmatrix} 1 & \chi_{6,jk} \geq 0.32 \\ 0 & \chi_{6,jk} < 0.32 \end{vmatrix}\right] \tag{8.24}$$

$$C_6 = \frac{1}{N}\sum_{i=1}^{N} C_{6,i} \Big/ \left\langle C_6 \right\rangle_{HEX} \tag{8.25}$$

where C_6 is the average normalized local six-fold connectivity, normalized by $\langle C_6\rangle_{\mathrm{HEX}}$, the C_6 value for 2D hexagonal close packed particles with a hexagonal morphology given by,[111]

$$\left\langle C_6 \right\rangle_{HEX} = N^{-1}6\left(3S^2 + S\right) \tag{8.26}$$

$$S = -(1/2) + \left[(1/3)(N-1) + (1/4)\right]^{1/2} \tag{8.27}$$

Brownian Dynamics Simulations: Brownian Dynamics (BD) simulations in the canonical ensemble were performed for 300 colloidal particles using numerical methods described in our previous papers.[122,128,129,131,227] A 0.1 ms time step was used for at least 2×10^7 steps, and reaction coordinates were stored every 1250 steps for subsequent analysis. Particles in simulations were confined within 2D planes. In the following sections, we provide additional details of the BD simulations, as well as, the models for the conservative forces based on potentials measured in our previous work.[113,114,136] All parameters used in the BD simulations are reported in Supplementary Table 1. The BD simulations were based on a Langevin equation as,

$$m\frac{d\mathbf{U}}{dt}=\mathbf{F}^{H}+\mathbf{F}^{P}+\mathbf{F}^{B} \tag{8.28}$$

where m is the particle buoyant mass, **U** is a velocity vector, and the force vector has three parts including dissipative hydrodynamic forces, $\mathbf{F}^{H}$, conservative forces due to potential fields, $\mathbf{F}^{P}$, and stochastic Brownian forces, $\mathbf{F}^{B}$. By letting $\mathbf{F}^{H}=-kT(\mathbf{D}^{-1})\cdot\mathbf{U}$, integrating Eq. (6.13) and using the mid-point algorithm, an equation of motion for particle displacements is obtained as,[139,140]

$$\mathbf{r}=\mathbf{r}^{0}+\left(\nabla\cdot\mathbf{D}^{0}\right)\Delta t+\left(kT\right)^{-1}\mathbf{D}^{0}\cdot\left(\mathbf{F}^{P,0}+\mathbf{F}^{B,0}\right)\Delta t \tag{8.29}$$

where the superscript "0" indicates quantities computed at the beginning of the time interval. Specific details of implementing Eq. (6.14) in dynamic simulations are described in previous publications.[128,129] The Brownian force $\mathbf{F}^{B}$ is characterized by a mean and variance given by,

$$\begin{gathered}\left\langle\mathbf{F}^{B}\right\rangle=\mathbf{0}\\ \left\langle\mathbf{F}^{B}(0)\mathbf{F}^{B}(t)\right\rangle=2\left(kT\right)^{2}\left(\mathbf{D}^{-1}\right)\delta(t)\end{gathered} \tag{8.30}$$

D in Eqs. (6.14) and (6.15) is a diffusivity tensor for finite numbers of particles above a no-slip plane computed using the methods of Brady and co-workers. **D** is related to the resistance tensor, **R**, through the generalized Stokes-Einstein relation, $\mathbf{D}=kT\mathbf{R}^{-1}$. Here **R** is computed to include hydrodynamic interactions, which are separated into far-field, multi-body, and near-field lubrication contributions as,[161]

$$\mathbf{R} = \left(\mathbf{M}^{\infty}\right)^{-1} + \mathbf{R}_{2B} - \mathbf{R}_{2B}^{\infty} \tag{8.31}$$

where $\mathbf{M}^{\infty}$ is the far-field mobility tensor constructed in a pairwise manner. The inverse of $\mathbf{M}^{\infty}$ is a true multi-body, far-field approximation to the resistance tensor. Lubrication is included by adding the exact two-body resistance tensor,[145,146,160] $\mathbf{R}_{2B}$, and subtracting the two-body, far-field resistance tensor, $\mathbf{R}_{2B}{}^{\infty}$, to avoid double counting. To specify an approximate configuration-dependent **D** to reduce computational cost, the diagonal elements of **D** (without cross terms) are parameterized in a look up table as a function of the ensemble R_{g} and the distance, R_{i}, of particle i from the configuration center of mass.

The interaction energy between colloids within the quadrupole electrode is modeled as the superposition of electrostatic double layer repulsion, dipole-field interactions, and dipole-dipole interactions. The net conservative forces, $\mathbf{F}^{P}$, in Eq. (6.14) are calculated based on the total conservative force acting on particle i as,

$$\mathbf{F}_{i}^{P} = -\nabla_{r_i}\left[u_{de,i}^{pf} + \sum_{j\neq i}\left(u_{e,i,j}^{pp} + u_{dd,i,j}^{pp}\right)\right] \tag{8.32}$$

where the electrostatic potential between particles i and j, $u^{\mathrm{pp}}_{\mathrm{e,i,j}}(\mathbf{r})$, is given by,[2]

$$u_{e,i,j}^{pp}\left(r_{ij}\right) = 32\pi\varepsilon_m a\left(\frac{kT}{e}\right)^{2}\tanh^{2}\left(\frac{e\psi}{4kT}\right)\exp\left[-\kappa\left(r_{ij}-2a\right)\right] \tag{8.33}$$

where r_{ij} is the particle center-to-center distance, e is the elemental charge, and ψ is the colloid surface potential. Dipole-field interactions can be described by,[113]

$$u_{de,i}^{pf}\left(\mathbf{r}_i\right) = -2kT\lambda f_{cm}^{-1}\left(\frac{E\left(\mathbf{r}_i\right)}{E_0}\right)^{2} \tag{8.34}$$

where $\mathbf{r}_i$ is the position of particle i relative to the center of the quadrupole electrode and $E(\mathbf{r}_i)$ is the electric field. Dipolar interactions between particles i and j are given by,[114]

$$u_{dd,i,j}^{pp}(\mathbf{r}) = -kT\lambda P_2\left(\cos\theta_{ij}\right)\left(\frac{2a}{r_{ij}}\right)^3\left(\frac{E(\mathbf{r}_i)}{E_0}\right)^2 \tag{8.35}$$

where $P_2(\cos\theta_{ij})$ is the second Legendre polynomial and θ_{ij} is the angle between the line that connects the two particle centers and the electric field. The quadrupole electric field is given by an approximate expression[228] corrected to fit numerical COMSOL results as,

$$\left|\frac{E(L)}{E_0}\right| = \frac{4L}{d_g}\begin{bmatrix} 2.081\times10^{-7}L^4 - 1.539\times10^{-9}L^3 + \\ 8.341\times10^{-5}L^2 + 1.961\times10^{-5}L + 1.028 \end{bmatrix} \tag{8.36}$$

where x and y are Cartesian coordinates with origin at the quadrupole center, and $L=(x^2+y^2)^{0.5}$.

Equilibrated ψ_6 values: Equilibrium ψ_6 values in Fig. 2 were obtained from BD simulations using the following procedure: (1) simulations at each λ were initiated from fluid-like configurations to construct free energy landscapes by fitting the Smoluchowski equation coefficients (described below), (2) equilibrated ψ_6 values at each λ were obtained as the global free energy minimum on each landscape.

Smoluchowski equation coefficients: Methods to fit the Smoluchowski equation coefficients are described in detail in our previous manuscripts.[120,122,131] Here we describe in brief the linear fitting method. The local drift and diffusion coefficients are obtained using,[121]

$$\mathbf{D}_i^{(1)}(\mathbf{x}) = \lim_{\tau\to0}\frac{1}{\tau}\left\langle \boldsymbol{\chi}_i(t+\tau) - \boldsymbol{\chi}_i(t)\right\rangle\Big|_{\boldsymbol{\chi}(t)=\mathbf{x}} = \frac{\partial\mu_i}{\partial t} \tag{8.37}$$

$$\mathbf{D}_{ij}^{(2)}(\mathbf{x}) = \lim_{\tau \to 0} \frac{1}{2\tau} \left\langle \left[\boldsymbol{\chi}_i(t+\tau) - \boldsymbol{\chi}_i(t) \right] \left[\boldsymbol{\chi}_j(t+\tau) - \boldsymbol{\chi}_j(t) \right] \right\rangle \Big|_{\boldsymbol{\chi}(t)=\mathbf{x}} = \frac{1}{2} \frac{\partial \sigma_{ij}^2}{\partial t}$$

(8.38)

where $\mathbf{D}^{(1)}$ is the drift vector field, $\mathbf{D}^{(2)}$ is the diffusivity tensor, $\boldsymbol{\chi}$ is a particular realization of **x**, the brackets represent an ensemble average, and the right hand side provides compact notation based on the definition of a derivative and traditional symbols of statistics (*i.e.*, mean, variance, covariance). The free energy landscape, $W(\mathbf{x})$, is obtained from $\mathbf{D}^{(1)}$ and $\mathbf{D}^{(2)}$ as,

$$\frac{W(\mathbf{x}_2) - W(\mathbf{x}_1)}{kT} = -\int_{\mathbf{x}_1}^{\mathbf{x}_2} (\mathbf{D}^{(2)})^{-1} \cdot (\mathbf{D}^{(1)} - \nabla \cdot \mathbf{D}^{(2)}) \tag{8.39}$$

Here, $\mathbf{x} = (\psi_6, C_6)$ trajectories for input into Eqs. (6.22) and (6.23) were generated from > 3000 simulations initiated from a library of experimental fluid and polycrystalline configurations. Trajectories were analyzed on (ψ_6, C_6) grid points with at least 4200 trajectories passing through each grid point. The resolution for the C_6 and ψ_6 coordinates were 0.025 and 0.025.

Markov State Model Construction: A Markov state model (MSM)[206] is characterized by a set of discretized states S, and a probability transition matrix $P(a)$ for each input a. $P(a)$ is composed of transition probability $P(a)_{ij}$, which denotes the probability of the system to be in state j, after a transition time of Δt, given the current state as i, under an input a. The state space is defined by the reaction coordinates (ψ_6, C_6). The discretization is fine enough to distinguish configurations that lead to different dynamics, but not too fine to lead to sampling issues in building the transition matrix and computational issues in solving for the control policy.[207] We discretized the reaction coordinate ψ_6 into 50 intervals and C_6

into 120 intervals after trial-and-error inspection. A total of 6000 discrete states were defined.

We generated sample data from the BD simulations to build four MSM for each of our four input levels: $\lambda = 0.2, 0.9, 2.0, 19.7$. For each model, BD simulations are initialized in different discrete states to cover a commonly visited region of the state space. The simulations were repeated to ensure the important states have enough samples to account for stochastic effects. Simulations were conducted under both constant and time-varying inputs to enrich sampling, with voltage switching at intervals of $\Delta t = 100$ s, corresponding to the transition time used in the MSM. To preserve the Markovity of the system, a large transition time Δt is desired for better accuracy,[207,209,229] but at the cost of intermediate information loss. After an investigation over a range of transition times on the model accuracy, the transition time $\Delta t = 100$s was chosen to balance the MSM accuracy with the ability to actuate at useful time intervals.

Markov Decision Process Based Optimal Control Policy Calculation: A Markov decision process (MDP) is composed of a MSM, a set τ of discrete time epoch i, and a set A of discrete actions, α.[210,211] If τ is a finite set, the MDP is called finite-horizon MDP, and it is called infinite-horizon MDP if τ is an infinite set. An optimal control policy associated with an infinite-horizon MDP is a time-independent policy, *i.e.*, the control policy is stationary at each update interval. Considering the convenience in practical use as well as its ability for visualization and understanding, we investigated the infinite-horizon MDP based optimization problem to solve for a stationary optimal control policy. In the infinite-horizon MDP, the optimization is achieved over an infinite number of time steps, i, and the objective function is defined as,

$$J(\mathbf{x}) = X\left\{\sum_{i=0}^{\infty} \gamma^i R(\mathbf{x}_i, \alpha_i)\right\} \tag{8.40}$$

where X is the expectation operator, $\alpha \in A$ is the control action, $\mathbf{x} \in S$ is the discrete state, $i \in \tau$ is the discrete time instant, and $\gamma \in (0,1)$ is the discount factor introduced to ensure the convergence of the optimality in dynamic programming. $R(\mathbf{x}, \alpha) : S \times A \rightarrow \mathbf{R}$ is the one-stage reward function obtained when the system is in state, $\mathbf{x}$, and a control action, α, is taken. The optimal value function and the optimal policy $\alpha^* \in A$ are defined as,

$$\begin{aligned} J^*(\mathbf{x}) &= \sup_{\alpha \in A} J(\mathbf{x}) \\ \alpha^*(\mathbf{x}) &= \arg\left\{\sup_{\alpha \in A} J(\mathbf{x})\right\} = \arg J^*(\mathbf{x}) \end{aligned} \tag{8.41}$$

In our particular calculation, the one-stage reward function is defined as $R(\mathbf{x}_i, \alpha_i) = \psi_6^2$, with a discount factor of $\gamma = 0.99$. With a discount factor so close to 1, the future values of the reward are nearly as important as the initial reward over the ten control intervals. The objective function was selected to achieve the highest possible ψ_6 value, which corresponds to a highly ordered, single domain crystalline state of the system. C_6 is not included explicitly in the objective function, but a high ψ_6 value state automatically requires a high C_6 value in that state due to physical constraints. The optimal control policy was solved with dynamic programming in the MDP framework, using a policy iteration algorithm embedded in the MDP Toolbox from MATLAB central distribution.[212]

9 CONTROLLED FINITE-SIZED COLLOIDAL CRYSTALLIZATION IN SEDIMENTATION WITH TUNABLE ATTRACTIONS

9.1 Abstract

We demonstrate a feedback control algorithm to control the growth of a colloidal crystal from a (100) template in a model sedimentation system with tunable, *kT*-scale depletion attractions. We first investigate the equilibrium sedimentation for a fixed number of particles at different amounts of attraction. A set of status parameters, crystallinity, $\langle C \rangle$ the number of crystalline layers, N_c, and layer-wise particle mobility L are developed to characterize the equilibrium and dynamical properties of the sedimentation process. A quench-relax cyclic feedback controller, with N_c and L as the 'detectors', and depletion attraction as the 'actuator', are then designed to detect and prevent/remove local defects and obtain a low-defect crystal in a batch-growth system. The controller efficiency at different quench depths is discussed.

9.2 Introduction

Colloidal crystallization can be viewed as one example of self-assembly in that individual colloidal particles spontaneously organize into ordered crystalline structures[230,231]. Even though the ordered crystalline state is the free energy global minimum, kinetic limitations, which manifest as point defects, grain boundaries, or far from equilibrium structures like glasses and gels, often frustrate the crystallization process. These kinetic traps arise due to strong thermodynamic driving forces (*e.g.,* fast condensation and strong particle attraction) that irreversibly quench the system into non-equilibrium structures. Since colloidal crystals with low defects are associated with many emerging technological areas, such as the photonics[232], a robust crystal growth method must be developed to achieve scalable manufacturing.

In colloidal systems, sedimentation serves as an extremely simple and widely used method to grow crystals[233]. Particles sedimenting due to gravity concentrate at lower elevations. This leads to a fluid-solid phase transition (*e.g.*, crystallization) as the pressure exceeds the freezing pressure of the colloidal spheres[234]. However, in a colloidal system undergoing sedimentation, metastable hexagonally-close-packed (HCP) structures typically form over more thermodynamically favorable, and thus, stable face-centered-cubic (FCC) crystals despite a 10^{-3} kT per particle free energy difference in these ordered structures[235], indicating a need to the control the microstructure that forms using this method. Even though the use of (110) templates can greatly reduce the formation of HCP structures[236], the crystal growth process is still highly uncontrollable in that there is no means of removing defects or dynamically arrested structures that form during the sedimentation process.

Recent advancements on tuning colloidal phase behavior *via* external fields[168], such as temperature[61,237,238] and electric[138,200,239] or magnetic fields[240], open up new possibilities for producing equilibrium colloidal structures. In these approaches to colloidal assembly, the evolution of the colloidal microstructure is governed by a thermodynamic driving force arising from either particle-field interactions or field mediated particle-particle interactions. In particular, we are interested in methods involving energy on the kT-scale. Weak colloidal interactions that fall on this thermal energy scale can be tuned to provide reversibility in colloidal assembly for structural defect removal[231]. For example, reversible colloidal melting and crystallization in a colloid-polymer binary system has been realized by temperature controlled colloidal particle attraction[61]. Other fields, such as electric[239] and magnetic fields[240], can serve as immediate actuators in ordered colloidal systems to tune particle interactions and control particle microstructures. The principles governing these tunable and controllable colloidal self-assembly processes can be applied to control colloidal crystallization *via* sedimentation—through tunable inter-particle attraction, the freezing pressure of colloidal spheres can be tuned to control phase transitions near the fluid-solid interface.

Beyond simply initiating the self-assembly process at fixed external field conditions and waiting for equilibrium, the kinetics can be optimized by tuning external fields as a function of time to further improve colloidal crystallization[16,17]. At different stages of a self-assembly process, the thermodynamic driving force may need to be increased to aid the system in overcoming energy barriers (*e.g.,* nucleation) or be delicately tuned to circumvent kinetic traps or remove undesired structures. To achieve an effective control strategy, there are several requirements: 1) some order parameters/state variables that distinguish the structural (*e.g.,* fluid or solid) and kinetic (*e.g.,* arrested or not) features of the particle configuration; 2) a model parameterized by order parameters/state variables to describe the response of the system to the varying external fields. 3) a controller integrating the order parameters/state variables as sensors, tunable external fields as actuators and the model as the 'roadmap' to actuate the system towards the targeted state. Recently, we have successfully applied such a control scheme to control the microstructure and morphology of a quasi-two dimensional (2D) colloidal cluster assembled *via* electric field mediated interactions[73,111]. However, the extension of this control scheme to scalable

2D/three dimensional (3D) crystal growth is not readily available for several reasons: First, the previous actuators[73,111] (*i.e.,* microelectrodes) are spatially fixed and thus limit the size of crystal that can be grown. Second, a 3D system generally has more kinetic barriers and traps compared to 2D system, and a new controller with the capability to detect and repair defects is needed.

In this work, we study the control of 3D colloidal crystal growth in a sedimentation system with tunable pair attraction using computer simulations. As a proof of concept, we limit our problem to a system of finite size and one dimensional (1D) growth. Despite the simplicity, it contains the essential issues we need to address in scalable, controlled growth. The manuscript is organized as follows: We first explore the equilibrium and dynamic properties of a finite-sized sedimentation system and identify order parameters/state variables to characterize the structural and kinetic features of the system with different amounts of depletion attraction. We then integrate these quantities into the design of a feedback controller. The success and efficiency of the controller is examined and discussed by applying the control scheme to 3D crystal growth from an initial fluid configuration. Finally, we discuss how to extend this controller to continuous 1D growth.

9.3 Equilibrium sedimentation model

9.3.1 Interaction potentials and Brownian dynamics (bd) simulation

We consider a sedimentation experiment carried out with an (100) FCC template at the bottom of a container. The net potential energy, $U_i(\mathbf{r}_i)$, for a colloidal particle i includes the sum of pairwise colloidal potentials, $u_{pp}(r)$, and external gravitational potential contributions, $\phi(z)$, given as,

$$U_i(\mathbf{r}_i)=\sum_{i\neq j}u_{pp,ij}(r)+Gz_i \tag{9.1}$$

where $\mathbf{r}_i$ is the position vector of particle i, r is the center-to-center separation between particles, G is the particle buoyant weight, and z_i is the center-to-wall surface separation for particle i. The particle-template interaction is modeled as particle interacting with each particle composing the template. The particle pair interactions contain double layer electrostatic repulsion[241] and a tunable deletion attraction[237], given by,

$$\begin{aligned} u_{pp}(r)&=B_{pp}\exp\left[-\kappa(r-2a)\right]+\Pi\Delta V \\ \Delta V&=\pi\left(\frac{4}{3}(a+L)^3\left(1-\frac{3}{4}\frac{r}{a+L}+\frac{1}{16}\left(\frac{r}{a+L}\right)^3\right)\right) \end{aligned} \tag{9.2}$$

where $2a$=2000 nm is the diameter of the particle, B_{pp}= 2297.4kT, κ^{-1}=10 nm is the Debye length, and $2L$=200 nm is the depletant diameter. The depletion attraction is written as the product of osmotic pressure,Π, and excluded volume, ΔV. In simulations, the depletion attraction is tuned by simply changing the Π term.

The equation of motion in BD simulations is given as,

$$\mathbf{r}_i(t+\Delta t)=\mathbf{r}_i(t)+\frac{D}{kT}(-\nabla_{r_i}U_i)\Delta t+\Delta\mathbf{r}_i^B \tag{9.3}$$

where t is time, Δt is the integration time, k is the Boltzmann's constant, T is the temperature, and D is the Stokes-Einstein diffusivity. The Brownian displacement vector obeys $\langle\Delta\mathbf{r}_i^B\rangle=0,\langle\Delta\mathbf{r}_i^B\Delta\mathbf{r}_i^B\rangle=2D\mathbf{I}\Delta t$, where $\mathbf{I}$ is the unit tensor.

9.3.2 Colloidal sedimentation equilibrium

At isothermal sedimentation equilibrium, the balance of pressure and gravitation force leads to,

$$\frac{\partial P(z)}{\partial z} = -G\rho\left(z\right) \tag{9.4}$$

where P(z) is the pressure at elevation z and $\rho(z)$ is the colloidal density profile in the z direction. The macroscopic balance equation will generally hold for length scales larger than radius a^{94}. It can also be written in terms of the 'local' volume fraction *via* ϕ(z)=$V_p\rho$(z), where V_p=4/3πa^3 is the volume of the particle, as

$$\frac{\partial P(z)}{\partial z} = -\frac{G}{V_p}\phi\left(z\right) \tag{9.5}$$

The integral form of Eq. **Error! Reference source not found.** is

$$P(z) = \int_z^{\infty} \frac{G}{V_p}\phi\left(z'\right)dz' \tag{9.6}$$

which indicates that, at equilibrium, the pressure at height z is equal to the bearing weight above z.

9.3.3 Sediment structure order parameters

The order parameter, R_z, as a condensation metric is defined as the mean value of the elevation of all particles, given by,

$$R_z = \frac{1}{N}\sum_i^N z_i \tag{9.7}$$

where N is the total number of particles in the system, z_i is the elevation of particle i.

A layer-based four-fold bond orientation order for particle i is obtained *via*

$$\psi_{4,i} = \left| \frac{1}{N_{b,i}} \sum_{j}^{N_{b,i}} \exp(4\theta_{ij}\sqrt{-1}) \right|, d_{ij} < d_c, \left| z_i - z_j \right| \le h_c \tag{9.8}$$

where $N_{b,j}$ is the number of neighbors for particle i within a 2D projected coordination radius d_c=2.3a. h_c=0.5 is vertical distance criterion for particles i and j in the same layer. θ_{ij} is the 2D projected orientation angle of the bond joining particles i and j. d_{ij} is the 2D projected distance between particles i and j.

The crystallinity of the system can be then calculated as

$$\langle C \rangle = \sum_{i=1}^{N} C_i \Big/ N \tag{9.9}$$

where C_i=1 if particle i has four neighbors in the same layer and $\psi_{4,i}$>0.95 and otherwise C_i=0.

The number of crystalline layers, N_c, is also an order parameter of interest since the crystal grows in a layer-by-layer manner in the sedimentation model. A crystalline layer is identified as at least 63 particles in the x-y plane (tolerating one vacancy per layer) with$\psi_{4,L}$ >0.99 for the layer, where $\psi_{4,L}$ is obtained by averaging $\psi_{4,i}$ for particle within the same layer, given as

$$\psi_{4,L}(z) = \left\langle \frac{\psi_{4,i} \cdot N_{b,i}}{4} \right\rangle, \left| z_i - z \right| \le h_c \tag{9.10}$$

9.3.4 Sedimentation equilibrium simulation

We first study a sedimentation system of 512 particles (*i.e.*, an 8 layer FCC crystal) in the *NVT* ensemble using BD simulation. Particles sediment onto an 8 × 8 squared lattice surface template (100 face of FCC crystal) with lattice constant L=2.125a. Periodic boundary conditions are applied in lateral x-y direction. Sedimentation equilibrium is achieved by melting an 8 layer FCC crystal in a simulation for at least 20 characteristic diffusion time (a^2/D), with integration time step 4.3×10^{-5} a^2/D.

In an equilibrated sedimentation system, solid-liquid co-existing pressure supports the total buoyant weight above the solid-liquid interface macroscopically (Eq. (9.6)). If we perturb the system by adding attraction between particles to lower the co-existing pressure[242], a certain number of particles above the interface will convert to solid-state particles to re-establish the equilibrium, as required by the force balance at the interface. This principle allows crystalline layers to be built by simply adding attraction, as illustrated in Fig. 1 with sedimentation equilibrium density profiles for different amounts of attraction.

Fig. 1a shows the equilibrium microstructure, the volume fraction profile, and representative renderings with at four different ε^* *(i.e.*, four different amounts of attraction). Here ε^* is the normalized attraction strength, with $\varepsilon^*=1$ corresponding to ~2.9kT of attraction resulting in a completely crystalline structure. For the case of $\varepsilon^*=0$ (*i.e.* no attraction), the coloring scheme based on $\psi_{4,i}$ indicates that there is barely any crystalline bonding in this system, and that there are no crystalline layers formed. The volume fraction profile, $\phi(z)$, shows oscillating peaks with decreasing magnitude for the initial several layers, which corresponds to layered liquid structures near the template at the bottom. $\psi_{4,L}$ at these layer positions shows a decrease from ~0.7 to ~0.4 for the first several structured layers and goes to 0 far from the surface where the particles are in a fluid configuration. At $\varepsilon^*=0.34$ (*i.e.*, ~1 kT attraction), two crystalline layers start to form above the template. Similar layered structures can be found above the topmost crystalline layer, as indicated by $\phi(z)$. $\psi_{4,L}$ is ~1 for the first two crystalline layers, ~0.8 for the third layer, and drops to 0 far from the surface where the particles are still fluid. As we further increase ε^*, more crystalline layers with similar interfacial structures form. By tuning up the attraction, ε^*, from 0 to 1, colloidal sediments with no crystalline layers to completely crystalline structures can be produced, as shown in Fig. 1b. Meanwhile, the equilibrium

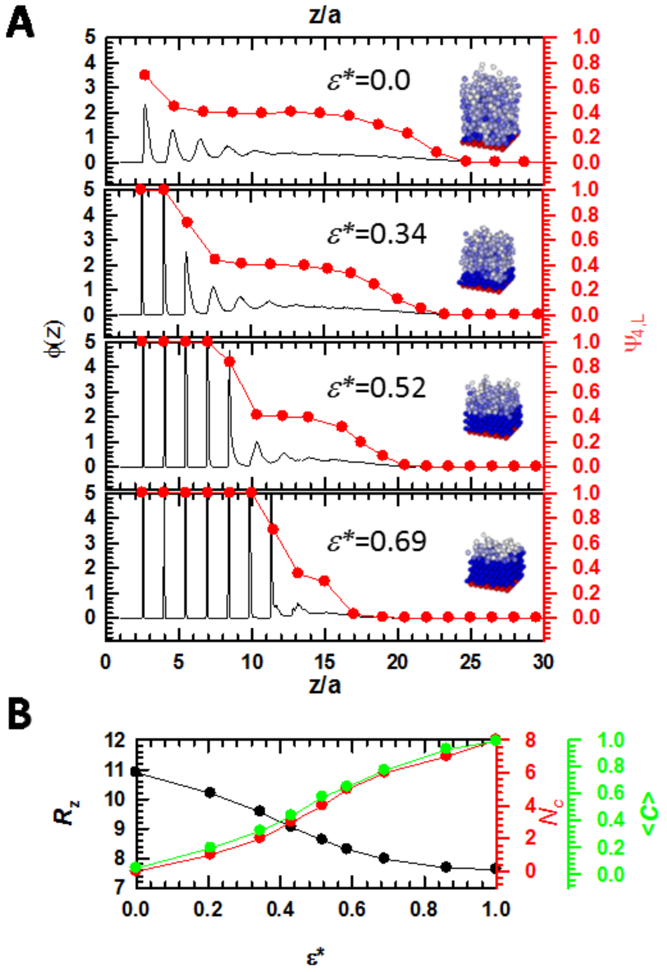

Figure 1. Equilibrium sedimentation model system at different ε^*: (A) sedimentation equilibrium profile of $\phi(z)$ and $\psi_{4,L}$, and representative equilibrium configuration at four different ε^*=0, 0.34, 0.52, 0.69. (B) Most probable R_z, N_c, $\langle C\rangle$ as a function of $\varepsilon^*$for 9 different ε^* ranging from 0 to 1. N_c ranges from 0 to 8.

structure will become more and more compact (*i.e.*, R_z decreases).

9.3.5 Dynamics and microstructure near the growth front

In our sedimentation model, we identify the growth front as the layer position just above the topmost crystalline layer. Dynamics and microstructures near the growth front are of particular importance because they determine the sediment structure formed as colloidal particles transform from fluid to solid configurations. We use a Lindemann-like parameter, given by[243],

$$L(t)=\frac{\left\langle (\mathbf{r}_{rel,i}(t)-\mathbf{r}_{rel,i}(0))^2\right\rangle}{a^2},\left|z_i-z\right|\le h_c \tag{9.11}$$

to quantify the layer-based particle mobility near the growth front, where $\mathbf{r}_{rel,i}(0)$ is the initial distance of particle *i* to its neighbors. and $\mathbf{r}_{rel,i}(t)$ is the distance at time *t* for the same initial particle neighbor pair. The bracket indicates that the average was taken for the particles located at similar elevations *z*). Distance between neighboring particles vs. absolute displacements[244] were used to later avoid error due to particle collective drift when varying ε^* in controlled crystal growth. In the dilute or short time limit, *L* will increase linearly with time, since particles perform random walks (*i.e.*, diffusion) without interacting with each other. In contrast, *L* will vanish or reach a finite plateau for an arrested structure (*i.e.*, solid state including crystalline and other arrested structures).

Fig. 2 shows *L*(*t*) for ε^*=0.34 at three specific layer positions, the layer below growth front(*gf*-), the growth front layer(*gf*), and the layer above growth front(*gf*+). These *L* curves all show an initial increase because of the short-time diffusion within “cages” formed by its neighbors. The slope of *L* will decrease to a smaller values at longer times depending on the local particle concentration at different elevations. For the layer below growth front(*i.e.*, second layer), *L* basically remains at 0 because particles are ‘fixed’ within the crystalline layer, as showed by the microstructure rendering in Fig. 2B. At the growth front (*i.e.*, third layer), only half particles are in the crystalline state, and particles experience less confinement in the z direction. Correspondingly, L displays a finite slope, which indicates that particles can move around lattice sites formed by the underlying crystalline layer at longer times. For the layer above growth front (*i.e.*, fourth layer), the mobility of the particles at longer times monotonically increases since particles are less confined at higher elevations.

We further define a one observation time, L_c, as $L(t_c)$, where $t_c=a^2/D$, for use in real-time controlled simulations. L_c is expected to be a complex function of the particle interactions and interfacial concentrations. We calculated the L_c below, at, and above the growth front (*i.e.*, $L_{c,gf-}$,$L_{c,gf}$ and $L_{c,gf+}$) at different ε^*, as showed in Fig. 2b. $L_{c,gf-}$ value are generally smaller than 0.02. $L_{c,gf+}$ values at layers above the growth front are generally greater than 0.3. $L_{c,gf+}$ values fall in the range of 0.16 to 0.20 except for the case that $\varepsilon^*=0.9$, where particles are very attractive to each other. The general features of L_c are used as a dynamic criterion to detect arrested structures in the control simulations, as we will show later.

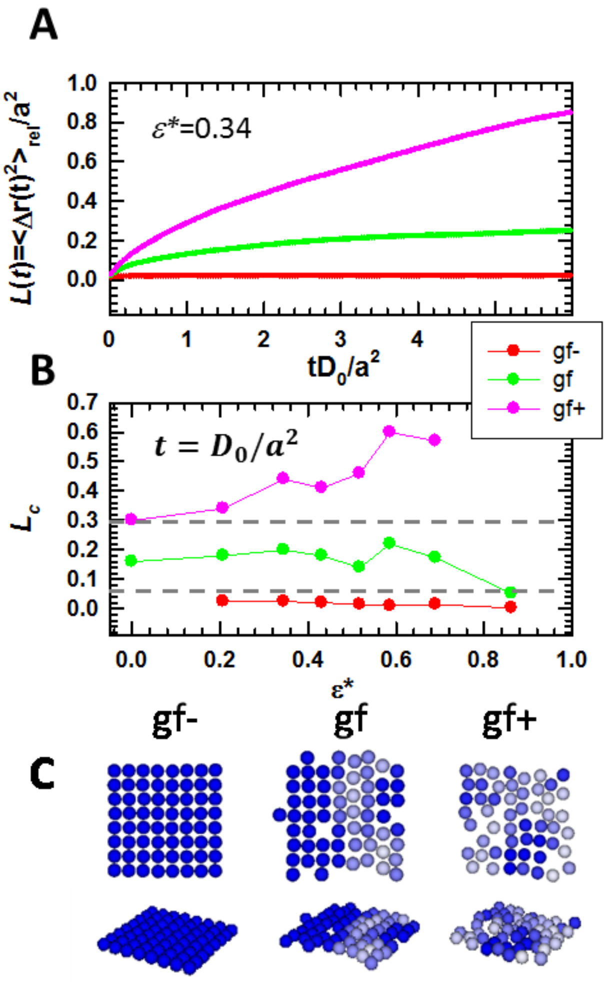

Figure 2. Dynamic properties of equilibrium sedimentation model near growth front. (A) L vs. t for particles at different layer positions of below growth front (*gf*-), growth front (*gf*) and above growth front (*gf*+). (B) L_c .vs. ε^* at *gf*-, *gf* and *gf*+ (C) Oblique view and top view rendering of layer structure at *gf*-, *gf* and *gf*+ for $\varepsilon^*=0.34$.

9.4 Controller design

9.4.1 Defective structures in direct deep quench

Before proceeding to the design of a controller, we first demonstrate the necessity of control in the attraction mediated crystal growth process. We examine the example in which we direct quench the system at $\varepsilon^*=1$ (The free energy minimum state at $\varepsilon^*=1$ is the fully crystalline structure.)from an initial fluid-like structure. Without loss of generality, the equilibrium fluid structure obtained at $\varepsilon^*=0$ is used as the initial configuration. As showed in Fig. 3a, upon turning on the attraction at $t=0$, R_z demonstrates a fast decrease from 0-100 s and a slow decrease at later times to $R_z\sim8.2$. $\langle C\rangle$ experiences a fast initial increase from 0-50 s, and then slowly levels off to $\langle C\rangle\sim0.4$. The final configuration shows that two highly ordered layers formed at the bottom, followed by an arrested disordered structure at higher elevations. The volume fraction profile (Fig. 3B) indicates the existence of interlayer peaks starting from the third layer and $\psi_{4,L}$ drops from ~1 from the third layers. Structures with different degrees of structural defects at different elevations are found, as shown Fig. 3C. For example, two point defects exist in the first two highly ordered layers (*i.e.*, $z=4a$), while at higher elevations (*i.e.*, $z=8a$ and $11a$) different crystalline domains and dislocations can be identified. L_c values for these arrested structures all take values of ~0.01. The initial liquid structure configuration with layer liqure structure at the bottom is expected to enhance the formation of the ordered layers at the bottom. Initially disordered liquid-like particles at higher elevations fail to rearrange themselves into an ordered crystal during the fast condensation process state and arrested structures containing defects result.

9.4.2 Quench-relax controller for crystal growth

Results above show that (1) increasing attraction can grow crystals and (2) deep quenching with lots of attraction can produce undesired, arrested structures containing defects. Here we propose a real-time feedback quench-relax controller with components: (1) N_c and L_c as sensors to detect structural and kinetic properties, (2) ε^* as an actuator to control N_c and (3) a thermodynamic model that relates ε^* to equilibrium N_c. In this controller, as demonstrated in Fig. 5, N_c and L_c characterize the real-time structural and dynamic properties of the sedimentation process, and ε^* controls the crystal growth in a

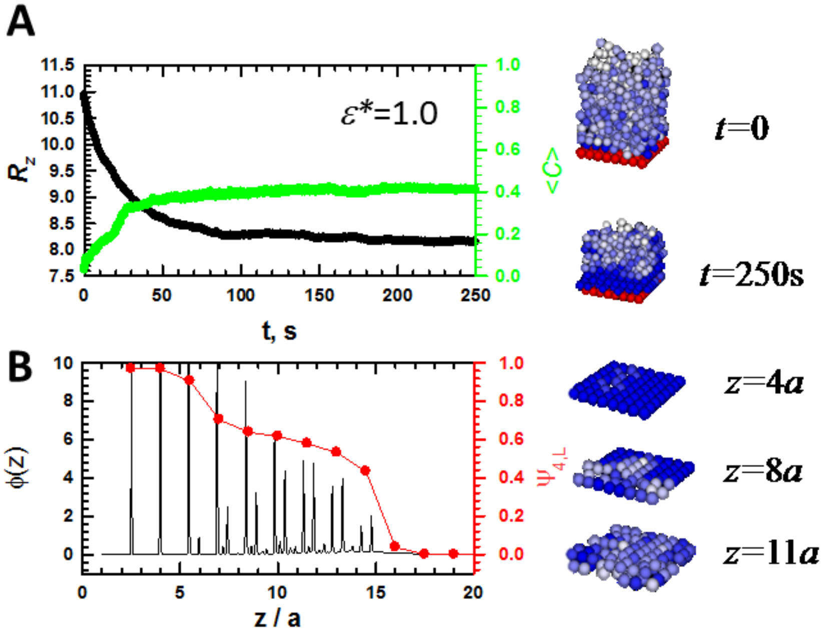

Figure 3. Crystallization *via* direct quench at ε^*=1. (A) R_z and $\langle C\rangle$ as a function of time. (B) profile of $\phi(z)$ and $\psi_{4,L}$, for the final sediment. Renderings of initial configuration, final configuration, and layer structures at z=4a, 8a, 11a are shown on the right-hand side.

layer-by-layer fashion based on the thermodynamic model. Starting with an initial configuration, N_c and L_c are calculated at a time interval, t_c, to decide whether to quench (*i.e.*, use high ε^*) or relax (*i.e.*, use low ε^*) the system. Briefly, if the system is arrested above the growth front, smaller ε^* is used to relax/melt the arrested structure Otherwise, a larger ε^* is used to grow more layers. Note that we based our decision making on the dynamic feature at the layer position above the growth front rather than the growth front. When a non-crystalline growth front layer is buried below an arrested layer, it cannot relax to a crystalline layer. By implementing our control scheme based on the layer above the growth front,…Formation and relaxation of arrested structures are identified by $L_{c,gf+}$. Specifically, when a system is in a 'quenching' stage, $L_{c,gf+}$ <0.03 is used to detect arrested structures, while when a system in the 'relaxing' stage, $L_{c,gf+}$ >0.3 is used to check the elimination of the arrested structure. These two criteria to distinguish disordered colloidal configurations as arrested vs. fluidare based on our findings from Fig. 2.

For simplicity, we employed a Boolean type variable QR as a status indicator, with QR=1 referring to a 'quench' stage and QR=0 referring to 'relax' stage. The value of ε^* used at the quenching stage is specified by the control parameter ΔN_c. For example, $\Delta N_c = 1$ means that the ε^* used will grow one more crystalline layer when equilibrium is established. In the relaxation stage, ε^* has a value that maintains the current N_c value when equilibrated, and consequently, the arrested layer above the growth front is eliminated. The relation between ε^* and the resulting equilibrium N_c is directly determined from Fig. 1b. The control process ends when the set-point crystalline layer number, $N_{c,SP}$, is reached. The performance of the controller with different ΔN_c is plotted in Fig. 5. In all cases, the initial configuration is a fluid-like equilibrium configuration at ε^*=0 with N_c=1, and $N_{c,SP}$ is set to 7. For ΔN_c =1, as shown in Fig. 5a, the actuator gradually takes higher ε^* as $\langle C \rangle$

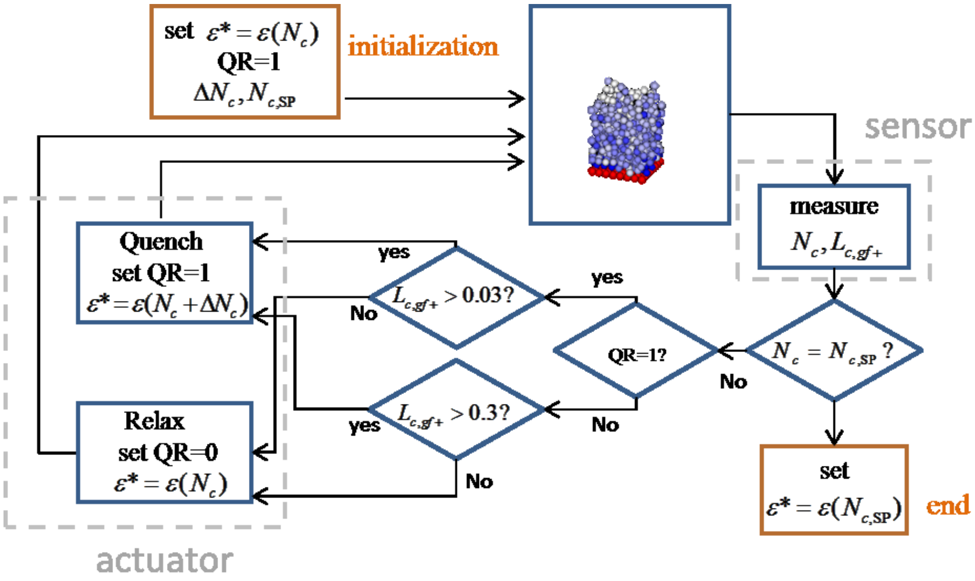
set $\varepsilon^* = \varepsilon(N_c)$
QR=1
$\Delta N_c, N_{c,SP}$
initialization
sensor
measure
$N_c, L_{c,gf+}$
$N_c = N_{c,SP}$?
No
QR=1?
yes
No
$L_{c,gf+} > 0.03$?
yes
No
$L_{c,gf+} > 0.3$?
yes
No
Quench
set QR=1
$\varepsilon^* = \varepsilon(N_c + \Delta N_c)$
Relax
set QR=0
$\varepsilon^* = \varepsilon(N_c)$
actuator
set
$\varepsilon^* = \varepsilon(N_{c,SP})$
end

Figure. 4. Schematic of quench-relax controller

and N_c increase and R_z decreases. We also observe $L_{c,gf+}$ fluctuating around 0.2 with no arrested structure above the growth front detected throughout the process (some realizations may have one chance to have $L_{c,gf+}$<0.03 when N_c=6, ε^*=0.86 and particle-particle attraction is strong). This is not surprising since the ε^* at ΔN_c =1 only provides a driving force strong enough to only crystallize/freeze the growth front layer and notthe layer above. It also confirms that the arrested criterion $L_{c,gf+}$ <0.03 is reasonable. Note that there are also some switches (say at t=200 s) between neighboring ε^* values and the N_c values, which is due to the fluctuation of $\psi_{4,L}$ around the criterion value for judging whether a layer is crystalline or not. For ΔN_c =2, as shown in Fig. 4b, arrested layers above the growth front are detected by $L_{c,gf+}$ <0.03 at t=120-140 s, t=195-205 s and t=300-400 s. During the relxation stage, ε^* will take a smaller value to melt the arrested layer, as indicated by the increase of R_z due to melting and expansion and the decrease of $\langle C \rangle$ due to melting of the partially crystalline structure. $N_{c,bat}$ generally follows a gradual increase in value since the existing crystalline layer will not be melted during the relaxation process. At t=300-400s, there are several quenching and relaxing alternating attempts, because particles are very attracted to each other at ε^*=1. For ΔN_c=3, dynamic arrest is more often encountered since the system is driven further from equilibrium using larger ε^*. The frequent alternation between quenching and relaxing will generally lower the efficiency of the controller in growing crystalline.

The efficiency of the controller for growing crystalline layers at different ΔN_c is analyzed by calculating the average time required to build each layer. Fig. 6 illustrates the results from averaging 120 realizations for each case. We found that using ΔN_c=2 or 3 is efficient for building the first 5 or 3 layers because of the large driving force, but the advantage will be cancelled out in building the last several layers due to the large amount of attraction between particles. The total time for growing crystal layers vs. ΔN_c shows (figure inset) that ΔN_c=2 is the most efficient, demonstrating that efficiently growing low defect colloidal crystals requires balance between the thermodynamic driving force and the kinetic accessibility[245,246]. At ΔN_c=1, the system has good kinetic accessibility, but the

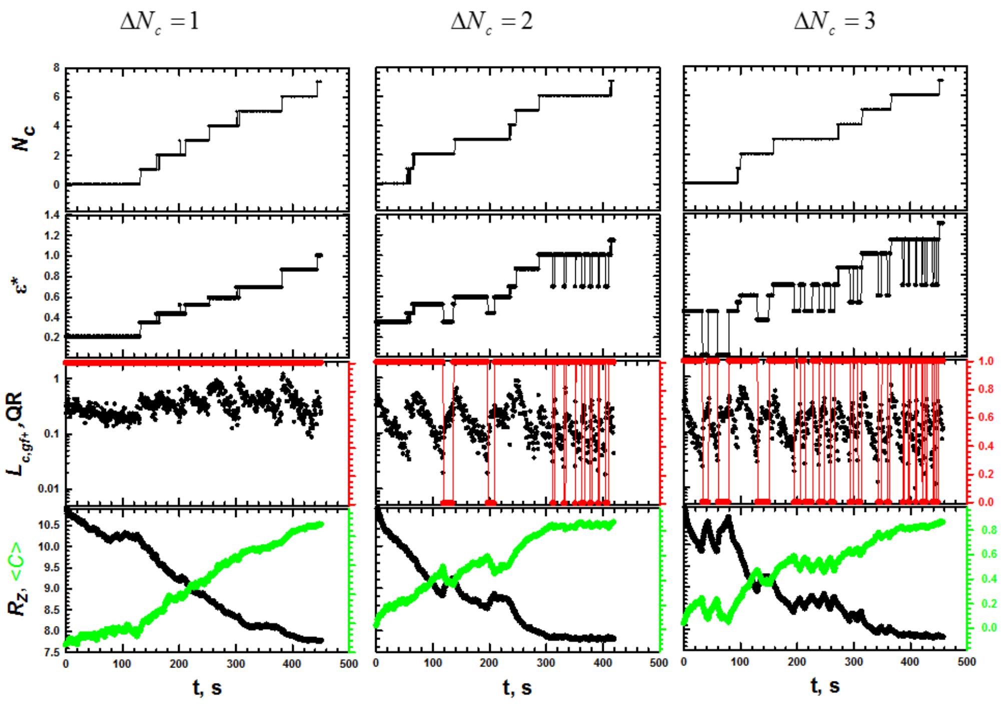

Figure 5. Results of controlled crystal growth using feed-back controller at (left) ΔN_c =1, (middle) ΔN_c =2, and (right) ΔN_c =3.

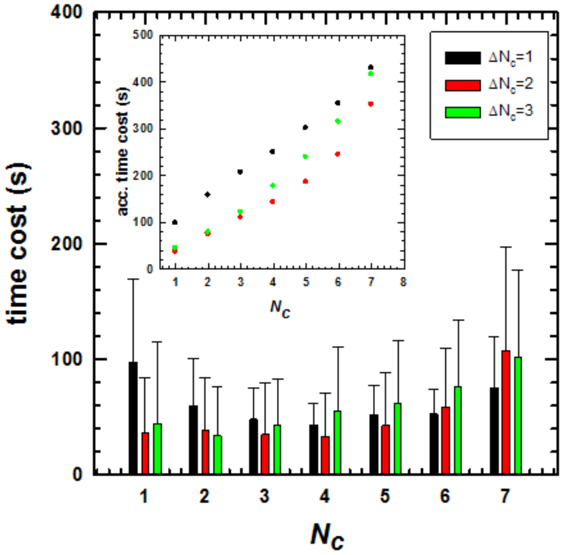

Fig. 6. Analysis of controller efficiency for ΔN_c =1, 2, 3: average time for building each layer and cumulative time (inset).

thermodynamic driving force is small. At N_c=2 or 3, the system has a greater thermodynamic driving force, but the kinetic accessibility is poor. It is quite straightforward that the controller can be further improved by using different ΔN_c when growing different layers: for example, the first five layers could be grown using ΔN_c=2 and last two layers could be grown using ΔN_c=1.

9.5 Conclusion and outlook

The results presented in this study demonstrate that by tuning attraction in a colloidal sedimentation system *via* feed-back control, layer-by-layer controlled crystallization can be realized. In a finite system with different inter-particle attractions, equilibrium sediment structures, including dense fluid, inhomogeneous fluid-solid, and completely crystalline configurations can be achieved. Using a Lindemann-like parameter, L_c, to investigate the particle mobility near the growth front at equilibrium allows criteria to be established to detect dynamic arrested structures. A controller using L_c and N_c as sensors, and tunable attraction as an actuatoris been demonstrated to effectively control the crystallization process based on a simple thermodynamic model. The performance of the controller shows that a fast, low defect crystallization process requires a balance between the strength of thermodynamic driving force and the kinetic accessibility[23,24].

In this controller model, the tunable attraction may be realized by temperature dependent depletion attractions[61] (though this is not an immediate actuator due to finite time heat transfer), or electric or magnetic field mediated interactions[168] (which are immediate actuators but both require complex set-ups). To extend the system to controlled continuous crystal growth, a particle feeding system can be added. The key issue that still needs to be addressed in continuous colloidal growth is that particle transport kinetics strongly affect the concentration near growth front, thus increasing the factors governing particle crystallization. This issue might be addressed by employing a dynamical density functional approach[247] to capture the density variation due to transport with a low-dimensional dynamic model[248] to capture the crystallization kinetics at the growth front.

10 MODELING DEPLETION MEDIATED COLLOIDAL ASSEMBLY ON TOPOGRAPHICAL PATTERNS§

10.1 Abstract

This work reports a model and Monte Carlo simulations of excluded volume mediated interactions between colloids and topographically patterned substrates in the presence of thermosensitive depletants. The model is matched to experiments to yield density, free energy, and potential energy landscapes that quantitatively capture particle microstructures varying from immobilized non-close packed configurations to random fluid states. A numerical model of local excluded volume affects is developed to enable computation of local depletion attraction in the presence of arbitrary geometries. Our findings demonstrate a quantitative modeling method to interpret and predict how surface patterns mediate local depletion interactions, which enables the design of colloidal based materials and devices.

keywords: tunable depletion attraction, patterned excluded volume, reconfigurable colloidal assembly, Monte Carlo simulations, non-close packed structures

10.2 Introduction

Depletion interactions arise between colloids and surfaces from "solute particles" being depleted, or excluded, from the gap between two interacting objects.[249] When this occurs, pure solvent in the excluded volume has a different chemical potential from the solution outside the excluded volume. This produces an attraction between particles and surfaces with a potential that is the product of osmotic pressure and the excluded volume. Although the depletion interaction can become more complicated based on how solute particles interact with each other and surfaces,[250] the basic picture presented above qualitatively captures the mechanism of colloidal depletion attraction for diverse solutes including polymers, micelles, hydrogel particles, and nanoparticles.[41] Because depletion interactions can occur in any mixture when a solute is excluded between two surfaces, such interactions are expected to be ubiquitous in complex industrial formulations as well as biological systems.[251]

---

§ Reprinted with permission from "Modeling depletion mediated colloidal assembly on topographical patterns." *Journal of colloid and interface science* 449 (2015): 270-278." by Yang, Yuguang, Tara D. Edwards, and Michael A. Bevan. Copyright © 2015 Elsevier

By understanding the mechanism of depletion attraction, there is an opportunity to engineer such potentials by either controlling the osmotic pressure or designing the excluded volume. Examples of tuning the depletant osmotic pressure have included thermosensitive micelles,[42] hydrogel particles,[43,44] and polymer chains.[45] However, in each of these examples, the osmotic pressure changes because the depletant size changes, which also means the excluded volume changes (which depends on relative depletant and colloid dimensions). Beyond tuning depletant dimensions, exclude volume has been manipulated via surface geometries in several key examples including confining surfaces,[252,253] surface features,[46] templates for crystallization,[47,48] surface roughness,[254,255] and lock-and-key colloids (*i.e.*, local curvature).[49] Although such studies demonstrate clever examples of tuning depletion interactions to affect colloidal assembly, accurate models have not been sufficiently developed to allow for systematic design and control of surface geometries that mediate local depletion potentials in colloidal materials and devices.

Here we report the development of a new method to compute local excluded volume and depletion interactions between particles and physically patterned surfaces. This method is used to analyze measurements of temperature dependent particle configurations on microfabricated surface topographies in the presence of thermosensitive depletants. Specifically, we analyze particles interacting with arrays of circles with sloping walls that produce additional local excluded volume (left side of Fig 1, experiments reported elsewhere[256]). These measurements, and the new model reported here, are distinct from our prior study of patterned depletion mediated colloidal crystallization on an underlying gravitational energy landscape.[44] The present work is both scientifically and technologically novel by exploiting local excluded volume effects in conjunction with thermosensitive depletants to create non-close-packed reconfigurable structures. Such non-close-packed structures with length scales comparable to electromagnetic radiation have important applications as metamaterials and their reconfigurability can allow such systems to be used as static materials or programmable devices.[97] Ultimately, our findings demonstrate a quantitative modeling tool to interpret and predict how local surface geometries alter local depletion interactions, which can enable new colloidal based materials and devices.

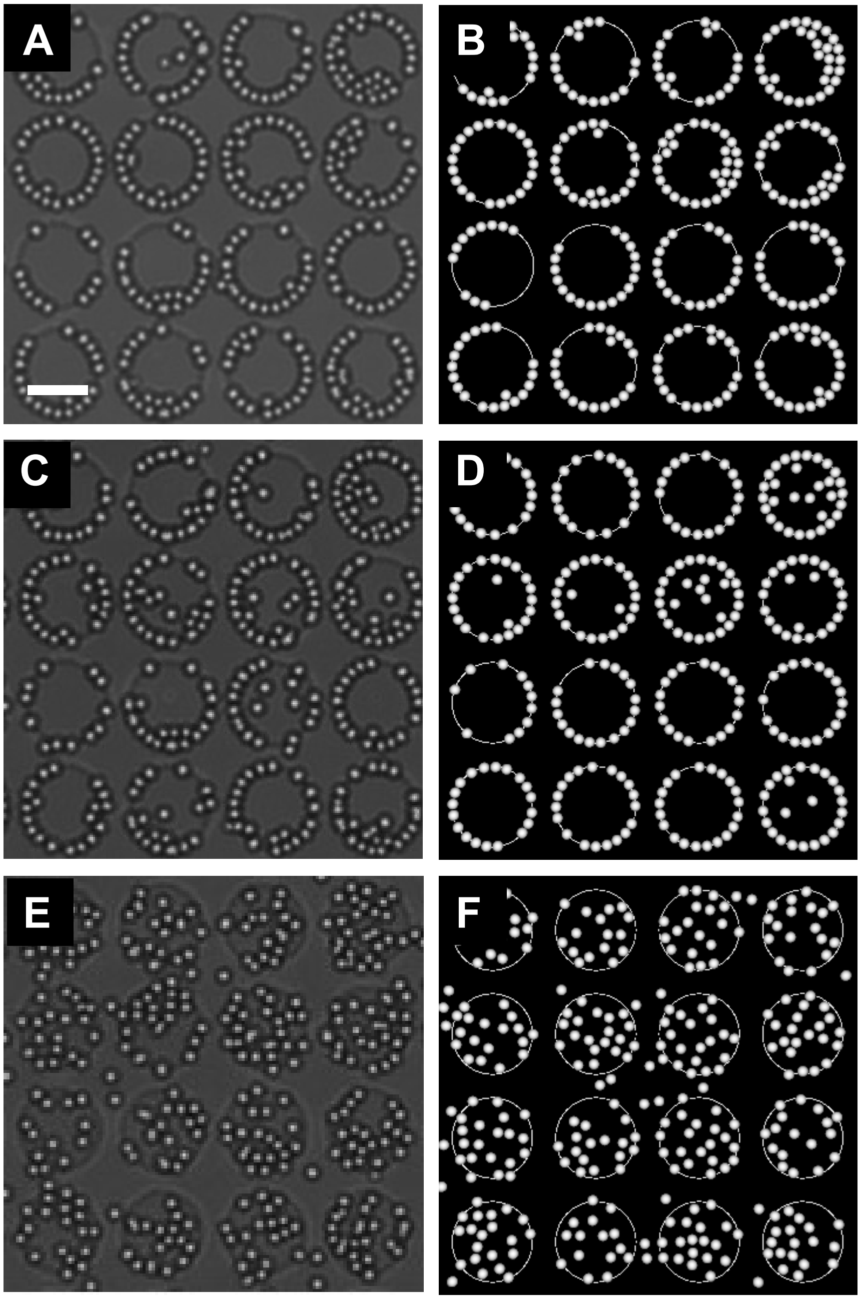

Figure 1. Experimental images (A,C,E) and simulation renderings (B,D,F) of charged ~2μm SiO_2 colloids at 0.18 area fraction experiencing depletion attraction with each other and a topographically patterned (well depth *H*=285nm) glass microscope slide surface. The depletion potential is tuned by the depletant size, 2*L*, at 25C, 2*L*=113nm (A,B), 35C, 2*L*=107nm (C,D), 37C, 2*L*=53nm (E,F).

10.3 Theory

10.3.1 Net interaction potential

The net potential energy for colloidal particles interacting with each other, an underlying surface, and gravity (see Fig. 2) can be modeled as the superposition of independent potentials. For a charged colloidal particle *i* with radius, *a*, in the presence of non-adsorbing depletant particles, the net interaction potential is given by,

$$u_i(\mathbf{r}_i) = u_D^{pw}(\mathbf{r}_i) + u_E^{pw}(\mathbf{r}_i) + u_G^{pf}(z_i) + \sum_{j \neq i}\left[u_D^{pp}(r_{ij}) + u_E^{pp}(r_{ij})\right] \tag{10.1}$$

where $\mathbf{r}_i=(x_i, y_i, z_i)$ is position vector of particle *i*, z_i is the particle center-to-surface elevation relative to the underlying surface, and r_{ij} is center-to-center separation between particles *i* and *j*. Subscripts refer to: (E) electrostatic, (G) gravitational, and (D) depletion, and superscripts refer to: (pp) particle-particle, (pw) particle-wall, and (pf) particle-field. The range of electrostatic repulsion in this work is sufficient so that van der Waals interactions van be neglected.

10.3.2 Gravitational potential

The gravitational potential energy of each particle depends on its elevation above the reference surface multiplied by its buoyant weight, *G*, given by,

$$u_G^{pf}(z) = Gz = (4/3)\pi a^3(\rho_p - \rho_f)gz \tag{10.2}$$

where *g* is acceleration due to gravity, and ρ_p and ρ_f are the particle and fluid densities.

10.3.3 Electrostatic interaction potentials

The colloidal particles are electrostatically stabilized against aggregation and deposition due to van der Waals attraction. The interaction between electrostatic double layers on adjacent particle and planar wall surfaces are given by,[159]

$$\begin{gathered} u_E^{pp}(r) = B\exp\left[-\kappa(r-2a)\right],\; u_E^{pw}(z) = 2B\exp\left[-\kappa(z-a)\right] \\ B = 32\pi\varepsilon a\left(\frac{kT}{e}\right)^2 \tanh\left(\frac{e\psi_1}{4kT}\right)\tanh\left(\frac{e\psi_2}{4kT}\right),\; \kappa = \left(2e^2 N_A C/\varepsilon kT\right)^{1/2} \end{gathered} \tag{10.3}$$

where κ is the inverse Debye length, ε is the solvent dielectric constant, k is Boltzmann's constant, T is absolute temperature, C is the 1:1 monovalent electrolyte molarity, N_A is Avogadro's number, e is the elemental charge, and ψ_1 and ψ_2 are the surface potentials.

10.3.4 AO depletion potentials

The depletion attraction between particles and underlying substrate surface can be given by a modified form of the usual AO depletion potential as,[249]

$$u_D^{pp}(r) = -\Pi V_{EX}^{pp}(r) \tag{10.4}$$

$$u_D^{pw}(\mathbf{r}) = -\Pi V_{EX}^{pw}(\mathbf{r}) \tag{10.5}$$

where Π is the depletant osmotic pressure, and $V^{pp}_{EX}(r, L)$ and $V^{pw}_{EX}(\mathbf{r}, L)$ are the excluded volume (see Fig. 1(b)) for particle-particle and particle-planar wall geometries given as,[2,59,257]

$$V_{EX}^{pp}(r) = \pi\left[(4/3)(a+L)^3\left(1-(3/4)r(a+L)^{-1}+(1/16)r^3(a+L)^{-3}\right)\right] \tag{10.6}$$

$$V_{EX}^{pp}(z) = \pi\left[(4/3)L^3 + 4L^2a - 4La(z-a) + a(z-a)^2 - L(z-a)^2 + (1/3)(z-a)^3\right]$$

(10.7)

where L is the depletant radius. For particles in the vicinity of a topographical pattern feature, the form of Eq. (10.5) remains the same in that the magnitude is determined by the depletant osmotic pressure, but the excluded volume term is computed numerically as

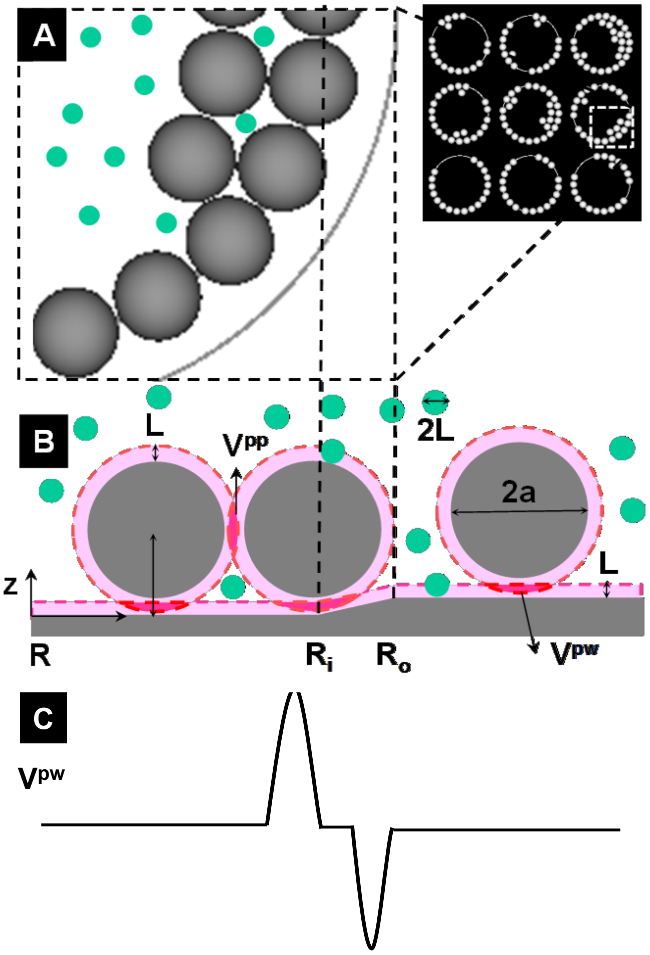

Figure. 2. Schematics of substrate geometry. (A) Snapshot (top views) of simulation rendering and magnified view of particles at pattern edge. (B) Cross sectional view of particles at pattern edge. Green and gray spheres are depletants and colloids. Red band (light) surrounding the gray sphere and the gray substrate is excluded volume (approximated via hard sphere repulsion).

described in the methods section of this paper. The numerical method is validated by producing the correct excluded volume terms given for particle-particle and particle-wall geometries in Eqs. (10.6) and (10.7).

10.3.5 Quasi-two dimensional models

In this paper, we perform quasi-2D measurements, simulations, and analyses of particles on patterned surfaces. The particles are assigned to a most probable elevation, z_M, above the substrate, which is the location of the net potential energy profile minimum normal to the substrate where the sum of the forces on the particle equal zero. This value can be determined as the value of z where the gradient of the net potential energy (z-dependent potentials in Eq. (10.1)) equals zero as given by,

$$\frac{\partial}{\partial z}\left[u_G^{pf}(z)+u_D^{pw}(z)+u_E^{pw}(z)\right]=0 \tag{10.8}$$

This approach allows the position dependent elevation of each particle, $z(\mathbf{r}_i)$, to be given as the sum of the local physical topography and the most probable height above the surface as,

$$z_i(x_i, y_i)=z_M+z(x_i, y_i) \tag{10.9}$$

which gives the net quasi-two dimensional potential energy (including a quasi-2D gravitational potential energy landscape[44,258]) for each particle as,

$$u_i(\mathbf{r}_i)=Gz_M(\mathbf{r}_i)+u_D^{pw}(\mathbf{r}_i)+\sum_{j\neq i}\left[u_E^{pp}(r_{ij})+u_D^{pp}(r_{ij})\right] \tag{10.10}$$

The goal of this work is to understand how particles sample the 2D energy landscape in the presence of gravity, depletion forces, and multi-particle packing effects. It has been shown that single particles (or sufficiently dilute to only interact with surface but not each other) will sample the landscape in Eq. (10.10) via a Boltzmann relation (and its algebraic inverse) given by,

$$\begin{aligned}\rho(\mathbf{r})/\rho_{ref} &= \exp\left[-\left(u(\mathbf{r})-u_{ref}\right)/kT\right] \\ \left[u(\mathbf{r})-u_{ref}\right]/kT &= -\ln\left[\rho(\mathbf{r})/\rho_{ref}\right]\end{aligned} \tag{10.11}$$

where $u(\mathbf{r})$ is the potential energy landscape in Eq. (10.10), and ρ_{ref} and u_{ref} are the reference density and potential at a given state and location in the in the system (e.g., single particle at the center of a pattern feature without any depletion attraction). For example, in the absence of particle-particle interactions or particle-wall depletion attraction, the potential energy landscape depends only on gravity and the height as,

$$u(x,y)-u_{ref} = G\left[z(x,y)-z_{ref}\right] \tag{10.12}$$

where h_{ref} is a reference height (*e.g.*, lowest or highest elevation on a surface). As particles begin to interact with each other and the underlying surface at finite concentration, the distribution of particles is related to the free energy landscape, $w(\mathbf{r})$, (and its algebraic inverse) given by,

$$\begin{aligned}\rho(\mathbf{r})/\rho_{ref} &= \exp\left[-\left(w(\mathbf{r})-w_{ref}\right)/kT\right] \\ \left[w(\mathbf{r})-w_{ref}\right]/kT &= -\ln\left[\rho(\mathbf{r})/\rho_{ref}\right]\end{aligned} \tag{10.13}$$

where ρ_{ref} and w_{ref} are again a reference density and potential at a given location (spatial position) and state (*i.e.*, global thermodynamic variables).

10.4 Methods

10.4.1 Excluded volume calculation

Considering the large ratio of the well diameter (*2R*) to the colloidal sphere diameter (2*a*), we approximate well slope in Fig. 2 (R_iR_o section) as a flat plane. The calculation of excluded volume is the intersection of colloidal particle excluded volume with the excluded volume from the three planes ($<R_i$, R_iR_o, $>R_o$ sections). The excluded volume of sphere and substrate are discretized with resolution $0.025a$ for each dimension (x,y,z), and then the volume elements inside the shaded region are added to obtain the overlap volume for the particle at each position (x,y,z). The accuracy of this method was validated by reproducing the particle-particle (Eq. (10.6)) and particle-wall (Eq. (10.7)) excluded volumes to <1% error.

10.4.2 Monte carlo simulations

Quasi-2D experiments are modeled in 2D Monte Carlo (MC) simulations where colloids samples landscapes determine by gravity and substrate topography mediated depletion potentials. In 2D MC simulations, trial moves in x and y directions are accepted or rejected using the energy function Eq. (10.10). In the implementation, real-time calculation of the excluded volume for every particle position would be computationally prohibitive. However, exploiting the natural system symmetry and periodicity (see Fig. 1), the particle position $[x,y,z(x,y)]$ is converted to $[R,z(R)]$, where R is the radial distance to the nearest well center. The excluded volume is then pre-calculated in a look-up table for use in the simulation. The MC simulations are performed at three different temperatures with all parameters listed in the Table 1. Initial configurations for simulations were obtained from experimental images. Each MC simulation was performed for $2.5\text{x}10^6$ steps with particle positions stored every 250 steps after an initial 10^6 step equilibration.

10.5 Results & discussion

10.5.1 2d density landscapes

In our experiment reported elsewhere[256], temperature sensitive poly-N-isoproplyacrylamide hydrogel(PNIPAM) were used as depletants to induce depletion attraction between silica particles. The temperature dependent depletant size can produce tunable excluded volumes and depletant osmotic pressures to tune the net depletion potential, leading to tunable colloidal phase behavior on topological surface, as shown in Figure 1 left column.We first compare time-averaged equilibrium configurations from microscopy experiments and MC simulations for the three temperatures reported in Fig. 1. The 2D density profiles, $\rho(x,y)$, are normalized by the maximum density and are reported in Fig 3. The experimental $\rho(x,y)$ were constructed from 50,156 images in 30 minute videos as reported in our separate paper on the experiments.[256] The vast majority of parameters used in the MC simulations were measured independently and reported in Table 1. To match experiment and MC simulations for each temperature, the particle-pattern excluded volume was computed using the numerical technique described in the methods section, which left the PNIPAM osmotic pressure as the sole adjustable parameter. The initial guess for the PNIPAM osmotic pressure was based on the Carnahan-Starling equation of state, DLS measured PNIPAM sizes, and concentration estimates.[43,44] We first fit our model to the experiment observation at 25C. Based on initial guess of depletant concentration, the measured depletant size, we can calculate the osmotic pressure, which is used as input in the Monte Carlo simulation. The concentration of depletant is adjusted until experiment and simulation are matched. Then we fixed the concentration, and tune the depletant size fit experiment at 35C, in the fitting process, we use Carnahan-Starling equation to calculate the osmotic pressure. At 37C, the osmotic pressure will not influence the net potentials since the depletant size is too small to induce any attraction.

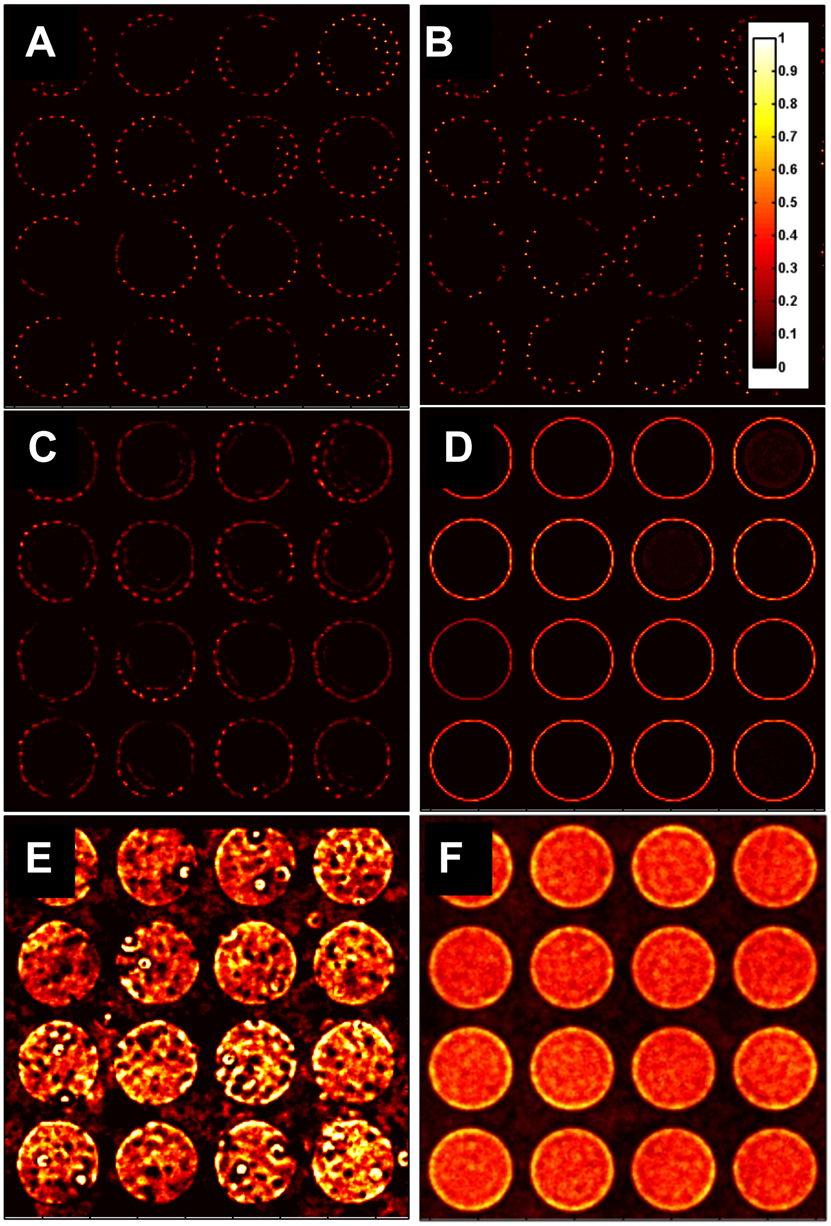

Figure. 3. 2D Density landscapes from experiments (A,C,E) and simulations (B,D,F) at 25C, 2*L*=113nm (A,B), 35C, 2*L*=107nm (C,D), 37C, 2*L*=53nm(E,F).

Fig. 3 shows that excellent agreement is observed between experiments and MC simulation at each temperature (within the statistical and spatial resolution of the experiments). Parts A, B in Figs. 1, 3 show that for the largest depletant size (2*L*=113nm) at the lowest temperature (*T*=25C), particles preferentially stick to pattern feature edge where the excluded volume is the greatest. Depending on the number of particles in the well, a second ring of particle forms via lateral particle-particle depletion attraction. As temperature increases (*T*=35C) and depletant size slightly decreases (2*L*=107nm) in parts C, D in Figs. 1, 3, particles near the pattern feature display an almost imperceptible increase in thermal motion and the second ring of particles now sample the pattern feature interior. Both effects show that reduced depletant size weakens the depletion attraction from a smaller excluded volume *and* a smaller depletant osmotic pressure (which scales as depletant volume, *e.g.*, second virial coefficient, volume fraction in equations of state[41,43,44,259,260]).

As the depletant size decreases considerably (2*L*=53nm) at a slightly higher temperature (*T*=37C) in parts E, F in Figs. 1, 3, depletion attraction between particles with each other and all surface locations vanishes, since the excluded volume becomes identically zero in all potentials. In this case, particles explore potential energy landscapes determined by multi-particle packing effects and gravity (*i.e.* elevation), similar to our previous studies.[43,44,258] The depletant size changes continuously vs. temperature, although somewhat more steeply in the vicinity of 35-37C, so the excluded volume, depletion potentials, and particle configuration on the underlying pattern also change more dramatically in this temperature range.

10.5.2 2d free energy landscapes

In addition to comparing the experimental and simulated density profiles, Fig. 4 shows a comparison of free energy landscapes, *w*(*x,y*), for the three cases in Figs. 1, 3. The *w*(*x,y*) are obtained from a Boltzmann inversion (Eq. (10.13)) of the density profiles in Fig. 3, which produces energy minima at the highest density positions in Fig. 3. Because $\rho(x,y)$ were matched between experiment and simulation in Fig. 3, the *w*(*x,y*) also naturally agree. For the 25C case in Fig. 4, the particles experience >10*kT* of depletion attraction with the pattern feature compared to all other locations on the surface. Because *w*(*x,y*) can only be constructed where particles sample, and they do not sample significantly other regions beside the pattern feature edge, it is not possible to determine the absolute depth of the energy minimum relative to the rest of the surface; it is >10*kT*, but not clear by how much. In short, particles only sample pattern feature edges in wells that are deep enough that they do not escape, so they appear to be irreversibly bound on the observation time of our experiments.

As temperature is increased to 35C, the attraction of particles to the pattern feature is ~3*kT* lower energy than the interior of the pattern feature and >5*kT* lower than outside the pattern feature edge. Because particle-particle interactions become weak enough that particles can sample the pattern interior, the ~3*kT* difference is accurately measured. However, the depletion attraction between particles and the pattern edge plus the additional effect of gravity to escape the lower elevation interior region are too great to obtain sufficient statistics from particles outside the pattern feature. Finally, in the absence of depletion attraction at 37C, there is no attraction to the pattern feature edge, and the free energy difference between the well interior and well exterior is ~4*kT*, which is close to the gravitational potential energy of particles escaping the well. The differences between free energy and potential energy landscapes at each temperature are discussed in more detail in the followings sections.

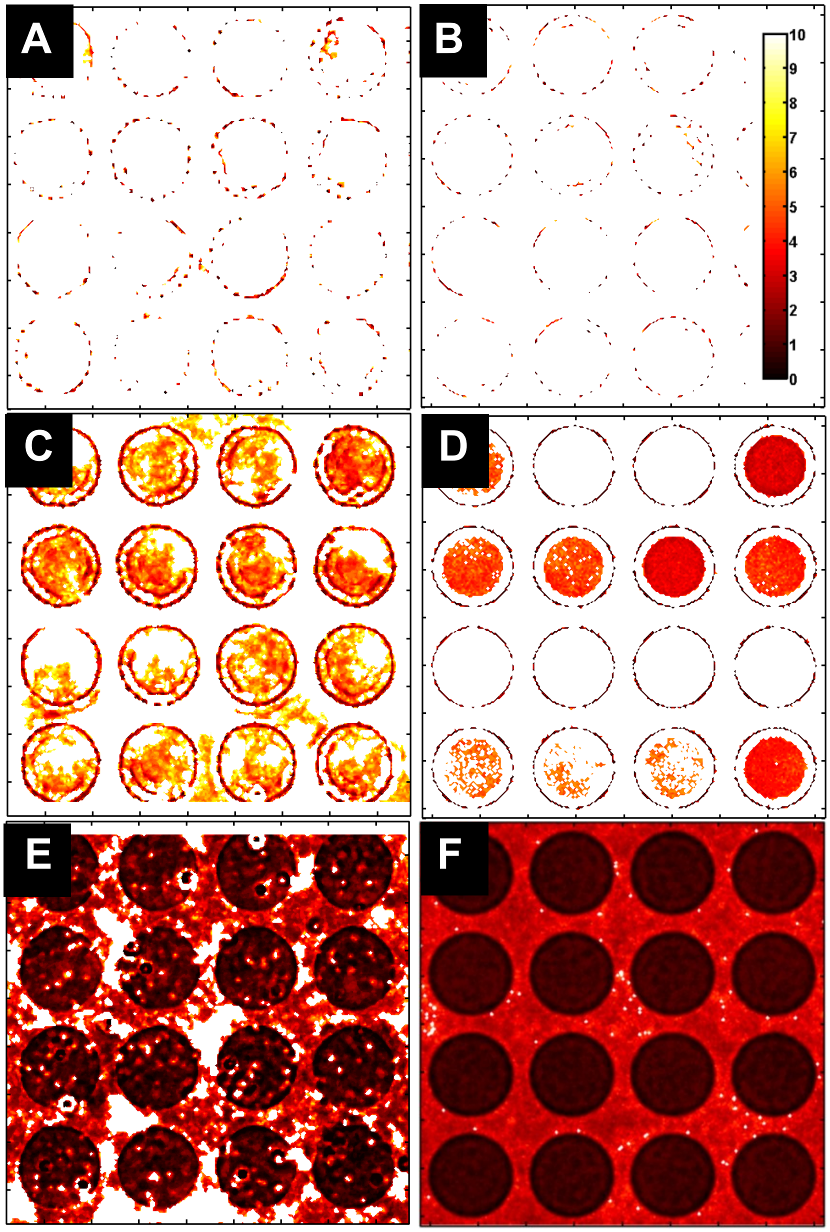

Figure. 4. 2D free energy landscapes from experiments (A,C,E) and simulations (B,D,F) at 25C, $2L$=113nm (A,B), 35C, $2L$=107nm (C,D), 37C, $2L$=53nm(E,F).

10.5.3 1d density & free energy landscapes

To generate more statistics in the experimental density and energy landscapes, and to take advantage of the pattern periodicity and circular symmetry, the density profiles in Fig. 3 are averaged over: (1) all features, which are considered to be nearly identical within the spatial limits of the microfabrication methods used to generate the pattern, and (2) and after converting to polar coordinates, over the angular coordinate, which the density and energy are not expected to have any dependence. This yields 1D radial density landscapes for each temperature, which are reported on the left hand side of Fig. 5. The 1D radial free energy landscapes are obtained from a Boltzmann inversion of the 1D density profiles and reported on the right hand side of Fig. 5. These results now show most clearly how the temperature dependent particle density and free energy vary relative to the pattern feature edge including the inner and outer radius of the sloped region. The oscillations in both landscapes clearly capture packing effects.

These results show at 25C that particles are attracted to the pattern feature edge and to each other as evident from the minimum at the pattern periphery and the local minimum at ~1.5a away from the edge towards the pattern interior. The diminished single well at 35C quantifies the strength to which particles are attracted to the feature edge, and the absence of another well shows that particle-particle attraction is negligible. In the absence of depletion attraction at 37C, particle are no longer preferentially attracted to the pattern edge. The free energy landscape depends on the balance of gravity and multi-particle packing effects, although the extent of multi-particle packing effects has yet to be determined. As a preliminary estimate, Fig. 5F shows the potential energy landscape due to single particles on the underlying pattern, which shows how multi-particle packing effects alter the interaction compared to single particles sampling. Although multi-particle packing effects were demonstrated to “push” particles out of patterned well features in more concentrated systems,[258] here the effect is less obvious. This effect is explored in more detail in the potentials obtained from the inverse MC analysis used to match the images, density landscapes, and free energy landscapes in Figs. 1-5.

10.5.4 Potential Energy Landscapes

By matching the experimental and simulated images, density, and free energy landscape in Figs. 1, 3-5, all contributing interaction potentials are determined, which means these can be discussed in addition to the free energy landscapes reported thus far. As described in the theory section, single particles can sample a potential energy landscape, $u(x,y)$, mediated by gravitational body forces and electrostatic and depletion colloidal forces. As particles become more concentrated, multi-particle packing influences how particle sample the underlying surface via a free energy landscape (that also includes an "entropy" landscape where $w(x,y)=u(x,y)-Ts(x,y)$). MC simulations naturally account for multi-particle packing effects, so that all particle-particle and particle-substrate interaction potentials are obtained unambiguously.

To understand the relevant potential energy contributions, Fig. 6 shows the radial and temperature dependence of: (A) the particle-substrate excluded volume (that determines attraction), (B) the particle-substrate potential energy landscape including electrostatics, depletion, and gravity (u^{pw} and u^{pf} in Eq. (10.10), electrostatic u^{pw} omitted but effectively considered from most probable elevation in Eqs. (10.8)-(10.9)), and (C) the net particle-particle separation dependent potential energy including electrostatics and depletion (u^{pp} in Eq. (10.1)).

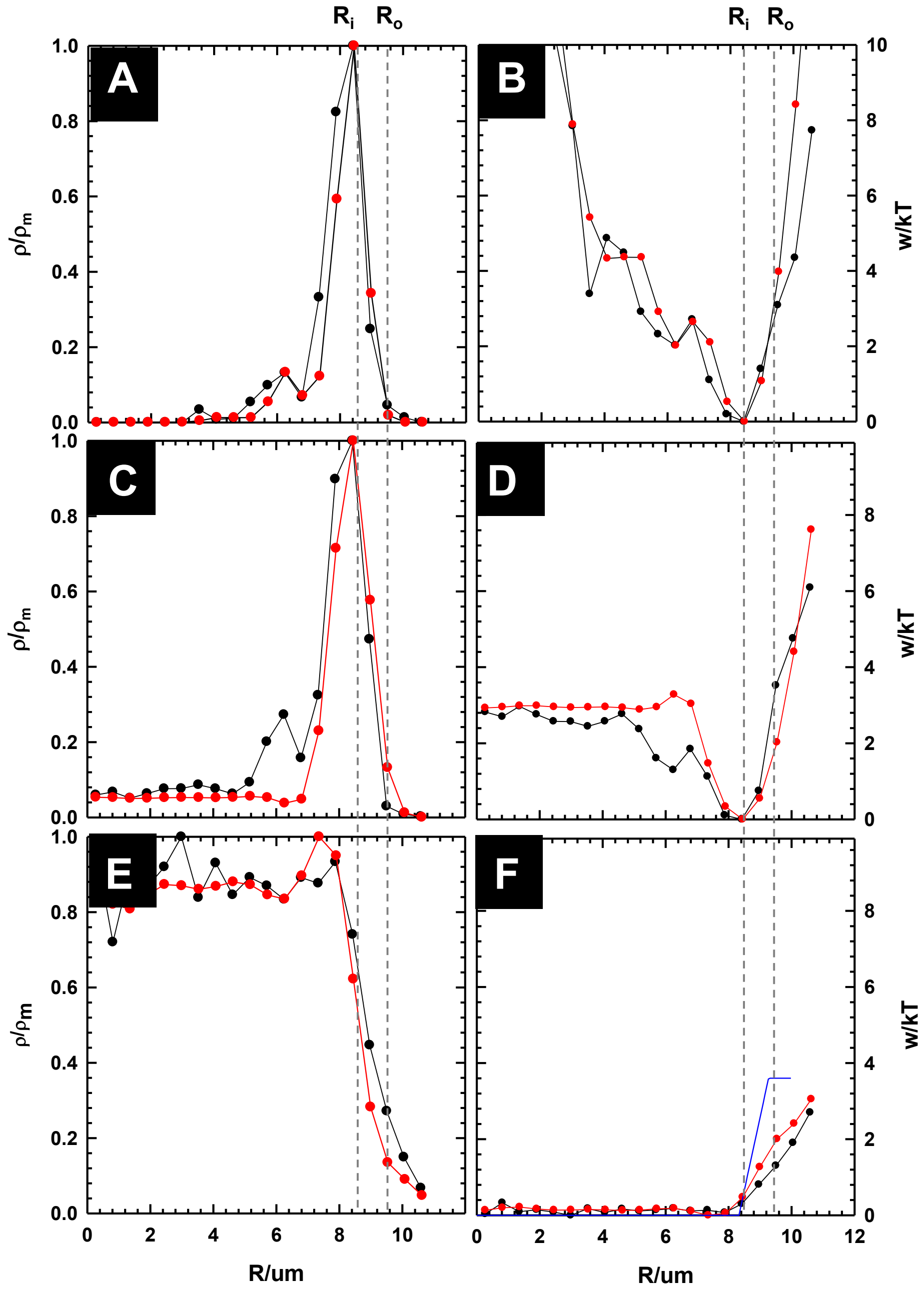

Figure. 5. 1D density profile (A, C, E) and free energy landscapes (B,D,F) from experiments(red line and symbol) and simulations(black line and symbol) at 25C, 2*L*=113nm (A,B), 35C, 2*L*=107nm (C,D), 37C, 2*L*=53nm(E,F). Blue line in (E) is gravitational potential energy landscape. Dash lines show inner (R_i) and outer (R_o) of pattern radius.

The results in Fig. 6A report the excluded volume as a difference between the value computed from the numerical method and the particle-wall value given in Eq. (10.7). This difference is reported as a function of lateral distance to the pattern feature edge for each temperature (*i.e.*, different depletant sizes, 2*L*). When the particle is far away from the pattern edge (R<<R_i, R>>R_o), there is no excluded volume difference. At 37C, ΔV_{EX}=0 everywhere since the 53nm PNIPAM particles are not excluded anywhere between the particles and patterned surface. At 35C and 25C, ΔV_{EX}=0 increases with increasing 2*L* at the inner edge of the feature, where the concave surface curvature complements the particle, and decreases at the outer edge, where the convex curvature bends away from the particle surface.

Fig, 6B shows a plot of the potential energy landscape vs. the radial pattern feature coordinate. Potential energy is plotted related to the energy at the pattern feature center, where particle-wall electrostatics, depletion, and gravity balance each other to produce a most probable elevation (*i.e.*, Eq. (10.8)). For T=37C, ΔV_{EX}=0 everywhere, and a purely gravitational potential energy landscape is obtained due to the elevation change of the surface. This explains the higher density of particle inside the pattern features. By multiplying the depletant osmotic pressure by ΔV_{EX} at 25C and 35C from Fig. 6A and adding it to the gravitational potential energy landscape, it is possible to obtain the potential energy landscape due to both contributions. It is now easy to see that single particles experience ~10*kT* of attraction to the concave inner feature edge at 35C and nearly ~20*kT* of attraction at 25C. In addition, the reduced excluded volume at the convex outer edge produce ~5*kT* and ~15*kT* potential energy barriers to single particles escaping the pattern outer edge. Together, the energy minimum at the inner edge and energy maximum at the outer edge produce energy changes (minimum depth to barrier maximum) of ~15*kT* and ~35*kT*, which is effective at preventing particle escape immobilizing particles with energies >>*kT*.

Finally, Fig. 6C also shows the pairwise particle-particle depletion attraction that contributes to the free energy landscapes in Fig. 5. The ~8*kT* and ~3*kT* particle-particle attraction at 25C and 35C are consistent with the degree of particle attachment to the first layer of particles immobilized at the pattern feature edge. In particular, the second layer of particles is completely immobile at 25C, whereas this layer shows intermittent attachment and detachment at 35C. At 37C, all depletion attraction vanishes including the particle-particle, particle-wall, and particle-edge feature attraction. The patterned surface mediated potential energy landscapes in combination with particle pair potentials reported in Fig. 6, when combined with multi-particle packing effects (*i.e.*, entropic contributions), clearly capture the free energy landscapes and density profiles obtained in the experimental studies reported in Fig. 1.

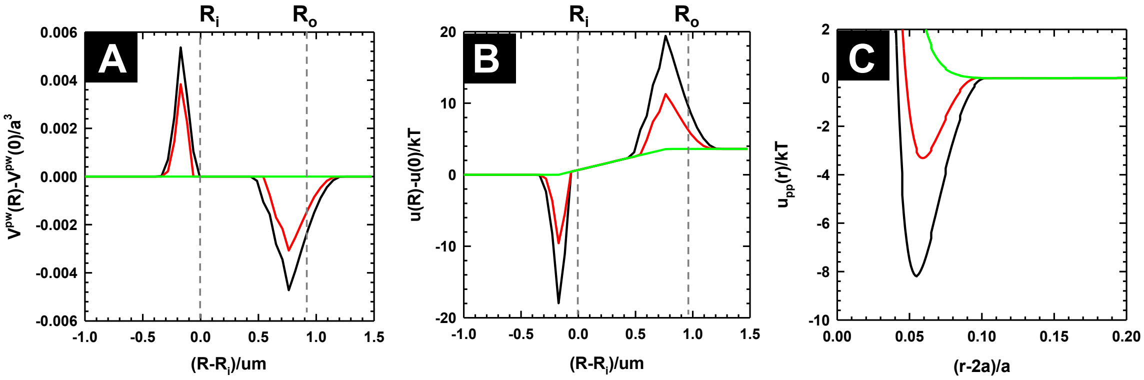

Figure. 6. Excluded volume difference (A), theoretical potential energy landscape (B), particle pair potential at 25C, $2L$=113nm (black), 35C, $2L$=107nm (red), 37C, $2L$=53nm (green).

10.6 Conclusions

Our results demonstrate the ability to accurately interpret and predict excluded volume effects between colloids with each other and topographically patterned surfaces in the presence of depletants with thermosensitive sizes. A new modeling approach is reported to numerically compute the excluded volume between colloids interacting with arbitrary surface geometries. This approach enables the computation of depletion attraction with local surface pattern features in the presence of depletants with varying dimensions. This method is used to match Monte Carlo simulations to experiments to model the temperature dependent density, free energy, and potential energy landscapes that determine non-close-packed colloidal configurations on periodic arrays of circular features. Ultimately, the ability to quantitatively understand the interplay of electrostatic, gravitational, and tunable depletion interactions on topographically patterned substrates provides a basis to design and control colloidal based reconfigurable materials and devices for micro- and nano-technologies.

Tables

Table 1. Parameters for MC simulations to match with experiments. (a) colloidal particle size, (b) Debye screening length, (c) particle and wall electrostatic potential,[132,137] (d) temperature, (e) patterned circle diameter, (f) center-to-center pattern spacing, (g) patterned depth, (h) depletant size, (i) osmotic pressure, (j) most probable height, (k) area fraction, (l) number of particles.

Variable	Theory/Simulation
a/nm[a]	**1100**
κ^{-1}/nm[b]	**9.54**

ψ/mV^{c}	**-50**
T/°C^{d}	**25, 35.0, 37.0**
$2R$/μm^{e}	17
D/μm^{f}	**21**
H/nm^{g}	**285**
$2L$/nm)^{h}	**113, 107, 53**
Π/kT (10^{-6}nm^{-3})^{i}	**26, 18, 7.4**
z_{m}/nm^{j}	**61, 66, 100**
ϕ^{k}	**0.178, 0.178, 0.175**
N^{l}	**332, 332, 324**

11 COLLOIDAL ROD MOTION NEAR A PLANAR WALL: TRANSPORT, SIMULATIONS AND TRAJECTORY ANALYSIS

11.1 Abstract

In this work, we study three closely interrelated aspects of single colloidal rod motion near a planar wall based on approaches derived from Stokesian dynamical (SD) simulations. Using the sphere-chain model of colloidal rods, we first calculate the diffusivity components in the 6 × 6 diffusivity tensor when a colloidal rod is in the bulk (far from the planar wall) and near the planar wall. By adding constraint forces into the Stokesian dynamical simulation, we develop a novel constraint SD that can simulate the rod in the bulk and electrostatically levitated above the plane with hydrodynamic interaction accounted. We develop an underlying theory for mean squared displacement analysis and equilibrium free energy landscape analysis for a single colloidal rod levitated. By analyzing the equilibrium distribution of the trajectory, and mean square translational displacement (MSTD), mean square angular displacement (MAD), we confirm the correctness of the algorithm and obtain insights of how rod moves near a planar wall.

Key words: hydrodynamics, constraint dynamics simulation, colloidal rod, diffusion

11.2 Introduction

Micro- and nano-sized colloidal rod-shaped objects exist in a wide variety of areas, ranging from biological macromolecules[54] to traditional industrial paints and ceramics, and novel building blocks in materials engineering[55]. When a rod-shaped colloidal particle suspended in a viscous fluid, it will undergo Brownian motion, known as diffusion, due to thermal agitation from solvent molecules.[261] The motion of rod-shaped particles in a fluid is inherently related to many fundamental processes of scientific interest and technological importance. In biology, the motion of rigid rod-shaped macromolecules or microorganisms, such as DNA, F-action, and Fd virus are essential for biological functionalities[53]. In material engineering, the Brownian motion of building block units, such as carbon nanotubes[262] and gold nano-rods,[263] in complex fluids plays a major role in mediating structural evolution. However, compared to the transport dynamics of spherical particles,[2,168,264] the transport dynamics for rod-shaped particle is still poorly understood. Recent research on rod-shaped particle dynamics has focused primarily on single particle transport dynamics[265,266], as well as the collective dynamic behavior of rod suspensions[267], such as phase transition[268], packing[269], aggregation[267] and assembly[270]. Regarding individual rod dynamics, the diffusivity tensor, **D**, play the key role in characterizing both the Brownian translational and rotational motion of rods, and its response to the external forces and torques. **D** is also related to the hydrodynamic friction of a moving rod via the fluctuation-dissipation theorem,[261] given by $\mathbf{D} = k_B T \mathbf{R}^{-1}$, where **R** is the resistance tensor, k_B is Boltzmann's constant, and T is temperature.

Considering a colloidal rod in the bulk, it will have different translational and rotational diffusion coefficients in directions along and perpendicular to its long axis due to the geometric anisotropy. Efforts to explore the relationship between diffusivity and geometry dated back to F. Perrin in 1905,[56] and followed by Broersma[271,272] in 1960, who provided the first calculation of translational and rotational diffusivities for a cylindrical rod in the bulk. The slender-body theory,[273] which represents a slender body using a line distribution of stokeslets, proved to be valid for calculating the diffusivities of rods with large aspect ratios (length over diameter, $L/2a$ >>1) in bulk. During the 1980s, Tirado et al.

developed a method to account for the end-correction and calculated the diffusivities of short rods with aspect ratios of 2-30. Tirado also found that Broersma's result is inaccurate for cylinders of finite length.[274] Tirado's results have been applied and corroborated in experiments.[9,10] Other numerical methods, such as the boundary element method[275] and path integral method,[276] are also used to calculate the transport properties of rod-shaped particles. The anisotropic aspects of diffusivities coefficients also manifests themselves in the diffusive behavior. In the short time scale, the rod exhibits anisotropic diffusion, whereas the coupling of rotation to translation will lead to a crossover timescale for anisotropic diffusion transitioning to isotropic diffusion in the longer time scale. Recently, the theoretical and experimental investigation of this fundamental property has been conducted for a quasi-2D system.[265] This anisotropic-to-isotropic diffusion property has also been employed in rod-shaped particles sorting via stochastic ratchets.[277] However, for 3D bulk diffusion, there does not yet exist an exact theory to describe this transition in dynamics, which limits the interpretation and manipulation of rod particle dynamics in 2D. One of the focuses of this work is to obtain such theory.

When a colloidal rod is near a no-slip planar wall, the existence of the bounding surface introduces additional complexities to its motion. Not only will the self-diffusion coefficients (*i.e.*, diagonal terms in **D**) of the rod be a function of its intrinsic geometry, but also depends on a complex function of a number of parameters (*e.g.*, aspect ratio, elevation, and orientation). Moreover, the couplings between different modes of motion will become subtle. Jeffrey et al.[7] derived a friction expression for an infinitely long cylindrical rod moving adjacent to a wall. De Mestre and Russell[278] obtained the hydrodynamic drag between a wall and a rod oriented either parallel or perpendicular to it using slender-body theory valid for separation distances on the order of cylinder length. Recently, Padding et al.[8] calculated the friction coefficient for a single sphere-chain rod with an aspect ratio of 10 at varying elevations and orientations above a wall by explicitly simulating the solvent molecules. However, this method is subject to error due to the coarse-graining procedure used in simulating the solvent molecules. In general, for a rod of varying length above a wall, how the components of the diffusivity tensor **D** depends on the separation distance, aspect ratio, and orientation, is largely unexplored. In additional, the conservative forces, i.e., gravitational force and electrostatic repulsion, will impose a further constraint on the configuration space of the rod. Being able to simulate and analyze rod motions near a wall can give insights on understanding the dynamics.

Stokesian Dynamics (SD) simulation provides the basis to calculate the diffusivity tensor and, and construct a simulation algorithm with hydrodynamics considered. For rod motion in the bulk and near a planar wall. The SD simulation[53,279] was first developed to capture multi-body hydrodynamic interactions for unbounded hard-sphere suspensions with low Reynold numbers. In SD, short-time self-diffusivities can be obtained from a grand resistance tensor built from particle hydrodynamic interactions, which has been showed in good agreement with experimental measurements.[280] A linear chain of touching spheres (sphere-chain model) has been used in SD to approximate the hydrodynamic drag for translating cylinders in the bulk fluid phase, demonstrating good agreement with slender-theory.[281] Recently, Swan and Brady et al.[10–12] adapted the previous SD scheme to colloidal suspensions with bounding surfaces (one or two no slip planes) by considering the image of a Stokeslet due to a no-slip wall. Even though SD is mainly used for simulating spherical colloidal particles with hydrodynamic interaction, we will show that, using the sphere-chain model to approximate a rod, we can develop an algorithm to simulating rods with hydrodynamic interactions. To achieve this, we will address one key issue on modifying the conservative and dissipative forces in the SD based on a rigid constraint strategy[282] such that spheres will maintain as the rod shape (i.e., a linear chain structure) during the simulation. In this way, we are able to use this Constraint Stokesian Dynamics simulations (CSD) to account for both multi-body hydrodynamic dissipative forces and conservative forces in bounded and unbounded situations in simulating a rod. There also exist other simulation methods for rod suspensions. For example, Brownian Dynamics simulations of hard rod systems developed by Lowen serve as a suitable approximation for dilute rod suspensions in which hydrodynamics can be safely neglected[283]. Including hydrodynamics in regular Brownian Dynamics simulation can also be achieve via by explicitly simulating a coarse-grained solvent *via* stochastic rotation dynamics.[284] Approximating colloidal rod using spheroid also offers an alternative approach in simulating rod motions with hydrodynamics.[285] Compared with these simulation methods, CSD has several advantages: 1) hydrodynamic interactions are naturally included in the grand resistance tensor, thus saving computational costs in simulating solvents; 2) Interactions between rods are obtained by summing up interactions between spherical beads composing the rod.[19] 3) CSD can easily be adapted to particles of other shapes, as long as the particle shape can be approximated as an assembly of spherical beads.

We organize the work as follows. We first provide the procedure for the construction of a grand resistance tensor and the calculation of the components in **D** via the method in SD. We then report the calculated diffusivities of a sphere-chain rod particle in the bulk. We continue by calculating the diffusivities of sphere-chain rods with aspect ratios ranging from 2-30 levitated parallel above and at oblique angles to the underlying planar no-slip wall. Then, the mid-step algorithm for simulating rigid sphere-chain rod is described. We then apply CSD to two simulated experiments: the diffusion of an isolated rod in 1) the bulk and 2) above a planar wall. Simulated trajectories are analyzed and compared with theoretical predictions for translational and rotational motions.

11.3 Theory

11.3.1 Coordinate system

We will use two coordinate frames, a lab frame and a body frame, in our following sections. As illustrated in Fig 1, the lab frame is a right-hand Cartesian coordinate system with basis vectors $\mathbf{e}_1$=(1,0,0), $\mathbf{e}_2$=(0,1,0), and $\mathbf{e}_3$=(0,0,1), and the body frame is a right-hand Cartesian coordinate system with the origin in the mass center of the rod and its axis directions given by $\mathbf{n}_{||}$, $\mathbf{n}_{\perp 1}$, and $\mathbf{n}_{\perp 1}$. Specifically, $\mathbf{n}_{||}$ is the unit vector pointing along the long axis of the rod, $\mathbf{n}_{\perp 1}$ is the unit vector perpendicular to $\mathbf{n}_{||}$ and parallel to the wall, and $\mathbf{n}_{\perp 1}$ is the unit vector perpendicular to the wall surface. The body frame is a translated and rotated version of the lab frame, with its rotation characterized by polar angle θ and azimuth angle φ.

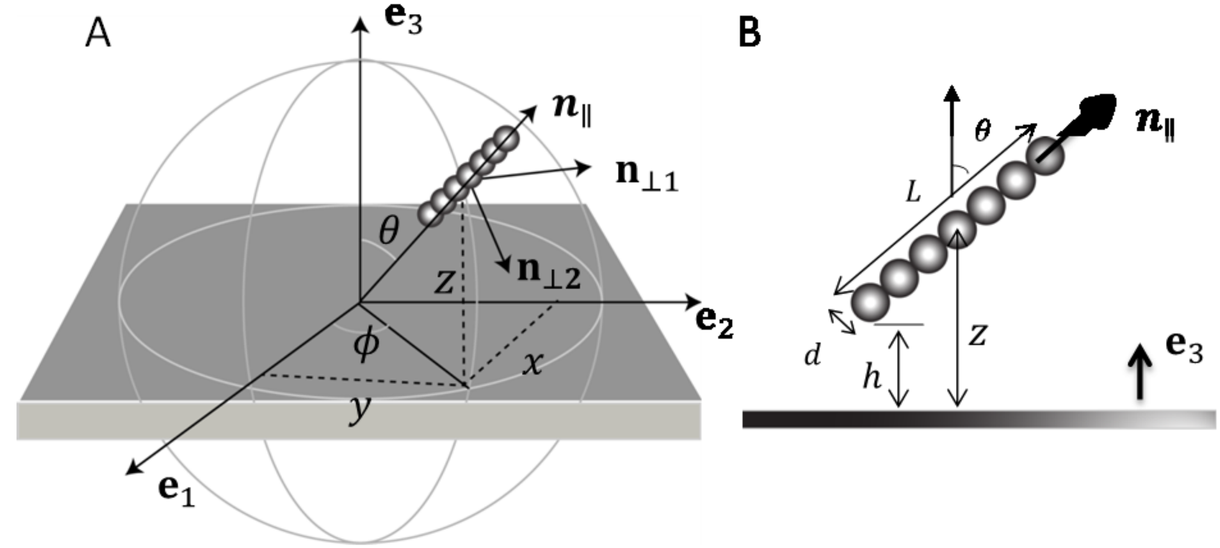

Figure. 1. Schematics of the sphere-chain model above a planar wall: (A) 3D view (B) side view looking along $\mathbf{n}_{\perp 1}$. $\mathbf{e}_1$, $\mathbf{e}_2$ and $\mathbf{e}_3$ are unit vectors of Cartesian coordinate of the lab frame, $\mathbf{n}_{\parallel}$, $\mathbf{n}_{\perp 1}$ and $\mathbf{n}_{\perp 2}$ are unit vectors of spherical coordinates of the body frame with its origin located at the mass center of the rod.

11.3.2 Grand resistance and mobility tensor for spheres

Consider the scenario where N hard spheres of radius a suspended in the unbounded impressible Newton flow without ambient flow. At the zero Reynolds number limit, the equation of motion is given by

$$\mathbf{U} = \mathbf{MF} \tag{11.1}$$

where $\mathbf{U}$ is the concatenation of translational and rotational velocity vectors of N spheres, $\mathbf{U}= (\mathbf{U}^{(1)}, \mathbf{U}^{(2)},\ldots,\mathbf{\Omega}^{(1)}, \mathbf{\Omega}^{(2)},\ldots)$, $\mathbf{F}$ is the concatenation of forces and torques acting on the spheres, $\mathbf{F}= (\mathbf{F}^{(1)}, \mathbf{F}^{(2)},\ldots,\mathbf{L}^{(1)}, \mathbf{L}^{(2)},\ldots)$, where the superscript denotes the index of individual spheres. $\mathbf{M}$ is the grand mobility tensor of size $6N \times 6N$. The corresponding resistance problem is to calculate the hydrodynamic forces and torques for N sphere moving in a flow in absence of ambient flow, formulated as

$$\mathbf{F} = \mathbf{R}\mathbf{U} \tag{11.2}$$

where **R** is the grand resistance tensor and relates to the grand mobility tensor as

$$\mathbf{R} = \mathbf{M}^{-1} \ . \tag{11.3}$$

It has been well established that the grand resistance tensor for spheres in bulk[53] is given as

$$\mathbf{R} = (\mathbf{M}_{\mathbf{PP}}^{\infty})^{\mathbf{-1}} + \mathbf{R}_{\mathbf{2B}} - \mathbf{R}_{\mathbf{2B}}^{\infty} \tag{11.4}$$

which includes both the far-field multi-body interaction (*i.e.* $(\mathbf{M}_{\mathbf{PP}}^{\infty})^{\mathbf{-1}}$)and the near-field pair-wise lubrication (*i.e.* $\mathbf{R}_{\mathbf{2B}}$). The far-field pairwise resistance (*i.e.* $\mathbf{R}_{\mathbf{2B}}^{\infty}$) is subtracted since the far-field two-body interaction is already accounted in $(\mathbf{M}_{\mathbf{PP}}^{\infty})^{\mathbf{-1}}$. Please see supporting information for details of these expressions.

The presence of a no-slip surface will significantly modify the flow field generated by a stokelet.[1] The effect of the no-slip boundary can be accounted by constructing an imaging system composed of stokeslet, stokes-doublet, and source-doublet on the other side of the surface.[1] Then, the Green function for the velocity field at **x** generated by a unit point force at **y** near a planar no-slip wall located at *H* with normal unit vector $\boldsymbol{\delta}_3$ is given as[1,286]

$$\begin{aligned} \mathbf{G}(\mathbf{x},\mathbf{y};H) = \mathbf{J}(\mathbf{x},\mathbf{y}) - \mathbf{J}(\mathbf{x},\mathbf{y}';H) + (\mathbf{y}\cdot\boldsymbol{\delta}_3 - H)^2 \nabla_{y'}^2 \mathbf{J}(\mathbf{x},\mathbf{y}')\cdot\mathbf{P} \\ + 2(\mathbf{y}\cdot\boldsymbol{\delta}_3 - H)(\mathbf{P}\cdot\nabla_{y'}\mathbf{J}(\mathbf{x},\mathbf{y}')\cdot\boldsymbol{\delta}_3)^T \end{aligned} \tag{11.5}$$

where $y' = y - 2(\mathbf{y}\cdot\boldsymbol{\delta}_3 - H)$, $\mathbf{P} = \mathbf{I} - 2\boldsymbol{\delta}_3\boldsymbol{\delta}_3$, T indicates transposition, **J** is the Green function for the velocity field at **x** generated by a unit point force at **y** when no wall is present, given as

$$\mathbf{J}(\mathbf{x},\mathbf{y}) = \frac{1}{8\pi\mu}\left(\frac{1}{r}+\frac{\mathbf{rr}}{r^3}\right) \qquad (11.6)$$

The grand resistance tensor for spheres above a planar no-slip wall is given as[286]

$$\mathbf{R} = (\mathbf{M}_{\mathbf{PW}}^{\infty})^{-1} + \mathbf{R}_{\mathbf{2B}} + \mathbf{R}_{\mathbf{W}} - (\mathbf{R}_{\mathbf{2B},\infty} + \mathbf{R}_{\mathbf{W},\infty}) \qquad (11.7)$$

which includes both the many-bodied far-field resistance tensor above a no-slip plane (*i.e.* $(\mathbf{M}_{\mathbf{PW}}^{\infty})^{-1}$), which is the inversion of many-bodied far-field mobility tensor, and the pair-wise lubrication interactions. The pair-wise lubrication interaction is obtained by first adding two-body particle-particle exact resistance tensor $\mathbf{R}_{\mathbf{2B}}$ and the particle-wall exact resistance tensor $\mathbf{R}_{\mathbf{W}}$, and then subtract the far-field resistance tensor $\mathbf{R}_{\mathbf{2B},\infty} + \mathbf{R}_{\mathbf{W},\infty}$ to avoid the double counting of the far-field particle-particle and particle-wall interaction in $(\mathbf{M}_{\mathbf{PW}}^{\infty})^{-1}$ and $\mathbf{R}_{\mathbf{2B}} + \mathbf{R}_{\mathbf{W}}$. The elements in the $\mathbf{R}_{2B}$ and $\mathbf{R}_{2B}^{\infty}$ are the same as Eqs. (11.4). The explicit expressions for $(\mathbf{M}_{\mathbf{PW}}^{\infty})^{-1}$ can be found in reference[286]. Please see supporting information for details of these expressions.

11.3.3 Calcuclating diffusivities for sphere-chain rod in bulk and above wall

We model the rod-like particle as a linear chain of touching spheres, as showed in Fig. 1. To model the motion of the rod, the system is constrained to only have six degree of freedoms (3 for translation,3 for rotation). The rigid motion of a rod can be further decomposed into three translational motions of the mass center and three rotational motions about the mass center. Similar to Eq. (11.2), we have

$$\begin{pmatrix} \mathbf{F}_{rod} \\ \mathbf{L}_{rod} \end{pmatrix} = \mathbf{R}_{rod} \begin{pmatrix} \mathbf{U}_{rod} \\ \mathbf{\Omega}_{rod} \end{pmatrix} . \qquad (11.8)$$

We note here that all the quantities in Eq. (11.8) are calculated and measured in the body frame of the rod throughout the paper. $\mathbf{R}_{rod}$ is a 6 × 6 resistance tensor of for the six degree of freedom of a single rod. The entries in $\mathbf{R}_{rod}$ can be calculated from Eq. (11.2)(11.8) by setting appropriate velocities to each sphere composing the rod. For example, if we set all spheres to translate with unit velocity in the $\mathbf{n}_{\|}$ direction, then from Eq. (11.2) we can calculate the $6N$ dimensional vector of forces and torques acting at the spheres. Those forces and torques can be converted to a 3-dimensional force $\mathbf{F}_{rod}$ acting on the mass center of the rod as a whole and a 3 dimensional torque $\mathbf{L}_{rod}$ acting on the rod about the mass center. Since the rod as a whole is equivalently translating with velocity vector $\mathbf{U}_{rod}$=(1,0,0), first row elements in $\mathbf{R}_{rod}$ can be calculated inversely via Eq. (11.8). We can design other velocities in the same scheme, as showed in Table 1, and obtain all the elements in $\mathbf{R}_{rod}$. The diffusivity tensor in the body frame of rod $\mathbf{D}_{rod}$ is then given by

$$\mathbf{D}_{rod} = k_B T(\mathbf{R}_{rod})^{-1} \tag{11.9}$$

For simplicity, we use $D_{\|}^{t,b}, D_{\perp 1}^{t,b}, D_{\perp 2}^{t,b}, D_{\|}^{r,b}, D_{\perp 1}^{r,b}, D_{\perp 2}^{r,b}$ to denote the six diagonal diffusivities components in $\mathbf{D}_{rod}$, representing the three bulk translational diffusivities and rotational diffusivities in the directions $\mathbf{n}_{\|}$, $\mathbf{n}_{\perp 1}$ and $\mathbf{n}_{\perp 2}$. Similarly, $D_{\|}^{t,w}, D_{\perp 1}^{t,w}, D_{\perp 2}^{t,w}, D_{\|}^{r,w}, D_{\perp 1}^{r,w}, D_{\perp 2}^{r,w}$ denote six diffusivities in the presence of a planar wall.

The presence of a wall introduces extra hydrodynamic drag to spheres composing the rod, and consequently slows down the motion. The extra hydrodynamic hindrance effect can be captured by using the height-dependent coefficient function, which is defined as the ratio of diffusivities above wall over the diffusivities in bulk, given as

$$\mathbf{G}(\mathbf{x},\mathbf{y};H)=\mathbf{J}(\mathbf{x},\mathbf{y})-\mathbf{J}(\mathbf{x},\mathbf{y}';H)+(\mathbf{y}\cdot\boldsymbol{\delta}_3-H)^2\nabla^2_{y'}\mathbf{J}(\mathbf{x},\mathbf{y}')\cdot\mathbf{P} \\ +2(\mathbf{y}\cdot\boldsymbol{\delta}_3-H)(\mathbf{P}\cdot\nabla_{y'}\mathbf{J}(\mathbf{x},\mathbf{y}')\cdot\boldsymbol{\delta}_3)^T \quad , \qquad (11.10)$$

where $f^t_{\|,p}(h)$ approaches 1 as h approaching infinity and approaches 0 when touching the wall. Usually, this coefficient function may vary for rods of different p. For practical purpose, we provide a rational fit for those functions as

$$f^t_{\|,p}(h)=\frac{a_1(\frac{h}{a})+a_2(\frac{h}{a})^2+a_3(\frac{h}{a})^3}{1+a_4(\frac{h}{a})+a_5(\frac{h}{a})^2} \qquad (11.11)$$

where a_i (i=1,2,..5) are fitting coefficients, which are documented in the supplement information.

Table 1

We label the N spheres comprising the rod as 1,2,…,N, and set the position vector for sphere i as ($2ai$, 0, $h+a$), then the velocity for each sphere is specified in the following table to calculate the $\mathbf{R}_{rod}$

Velocities of spheres in the body frame	Velocities of rod
$U_{i,1}$=1,for i=1,2…N	$\mathbf{U}_{rod}$=(1,0,0)
$U_{i,2}$=1,for i=1,2…N	$\mathbf{U}_{rod}$=(0,1,0)
$U_{i,3}$=1,for i=1,2…N	$\mathbf{U}_{rod}$=(0,0,1)
$\Omega_{i,1}$=1,for i=1,2…N	$\mathbf{\Omega}_{rod}$=(1,0,0)
$U_{i,2}$=(i-(N+1)/2),for i=1,2…N	$\mathbf{\Omega}_{rod}$=(0,1,0)
$U_{i,3}$=(i-(N+1)/2),for i=1,2…N	$\mathbf{\Omega}_{rod}$=(0,0,1)

11.3.4 Mid-step algorithm for equation of motion under constraint

For N identical particles in the low Reynold number flow with generalized coordinates $\boldsymbol{Q}$=q_1, q_2,…q_{6N} (including 3N positional coordinates and 3N rotational coordinates)under K constraints

$$C_\mu(q_1, q_2, ..., q_{6N}) = 0, \mu = 1, 2, ..., K \tag{11.12}$$

the equation of motion is given as

$$\frac{d\mathbf{Q}}{dt} = \mathbf{U} = \mathbf{M} \cdot \mathbf{F} \tag{11.13}$$

$$\mathbf{F} = \mathbf{F}^P + \mathbf{F}^B + \mathbf{F}^C \tag{11.14}$$

where $\mathbf{U}$ is a 6N dimensional velocity vector, including 3N translational velocities and 3N rotational velocities. $\mathbf{F}$ is a 6N dimensional force vector, including 3N forces and 3N torques acting on the center of each bead. $\mathbf{M}$ is a 6N×6N grand mobility tensor depending on the instantaneous configuration of N particles. The grand mobility tensor relates to grand resistance tensor *via* $\mathbf{M} = (\mathbf{R})^{-1}$ .The procedure to obtain those tensors is discussed in the previous section and Supporting materials. Generally, $\mathbf{F}$ have contributions from conservative forces $\mathbf{F}^P$, dissipative (Brownian) forces $\mathbf{F}^B$ and constraint forces $\mathbf{F}^C$.

The conservative forces on each sphere composing the rod experience electrostatic force from wall and gravitation force[287]:

$$\mathbf{F}^p = \kappa B^{pw} \exp(-\kappa(z-a))\mathbf{e}_3 + m\mathbf{g} \tag{11.15}$$

In the electrostatic part a is the radius of the sphere, z is the mass center height of the sphere, κ is the Debye length, B^{pw} is the pre-factor for electrostatic repulsion between colloidal pairs; in the gravitational force part, m is the buoyant sphere mass, $\mathbf{g}$ is the acceleration due to gravity. The inter-sphere interactions are not considered because they are internal forces cancelling out with each other.

A rod with aspect ratio p can be modeled by p spheres under two types of constraints: positional constraints and rotational constraint. The positional constraints are used to ensure all the spheres are positioned in one line and each sphere is touching with its neighbors. The rotational constraints are that all the spheres can only rotate along the long axis of the rod with the same speed. The consequences of these constraints are each coordinate q_j will experience an extra constraint force given as [282,288]

$$F_j^C = \sum_{\mu=1}^{K} \lambda_\mu \frac{\partial C_\mu}{\partial q_j} \tag{11.16}$$

Note that the constraint force expression has its roots in the Lagrange multiplier method in constraint optimizations. By imposing the condition that the K constraints should always be satisfied during the simulation, we have

$$\frac{\partial C_\mu}{\partial t} = \sum_{j=1}^{6N} \frac{\partial C_\mu}{\partial q_j} U_j = 0, \mu = 1, 2, ..., K \tag{11.17}$$

Then λ in Eq. (11.16)can be solved from Eqs. (11.13)(11.14)(11.16)(11.17).

The Brownian forces $\mathbf{F}^{\mathbf{B}}$ is generated from two steps: first generate the regular Brownian force according to dissipation-fluctuation theorem following

$$\left\langle \mathbf{F}^{B'} \right\rangle = 0, \left\langle \mathbf{F}^{B'} \mathbf{F}^{B'} \right\rangle = \frac{2k_B T}{\Delta t} \mathbf{R} \qquad (11.18)$$

And then project the generated forces $\mathbf{F}^{\mathbf{B'}}$ via:

$$P_{ij} = \delta_{ij} - \sum_{v=1}^{K} \sum_{\mu=1}^{K} \frac{\partial C_\mu}{\partial q_i} \left(\sum_{k=1}^{6N} \frac{\partial C_\mu}{\partial q_k} \frac{\partial C_v}{\partial q_k}\right)^{-1} \frac{\partial C_v}{\partial q_j}, \mathbf{F}^{\mathbf{B}} = \mathbf{P} \cdot \mathbf{F}^{\mathbf{B'}} \qquad (11.19)$$

such that Brownian forces will be locally tangent to the 6*N*-*K* hyper-surface defined by the *K* constraints. Please see the supporting materials for a detailed description.

With forces calculated, the mid-step algorithm is used to update the coordinate.[288] Specifically, the initial velocity and mid-point coordinate are first calculated:

$$\mathbf{U}^0 = (\mathbf{R}^0)^{-1} \cdot (\mathbf{F}^{P,0} + \mathbf{F}^{B,0} + \mathbf{F}^{C,0}) \qquad (11.20)$$

$$\mathbf{q}^* = \mathbf{q}^{\mathbf{0}} + \frac{1}{2} \mathbf{U}^0 \Delta t \qquad (11.21)$$

Then the intermediate velocity and finial position are calculated:

$$\mathbf{U}^* = (\mathbf{R}^*)^{-1} \cdot (\mathbf{F}^{P,*} + \mathbf{F}^{B,*} + \mathbf{F}^{C,*}) \qquad (11.22)$$

$$\mathbf{q} = \mathbf{q}^0 + \mathbf{U}^* \Delta t \qquad (11.23)$$

where Δt is the integration time, and the ‘0’ and the ‘*’ denotes quantity that is calculated using the initial and midpoint configuration respectively.

11.3.5 Equilibrium and dynamical analysis

11.3.5.1 Equilibrium distribution for single rod levitated above wall

For a rod levitated above the wall, we are mainly interested in its position characterized by (x, y, z) and its orientation characterized by the polar angle θ. The potential energy for a rod levitated above wall is obtained by summing up the potential energy of spheres composing the rod (except for the inter-sphere interaction potentials). The net potential has contributions from gravity and electrostatic repulsion, given by

$$U_{rod}(z,\theta) = \sum_{i=1}^{p} G_s z_i + B^{pw} \exp(-\kappa(z_i - a)) \tag{11.24}$$

where G_s is the buoyant weight of each sphere, z_i is the mass center of particle i composing the rod, and can be related to z and θ by

$$z_i = z + 2a\cos(\theta)(i - \frac{1+p}{2}) \tag{11.25}$$

For a conservative system conjugate to heat bath, the equilibrium probability density of a rod parameterized by (z, θ) is given by Boltzmann distribution:

$$\rho^{eq}(\mathrm{z},\theta) = N_0 \sin(\theta)\exp(-\frac{U_{rod}(z,\theta)}{k_B T}) \tag{11.26}$$

where $\sin(\theta)$ is the factor accounting for the degeneracy when integrating out the variable ϕ, N_0 is the normalizing factor to ensure $\iint \rho^{eq}(z,\theta)\,\mathrm{d}z\,\mathrm{d}\theta = 1$. The free energy landscape can be readily obtained as

$$\frac{W(z,\theta)}{k_B T} = -\ln(\rho^{eq}(z,\theta)) + C \tag{11.27}$$

where C is a constant. 2D free energy landscape can be converted to 1D free energy landscape by integrating out one variable, for example

$$\begin{aligned} \frac{W_\theta(\theta)}{k_B T} &= \int \exp(-\frac{W(z,\theta)}{k_B T})dz + C \\ \frac{W_z(z)}{k_B T} &= \int \exp(-\frac{W(z,\theta)}{k_B T})d\theta + C \end{aligned} \tag{11.28}$$

11.3.5.2 Mean squared displacement analysis for single rod random walk in bulk

The anisotropic diffusion behavior of rod-shaped particle can be characterized by the time-lapsed mean squared translational displacement (MSTD) along directions parallel and perpendicular to the long axis. The displacement vector of the mass center at time t can be decomposed into parallel and perpendicular components based on the initial orientation of the body frame(Fig. 1). For the MSTD in parallel and perpendicular directions, our derivation (See Supporting materials) shows:

$$\begin{aligned} \langle \Delta x_{\parallel}(t)\Delta x_{\parallel}(t)\rangle &= 2D^t_{\perp 1}t + \frac{2}{3}(D^t_{\parallel} - D^t_{\perp 1})t + \frac{4}{3}(D^t_{\parallel} - D^t_{\perp 1})\frac{1}{6D^r_{\perp 1}}(1-\exp(-6D^r_{\perp 1}t) \\ \langle \Delta x_{\perp 1}(t)\Delta x_{\perp 1}(t)\rangle &= 2D^t_{\perp 1}t + \frac{2}{3}(D^t_{\parallel} - D^t_{\perp 1})t - \frac{2}{3}(D^t_{\parallel} - D^t_{\perp 1})\frac{1}{6D^r_{\perp 1}}(1-\exp(-6D^r_{\perp 1}t) \end{aligned}$$

(11.29)

where <> is the ensemble average. Also note that for diffusion in the bulk, $\langle \Delta x_{\perp 1}(t)\Delta x_{\perp 1}(t)\rangle$ and $\langle \Delta x_{\perp 2}(t)\Delta x_{\perp 2}(t)\rangle$ are equivalent. If the MSTD is calculated by averaging over all trajectories with different initial orientations, then for all time scales, we have

$$\left\langle \Delta x(t)\Delta x(t) \right\rangle = 4D_{\perp 1}^{t}t + 2D_{\parallel}^{t} \tag{11.30}$$

where $(\Delta x)^2 = (\Delta x_{\parallel})^2 + (\Delta x_{\perp 1})^2 + (\Delta x_{\perp 2})^2$. Brownian rotational motion in 3D is usually characterized by orientation auto-correlation function, which is connected to the rotational diffusivity as[289]

$$\left\langle \mathbf{n}_{\parallel}(t) \cdot \mathbf{n}_{\parallel}(0) \right\rangle = \exp(-2D_{\perp 1}^{r}t) \tag{11.31}$$

where $\mathbf{n}_{\parallel}(t)$ is the rod's orientation vector at lapsed-time t.

11.3.5.3 2D projected mean squared displacement analysis for single rod levitated above a wall

When a rod is levitated above a wall, 2D projected MSTD and mean squared angular displacements (MSAD) are important experimental measurement quantities that characterize the motion of a particle in the confining environment. Assuming that the rod is moving strictly in 2D, then, for the parallel and perpendicular MSTD, we have[265]

$$\begin{aligned} \left\langle \Delta x_{\parallel}(t)\Delta x_{\parallel}(t) \right\rangle &= (D_{\parallel}^{t} + D_{\perp 1}^{t})t - (D_{\perp 1}^{t} - D_{\parallel}^{t})\frac{1}{4D_{\perp 2}^{r}}(1 - \exp(-4D_{\perp 2}^{r}t) \\ \left\langle \Delta x_{\perp 1}(t)\Delta x_{\perp 1}(t) \right\rangle &= (D_{\parallel}^{t} + D_{\perp 1}^{t})t + (D_{\perp 1}^{t} - D_{\parallel}^{t})\frac{1}{4D_{\perp 2}^{r}}(1 - \exp(-4D_{\perp 2}^{r}t) \end{aligned} \tag{11.32}$$

Add Eq. (11.32) together, we then obtain the MSTD for the system averaged over all the orientations,

$$\left\langle \Delta x(t)\Delta x(t) \right\rangle = 2(D_{\parallel}^{t} + D_{\perp 1}^{t})t \tag{11.33}$$

In a situation where z and θ are not strictly constrained, 2D projected MSTD expression is given by replacing diffusivities in Eq. (11.32) with probability-weighted diffusivities[54]. We have

$$\begin{aligned}\left\langle D_{\parallel}^{t}\right\rangle_{z,\theta} &= \int (D_{\parallel}^{t}\sin^2\theta + D_{\perp 2}^{t}\cos^2\theta)\rho^{eq}(z,\theta)d\theta dz \\ \left\langle D_{\perp 2}^{t}\right\rangle_{z,\theta} &= \int D_{\perp 2}^{t}\rho^{eq}(z,\theta)d\theta dz\end{aligned} \quad . \tag{11.34}$$

where the subscript means taking an average of that variable.

Diffusion normal to wall

When a rod is close to a bounding surface (*e.g.*, a wall surface), the diffusion normal to the wall has a strong dependence on the separation between the rod and the surface due to the hydrodynamic lubrication forces[50,51]. The diffusion coefficients are connected to the normal-to- wall component in the MSTD *via*

$$D_3^t(z) = \frac{1}{2}\frac{d}{dt}\left\langle (\Delta x_3(z,t))^2 \right\rangle \tag{11.35}$$

which can be used to extract the diffusion coefficient from particle diffusion trajectories. The diffusion coefficients can also related to diffusion coefficients in the body frame as

$$D_3^t(z) = \int (D_{\parallel}^{t}\cos^2\theta + D_{\perp 2}^{t}\sin^2\theta)\rho^{eq}(\theta)d\theta \ . \tag{11.36}$$

11.3.5.4 Simulation Methods

We implemented CSD for two types of experiments: isolated rod diffusion in bulk and above a no-slip planar wall. The forces **F** are formulated in *Supporting materials*. In both cases, the radius of the sphere composing the rod is 200nm. In the case that single rod diffuses in bulk, the rod has the aspect ratio of 4 and is only subject to Brownian forces. In the case that a rod is levitated above a wall, the rod is subject to gravitational force, electrostatic repulsion and Brownian forces. The material properties corresponded to gold(Au) nano-rods of different aspect ratio (p=4, 7, 12) in aqueous media with 0.1mM 1:1 univalent electrolyte (G_s/a=0.297kT ,B^{pw}=486.6kT and κ^{-1}=30nm). For single rod in bulk, the integration time step is 0.5ms. Mass center and orientation of the rod is recorded every 50 steps for a total 10000s. For single rod above the wall, the integration time step is 0.2ms. Mass center and orientation of the rod is recorded every 50 steps for a total 2000s.

We use Boltzmann inversion to construct the free energy landscapes from simulation trajectories. We discretize the vertical position z and polar angle θ with a resolution of 20 nm and 1 degree respectively. For dynamic analysis, time-resolved MSTD, MSAD and orientation auto-correlation function are calculated.

11.4 Results and discussion

11.4.1 Diffusivities of rod-shaped particle in bulk

Fig. 2 depicts the diffusivities for a sphere-chain rod of aspect ratio p=2-30 calculated via SD method and its comparison with the widely used cylindrical rod results from Tirado's model[290]. For a single rod in the bulk, off-diagonal terms of $\mathbf{D}_{rod}$ in the body frames will vanish since there are no correlations between different types of motion**.** In the bulk, translational and rotational diffusivities in directions $\mathbf{n}_{\perp 1}$ and $\mathbf{n}_{\perp 2}$ are equivalent, and we only plot result in direction $\mathbf{n}_{\perp 1}$. In Fig. 2 (A), translational diffusivities (normalized by $kT/6\pi\mu a$) in direction $\mathbf{n}_{\perp 1}$ in our calculation shows a systematic positive deviation (within 10%) from the Tirado's model for p > 3. The positive deviation can be understood through the fact that when a sphere translates through a quiescent flow, it experienced less drag than a cylindrical surface of length $2a$ translating in direction perpendicular to its axis. For translational diffusivity along the axis (in the direction of $\mathbf{n}_{||}$), sphere-chain model yields an overall smaller value (within 20%) than results from the cylinder model. In Tirado's method, he used small spherical beads to model the shape of cylinder. The translational diffusivity in the parallel direction will decrease when he increase the density of spherical beads composing the rod to make the cylinder surface smoother. Therefore, we speculated that the difference is due to the finite size effect of the spheres in the sphere-chain rod. The sphere-chain surface in is obviously rougher than a cylindrical surface, thus experiencing more friction when translates parallel.

In Fig. 2(B), we observed a close result (within 5%) between rotational diffusivities (normalized by $kT/8\pi\mu a^3$) in $\mathbf{n}_{\perp 1}$ directions in the two models. However, for rotational diffusivity in $\mathbf{n}_{||}$ direction (rotation along the axis of the rod), our sphere model shows overall larger diffusivities (within 20%). We ascribe this to the same reason that we used to explain the perpendicular translation: the rotation of sphere will experience less drag than the rotation of a short cylindrical surface of length $2a$.

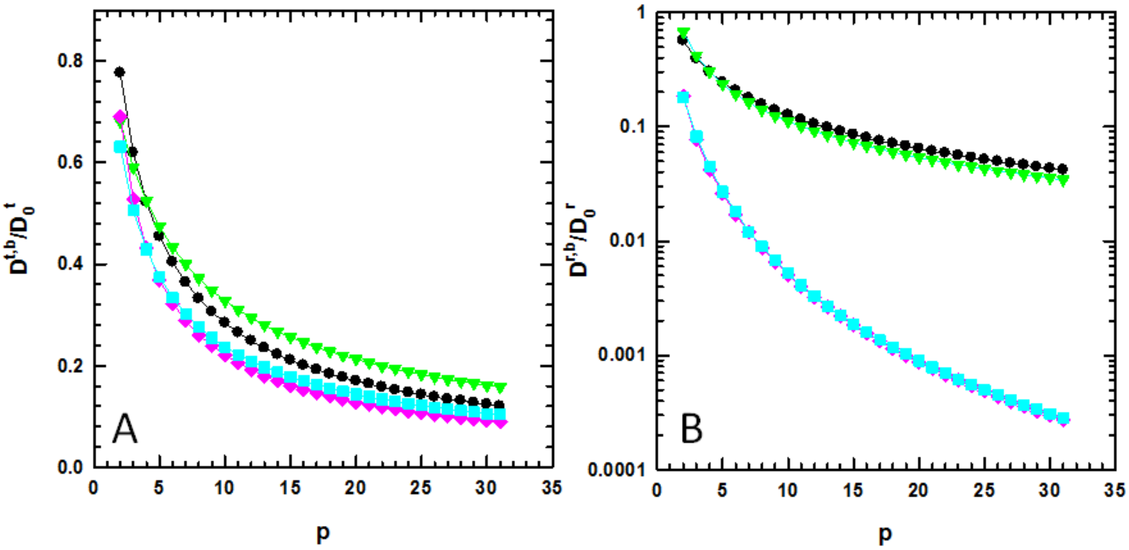

Figure.2. Diffusivities for sphere-chain rod and cylindrical rod of p=2-30 in bulk: (A) Translational diffusivities in direction $\mathbf{n}_{\|}$ (filled black circle), $\mathbf{n}_{\perp 1}$ (filled cyan square), for sphere-chain rod from our model and diffusivities in direction $\mathbf{n}_{\|}$ (filled green triangle) and $\mathbf{n}_{\perp 1}$ (filled pink down triangle) for cylindrical rod from Tirado's model. (B) Rotational diffusivities in direction $\mathbf{n}_{\|}$ (filled green down triangle), $\mathbf{n}_{\perp 1}$ (filled black circle) for sphere-chain rod and diffusivities in direction $\mathbf{n}_{\|}$ (filled pink square) and $\mathbf{n}_{\perp 1}$ (filled red up triangle) for cylindrical rod.

11.4.2 Diffusivities of sphere-chain rod particle parallel above a planar wall

Fig. 3 depicts height-dependent coefficient function of the diffusivities for the sphere-chain rod of aspect ratio 7 and 12 parallel above a wall. These coefficient functions f all approach 1 as h approaches infinity and approach 0 when touching the wall. Fig. 3 (A) shows that the translational diffusivities coefficients in the three directions have a distinct dependence on the elevation and the length of the rod. Specifically, translational diffusivity along $\mathbf{n}_{\|}$ direction decreases the slowest, while along $\mathbf{n}_{\perp 2}$ direction decreases the fastest. This is reminiscent of the translational diffusivity of single particle above wall[51]: diffusivity normal to wall drops much faster than diffusivity parallel to the wall when the sphere is approaching the wall. And all the diffusivities start to drop even when h/a~50, which reflects the far-field nature (scales as O(h/a))of hydrodynamic interactions. Translational diffusivities for the sphere-chain rod, analog to the diffusivities of the single sphere above the wall, are expected to vanish when it touches the wall. Specifically, diffusivities decrease in $O(\ln(h/a))$ manner along $\mathbf{n}_{\|}$ and $\mathbf{n}_{\perp 1}$, and in $O(h/a)$ manner along $\mathbf{n}_{\perp 2}$. We can also observe that the average hydrodynamic hindrance effect due to each sphere will increase for longer rods. This is because, for spheres above a no-plane wall, each sphere will not only experience drag due to its own image (the effect is experiencing more drag in the presence of wall) but also experience drags due to images of its neighboring spheres. One thing to note is that this drag increment effect will become smaller as the rod length increase above a threshold (p~20), since the drag from the image at the distant neighbors will become insignificant. Also this effect is most pronounced at the intermediate range ($1<h/a<12$) In the far-field limit ($h/a>12$), each particle only interact with its own image and images of its nearby spheres, thus, the length dependence averaged hydrodynamic drag will become relatively weaker in the lubrication limit ($h/a<<1$), the lubrication interaction of each sphere with the wall will dominate, therefore the curves will behave asymptotically the same.

The height dependent rotational diffusivities in the three directions are showed in Fig. 2 (D)-(F). Rotations in $\mathbf{n}_{\perp 1}$ and $\mathbf{n}_{\perp 2}$ start to experience evident drag when h is around $20a$ and $30a$, while rotation along $\mathbf{n}_{\|}$ only experience pronounced drag around $5a$. Even though translation and rotation in $\mathbf{n}_{\perp 1}$ and $\mathbf{n}_{\perp 2}$ both involve spheres translate in $\mathbf{n}_{\perp 1}$ and $\mathbf{n}_{\perp 2}$, the drag for rotation seems to be short-ranged compared to that for translation. This can be understood by considering the wall effect on the collective motion of spheres. Considering one sphere translating in bulk and generating a flowing field along the translation direction, a nearby sphere will experience a higher mobility when translates in the same direction, and a lower mobility when translating reverse. When the two spheres are near a wall, the no-slip boundary will significantly change the flow field. In general, the mobility of collective motion will decrease, yet the mobility for relative motion will increase. This hydrodynamic screening effect due to the no-slip boundary has been discussed elsewhere[291]. For translations in $\mathbf{n}_{\parallel}$, $\mathbf{n}_{\perp 1}$, $\mathbf{n}_{\perp 2}$, spheres are all moving in the same direction; therefore the wall will exert a long-range hindrance to these motions. For rotations in $\mathbf{n}_{\perp 1}$ and $\mathbf{n}_{\perp 2}$, half of the spheres composing the rod are moving in the opposite direction of the other half, the wall thus exert a relatively weaker and short-ranged hindrance. Note that the above argument is based on far-field hydrodynamics, and only applies to explain the different initial decreasing trend for rotation when rod is far away ($h/a>10$). When a rod is sufficiently close, the near-field effect will dominate, and the diffusivities will drop dramatically. Note that the axial rotation experience a smaller and short-ranged drag from the wall compared to other types motion. This is because when $h >> a$, the rotation of a sphere parallel to wall scales as $(h/a)^3$, but the decreases of translation diffusivity of spheres scales as (h/a).[292] The rotation diffusivity in $\mathbf{n}_{\perp 1}$ will decrease much faster than rotation in $\mathbf{n}_{\perp 2}$, as rotation in $\mathbf{n}_{\perp 1}$ involves translation of spheres normal to the wall. In the lubrication limit, rotational diffusivities in $\mathbf{n}_{\parallel}$ and $\mathbf{n}_{\perp 2}$ directions will vanish as $O(\ln(h/a))$, but will vanish as $O(h/a)$ in $\mathbf{n}_{\perp 1}$. However, this effect is rather weak for rotation in the $\mathbf{n}_{\parallel}$ direction. This is because the rotation of sphere parallel to wall interact with images of its neighbor in a fashion of ($O(R^{-3})$) (R is the distance between the sphere and the image it interacts with), while for translation of sphere, the fashion is ($O(R^{-1})$).

In contrast with diffusion in bulk, there are coupling effect between different types of motions in the presence of a wall, which manifest themselves as non-zero terms in the off-diagonal entries in the diffusivity tensor. In order to characterize such coupling effect, we define the correlation coefficient as:

$$Cov_{ij} = \frac{D_{ij}}{\sqrt{D_{ii}D_{jj}}} \ . \tag{11.37}$$

For simplicity, *i* and *j* are taking value from 1 to 6, with 1, 2, 3 representing translation in directions of $\mathbf{n}_{\|}$, $\mathbf{n}_{\perp 1}$, and $\mathbf{n}_{\perp 2}$, and 4,5,6 representing rotation in directions $\mathbf{n}_{\|}$, $\mathbf{n}_{\perp 1}$ and $\mathbf{n}_{\perp 2}$. For the configuration that a rod is parallel above a wall, though highly symmetrical, there still exist some weak coupling, a rather weak coupling still exists between translation in directions $\mathbf{n}_{\|}$ and rotation in direction $\mathbf{n}_{\perp 1}$.(Supporting information Fig. S1)

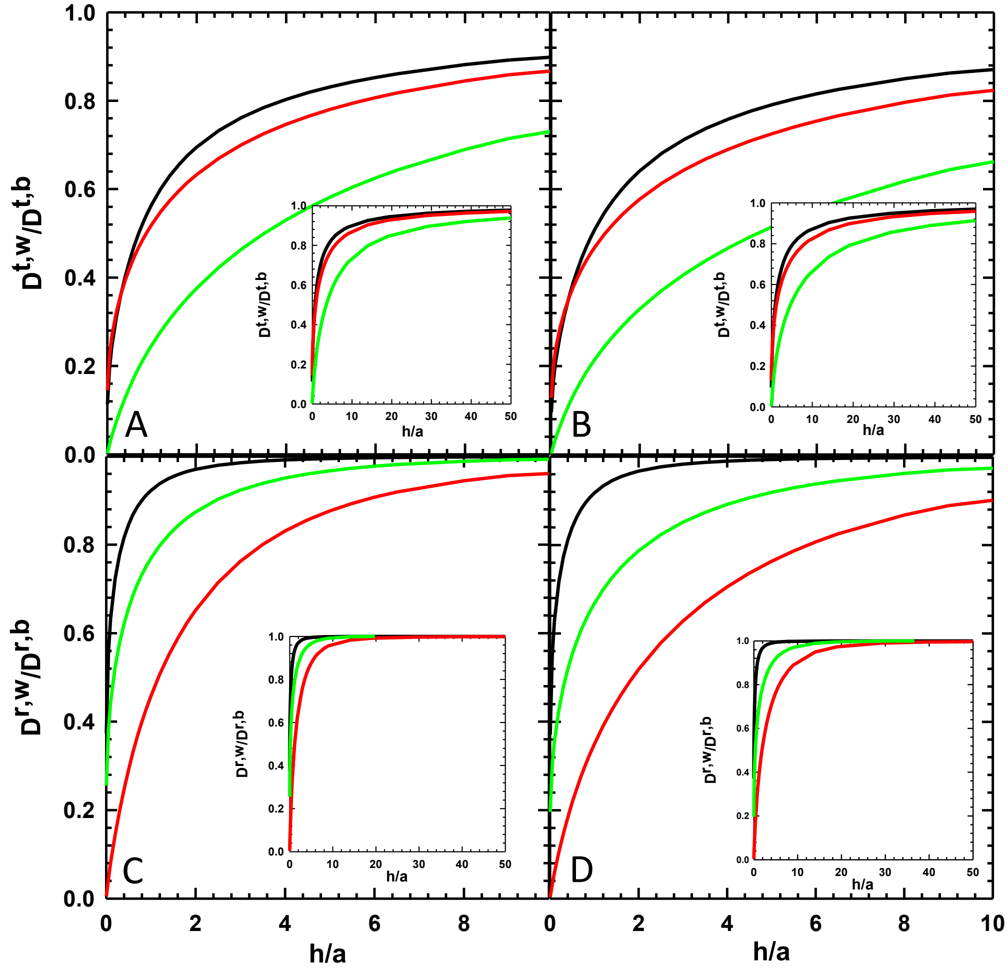

Fig.3. Diffusivities for single sphere-chain rods parallel above a wall: (A)(B) height dependent coefficients for translational diffusivities as a function of *h/a* in direction $\mathbf{n}_{\parallel}$, $\mathbf{n}_{\perp 1}$, $\mathbf{n}_{\perp 2}$ for *p*=7(A), *p*=12(B); (C)(D)) height dependent coefficients for rotational diffusivities as a function of *h/a* in direction $\mathbf{n}_{\parallel}$, $\mathbf{n}_{\perp 1}$, $\mathbf{n}_{\perp 2}$ for *p*=7(A), *p*=12(B).

11.4.3 Diffusivities and couplings of sphere-chain rod particle inclined above a planar wall

We consider the case that a rod *p*=7 forms a 45° angle to the wall (the angle between $\mathbf{n}_{\parallel}$ and $\mathbf{e}_3$ is 45°). Fig. 4 (A)(B) shows self-diffusivities (*i.e.* diagonal terms) as a function of *h*. Note here *h* is defined as the separation distance of the lowest sphere to the plane. When the rod is getting closer to the wall, all self-diffusivities will decrease similarly as the case that a rod is parallel to the wall. However, the exact coefficient function might take different forms. For example, the translational diffusivity decreases much faster than the case rod parallel to the wall, because the motion along $\mathbf{n}_{||}$ involves the normal motion component to the wall. We are particularly interested in the hydrodynamic couplings between different modes of motions. Fig. 4 (C) shows the correlation coefficients (*i.e.* off-diagonal/coupling terms) as a function of h for Cov_{13}, Cov_{15}, Cov_{24} and Cov_{35} in the diffusivity tensor. A translation along $\mathbf{n}_{||}$ direction will induce translation and rotation in $\mathbf{n}_{\perp 2}$ and $\mathbf{n}_{\perp 1}$ (Fig. 4 (E)(F)), with the net effect of aligning itself with and attracting to the wall (i.e. the rod will move less further compared to the case only translation along $\mathbf{n}_{||}$ is allowed). This hydrodynamic effect due to the presence of wall is common in micro-objects moving close to a wall[293]. The coupling between translation in $\mathbf{n}_{\perp 1}$ and rotation in $\mathbf{n}_{\perp 2}$ (Fig. 4 (G)) is due to the non-uniform drag experienced by the rod: lower end experiences more drag than the upper end. When a lateral force applies at $\mathbf{n}_{\perp 1}$, the upper end tends to move faster than the lower end, and consequently the rod rotates. The same reasoning applies to the coupling between translation in $\mathbf{n}_3$ and rotation in $\mathbf{n}_{\perp 1}$ (Fig. 4 (H)). All these correlation coefficients become no longer negligible when the separation height h/a less than 1. We also investigate the angle dependence of the correlation coefficients at fixed separation h/a=0.05, as showed in Fig. 4(D). The coupling of translation in $\mathbf{n}_{||}$ with translation in $\mathbf{n}_{||}$ and rotation in $\mathbf{n}_{\perp 1}$ peaks at ~30° and vanishes at both normal and parallel configurations. The coupling between translation in $\mathbf{n}_{\perp 1}$ and rotation in $\mathbf{n}_3$ is monotonically decreasing from norm configuration, where the imbalance of the drag between two ends is largest, to parallel configuration, where the imbalance disappears. For coupling between translation in $\mathbf{n}_{\perp 2}$ and rotation in $\mathbf{n}_{\perp 1}$ surprisingly peaks at ~80°. This is the reverse upwards flow when particles are moving towards a wall that induces strong rotation in $\mathbf{n}_{\perp 1}$. Note that due to the symmetry of the problem, there is always no coupling between translations in $\mathbf{n}_{\parallel}$ and

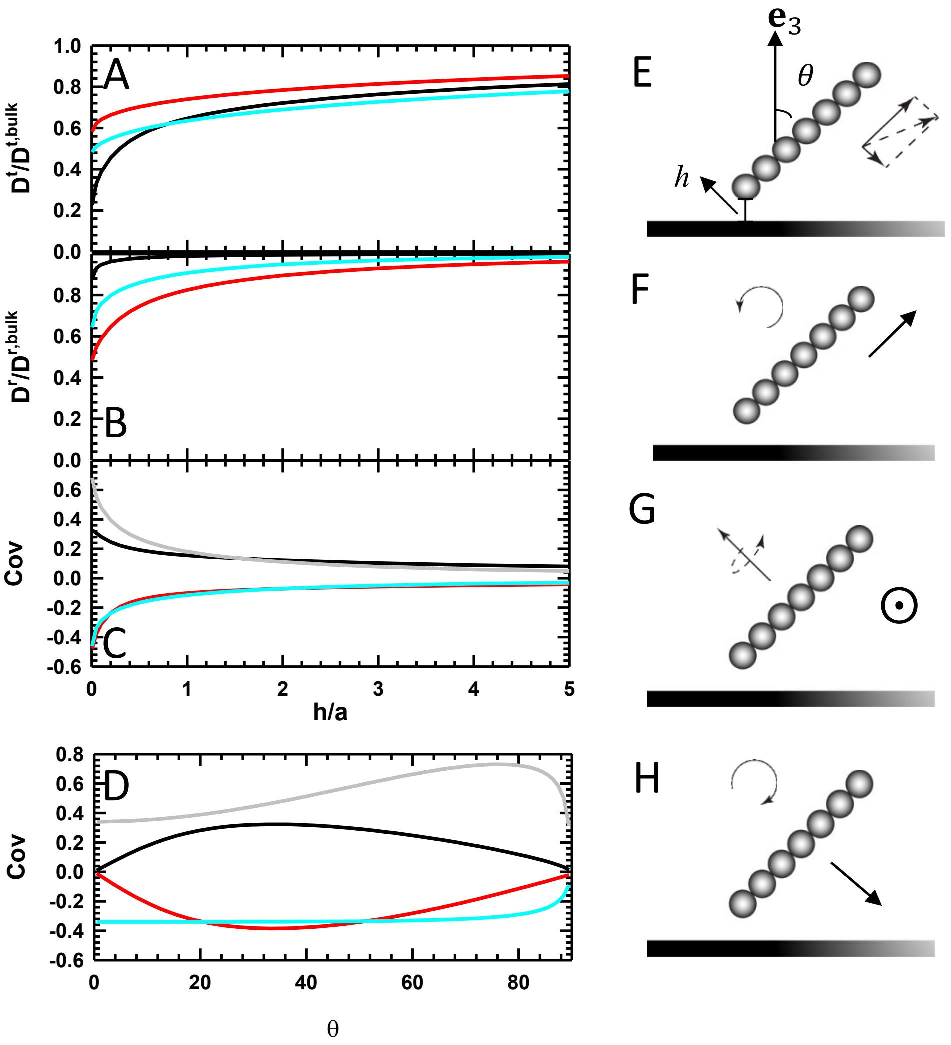

Figure 4. Diffusivities for single sphere-chain of aspect ratio 7 oblique to wall (45 degree polar angle): (A)(B) height dependent coefficients for translational and rotational diffusivities as a function of normalized height *h/a* in direction $\mathbf{n}_{\parallel}$, $\mathbf{n}_{\perp 1}$, $\mathbf{n}_{\perp 2}$; (C) correlation coefficients Cov_{13}, Cov_{15}, Cov_{24} and Cov_{35} for diffusivity tensor components as a function of normalized height *h/a*; (D) correlation coefficients Cov_{13}, Cov_{15}, Cov_{24} and Cov_{35} as a function of θ at h/a=0.05; Schematics for the correlated motions: (E) translation in $\mathbf{n}_{\parallel}$ and translation in $\mathbf{n}_{\perp 2}$, (F) translation in $\mathbf{n}_{\parallel}$ and rotation in $\mathbf{n}_{\perp 1}$, (G) translation in $\mathbf{n}_{\perp 1}$ and rotation in $\mathbf{n}_{\perp 1}$, (H) translation in $\mathbf{n}_{\perp 2}$ and rotation in $\mathbf{n}_{\perp 1}$.

translation in $\mathbf{n}_{\perp 1}$, translation in $\mathbf{n}_{\parallel}$ and rotation in $\mathbf{n}_{\parallel}$, translation in $\mathbf{n}_3$ and rotation in $\mathbf{n}_{\parallel}$.

11.4.4 Dynamic analysis for single rod diffusion in the bulk

Fig. 5 reports the analysis of diffusion trajectories of a single rod with aspect ratio 5. CSD was used to produce simulated random walk trajectories including only Brownian forces. Fig. 5 (B) depicts the parallel and perpendicular MSTD curves extracted from simulation trajectories at different observation times and theoretical predictions from Eq.(11.29). Excellent agreement is reached between simulation and theory. The Brownian rotation characteristic time $\tau_c=1/2D^r$ characterizes time scale for losing directional memory and, therefore, the crossover from anisotropic translational diffusion to isotropic diffusion. At the short time limit $t \ll \tau_c$, the anisotropic translation diffusion behavior is demonstrated by the fast and the slow MSTD curves in parallel and perpendicular directions, respectively. As the observation time t exceeds t_c, the two curves finally converge towards one curve, indicating the transition from anisotropic diffusion to isotropic. Fig. 5 (C) shows the orientation auto-correlation function calculated from simulation trajectories and theoretical prediction from Eq.(11.31). Excellent agreement is reached between simulation and theory. The autocorrelation function curve also confirms that the rod will quickly lose correlation in orientation at the characteristic time scale τ_c, leading to the transition from anisotropic diffusion to isotropic diffusion,

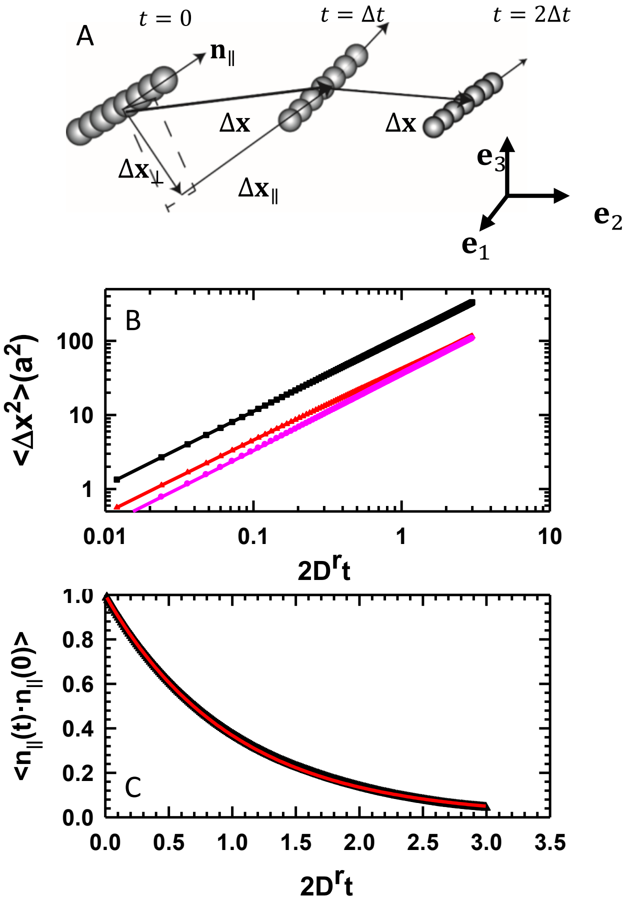

Figure 5. Mean squared translational displacement (MSTD) and orientation autocorrelation function for simulation trajectories of single rod *p*=5 in bulk: (A) 3D sequential snapshots of colloidal rod configuration. Displacement vector $\Delta\mathbf{x}$ can be decomposed into components parallel and perpendicular to its axis (in $\mathbf{n}_{\parallel}$ direction). $\mathbf{e}_1$=(1,0,0), $\mathbf{e}_2$=(0,1,0) and $\mathbf{e}_3$=(0,0,1) are unit vectors of the lab frame. (B) Simulation extracted and theoretical predicted MSTD curve from Eq.(11.29)(11.30) (black square and solid line) and components in parallel direction (red triangle and solid line) and perpendicular direction (pink circle and solid line). (C) Orientation autocorrelation function from simulation and theoretical prediction from Eq. (11.31) (black triangle and red solid line).

11.4.5 Single rod levitated above a planar wall: equilibrium configuration and dynamics

Fig. 6 report equilibrium distributions of rods with aspect ratio 4, 7, 12 levitated above a planar wall. In the simulations, rods are subject to gravitational force, electrostatic repulsion, and Brownian motion. The balance between gravitational force and electrostatic repulsion confines the rod to the vicinity of the wall. We use free energy landscapes parameterized by (z, θ) to characterize the equilibrium distribution of the configuration. As shown in Fig. 6 (A)-(F), 2D free energy landscape from theoretical prediction (Eq.(11.27)(11.28)) and constructed from simulations via Boltzmann inversion are in good agreements for rods of three aspect ratios. For rods of different length, the most probable configuration is aligning with the wall (i.e. θ=90°) from the effect of gravity and the electrostatic repulsion from wall. Note that longer rods generally is more constrained in the sampled configuration space parameterized by (z, θ). At the same height, longer rods will be more constrained in θ due to electrostatic repulsion from the wall, whose total strength proportional to length. In addition, longer rods will be more constrained in z due to the increased gravity of the longer rods. We also plot the projected one-dimensional free energy landscape in z and θ using Eq.(11.28), as shown in Fig. 6 (G)(H). As the aspect ratio increases, the frequent sampling region ($W<6kT$) in height z is reduced from $6a$ to $2a$. Regarding orientation, a rod of aspect 4 has a non-vanishing probability to take the stand-up configuration(i.e. θ=0°), yet a rod of aspect 12 can only sample ±10° deviation from the parallel configuration.

In experiments of particle tracking near a planar wall, MSTD is often the dynamic aspect of interest. Fig. 7 (A) shows the time-lapsed 2D parallel and perpendicular components of MSTD from the simulation and the theoretical curves from Eq. **Error! Reference source not found.**(11.34). Similar to the 3D translational Brownian motion in bulk, faster diffusion is observed along director direction until the crossover to isotropic diffusion occurs at the Brownian rotation time scales. As for the longer time scale isotropic diffusion, the longer rod will have a smaller average diffusivity due to the

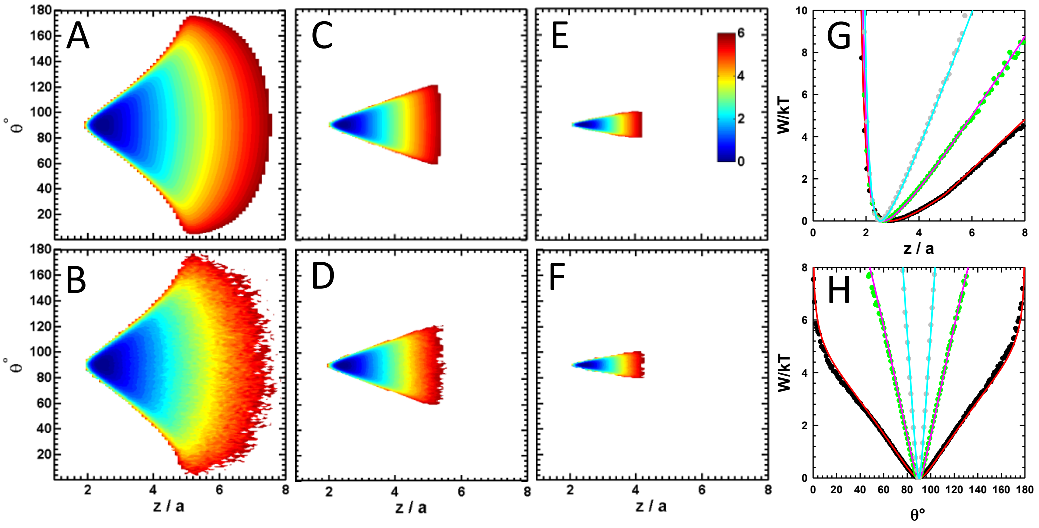

Figure 6. Free energy landscape analysis for single rod electrostatically levitated above wall: (A-F) 2D theoretical FEL from (11.27)(top row,(A)(C)(E)) and simulation extracted via inverse Boltzmann analysis (bottom row,(B)(D)(F))as a function of *z/a* and *θ* for rods of aspect ratio 4 7, 12. (G)(H) 1D FEL as a function of *z/a* and *θ* for rods of aspect ratio 4, 7 and 12. Symbols are results from inverse Boltzmann analysis, solid lines are theoretical prediction from Eq.(11.28).

increased length and average lower heighted sampled, as showed in Fig.7 (B). Fig. 7(C) shows results on the diffusion dynamics of rod particle (*p*=7) normal to the underlying wall: the *z*-direction component of MSTD curves show a systematic decreasing as the elevation of the rod decreases, which is due to the increasing hydrodynamic hindrance as the rod is closer to the wall. The diffusivities extracted from the initial slopes of these curves based on Eq. (11.35) have good agreement with theory prediction from Eq. (11.36), as showed in Fig. 7(D). The large variation of the diffusivity along the elevation also suggests that we treating the diffusivities as a constant might result in significant error.

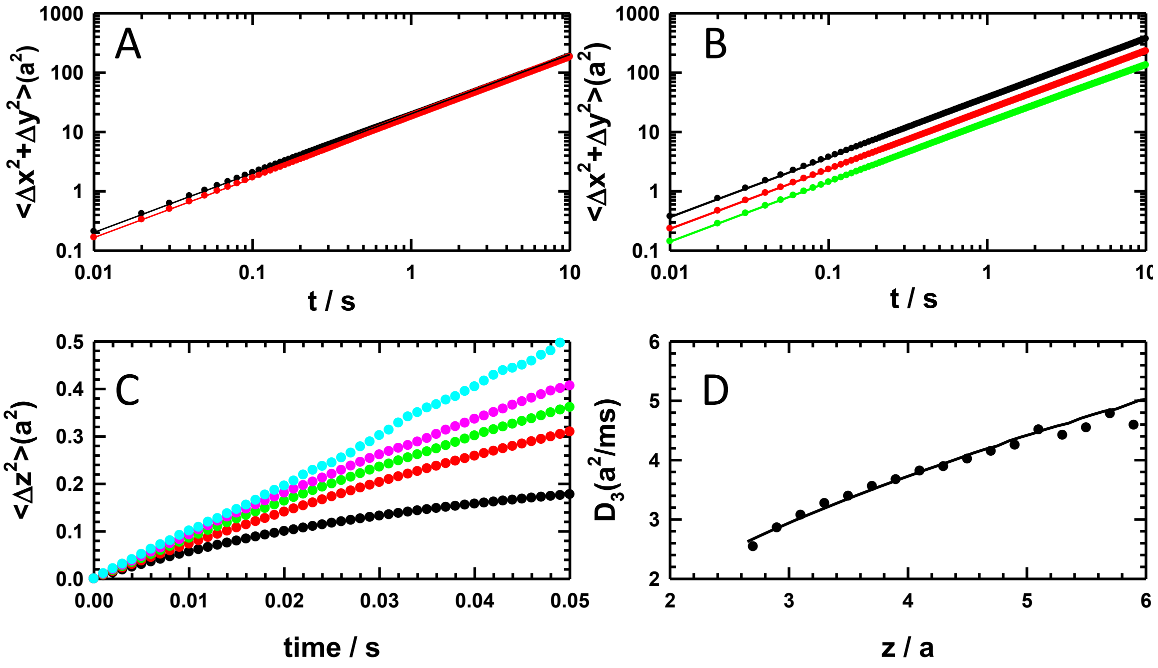

Figure 7. Analysis of trajectories for single rod electrostatically levitated above wall: (A) Simulation extracted and theoretical predicted (Eq. (11.32)) MSTD curve and components in parallel direction (black circle and solid line) and perpendicular direction (red circle and solid line) for a rod with p=4. (B) MSTD as a function of lapsed time from simulation and theory on the log-log plot for aspect ratio 4, 7 and 12. Symbols are results from simulation data, solid lines are theoretical predictions(Eq. **Error! Reference source not found.**). (C) MSTD curves (from bottom to top) as a function of time at elevation of 2.9a, 3.9a, 4.9a, 5.9a, 6.9a; (D) extracted elevation dependent diffusivity via Eq. (11.35), and theory predicted values via Eq. (11.36) .

11.5 Conclusion

We present a diffusivity calculation method and simulation method for colloidal rods motion near a planar wall. The method is adapted from Stokesian Dynamics method by modeling a rod-shape particle as a chain of touching spheres. The calculated diffusivities for the sphere-chain rod is compared with the widely used cylindrical result from Tirado. A similar trend of diffusivities changing with rod's aspect ratio is identified. In this work, we have developed the CSD algorithm for simulating rod-shaped particle suspensions with hydrodynamic interactions. We have simulated and analyzed two experiments: an isolated rod diffuses in bulk and above a planar wall. We have demonstrated that this algorithm can produce trajectories matched with an underlying theory for dynamic analysis and equilibrium analysis. The analysis procedure for MSTD and FEL is of practical importance for research on the experimental measurement of forces and motions for isolated rods.[294] Even though we only demonstrated the simulation techniques on the single particle level, we can readily extend to multiple rods simulation by including extra components of constraints, resistance tensors, and forces.

11.6 Supplementary materials

A. Complete description for constructing grand resistance tensor

Consider the problem where N hard spheres of radius a suspended in the impressible Newton unbounded flow without ambient flow at zero Reynolds number limit, the equation of motion is

$$\begin{pmatrix} \mathbf{U} \\ \mathbf{\Omega} \end{pmatrix} = \mathbf{M} \begin{pmatrix} \mathbf{F} \\ \mathbf{L} \end{pmatrix} \tag{11.38}$$

where $\mathbf{U}$ and $\mathbf{\Omega}$ are translational and rotational velocities for N spheres, $\mathbf{U}= (\mathbf{U}^{(1)}, \mathbf{U}^{(2)},\ldots)$, $\mathbf{\Omega}= (\mathbf{\Omega}^{(1)}, \mathbf{\Omega}^{(2)},\ldots)$, $\mathbf{F}$ and $\mathbf{L}$ are the forces and torques acting on the spheres, $\mathbf{F}= (\mathbf{F}^{(1)}, \mathbf{F}^{(2)},\ldots)$, $\mathbf{L}= (\mathbf{L}^{(1)}, \mathbf{L}^{(2)},\ldots)$. $\mathbf{M}$ is the grand mobility tensor of size $6N$ by $6N$. The corresponding resistance problem is to calculate the hydrodynamic forces and torques for N sphere moving in a flow without external imposed flow, and can be formulated as

$$\begin{pmatrix} \mathbf{F} \\ \mathbf{L} \end{pmatrix} = \mathbf{R} \begin{pmatrix} \mathbf{U} \\ \mathbf{\Omega} \end{pmatrix} \tag{11.39}$$

where $\mathbf{R}$ is the grand resistance tensor and relates to the grand mobility tensor as

$$\mathbf{R} = \mathbf{M}^{-1} \ . \tag{11.40}$$

Grand resistance tensor for spheres in bulk

The Faxen's first law[295] relates the velocities of a spherical particle α to force $\mathbf{F}^\alpha$ and torque $\mathbf{L}^\alpha$ on it and the effect of the disturbance flow generated by all the other particles as:

$$U_i^\alpha = \frac{F_i^\alpha}{6\pi\mu a} + (1 + \frac{a^2}{6}\nabla_\alpha^2) u_i(\mathbf{r}^\alpha) \tag{11.41}$$

$$\Omega_i^\alpha = \frac{L_i^\alpha}{8\pi\mu a^3} + \frac{1}{2}\nabla \times u_i(\mathbf{r}^\alpha) \tag{11.42}$$

where μ is the viscosity of the fluid, $u_i(\mathbf{r}^\alpha)$ is the disturbance velocity field at the position of sphere α caused by the motion of all the other particle, given as

$$\mathbf{u}(\mathbf{r}^\alpha) = \sum_{\beta,\beta\neq\alpha}^{N} \begin{matrix} [(1+\frac{a^2}{6}\nabla_\beta^2)\mathbf{J}(\mathbf{r}^\alpha,\mathbf{r}^\beta)\cdot\mathbf{F}^\beta + \frac{1}{2}\nabla_\beta \mathbf{J}(\mathbf{r}^\alpha,\mathbf{r}^\beta)\cdot\mathbf{L}^\beta \\ +\frac{1}{2}(1+\frac{a^2}{10}\nabla_\beta^2)\mathbf{K}:\mathbf{S}^\beta + \ldots \end{matrix} \tag{11.43}$$

where $\mathbf{J}$ is the green function for the velocity field at $\mathbf{x}$ generated by a unit point force at $\mathbf{y}$, and is given as

$$\mathbf{J}(\mathbf{x},\mathbf{y}) = \frac{1}{8\pi\mu}(\frac{1}{r} + \frac{\mathbf{rr}}{r^3}) \tag{11.44}$$

where $\mathbf{r} = \mathbf{x} - \mathbf{y}$. $\mathbf{S}$ is stresslet, and

$$\mathbf{K} = \frac{1}{2}[\nabla_\beta \mathbf{J}(\mathbf{r}^\alpha,\mathbf{r}^\beta) + (\nabla_\beta \mathbf{J}(\mathbf{r}^\alpha,\mathbf{r}^\beta))^T] \tag{11.45}$$

We only consider the forces and torques in this paper, which has been shown as a good approximation to the original system without imposed shear flow[280,281]. The far-field multi-body interaction then can be expressed in a grand tensorial form as:

$$\begin{pmatrix}\mathbf{U}\\ \mathbf{\Omega}\end{pmatrix}=\mathbf{M}_{pp}^{\infty}\begin{pmatrix}\mathbf{F}\\ \mathbf{L}\end{pmatrix}=\begin{pmatrix}\mathbf{M}_{UF}^{\infty} & \mathbf{M}_{\Omega F}^{\infty}\\ \mathbf{M}_{UL}^{\infty} & \mathbf{M}_{\Omega L}^{\infty}\end{pmatrix}\begin{pmatrix}\mathbf{F}\\ \mathbf{L}\end{pmatrix} \tag{11.46}$$

where ∞ denotes that only far-field interaction is considered. The elements of $\mathbf{M}_{\mathrm{UF}}$ is obtained through assembling N mobility tensor $\mathbf{M}_{UF,\alpha\alpha}^{\infty}$ and $N\times(N-1)$ mobility tensor $\mathbf{M}_{UF,\alpha\beta}^{\infty}$, which are given as

$$\mathbf{M}_{UF,\alpha\beta}^{\infty}=\frac{\mathbf{I}\delta_{\alpha\beta}}{6\pi\mu a}+(1-\delta_{\alpha\beta})(1+\frac{a^2}{6}\nabla_{\alpha}^2)(1+\frac{a^2}{6}\nabla_{\beta}^2)\mathbf{J}(\mathbf{r}^{\alpha},\mathbf{r}^{\beta}) \tag{11.47}$$

Similarly, we can construct the $\mathbf{M}_{\Omega\mathrm{F}}$, $\mathbf{M}_{\mathrm{UL}}$ and $\mathbf{M}_{\Omega\mathrm{L}}$

$$\mathbf{M}_{\Omega L,\alpha\beta}^{\infty}=\frac{\mathbf{I}}{8\pi\mu a^3}\delta_{\alpha\beta}+(1-\delta_{\alpha\beta})(\frac{1}{2}\nabla_{\alpha}\times\frac{1}{2}\nabla_{\beta}\times)\mathbf{J}(\mathbf{r}^{\alpha},\mathbf{r}^{\beta}) \tag{11.48}$$

$$\mathbf{M}_{\Omega F,\alpha\beta}^{\infty}=(1-\delta_{\alpha\beta})(\frac{1}{2}\nabla_{\alpha}\times)(1+\frac{a^2}{6}\nabla_{\beta}^2)\mathbf{J}(\mathbf{r}^{\alpha},\mathbf{r}^{\beta}) \tag{11.49}$$

$$\mathbf{M}_{UL,\alpha\beta}^{\infty}=(1-\delta_{\alpha\beta})(1+\frac{a^2}{6}\nabla_{\alpha}^2)(\frac{1}{2}\nabla_{\beta}\times)\mathbf{J}(\mathbf{r}^{\alpha},\mathbf{r}^{\beta}) \tag{11.50}$$

The explicit expressions can be found in the reference[281].

The inversion of M^{∞} provides an approximation to the resistance tensor R^{∞} with multi-body hydrodynamics in the far-field regime[281]. However, the lubrication interaction when particles are closed enough to each other is still lacking. A proper account for the near-field interaction in the resistance tensor is by adding the pair-wise resistance tensor to **R**. Then, the grand resistance tensor for spheres in bulk is given as

$$\mathbf{R} = (\mathbf{M}_{\mathbf{PP}}^{\infty})^{-1} + \mathbf{R}_{\mathbf{2B}} - \mathbf{R}_{\mathbf{2B}}^{\infty} \tag{11.51}$$

which includes both the far-field multi-body interaction (*i.e.* $(\mathbf{M}_{\mathbf{PP}}^{\infty})^{-1}$)and the near-field pair-wise lubrication (*i.e.* $\mathbf{R}_{\mathbf{2B}}$). The far-field pairwise resistance (*i.e.* $\mathbf{R}_{\mathbf{2B}}^{\infty}$) is subtracted since the far-field two-body interaction is already accounted in $(\mathbf{M}_{\mathbf{PP}}^{\infty})^{-1}$.

The two-body exact resistance tensor $\mathbf{R}_{\mathbf{2B}}$ is a $6N \times 6N$ tensor, which is constructed by assembling $N\times(N-1)$ $\mathbf{R}_{2B,\alpha\beta}$ tensor (12 by 12) between particle α and β:

$$\mathbf{R}_{2B,\alpha\beta} = \begin{pmatrix} \mathbf{A}_{\alpha\alpha} & \mathbf{A}_{\alpha\beta} & \mathbf{B}'_{\alpha\alpha} & \mathbf{B}'_{\alpha\beta} \\ \mathbf{A}_{\beta\alpha} & \mathbf{A}_{\beta\beta} & \mathbf{B}'_{\beta\alpha} & \mathbf{B}'_{\beta\beta} \\ \mathbf{B}_{\alpha\alpha} & \mathbf{B}_{\alpha\beta} & \mathbf{C}_{\alpha\alpha} & \mathbf{C}_{\alpha\beta} \\ \mathbf{B}_{\beta\alpha} & \mathbf{B}_{\beta\beta} & \mathbf{C}_{\beta\alpha} & \mathbf{C}_{\beta\beta} \end{pmatrix} \tag{11.52}$$

This resistance tensor contains second-rank 3 by 3 tensors **A**, **B**, **C**. These tensors have the following symmetry properties:

$$A_{\alpha\beta,ij} = A_{\beta\alpha,ji}, B_{\alpha\beta,ij} = B'_{\beta\alpha,ji}, C_{\alpha\beta,ij} = C_{\beta\alpha,ji} \tag{11.53}$$

And can be written as

$$\begin{aligned} A_{\alpha\beta,ij} &= X^{A}_{\alpha\beta}\hat{r}_i\hat{r}_j + Y^{A}_{\alpha\beta}(\delta_{ij} - \hat{r}_i\hat{r}_j) \\ B_{\alpha\beta,ij} &= Y^{B}_{\alpha\beta}\varepsilon_{ijk}\hat{r}_k \\ C_{\alpha\beta,ij} &= X^{C}_{\alpha\beta}\hat{r}_i\hat{r}_j + Y^{C}_{\alpha\beta}(\delta_{ij} - \hat{r}_i\hat{r}_j) \end{aligned} \tag{11.54}$$

where $\hat{\mathbf{r}} = \mathbf{r}^{\alpha\beta} / r^{\alpha\beta}$ is the unit vector joining along the line of centers, and **X**, **Y** are resistance functions for motions in directions along and perpendicular to axis, respectively. Those functions, and errata, are documented elsewhere[279,296]. Similarly The two-body far field resistance tensor $\mathbf{R}_{2B}^{\infty}$ is assemblage of N×(N–1) tensor $\mathbf{R}_{2B,\alpha\beta}^{\infty}$ (12 by 12), which is given as

$$\mathbf{R}_{2B,\alpha\beta}^{\infty} = (\mathbf{M}_{2B,\alpha\beta}^{\infty})^{-1} \, . \tag{11.55}$$

The explicit expressions are given in reference[281].

Grand resistance tensor for spheres in near a planar wall

The presence of a no-slip surface will significantly modify the fluid field of a stokelet. The effect of no-slip boundary can be accounted by constructing an image system composed of stokeslet, stokes-doublet and source-doublet on the other side of the surface[1]. Then, the green function for the velocity field at **x** generated by a unit point force at **y** near a planar no-slip wall located at H with normal unit vector $\boldsymbol{\delta}_3$ is given as[1,286]

$$\begin{aligned} \mathbf{G}(\mathbf{x},\mathbf{y};H) = \mathbf{J}(\mathbf{x},\mathbf{y}) - \mathbf{J}(\mathbf{x},\mathbf{y}';H) + (\mathbf{y}\cdot\boldsymbol{\delta}_3 - H)^2 \nabla_{y'}^2 \mathbf{J}(\mathbf{x},\mathbf{y}')\cdot\mathbf{P} \\ + 2(\mathbf{y}\cdot\boldsymbol{\delta}_3 - H)(\mathbf{P}\cdot\nabla_{y'}\mathbf{J}(\mathbf{x},\mathbf{y}')\cdot\boldsymbol{\delta}_3)^T \end{aligned} \tag{11.56}$$

where $y'=y-2(\mathbf{y}\cdot\boldsymbol{\delta}_3-H)$, $\mathbf{P}=\mathbf{I}-2\boldsymbol{\delta}_3\boldsymbol{\delta}_3$, T indicates transposition.

The grand resistance tensor for spheres above a planar no-slip wall is given as[286]

$$\mathbf{R} = (\mathbf{M}_{\mathbf{PW}}^{\infty})^{-1} + \mathbf{R}_{\mathbf{2B}} + \mathbf{R}_{\mathbf{W}} - (\mathbf{R}_{\mathbf{2B},\infty} + \mathbf{R}_{\mathbf{W},\infty}) \tag{11.57}$$

which includes both the many-bodied far-field resistance tensor above a no-slip plane (*i.e.* $(\mathbf{M}_{\mathbf{PW}}^{\infty})^{-1}$), which is the inversion of many-bodied far-field mobility tensor, and the pair-wise lubrication interactions. The pair-wise lubrication interaction is obtained by first adding two-body particle-particle exact resistance tensor $\mathbf{R_{2B}}$ and the particle-wall exact resistance tensor $\mathbf{R_W}$, and then subtract the far-field resistance tensor $\mathbf{R_{2B,\infty}} + \mathbf{R_{W,\infty}}$ to avoid the double counting of the far-field particle-particle and particle-wall interaction in $(\mathbf{M_{PW}^{\infty}})^{-1}$ and $\mathbf{R_{2B}} + \mathbf{R_W}$. The elements in the $\mathbf{R}_{2B}$ and $\mathbf{R}_{2B}^{\infty}$ are the same as Eqs. (11.52)(11.55), and $(\mathbf{M_{PW}^{\infty}})^{-1}$ can be obtained similarly through (11.47)-(11.50) but replacing **J** with **G**. The explicit expressions for $(\mathbf{M_{PW}^{\infty}})^{-1}$ can be found in reference[286].

The tensor $\mathbf{R}_w$ is constructed by assembling *N* tensors of $\mathbf{R}_{w,\alpha}$ (6 by 6), which consists of the exact resistance function of particle α moving above a planar wall. The explicit expression of resistance functions are summarized in references[51,297]. The tensor $\mathbf{R}_w^{\infty}$ is constructed through *N* tensor $\mathbf{R}_{w,\alpha}^{\infty}$ of size 6 by 6, which consists the far-field resistance functions of particle α moving above a planar wall. The explicit expression of resistance functions are summarized in references[51,297].

Sphere-chain model of rod-shaped particle

We model the rod-like particle as a linear chain of touching spheres, as showed in Fig. 1. In this model, the spheres are only allowed to rotate along the axis of the rod. In other words, non-axial rotation (rotation in the direction perpendicular to the rod) will not couple with motions of any other types. Therefore, we can set off-diagonal terms that coupled with non-axis rotation terms to be 0 in the resistance tensor $\mathbf{R}_{2B,\alpha\beta}^{\infty}$, $\mathbf{R}_{2B,\alpha\beta}$, $\mathbf{R}_{w,\alpha}$, $\mathbf{R}_{w,\alpha}^{\infty}$ before adding up to the grand resistance tensor. For the far-field grand mobility tensor

$\mathbf{M}^{\infty}$, we first set off diagonal terms involving coupling to non-axis to be zero before we inverting the matrix.

Extra care needs to be taken when calculating the resistance tensor $\mathbf{R}_{2B,\alpha\beta}$ for neighboring touching sphere, since resistance function $X_{\alpha\beta}^{A}$ diverge as $O((r\text{-}2a)^{-1})$ and require summation of infinite series when two spheres are close to touching[296]. Due to the axisymmetry of this problem, we could calculate $X_{\alpha\beta}^{A}$ by inverting the mobility tensor function $x_{\alpha\beta}^{a}$, specifically

$$\begin{pmatrix} X_{11}^{A} & X_{12}^{A} \\ X_{21}^{A} & X_{22}^{A} \end{pmatrix} = \begin{pmatrix} x_{11}^{a} & x_{12}^{a} \\ x_{21}^{a} & x_{22}^{a} \end{pmatrix}^{-1} \tag{11.58}$$

where $x_{\alpha\beta}^{a}$ values comes from the classic problem of the drag on two sphere following each other along their line of centers. From Batchelor's[298] result for touching spheres, we have: $x_{11}^{a} = x_{12}^{a} = x_{21}^{a} = x_{22}^{a} = 0.775$. However, the mobility tensor cannot be directly inverted since it is a singular matrix. We could slightly perturb the matrix and invert it, and the resistance matrix is given as

$$\begin{pmatrix} X_{11}^{A} & X_{12}^{A} \\ X_{21}^{A} & X_{22}^{A} \end{pmatrix} = \begin{pmatrix} 0.775+\varepsilon & 0.775-\varepsilon \\ 0.775-\varepsilon & 0.775+\varepsilon \end{pmatrix}^{-1} \tag{11.59}$$

where ε is a small number, say 1e-5. The resistance function $Y_{\alpha\beta}^{A}$ will diverge as O(ln(r-2a)$^{-1}$), and we use r=(2+1e-3)a in the calculation. The resistance function of axial rotation for nearby spheres is not singular when touching, and is given as $X_{11}^{C} = 1.052$, and $X_{12}^{C} = -0.15$.

B. Summary of fitting equations for diffusivities

Diffusivity in bulk for cylindrical rod particle from Tirado's model[290,299,300]

$$D_{\parallel}^{t,b}(L,p) = \frac{kT}{2\pi\mu L}(\ln p - 0.207 + \frac{0.980}{p} - \frac{0.1333}{p^2}) \tag{11.60}$$

$$D_{\perp}^{t,b}(L,p) = \frac{kT}{4\pi\mu L}(\ln p + 0.839 + \frac{0.185}{p} + \frac{0.2333}{p^2}) \tag{11.61}$$

$$D_{\parallel}^{r,b}(L,p) = \frac{kT}{3.841\pi\mu La^2}(1 + \frac{0.693}{p} - \frac{0.2263}{p^2} + \frac{0.0326}{p^3})^{-1} \tag{11.62}$$

$$D_{\perp}^{r,b}(L,p) = \frac{3kT}{\pi\mu L^3}(\ln p - 0.662 + \frac{0.917}{p} - \frac{0.05}{p^2}) \tag{11.63}$$

Diffusivity in bulk for sphere-chain rod particle from our model

$$D_{\parallel}^{t,b}(\mathrm{L},p) = \frac{kT}{2\pi\mu L}(\ln p + \frac{-1.951p^2 - 9.132p + 69.16}{p^2 + 39p + 44.4}) \tag{11.64}$$

$$D_{\perp}^{t,b}(\mathrm{L},p) = \frac{kT}{4\pi\mu L}(\ln p + \frac{-0.3604p^2 + 28.36p + 72.36}{p^2 + 36.29p + 34.9}) \tag{11.65}$$

$$D_{\perp}^{r,b}(L,p) = \frac{3kT}{\pi\mu L^3}(\ln p + \frac{-1.373p^3 - 19.39p^2 - 148p + 265.1}{p^3 + 56.43p^2 + 54.29p + 268.5}) \tag{11.66}$$

$$D_{\parallel}^{r,b}(L,p)=\frac{kT}{\pi\mu La^2}(\frac{0.3264p^2+0.01547p-0.01341}{p^2+0.4029p-0.1136}) \tag{11.67}$$

where μ is the viscosity of the solvent, $2a$ and L are the diameter and length of the cylinder, L is the length of the cylinder, p=L/2a is the aspect ratio of the cylinder.

Analytical result of diffusivities of infinitely long cylindrical rod above wall[54,301,302]

$$D_1^{t,w}(L,h)=\frac{kT}{2\pi\mu L}(\cosh(\frac{h+a}{a})) \tag{11.68}$$

$$D_2^{t,\mathrm{w}}(L,h)=\frac{kT}{4\pi\mu L}(\cosh(\frac{h+a}{a})) \tag{11.69}$$

$$D_3^{t,\mathrm{w}}(L,h)=\frac{kT}{4\pi\mu L}(\log(\frac{h+a+\sqrt{(h+a)^2-a^2}}{a})-\frac{\sqrt{(h+a)^2-a^2}}{h+a}) \tag{11.70}$$

$$D_1^{\mathrm{r,w}}(L,h)=\frac{kT}{4\pi\mu La^2}(\frac{\sqrt{(h+a)^2-a^2}}{h+a}) \tag{11.71}$$

$$D_2^{\mathrm{r,w}}(L,h)=\frac{3kT}{\pi\mu L^3}(\cosh(\frac{h+a}{a})) \tag{11.72}$$

$$D_3^{\mathrm{r,w}}(L,h)=\frac{3kT}{\pi\mu L^3}(\log(\frac{h+a+\sqrt{(h+a)^2-a^2}}{a})-\frac{\sqrt{(h+a)^2-a^2}}{h+a}) \tag{11.73}$$

C. Approximate diffusivities for cylindrical rod above wall

Here we showed that the height dependent coefficients from the chain-sphere rod model can be used to approximate the diffusivities of cylinder rod. In the far-field limit, the flow field generated by the translating object, irrespective of its shape, can be approximated by the flow field generated by a point force acting on the center of the translating object.[50] This represents the leading term of the multipole expansion of the flow field generated by a force distribution on the translating object. In the far-field limit, the hydrodynamic interaction between a cylindrical object and a wall can therefore be approximated by the interaction between sphere-chain rod and wall.[303] The leading error in the approximation is expected not to exceed $O((a/(h+a))^3)$. Therefore, at $h/a >> 1$, the height dependent coefficients of the sphere-chain rod model are the asymptote limit of the height-dependent coefficients of the cylindrical rod.

At separations of $h/a << 1$, the height-dependent coefficient can be approximated using the analytical results for infinite cylinders adjacent to a plane. The analytical result is another asymptote limit of for the diffusivities of a cylinder. When h is about the magnitude of a (radius of the sphere), it is no longer appropriate to approximate the cylindrical particle by either method. The coefficient within this range is found by fitting a curve that matches the two asymptote limits.

Below, we summarize the fitted curves that approximate the common height dependent diffusivities for cylinder rod with different aspect ratio p parallel above a no-slip wall:

i) ***(the rod close or far away from the wall)****$h<a$ or $h>10a$, $6< p < 30$*

$$D_1^{t,\mathrm{w}}(L,p,h) = D_{\parallel}^{t,b}(L,p) f_{\parallel}(h)$$

$$f_{\parallel}(h) = \frac{\left(0.9909(z/a)^3 + 0.3907(z/a)^2 - 0.1832(z/a) - 0.001815\right)}{\left((z/a)^3 + 2.03(z/a)^2 - 0.3874(z/a) - 0.07533\right)} \quad (11.74)$$

$$D_2^{t,b}(L,p,h) = D_\perp^{t,b}(L,p) f_\perp(h)$$
$$f_\perp(h) = \frac{\left(0.9888(z/a)^3 + 0.788(z/a)^2 - 0.207(z/a) - 0.004766\right)}{\left((z/a)^3 + 3.195(z/a)^2 - 0.09612(z/a) - 0.1523\right)} \quad (11.75)$$

$$D_3^{r,b}(L,p,h) = D_\perp^{r,b}(L,p) f_R(h)$$
$$f_R(h) = \frac{\left(0.998(z/a)^3 + 131.1(z/a)^2 + 21.25(z/a) + 0.01275\right)}{\left((z/a)^3 + 128.7(z/a)^2 + 121.1(z/a) + 2.897\right)} \quad (11.76)$$

ii) ***(the rod is in the intermediate distance to the wall)****a<h<10a, 6< p < 30*

$$\begin{aligned} D_1^{t,\mathrm{w}}(L,p,h) &= D_\parallel^{t,b}(L,p) f_\parallel(h) g_\parallel(p) \\ g_\parallel(p) &= 1.1669 - 0.0091p \end{aligned} \quad (11.77)$$

$$\begin{aligned} D_2^{t,b}(L,p,h) &= D_\perp^{t,b}(L,p) f_\perp(h) g_\perp(h) \\ g_\perp(p) &= 1.2239 - 0.0120p \end{aligned} \quad (11.78)$$

$$\begin{aligned} D_3^{r,b}(L,p,h) &= D_\perp^{r,b}(L,p) f_R(h) g_R(p) \\ g_R(p) &= 1.154 - 0.0096p \end{aligned} \quad (11.79)$$

where in Eq. (11.77)(11.78)(11.79) we introduce extra correction factor g(p) to correct the extra length dependence for diffusivities above wall when h is about the magnitude of *a*. The error for these expressions are generally less than 10%.

D. Derivation of Time-lapsed mean squared displacement for single rod diffusion in the bulk

The transform matrix from spherical coordinates to Cartesian coordinate is given as

$$\mathbf{T} = \begin{pmatrix} \sin\theta\cos\phi & \cos\theta\cos\phi & -\sin\phi \\ \sin\theta\sin\phi & \cos\theta\sin\phi & \cos\phi \\ \cos\theta & -\sin\theta & 0 \end{pmatrix}. \tag{11.80}$$

In the body frame, the translational diffusivity tensor of rod in the body frame is given as

$$\mathbf{D}' = \begin{pmatrix} D^t_{n'_1} & 0 & 0 \\ 0 & D^t_{n'_2} & 0 \\ 0 & 0 & D^t_{n'_3} \end{pmatrix}. \tag{11.81}$$

In the lab frame, the translational diffusivity tensor can be obtains as

$$\mathbf{D} = \mathbf{T}\mathbf{D}'\mathbf{T}^T \tag{11.82}$$

where the superscript 'T' denotes the transpose operation.

For 3D Brownian rotation, the conversation of the probability requires that

$$\frac{\partial \rho(\theta,\phi,t \mid \theta_0,\phi_0,0)}{\partial t} = D^r_{n'_2}\nabla^2 \rho(\theta,\phi,t \mid \theta_0,\phi_0,0) \tag{11.83}$$

where $D^r_{\perp 1}$ is the rotational diffusivity, $\rho(\theta,\phi,t \mid \theta_0,\phi_0,0)$ is the conditional probability density of observing configuration (θ, ϕ) at time t if initial configuration is (θ_0, ϕ_0).

By expanding ρ in spherical harmonics, we can obtain the general solution of this equation as

$$\rho(\theta,\phi,t \mid \theta_0,\phi_0,0) = \sum_{l \ge |\mathrm{m}|}^{\infty} \sum_{m=-\infty}^{\infty} Y_{lm}(\theta,\phi) Y_{lm}^{*}(\theta_0,\phi_0) \exp(-l(l+1)D^r_{\perp 1} t) \tag{11.84}$$

where Y_{lm} is the spherical harmonic function of degree *l* and order *m*, and '*' denotes conjugation. For a single rod particle, with its position characterized by (x_1, x_2, x_3) in the lab frame, the time-lapse displacement covariance matrix component due to the random walk is given as

$$\left\langle \Delta x_i(t)\Delta x_j(t)\right\rangle_{\theta_0,\phi_0} = \int_0^t dt_1 \int_0^t dt_2 2\left\langle D_{ij}(\mathrm{t}_1)\right\rangle_{\theta_0,\phi_0} \delta(t_1 - t_2) = \int_0^t dt_1 2\left\langle D_{ij}(t_1)\right\rangle_{\theta_0,\phi_0}, i, j = 1,2,3$$

(11.85)

where the bracket denotes the ensemble average of all possible configurations at time t_1 starting from the initial configuration (θ_0, ϕ_0) at time 0,given as

$$\left\langle \mathrm{D}_{ij}(t)\right\rangle_{\theta_0,\phi_0} = \int \sin\theta d\theta \int d\phi \rho(\theta,\phi,t \,|\, \theta_0,\phi_0,0) D_{ij}(\theta,\phi) \qquad (11.86)$$

Expanding(11.82), we have the expressions for configuration dependent diffusivity component as a function of rod orientation (θ,ϕ)

$$\begin{aligned} D_{11}(\theta,\phi) &= D^t_{\perp 1} + (D^t_{\parallel} - D^t_{\perp 1})\sin^2\theta(t)\frac{(1+\cos 2\phi(t))}{2} \\ D_{22}(\theta,\phi) &= D_{33}(\theta,\phi) = D^t_{\perp 1} + (D^t_{\parallel} - D^t_{\perp 1})\cos^2\theta(t) \end{aligned} \qquad (11.87)$$

Briefly, by noticing that

$$Y_{00} = \frac{1}{\sqrt{4\pi}}, Y_{20} = \sqrt{\frac{5}{4\pi}}(\frac{3}{2}\cos^2(\theta) - \frac{1}{2}), Y_{22} = \frac{1}{4}\sqrt{\frac{15}{4\pi}}\sin^2(\theta)\exp(2i\phi)$$

(11.88)

we can write

$$\cos^2\theta = (\sqrt{\frac{4\pi}{5}}Y_{20} + \sqrt{\pi}Y_{00})\frac{2}{3}, \sin^2\theta = \frac{2}{3}(\sqrt{\frac{4\pi}{5}}Y_{20} - \sqrt{4\pi}Y_{00}), \sin^2\theta\cos 2\phi = 4\sqrt{\frac{2\pi}{15}}(Y_{22} + Y_{22}^*)$$

(11.89)

Using the Eq. (11.89) and the orthogonal properties of spherical harmonics, we are able to evaluate Eq. (11.86) (Note that we set (θ_0, ϕ_0)=(0, 0) for no loss of generality)as

$$\begin{aligned}\left\langle \mathrm{D}_{11}(t)\right\rangle &= D^t_{\perp 1} + (D^t_{\|} - D^t_{\perp 1})(\frac{1}{3} + \frac{2}{3}\exp(-6D^r_{\perp 1}\,\mathrm{t})) \\ \left\langle \mathrm{D}_{22}(t)\right\rangle &= D^t_{\perp 1} + (D^t_{\|} - D^t_{\perp 1})(\frac{1}{3} - \frac{1}{3}\exp(-6D^r_{\perp 1}\,\mathrm{t})))\end{aligned} \tag{11.90}$$

For parallel and vertical diffusion, combining Eq. (11.85)(11.90), we have

$$\begin{aligned}\left\langle \Delta x_{\|}(t)\Delta x_{\|}(t)\right\rangle &= 2D^t_{\perp 1}t + \frac{2}{3}(D^t_{\|} - D^t_{\perp 1})t + \frac{4}{3}(D^t_{\|} - D^t_{\perp 1})\frac{1}{6D^r_{\perp 1}}(1 - \exp(-6D^r_{\perp 1}t) \\ \left\langle \Delta x_{\perp 1}(t)\Delta x_{\perp 1}(t)\right\rangle &= 2D^t_{\perp 1}t + \frac{2}{3}(D^t_{\|} - D^t_{\perp 1})t - \frac{2}{3}(D^t_{\|} - D^t_{\perp 1})\frac{1}{6D^r_{\perp 1}}(1 - \exp(-6D^r_{\perp 1}t)\end{aligned}$$

(11.91)

For short time limit, we have

$$\begin{aligned}\left\langle \Delta x_{\perp 1}(t)\Delta x_{\perp 1}(t)\right\rangle_{\theta_0,\phi_0} &= \left\langle \Delta x_{\perp 2}(t)\Delta x_{\perp 2}(t)\right\rangle_{\theta_0,\phi_0} = 2D^t_{\perp 1}t \\ \left\langle \Delta x_{\|}(t)\Delta x_{\|}(t)\right\rangle_{\theta_0,\phi_0} &= 2D^t_{\|}t\end{aligned} \tag{11.92}$$

For long time limit, we have

$$\left\langle \Delta x_{\|}(\mathrm{t})\Delta x_{\|}(t)\right\rangle_{\theta_0,\phi_0} = \left\langle \Delta x_{\perp 2}(t)\Delta x_{\perp 2}(t)\right\rangle_{\theta_0,\phi_0} = \left\langle \Delta x_{\perp 1}(t)\Delta x_{\perp 1}(t)\right\rangle_{\theta_0,\phi_0} = \frac{4D^t_{\perp 1}t + 2D^t_{\|}t}{3}$$

(11.93)

E. Complete description for constraint dynamics

For *N* identical particles in the low Reynold number flow with position coordinates $q_1, q_2, \ldots q_{6N}$ under *K* constraints

$$C_\mu(q_1, q_2, \ldots, q_{6N}) = 0, \mu = 1, 2, \ldots, K \tag{11.94}$$

the equation of motion is given as

$$\mathbf{U} = \mathbf{M} \cdot \mathbf{F} \tag{11.95}$$

$$\mathbf{F} = \mathbf{F}^P + \mathbf{F}^B + \mathbf{F}^C \tag{11.96}$$

where $\mathbf{U}$ is a 6*N* dimensional velocity vector, including 3*N* translational velocities and 3*N* rotational velocities. $\mathbf{F}$ is a 6*N* dimensional force vector, including 3*N* forces and 3*N* torques acting on the center of each bead. $\mathbf{M}$ is a 6*N*×6*N* grand mobility tensor depending on the instantaneous configuration of *N* particles. The grand mobility tensor relates to grand resistance tensor *via* $\mathbf{M} = (\mathbf{R})^{-1}$ .The procedure to obtain those tensors is discussed in the previous section and Supporting materials. Generally, $\mathbf{F}$ have contributions from conservative forces $\mathbf{F}^P$, dissipative (Brownian) forces $\mathbf{F}^B$ and constraint forces $\mathbf{F}^C$.

Conservative forces

The conservative forces on each sphere composing the rod have three parts[287]:

$$\mathbf{F}^p = \mathbf{F}^{pp} + \mathbf{F}^{pw} + \mathbf{F}^{grav} \tag{11.97}$$

where $\mathbf{F}^{pp}$ is the force due to the particle-particle interaction, $\mathbf{F}^{pw}$ is the force due to particle wall interaction, $\mathbf{F}^{grav}$ is gravitational force. When there is only one rod, $\mathbf{F}^{pp}$ is the internal force and could be set to be zeros. $\mathbf{F}^{pw}$ is the electrostatic repulsion between particle and wall due to the double layer overlapping. The electrostatic repulsion force for thin electrostatic double layers $(\kappa a >> 1)$ is given by[2]

$$F^{pw} = \kappa B^{pw} \exp(-\kappa(z-a)) \tag{11.98}$$

where a is the radius of the sphere, z is the mass center height of the sphere, κ is the Debye length, B^{pw} is the pre-factor for electrostatic repulsion between colloidal pairs.

The gravitational body force is given by $\mathbf{F}^{grav}=m\mathbf{g}$, where m is the buoyant sphere mass, $\mathbf{g}$ is the acceleration due to gravity.

General theory of constraint forces

The constraints on coordinates are equivalent to applying constraint forces onto coordinates. The constraint forces from all K constraints conjugate to (*i.e.* acting on) coordinate q_j are given by

$$F_j^C = \lambda_\mu n_{j\mu} \tag{11.99}$$

where $n_{j\mu}$ is given as

$$n_{j\mu} = \frac{\partial C_\mu}{\partial q_j} \tag{11.100}$$

Summation over repeated indices in implied throughout this section.

The value of $\lambda_1, \lambda_2, \ldots, \lambda_K$ is determined by requiring the constraints hold all the time, which is given by

$$\frac{\partial C_\mu}{\partial t} = n_{j\mu}\frac{\partial q_j}{\partial t} = 0, \mu = 1, 2, ..., \mathrm{K} \tag{11.101}$$

Combine the equation of motion $\mathbf{U} = \mathbf{M}\cdot(\mathbf{F}^P + \mathbf{F}^B + \mathbf{F}^C)$ with Eqs. (11.99)-(11.17), we can show that

$$H_{\mu\nu}\lambda_\nu = n_{j\mu}M_{ji}(\mathrm{F}_i^P + \mathrm{F}_i^B) \tag{11.102}$$

where

$$H_{\mu\nu} = n_{i\mu}M_{ij}n_{j\nu} \tag{11.103}$$

and λ can be obtained by solving the linear system Eq. (11.102).

As Hinch and Morse found[282,288], a pseudo-force is need to add to the right-hand side of Eq. (11.102) to correct the curvature effect of the constraint. The force is given as

$$F_j^{ps} = k_B T\frac{\partial}{\partial q_j}\ln(\mathrm{Det}(\mathbf{G})) \tag{11.104}$$

where

$$G_{ij} = n_{ik}n_{jk} \tag{11.105}$$

and Det is the operation of calculating the determination of the matrix **G**.

Brownian forces under rigid constraints

In the constraint dynamics, the Brownian forces $\mathbf{F}^\mathbf{B}$, termed geometrically projected random forces by Morse[288], needs to satisfy

$$F_i^B n_{i\mu} = 0, \mu = 1, 2, \ldots, K \tag{11.106}$$

which essentially says that the 6N dimensional random force $\mathbf{F^B}$ will have zero value on the directions normal to the 6N-K dimensional hyper-surfaces specified by the K constraints. To construct those projected Brownian forces, we need to first generate un-projected Brownian forces $\mathbf{F^{B'}}$ conjugated to 6N coordinates, which are characterized by a mean and a variance as

$$\begin{aligned} \left\langle \mathbf{F}^{B'} \right\rangle &= 0 \\ \left\langle \mathbf{F}^{B'} \mathbf{F}^{B'} \right\rangle &= \frac{2k_B T}{\Delta t} \mathbf{R} \end{aligned} \tag{11.107}$$

Use a geometrical projection operator $P_{ij} = \delta_{ij} - n_{i\mu}(n_{k\mu}n_{k\mu})^{-1} n_{j\nu}$, termed by Morse, the projected random forces $\mathbf{F^B}$ is related to $\mathbf{F^{B'}}$ via

$$\mathbf{F^B} = \mathbf{P} \cdot \mathbf{F^{B'}} \tag{11.108}$$

then $\mathbf{F^B}$ will satisfy the condition specified by Eq. (11.106).

Construction of constraints for sphere-chain of a rod

A rod with aspect ratio p can be modeled by p spheres under proper appropriate constraints. There are two types of constraints: positional constraints and rotational constraint. The positional constraints are used to ensure all the spheres are positioned in one line and each sphere is touching with its neighbors. If we index the p spheres from 1 to p, denote $\mathbf{r}_i$ as the position vector of sphere i, and $r_{i,j}$ the j component in $\mathbf{r}_i$, then the positional constraints can be expressed as a set of 3p-1 equations, given as:

$$\left|\mathbf{r}_1 - \mathbf{r}_p\right| = 2ap \qquad (11.109)$$

$$r_{i,j} = r_{1,j} + \frac{r_{p,j} - r_{1,j}}{p-1}, j = 1,2,3, i = 2,3,..., p-1 \qquad (11.110)$$

where a is the sphere radius. Note that there are $3(p\text{-}2)$ equations represented by Eq. (11.110) .

The rotational constraints are placed onto the angular displacement of each sphere to ensure that all the spheres can only rotate along the long axis of the rod with the same speed. If $\Theta_{i,j}$ denotes angular displacement of i sphere in the j direction axis of the lab frame, then we have 3(p-1) constraints given as

$$T_{1j}\Theta_{1,j} = T_{1j}\Theta_{i,j}, i = 2,3,\ldots p \qquad (11.111)$$

$$T_{2j}\Theta_{i,j} = 0, i = 1,2,\ldots, p \qquad (11.112)$$

$$T_{3j}\Theta_{i,j} = 0, i = 1,2,\ldots, p \qquad (11.113)$$

where **T** is the transformation tensor between lab frame and body frame, and is given as $T_{ij}=\mathbf{n}_i\cdot\mathbf{e}_j$. Eq. (11.111) says all the spheres should rotate in the same speed along the long axis of the rod. Eq. (11.112)(11.113) says the angular displacement around axes perpendicular to the long axis of the rod should vanish.

Supplementary figures

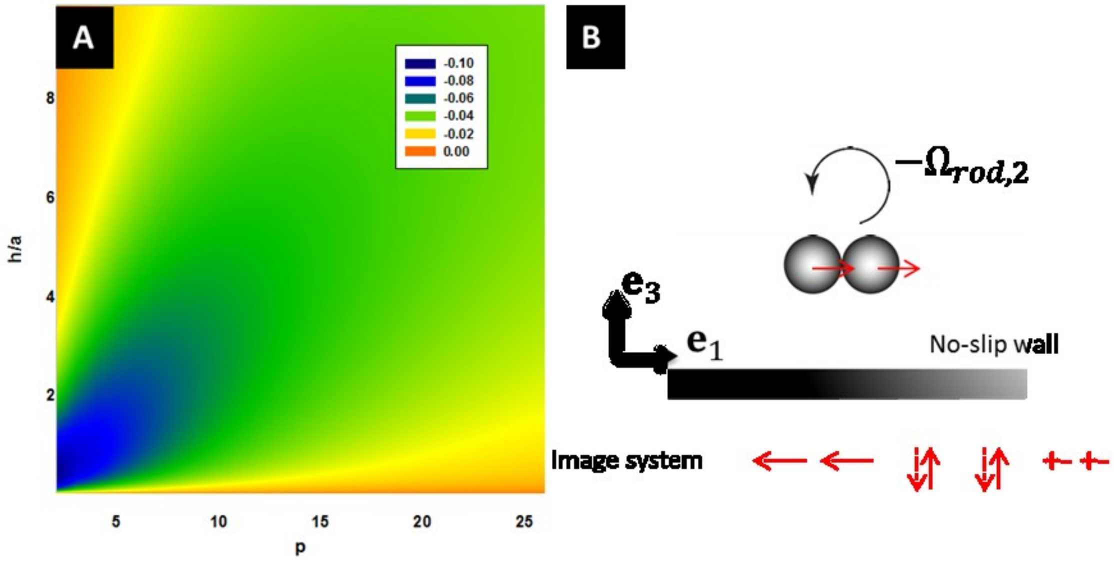

Figure. S1 (A) the correlation coefficient Cov_{15} (coupling between translation in direction $\mathbf{n}_{\parallel}$ rotation and in direction $\mathbf{n}_{\perp 1}$) as a function of p and h. (B) The image system for two point forces above the wall. This correlation Cov_{15} is most pronounced at $h/a{\sim}1$ and p=2(*i.e.* doublet rod). This coupling stems from the fluid velocity field created by the dipoles in image system of an array of point force stokelet that sets the rod to rotate, as showed in the schematics in Fig. S1 (B).[1] For longer rods, the dipole array will cancel each other out in the middle part and decrease the coupling strength.

12 CONCLUSIONS

This dissertation is mainly aimed at: (1) understanding the principle in harnessing non-equilibrium phenomenon in the colloidal system; (2) developing quantitative low dimensional dynamic models for colloidal self-assembly processes; (3) developing model-based optimal control to engineer kinetical pathways in the self-assembly; (4) developing Stokesian dynamics tools in modeling hydrodynamic interaction; (5) developing generic geometric computational methods in modeling depletion interaction. This section summarizes the conclusions drawn from the work presented in this dissertation.

12.1 Optimal control of self-propelled colloids for maze navigation and machines

In *Chapter 4*, we have demonstrated the application of Markov decision framework to construct an optimal control policy in navigation task in free space and complex mazes. The optimal control policy can achieve orders-of-magnitude faster in first passage time in navigation tasks compared to uncontrolled random explorations. The performance under optimal control can linearly scale up with length of the shortest path connecting the initial position and final position. We identify non-dimension parameters in the control system, and we generalize the optimal control by investigating how these non-dimensional parameters affect the positioning error and first passage time performance. The optimal control framework will find potential application in employing self-propelled devices performing tasks, such as cargo transport in complex environments. Generalization the optimal control framework to 3D is straightforward. The MDP framework remains the same except that the system state is defined as $s=(x, y, z, \theta, \phi)$, where θ is the polar angle and ϕ is the azimuth angle.

In *Chapter 5*, we developed the multiple motor multiple target optimal control algorithm. This algorithm is used to implement a new paradigm design for cargo capture and transport. The steady structures during the capture and transport process are found to depend on the pair attraction between motors and number of motors. We found that active forces resulting from self-propulsion to essential maintain the caging structure during the cargo capture, and play two roles during the cargo transport: both maintaining the structure by balancing with the osmotic pressure and providing the transport momentum for the system.

12.2 Low dimensional modeling and optimal control for colloidal assembly

In *chapter 6,* we report agreement between optical microscopy measurements, Brownian Dynamic simulations, and low-dimensional models of stochastic grain boundary formation and motion in quasi-2D colloidal bicrystals. Our results show that two reaction coordinates, one for condensation and one for global order, are sufficient to quantitatively capture first passage times between critical configurations at each applied voltage. Free energy and diffusivity landscapes show that the relative misorientation angles and domain sizes formed during condensation determine the subsequent grain boundary motion. Bicrystals with similar sized domains and a near 30° maximum misorientation angle relax *via* slow grain boundary diffusion mediated by high friction and vanishing free energy gradients, whereas bicrystals with asymmetrically sized and/or less misoriented domains relax *via* much faster grain boundary migration due to greater thermodynamic driving forces. By quantifying such dynamics as a function of voltage, ongoing work is developing optimal control algorithms to dynamically tune voltages to avoid kinetic bottlenecks associated with slow grain boundary dynamics. Future work will extend the approaches reported here for bicrystals to many-domain crystals, where different reaction coordinates might be required to track the how polycrystallinity evolves at stages well before a single domain emerges.

In *chapter 7,* We reported the development of a low-dimensional Smoluchowski equation to quantify the thermodynamics and kinetics of colloidal crystal assembly in electric fields. The dimensionality and order parameter choice was supported by a diffusion mapping analysis. Order parameters describing global order, ψ_6, and degree of condensation, R_g, were found to yield a low-dimensional model that quantitatively captured assembly dynamics as determined by first passage times in agreement with N-dimensional dynamic data. The free energy and diffusivity landscapes from the Smoluchowski model revealed two types of kinetic pathways; one where condensation and global order emerge simultaneously to rapidly yield single domain crystals, and another one where fast condensation with local ordering, but not global ordering, results in polycrystal formation. Numerical solution of the low-dimensional Smoluchowski equation shows the temporal evolution of the probability of states for different voltages and system sizes, which quantifies how these two variables determine the evolution of order in electric field mediated quasi-2D crystallization. Ultimately, the low dimensional model quantitatively captures slow grain boundary dynamics in the presence of vanishing free energy gradients, where friction associated with configurational rearrangements determines the relaxation rate for polycrystals to form single crystals via grain boundary motion. These low-dimensional models are currently being used to design optimal control policies for closed loop and open loop control of colloidal assembly processes designed to form single crystal structures.

In *chapter 8*, our results demonstrate optimal feedback control to robustly assemble perfect colloidal crystals orders of magnitude faster than a slow quasi-equilibrium ramp and much more reliably than rapid quenches. An optimal policy is computed with dynamic programming based on a low-dimensional reaction coordinate dynamic model. By tracking real-time stochastic particle configurations and employing the optimal policy to adjust applied electric fields *via* feedback, the evolution of unassembled particles is guided through polycrystal states into single domain crystals.

There are a number of ways this approach could be adapted and extended. For example, our approach could be implemented to constructively employ multiple complementary actuators (*e.g.*, magnetic fields to exert torques,[221] tunable depletion attraction to quench final states)[43] or be combined with other methods such as templated self-assembly (either unactuated[48,222] or actuatable[223]). Based on our prior work on nanoparticle assembly,[158] system size effects,[112] and three dimensional assembly in electric[138] and gravitational fields,[224] our approach can also be adapted to: (1) smaller nanoparticles (with different sensors; *e.g.*, attenuation based imaging,[158,224] scattering/diffraction),[199] (2) larger systems either through continuous processing (rather than batch processing; *e.g.*, a microfluidic device), parallelization (*e.g.*, electrode arrays),[225] or informing open-loop schemes (*e.g.*, toggling),[186] and (3) 3d crystals in thin films and possibly bulk crystals.

Further extensions of the methods and analyses developed in this work could be applied to other nano- and micro- scale processes involving: anisotropic particles or multi-component mixtures (with more states and bottlenecks), dynamical steady-states and out-of-equilibrium end points (where a Fokker-Planck equation describes the dynamics rather than a Smoluchowski equation), active micromachines and reconfigurable device elements (rather than static targets), and even synthetic materials systems that mimic basic control elements in biological systems (*e.g.*, chaperone control of protein folding and aggregation).[226] Our approach is based on first-principle concepts that are general to any molecular, nano-, or micro- scale assembly process where components thermally sample different configurations based on their relative free energies, states can be measured in real-time, an actuation mechanism exists to alter driving forces, and a dynamic model connects system responses to actuator settings.

In chapter 9, the results presented demonstrate that by tuning attraction in a colloidal sedimentation system *via* feed-back control, layer-by-layer controlled crystallization can be realized. In a finite system with different inter-particle attractions, equilibrium sediment structures, including dense fluid, inhomogeneous fluid-solid, and completely crystalline configurations can be achieved. Using a Lindemann-like parameter, L_c, to investigate the particle mobility near the growth front at equilibrium allows criteria to be established to detect dynamic arrested structures. A controller using L_c and N_c as sensors, and tunable attraction as an actuatoris been demonstrated to effectively control the crystallization process based on a simple thermodynamic model. The performance of the controller shows that a fast, low defect crystallization process requires a balance between the strength of thermodynamic driving force and the kinetic accessibility[23,24].

In this controller model, the tunable attraction may be realized by temperature dependent depletion attractions[61] (though this is not an immediate actuator due to finite time heat transfer), or electric or magnetic field mediated interactions[168] (which are immediate actuators but both require complex set-ups). To extend the system to controlled continuous crystal growth, a particle feeding system can be added. The key issue that still needs to be addressed in continuous colloidal growth is that particle transport kinetics strongly affect the concentration near growth front, thus increasing the factors governing particle crystallization. This issue might be addressed by employing a dynamical density functional approach[247] to capture the density variation due to transport with a low-dimensional dynamic model[248] to capture the crystallization kinetics at the growth front.

12.3 Advanced stochastic modeling methods

In *chapter 10*, our results demonstrate the ability to accurately interpret and predict excluded volume effects between colloids with each other and topographically patterned surfaces in the presence of depletants with thermosensitive sizes. A new modeling approach is reported to numerically compute the excluded volume between colloids interacting with arbitrary surface geometries. This approach enables the computation of depletion attraction with local surface pattern features in the presence of depletants with varying dimensions. This method is used to match Monte Carlo simulations to experiments to model the temperature dependent density, free energy, and potential energy landscapes that determine non-close-packed colloidal configurations on periodic arrays of circular features. Ultimately, the ability to quantitatively understand the interplay of electrostatic, gravitational, and tunable depletion interactions on topographically patterned substrates provides a basis to design and control colloidal based reconfigurable materials and devices for micro- and nano- technologies.

In *chapter 11*, we present a diffusivity calculation method and simulation method for colloidal rods motion near a planar wall. The method is adapted from Stokesian Dynamics method by modeling a rod-shape particle as a chain of touching spheres. The calculated diffusivities for the sphere-chain rod is compared with the widely used cylindrical result from Tirado. A similar trend of diffusivities changing with rod's aspect ratio is identified. In this work, we have developed the CSD algorithm for simulating rod-shaped particle suspensions with hydrodynamic interactions. We have simulated and analyzed two experiments: an isolated rod diffuses in bulk and above a planar wall. We have demonstrated that this algorithm can produce trajectories matched with an underlying theory for dynamic analysis and equilibrium analysis. The analysis procedure for MSTD and FEL is of practical importance for research on the experimental measurement of forces and motions for isolated rods.[294] Even though we only demonstrated the simulation techniques on the single particle level, we can readily extend to multiple rods simulation by including extra components of constraints, resistance tensors, and forces.

13 FUTURE DIRECTIONS

This chapter presents several ongoing research projects, which are extensions or generalizations of current research projects in the previous chapters.

13.1 Reinforcement learning for stochastic optimal control

The dynamical programming principle used in Chapter 4,5,8 has computational complexity increasing exponentially with the dimensionality of the state space. Therefore, for systems with large state space, the dynamical programming based method will fail due to its prohibitive computational cost. In addition, dynamical programming method requires a proposed model to be calibrated first from the trajectory data. This requirement imposes two potential issues: (1) the real dynamical system might not be well described by the proposed model; (2) large amount of data will be needed if the number of model parameters are proportional to the size of the state space. Reinforcement learning based optimal control is a data-driven and model-free method designed to address issues of 'curse of dimensionality' and data inefficiency.

Using electric field mediated assembly in *chapter 8* as the test model, we have the following setup: system state: $s = (\psi_6,\ R_g)$, action space: A consisting of low voltage, medium voltage and high voltage, and reward function: $R = -(1 - \psi_6)$. The goal is to maximize the expected sum of discounted rewards along the whole assembly process by seeking an optimal policy π (the optimal policy specifies choosing the optimal action $a \in A$ given a system state s), given as

$$\max_{\pi} \mathbf{E}[\sum_{n=0}^{\infty} R(s_n)\gamma^n] \tag{13.1}$$

Different from dynamic programming approach, the reinforcement learning using a stochastic optimization method to solve Eq. (13.1). The algorithm needs a definition of a function $Q: S \times A \rightarrow \mathrm{R}$, given as

$$Q(s,a) = R(s) + \max_a \sum_{s' \in S} \gamma P(s' \mid s,a) Q(s,a) \tag{13.2}$$

The reinforcement learning algorithm is given below as[304]

```
Input: $\varepsilon$ greedy coefficient, and $\alpha$ learning rate
Initialize $Q(s, a)$ arbitrarily
Loop (for each episode):
  Initialze $s$
  Repeat (for each step in an episode)
    Choose $a$ given s such that Q(s,a) is maximized with probability 1- $\varepsilon$ and choose $a$ randomly with probability $\varepsilon$
    Observe $R$ and $s'$ from the model
    Update Q(s,a) via:
      $Q(s,a) = (1-\alpha)Q(s,a) + \alpha[R + \max_{a'} Q(s',a')]$    (13.3)
    Set s = s'
  End Repeat
Until s is terminal
```

Theoretically, after training infinitely number of episodes, $Q(s,a)$ converge. Then the optimal control policy at s is given as $a = \operatorname{argmax} Q(s, a)$.

Fig. 1 shows the assembly result of 100 trajectories starting from fluid state using reinforcement learning control vs. no control. The reinforcement learning algorithm can steer the system around the grain boundary region (small Rg and ψ6); while the

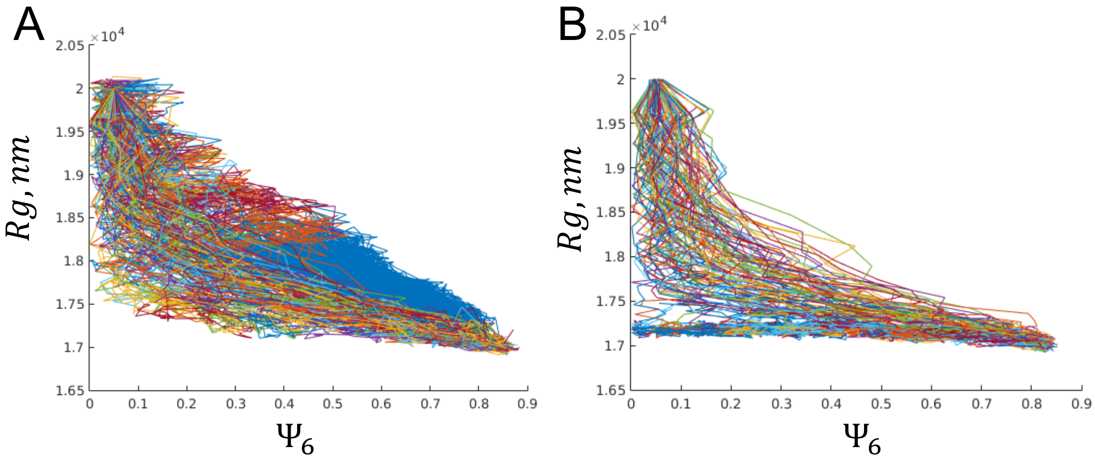

Figure. 1. Optimal control colloidal assembly via reinforcement learning. (A) 100 trajectories starting at (0.05, 20000) under optimal control via reinforcement learning. (B) 100 trajectories starting at (0.05, 20000) under direct deep quench using highest voltages.

uncontrolled self-assembly process will get stuck there with around 30% of chances.

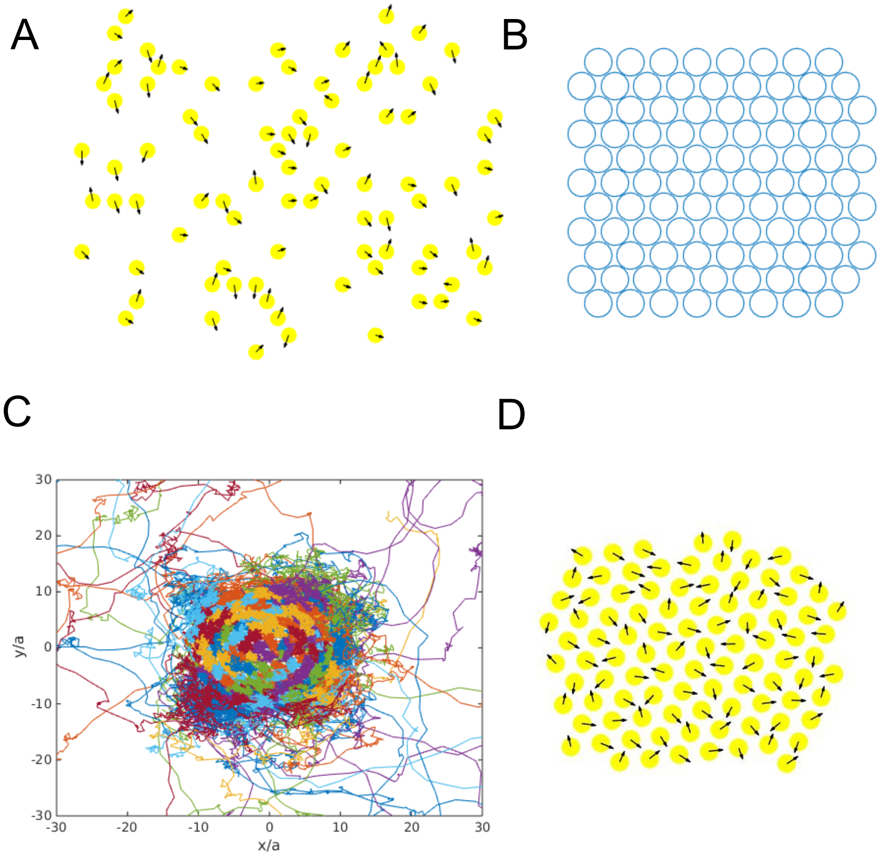

Figure. 2. Optimal controlled self-propelled colloids for active assembly. (A) Initial configuration of self-propelled colloids. (B) Target sites with hexagonal closed packing order. (C) Trajectories of self-propelled colloids under multiple agent control. (D) Final configuration of self-propelled colloids.

13.2 Multiple agent control framework for active assembly

The multiple agent multiple target algorithm developed in Chapter 4 can be used to construct a new paradigm for self-assembly into arbitrary pre-designed structures. Fig. 2 shows the optimal control of 90 self-propelled colloids into the pre-designed squared lattice structures. The process starts from initial configuration in Fig. 2A and ends with configuration in Fig. 2D. By optimizing over the kinetic pathways, the new assembly paradigm *via* multiple agent control algorithm has the ability to assemble into structure highly unlikely via equilibrium thermodynamics.

14 REFERENCES

1 Blake, J. R. A note on the image system for a stokeslet in a no-slip boundary. *Mathematical Proceedings of the Cambridge Philosophical Society* **70**, 303-310, doi:doi:10.1017/S0305004100049902 (1971).

2 Russel, W. B., Saville, D. A. & Schowalter, W. R. *Colloidal Dispersions*. (Cambridge University Press, 1989).

3 Manoharan, V. N. Colloidal matter: Packing, geometry, and entropy. *Science* **349**, 1253751 (2015).

4 Rogers, W. B. & Manoharan, V. N. Programming colloidal phase transitions with DNA strand displacement. *Science* **347**, 639-642 (2015).

5 Li, B. *et al.* Modes of surface premelting in colloidal crystals composed of attractive particles. *Nature* **531**, 485-488 (2016).

6 Wang, Z., Wang, F., Peng, Y. & Han, Y. Direct observation of liquid nucleus growth in homogeneous melting of colloidal crystals. *Nature communications* **6** (2015).

7 Wang, Z., Wang, F., Peng, Y., Zheng, Z. & Han, Y. Imaging the homogeneous nucleation during the melting of superheated colloidal crystals. *Science* **338**, 87-90 (2012).

8 Edwards, T. D. & Bevan, M. A. Controlling colloidal particles with electric fields. *Langmuir* **30**, 10793-10803 (2014).

9 Bevan, M. A. *et al.* Controlling assembly of colloidal particles into structured objects: Basic strategy and a case study. *Journal of Process Control* **27**, 64-75, doi:http://dx.doi.org/10.1016/j.jprocont.2014.11.011 (2015).

10 Vlasov, Y. A., Bo, X.-Z., Sturm, J. C. & Norris, D. J. On-chip natural assembly of silicon photonic bandgap crystals. *Nature* **414**, 289-293 (2001).

11 Koumakis, N., Lepore, A., Maggi, C. & Di Leonardo, R. Targeted delivery of colloids by swimming bacteria. *Nature communications* **4** (2013).

12 Soler, L., Magdanz, V., Fomin, V. M., Sanchez, S. & Schmidt, O. G. Self-propelled micromotors for cleaning polluted water. *ACS nano* **7**, 9611-9620 (2013).

13 Wang, J. & Gao, W. Nano/microscale motors: biomedical opportunities and challenges. *ACS nano* **6**, 5745-5751 (2012).

14 Tasci, T. O., Herson, P. S., Neeves, K. B. & Marr, D. W. Surface-enabled propulsion and control of colloidal microwheels. *Nat Commun* **7**, 10225, doi:10.1038/ncomms10225 (2016).

15 Stenhammar, J., Wittkowski, R., Marenduzzo, D. & Cates, M. E. Light-induced self-assembly of active rectification devices. *Science Advances* **2**, doi:10.1126/sciadv.1501850 (2016).

16 Buttinoni, I., Volpe, G., Kummel, F., Volpe, G. & Bechinger, C. Active Brownian motion tunable by light. *J Phys Condens Matter* **24**, 284129, doi:10.1088/0953-8984/24/28/284129 (2012).

17 Glotzer, S. C. & Solomon, M. J. Anisotropy of building blocks and their assembly into complex structures. *Nat Mater* **6**, 557-562 (2007).

18 Grzelczak, M., Vermant, J., Furst, E. M. & Liz-Marzán, L. M. Directed Self-Assembly of Nanoparticles. *ACS Nano* **4**, 3591-3605, doi:10.1021/nn100869j (2010).

19 Velev, O. D. & Gupta, S. Materials Fabricated by Micro- and Nanoparticle Assembly – The Challenging Path from Science to Engineering. *Advanced Materials* **21**, 1897-1905, doi:10.1002/adma.200801837 (2009).

20 Davis, K., Russel, W. & Glantschnig, W. Disorder-to-order transition in settling suspensions of colloidal silica: X-ray measurements. *Science* **245**, 507-511 (1989).

21 Yeh, S.-R., Seul, M. & Shraiman, B. I. Assembly of ordered colloidal aggregrates by electric-field-induced fluid flow. (1997).

22 Tulpar, A., Subramanian, V. & Ducker, W. Decay lengths of double-layer forces in solutions of partly associated ions. *Langmuir* **17**, 8451-8454, doi:10.1021/la001216h (2001).

23 Vickreva, O., Kalinina, O. & Kumacheva, E. Colloid crystal growth under oscillatory shear. *Advanced Materials* **12**, 110-112 (2000).

24 Damasceno, P. F., Engel, M. & Glotzer, S. C. Predictive Self-Assembly of Polyhedra into Complex Structures. *Science* **337**, 453-457, doi:10.1126/science.1220869 (2012).

25 Millan, J. A., Ortiz, D., van Anders, G. & Glotzer, S. C. Self-Assembly of Archimedean Tilings with Enthalpically and Entropically Patchy Polygons. *ACS Nano* **8**, 2918-2928, doi:10.1021/nn500147u (2014).

26 Zhang, J., Yan, J. & Granick, S. Directed Self-Assembly Pathways of Active Colloidal Clusters. *Angewandte Chemie International Edition* **55**, 5166-5169 (2016).

27 Sánchez, S., Soler, L. & Katuri, J. Chemically Powered Micro- and Nanomotors. *Angewandte Chemie International Edition* **54**, 1414-1444, doi:10.1002/anie.201406096 (2015).

28 Dreyfus, R. *et al.* Microscopic artificial swimmers. *Nature* **437**, 862-865, doi:http://www.nature.com/nature/journal/v437/n7060/suppinfo/nature04090_S1.html (2005).

29 Solon, A. P. *et al.* Pressure is not a state function for generic active fluids. *Nat Phys* (2015).

30 Balasubramanian, S. *et al.* Micromachine-Enabled Capture and Isolation of Cancer Cells in Complex Media. *Angewandte Chemie International Edition* **50**, 4161-4164 (2011).

31 Kagan, D. *et al.* Rapid delivery of drug carriers propelled and navigated by catalytic nanoshuttles. *Small* **6**, 2741-2747 (2010).

32 Palacci, J., Sacanna, S., Steinberg, A. P., Pine, D. J. & Chaikin, P. M. Living crystals of light-activated colloidal surfers. *Science* **339**, 936-940 (2013).

33 Baraban, L. *et al.* Catalytic Janus Motors on Microfluidic Chip: Deterministic Motion for Targeted Cargo Delivery. *ACS Nano* **6**, 3383-3389, doi:10.1021/nn300413p (2012).

34 Takagi, D., Palacci, J., Braunschweig, A. B., Shelley, M. J. & Zhang, J. Hydrodynamic capture of microswimmers into sphere-bound orbits. *Soft Matter* **10**, 1784, doi:10.1039/c3sm52815d (2014).

35 Ozin, G. A., Manners, I., Fournier-Bidoz, S. & Arsenault, A. Dream Nanomachines. *Advanced Materials* **17**, 3011-3018, doi:10.1002/adma.200501767 (2005).

36 Sriraman, S., Kevrekidis, I. G. & Hummer, G. Coarse Master Equation from Bayesian Analysis of Replica Molecular Dynamics Simulations†. *The Journal of Physical Chemistry B* **109**, 6479-6484, doi:10.1021/jp046448u (2005).

37 Risken, H. & Frank, T. *The Fokker-Planck Equation: Methods of Solution and Applications*. (Springer, 1996).

38 Kopelevich, D. I., Panagiotopoulos, A. Z. & Kevrekidis, I. G. Coarse-grained kinetic computations for rare events: Application to micelle formation. *J. Chem. Phys.* **122**, 044908 (2005).

39 Juarez, J. J. & Bevan, M. A. Feedback Controlled Colloidal Self-Assembly. *Adv. Funct. Mater.* **22**, 3833-3839, doi:10.1002/adfm.201200400 (2012).

40 Xue, Y., Beltran-Villegas, D. J., Tang, X., Bevan, M. A. & Grover, M. A. Optimal Design of a Colloidal Self-Assembly Process. *IEEE Trans. Control Sys. Tech.* **PP**, 1-1, doi:10.1109/tcst.2013.2296700 (2014).

41 Edwards, T. D. & Bevan, M. A. Depletion-Mediated Potentials and Phase Behavior for Micelles, Macromolecules, Nanoparticles, and Hydrogel Particles. *Langmuir* **28**, 13816-13823, doi:10.1021/la302805n (2012).

42 Savage, J. R., Blair, D. W., Levine, A. J., Guyer, R. A. & Dinsmore, A. D. Imaging the Sublimation Dynamics of Colloidal Crystallites. *Science* **314**, 795-798 (2006).

43 Fernandes, G. E., Beltran-Villegas, D. J. & Bevan, M. A. Interfacial Colloidal Crystallization via Tunable Hydrogel Depletants. *Langmuir* **24**, 10776-10785, doi:10.1021/la802025d (2008).

44 Fernandes, G. E., Beltran-Villegas, D. J. & Bevan, M. A. Spatially Controlled Reversible Colloidal Self-Assembly. *J. Chem. Phys.* **131**, 134705, doi:10.1063/1.3243686 (2009).

45 Shelley, L. T., Robert, E. & Royall, C. P. Temperature as an external field for colloid–polymer mixtures: ‘quenching’ by heating and ‘melting’ by cooling. *Journal of Physics: Condensed Matter* **24**, 464128 (2012).

46 Dinsmore, A. D., Yodh, A. G. & Pine, D. J. Entropic control of particle motion using passive surface microstructures. *Nature* **383**, 239-242 (1996).

47 Lin, K.-H. *et al.* Entropically Driven Colloidal Crystallization on Patterned Surfaces. *Phys. Rev. Lett.* **85**, 1770-1773 (2000).

48 Lee, W., Chan, A., Bevan, M. A., Lewis, J. A. & Braun, P. V. Nanoparticle-Mediated Epitaxial Assembly of Colloidal Crystals on Patterned Substrates. *Langmuir* **20**, 5262-5270, doi:10.1021/la035694e (2004).

49 Sacanna, S., Irvine, W. T. M., Chaikin, P. M. & Pine, D. J. Lock and key colloids. *Nature* **464**, 575-578, doi:10.1038/nature08906 (2010).

50 Kim, S. & Karrila, S. J. *Microhydrodynamics: Principles and Selected Applications*. (Dover Publications, 2005).

51 Bevan, M. A. & Prieve, D. C. Hindered diffusion of colloidal particles very near to a wall: Revisited. *J Chem Phys* **113**, 1228-1236, doi:doi:http://dx.doi.org/10.1063/1.481900 (2000).

52 Coughlan, A. C. & Bevan, M. A. Rotating colloids in rotating magnetic fields: Dipolar relaxation and hydrodynamic coupling. *Physical Review E* **94**, 042613 (2016).

53 Brady, J. F. & Bossis, G. Stokesian Dynamics. *Annual Review of Fluid Mechanics* **20**, 111-157, doi:10.1146/annurev.fl.20.010188.000551 (1988).

54 Li, G. & Tang, J. X. Diffusion of actin filaments within a thin layer between two walls. *Physical Review E* **69**, 061921 (2004).

55 Lu, M.-H., Feng, L. & Chen, Y.-F. Phononic crystals and acoustic metamaterials. *Materials Today* **12**, 34-42, doi:http://dx.doi.org/10.1016/S1369-7021(09)70315-3 (2009).

56 Perrin, F. Mouvement brownien d'un ellipsoide - I. Dispersion diélectrique pour des molécules ellipsoidales. *J. Phys. Radium* **5**, 497-511 (1934).

57 Asakura, S. & Oosawa, F. On the interaction between two bodies immersed in a solution of macromolecules. *Journal of Chemical Physics* **22**, 1255-1256 (1954).

58 Vrij, A. Polymers at interfaces and the interactions in colloidal dispersions. *Pure and Applied Chemistry* **48** (1976).

59 Sharma, A. & Walz, J. Y. Direct measurement of the depletion interaction in a charged colloidal dispersion. *Journal of the Chemical Society-Faraday Transactions* **92**, 4997-5004 (1996).

60 Jones, T. B. & Washizu, M. Equilibria and dynamics of DEP-levitated particles: multipolar theory. *Journal of Electrostatics* **33**, 199-212 (1994).

61 Fernandes, G. E., Beltran-Villegas, D. J. & Bevan, M. A. Interfacial Colloidal Crystallization via Tunable Hydrogel Depletants. *Langmuir* **24**, 10776-10785, doi:10.1021/la802025d (2008).

62 Fernandes, G. E., Beltran-Villegas, D. J. & Bevan, M. A. Spatially controlled reversible colloidal self-assembly. *Journal of Chemical Physics* **131**, doi:134705

10.1063/1.3243686 (2009).

63 Nelson, D. R. & Halperin, B. I. Dislocation-mediated melting in two dimensions. *Physcial Review B*, 2457-2484 (1979).

64 Chirikjian, G. S. *Stochastic Models, Information Theory, and Lie Groups, Volume 1: Classical Results and Geometric Methods*. (Birkhäuser Boston, 2009).

65 Volpe, G., Helden, L., Brettschneider, T., Wehr, J. & Bechinger, C. Influence of noise on force measurements. *Physical review letters* **104**, 170602 (2010).

66 Bertsekas, D. P., Bertsekas, D. P., Bertsekas, D. P. & Bertsekas, D. P. *Dynamic programming and optimal control*. Vol. 1 (Athena Scientific Belmont, MA, 1995).

67 Debnath, L. & Mikusiński, P. *Hilbert spaces with applications*. (Academic press, 2005).

68 Volpe, G., Buttinoni, I., Vogt, D., Kümmerer, H.-J. & Bechinger, C. Microswimmers in patterned environments. *Soft Matter* **7**, 8810, doi:10.1039/c1sm05960b (2011).

69 Takatori, S. C. & Brady, J. F. Towards a thermodynamics of active matter. *Physical Review E* **91**, 032117 (2015).

70 Bregulla, A. P., Yang, H. & Cichos, F. Stochastic Localization of Microswimmers by Photon Nudging. *ACS Nano* **8**, 6542-6550, doi:10.1021/nn501568e (2014).

71 Qian, B., Montiel, D., Bregulla, A., Cichos, F. & Yang, H. Harnessing thermal fluctuations for purposeful activities: the manipulation of single micro-swimmers by adaptive photon nudging. *Chemical Science* **4**, 1420-1429, doi:10.1039/C2SC21263C (2013).

72 Yang, Y., Thyagarajan, R., Ford, D. M. & Bevan, M. A. Dynamic colloidal assembly pathways via low dimensional models. *J Chem Phys* **144**, 204904, doi:doi:http://dx.doi.org/10.1063/1.4951698 (2016).

73 Juárez, J. J. & Bevan, M. A. Feedback Controlled Colloidal Self-Assembly. *Advanced Functional Materials* **22**, 3833-3839, doi:10.1002/adfm.201200400 (2012).

74 Edwards, T. D., Yang, Y., Beltran-Villegas, D. J. & Bevan, M. A. Colloidal crystal grain boundary formation and motion. *Scientific Reports* **4**, 6132, doi:10.1038/srep06132

http://www.nature.com/articles/srep06132#supplementary-information (2014).

75 Palacci, J. *et al.* Light-activated self-propelled colloids. *Philosophical Transactions of the Royal Society of London A: Mathematical, Physical and Engineering Sciences* **372** (2014).

76 Puterman, M. L. *Markov Decision Processes: Discrete Stochastic Dynamic Programming*. (Wiley-Interscience, 2005).

77 Stengel, R. F. *Optimal Control and Estimation*. 639 (Dover Publications, 1994).

78 LaValle, S. M. *Planning algorithms*. (Cambridge university press, 2006).

79 Toyabe, S., Sagawa, T., Ueda, M., Muneyuki, E. & Sano, M. Experimental demonstration of information-to-energy conversion and validation of the generalized Jarzynski equality. *Nat Phys* **6**, 988-992, doi:10.1038/Nphys1821 (2010).

80 Howse, J. R. *et al.* Self-motile colloidal particles: From directed propulsion to random walk. *Physical Review Letters* **99**, doi:ARTN 048102

10.1103/PhysRevLett.99.048102 (2007).

81 *Random Walks, Brownian Motion, and Interacting Particle Systems: A Festschrift in Honor of Frank Spitzer* (Birkhäuser, 1991).

82 Redner, S. *A Guide to First-Passage Processes*. (Cambridge University Press, 2007).

83 Condamin, S., Benichou, O., Tejedor, V., Voituriez, R. & Klafter, J. First-passage times in complex scale-invariant media. *Nature* **450**, 77-80, doi:http://www.nature.com/nature/journal/v450/n7166/suppinfo/nature06201_S1.html (2007).

84 Bechinger, C. *et al.* Active Brownian particles in complex and crowded environments. *arXiv preprint arXiv:1602.00081* (2016).

85 Angelani, L., Di Leonardo, R. & Ruocco, G. Self-Starting Micromotors in a Bacterial Bath. *Physical Review Letters* **102**, 048104 (2009).

86 Takatori, S. C., Yan, W. & Brady, J. F. Swim Pressure: Stress Generation in Active Matter. *Physical Review Letters* **113**, 028103 (2014).

87 Bricard, A., Caussin, J.-B., Desreumaux, N., Dauchot, O. & Bartolo, D. Emergence of macroscopic directed motion in populations of motile colloids. *Nature* **503**, 95-98 (2013).

88 Yan, W. & Brady, J. F. The swim force as a body force. *Soft matter* **11**, 6235-6244 (2015).

89 Marchetti, M. *et al.* Hydrodynamics of soft active matter. *Reviews of Modern Physics* **85**, 1143 (2013).

90 Popkin, G. The physics of life. *Nature* **529**, 16-18 (2016).

91 Grier, D. G. A revolution in optical manipulation. *Nature* **424**, 810-816 (2003).

92 Yang, Y., Edwards, T. D. & Bevan, M. A. Modeling depletion mediated colloidal assembly on topographical patterns. *Journal of colloid and interface science* **449**, 270-278 (2015).

93 Papadimitriou, C. H. & Steiglitz, K. *Combinatorial Optimization: Algorithms and Complexity*. (Dover Publications, 2013).

94 Beckham, R. E. & Bevan, M. A. Interfacial colloidal sedimentation equilibrium. I. Intensity based confocal microscopy. *The Journal of Chemical Physics* **127**, -, doi:doi:http://dx.doi.org/10.1063/1.2794340 (2007).

95 Long, A. W., Wolfe, K. C., Mashner, M. J. & Chirikjian, G. S. The banana distribution is Gaussian: a localization study with exponential coordinates. *Robotics: Science and Systems VIII*, 265 (2013).

96 Sherman, Z. M. & Swan, J. W. Dynamic, directed self-assembly of nanoparticles via toggled interactions. *ACS nano* **10**, 5260-5271 (2016).

97 Arpin, K. A. *et al.* Multidimensional Architectures for Functional Optical Devices. *Adv. Mater.* **22**, 1084-1101, doi:10.1002/adma.200904096 (2010).

98 Hulliger, J. Chemistry and Crystal Growth. *Angewandte Chemie International Edition in English* **33**, 143-162, doi:10.1002/anie.199401431 (1994).

99 Hammadi, Z. & Veesler, S. New approaches on crystallization under electric fields. *Progress in Biophysics and Molecular Biology* **101**, 38-44, doi:http://dx.doi.org/10.1016/j.pbiomolbio.2009.12.005 (2009).

100 Zahn, K., Lenke, R. & Maret, G. Two-Stage Melting of Paramagnetic Colloidal Crystals in Two Dimensions. *Physical Review Letters* **82**, 2721-2724 (1999).

101 Pertsinidis, A. & Ling, X. S. Diffusion of point defects in two-dimensional colloidal crystals. *Nature* **413**, 147-150, doi:http://www.nature.com/nature/journal/v413/n6852/suppinfo/413147a0_S1.html (2001).

102 Skinner, T. O. E., Aarts, D. G. A. L. & Dullens, R. P. A. Grain-Boundary Fluctuations in Two-Dimensional Colloidal Crystals. *Physical Review Letters* **105**, 168301 (2010).

103 de Villeneuve, V. W. A. *et al.* Colloidal Hard-Sphere Crystal Growth Frustrated by Large Spherical Impurities. *Science* **309**, 1231-1233, doi:10.1126/science.1113207 (2005).

104 Nagamanasa, K. H., Gokhale, S., Ganapathy, R. & Sood, A. K. Confined glassy dynamics at grain boundaries in colloidal crystals. *Proceedings of the National Academy of Sciences* **108**, 11323-11326, doi:10.1073/pnas.1101858108 (2011).

105 Alsayed, A. M., Islam, M. F., Zhang, J., Collings, P. J. & Yodh, A. G. Premelting at Defects Within Bulk Colloidal Crystals. *Science* **309**, 1207-1210 (2005).

106 Gokhale, S., Nagamanasa, K. H., Ganapathy, R. & Sood, A. K. Grain growth and grain boundary dynamics in colloidal polycrystals. *Soft Matter* **9**, 6634-6644, doi:10.1039/c3sm50401h (2013).

107 Janssens, K. G. F. *et al.* Computing the mobility of grain boundaries. *Nat Mater* **5**, 124-127 (2006).

108 Thompson, C. V. Structure Evolution During Processing of Polycrystalline Films. *Annual Review of Materials Science* **30**, 159-190, doi:doi:10.1146/annurev.matsci.30.1.159 (2000).

109 Bragg, L. & Nye, J. F. A Dynamical Model of a Crystal Structure. *Proceedings of the Royal Society of London. Series A. Mathematical and Physical Sciences* **190**, 474-481, doi:10.1098/rspa.1947.0089 (1947).

110 Kurasch, S. *et al.* Atom-by-Atom Observation of Grain Boundary Migration in Graphene. *Nano Letters* **12**, 3168-3173, doi:10.1021/nl301141g (2012).

111 Juarez, J. J., Mathai, P. P., Liddle, J. A. & Bevan, M. A. Multiple electrokinetic actuators for feedback control of colloidal crystal size. *Lab on a Chip* **12**, 4063-4070, doi:10.1039/c2lc40692f (2012).

112 Edwards, T. D., Beltran-Villegas, D. J. & Bevan, M. A. Size dependent thermodynamics and kinetics in electric field mediated colloidal crystal assembly. *Soft Matter* **9**, 9208-9218, doi:10.1039/c3sm50809a (2013).

113 Juarez, J. J., Cui, J.-Q., Liu, B. G. & Bevan, M. A. kT-Scale Colloidal Interactions in High Frequency Inhomogeneous AC Electric Fields. I. Single Particles. *Langmuir* **27**, 9211-9218, doi:10.1021/la201478y (2011).

114 Juarez, J. J., Liu, B. G., Cui, J.-Q. & Bevan, M. A. kT-Scale Colloidal Interactions in High-Frequency Inhomogeneous AC Electric Fields. II. Concentrated Ensembles. *Langmuir* **27**, 9219-9226, doi:10.1021/la2014804 (2011).

115 Rohrdanz, M. A., Zheng, W. & Clementi, C. Discovering Mountain Passes via Torchlight: Methods for the Definition of Reaction Coordinates and Pathways in Complex Macromolecular Reactions. *Annual Review of Physical Chemistry* **64**, 295-316, doi:doi:10.1146/annurev-physchem-040412-110006 (2013).

116 Hummer, G. Position-dependent diffusion coefficients and free energies from Bayesian analysis of equilibrium and replica molecular dynamics simulations. *New J. Phys.* **7**, 34 (2005).

117 Nelson, D. R. & Halperin, B. I. Dislocation-mediated melting in two dimensions. *Phys. Rev. B*, 2457-2484, doi:10.1103/PhysRevB.19.2457 (1979).

118 Coifman, R. R., Kevrekidis, I. G., Lafon, S., Maggioni, M. & Nadler, B. Diffusion Maps, Reduction Coordinates, and Low Dimensional Representation of Stochastic Systems. *Multiscale Model. Simul.* **7**, 842-864, doi:10.1137/070696325 (2008).

119 Ferguson, A. L., Panagiotopoulos, A. Z., Debenedetti, P. G. & Kevrekidis, I. G. Systematic determination of order parameters for chain dynamics using diffusion maps. *PNAS* **107**, 13597-13602, doi:10.1073/pnas.1003293107 (2010).

120 Beltran-Villegas, D. J., Sehgal, R. M., Maroudas, D., Ford, D. M. & Bevan, M. A. Colloidal cluster crystallization dynamics. *J. Chem. Phys.* **137**, 134901, doi:10.1063/1.4754870 (2012).

121 Risken, H. *The Fokker-Planck Equation: Methods of Solution and Applications*. Second edn, Vol. 18 (Springer, 1996).

122 Beltran-Villegas, D. J., Sehgal, R. M., Maroudas, D., Ford, D. M. & Bevan, M. A. A Smoluchowski model of crystallization dynamics of small colloidal clusters. *J. Chem. Phys.* **135**, 154506, doi:10.1063/1.3652967 (2011).

123 Brady, J. F. The Long-Time Self-Diffusivity in Concentrated Colloidal Dispersions. *J. Fluid Mech.* **272**, 109-133 (1994).

124 Hanggi, P. & Talkner, P. Reaction-rate theory: fifty years after Kramers. *Rev. Mod. Phys.* **62**, 251-341 (1990).

125 Zwanzig, R. Diffusion in a rough potential. *Proceedings of the National Academy of Sciences* **85**, 2029-2030 (1988).

126 Zhang, H., Srolovitz, D. J., Douglas, J. F. & Warren, J. A. Characterization of atomic motion governing grain boundary migration. *Physical Review B* **74**, 115404 (2006).

127 Xue, Y., Beltran-Villegas, D. J., Tang, X., Bevan, M. A. & Grover, M. A. Optimal Design of a Colloidal Self-Assembly Process. *Control Systems Technology, IEEE Transactions on* **PP**, 1-1, doi:10.1109/tcst.2013.2296700 (2014).

128 Anekal, S. & Bevan, M. A. Interpretation of Conservative Forces from Stokesian Dynamic Simulations of Interfacial and Confined Colloids. *J. Chem. Phys.* **122**, 034903, doi:10.1063/1.1830012 (2005).

129 Anekal, S. & Bevan, M. A. Self Diffusion in Sub-Monolayer Colloidal Fluids Near a Wall. *J. Chem. Phys.* **125**, 034906, doi:10.1063/1.2211616 (2006).

130 Anekal, S. G., Bahukudumbi, P. & Bevan, M. A. Dynamic signature for the equilibrium percolation threshold of attractive colloidal fluids. *Physical Review E* **73**, 020403, doi:10.1103/PhysRevE.73.020403 (2006).

131 Beltran-Villegas, D. J., Sehgal, R. M., Maroudas, D., Ford, D. M. & Bevan, M. A. Fokker–Planck Analysis of Separation Dependent Potentials and Diffusion

Coefficients in Simulated Microscopy Experiments. *J. Chem. Phys.* **132**, 044707, doi:10.1063/1.3299731 (2010).

132 Wu, H.-J., Pangburn, T. O., Beckham, R. E. & Bevan, M. A. Measurement and Interpretation of Particle−Particle and Particle−Wall Interactions in Levitated Colloidal Ensembles. *Langmuir* **21**, 9879-9888, doi:10.1021/la050671g (2005).

133 Pangburn, T. O. & Bevan, M. A. Role of polydispersity in anomalous interactions in electrostatically levitated colloidal systems. *J. Chem. Phys.* **123**, 174904, doi:10.1063/1.2074887 (2005).

134 Pangburn, T. O. & Bevan, M. A. Anomalous potentials from inverse analyses of interfacial polydisperse attractive colloidal fluids. *J. Chem. Phys.* **124**, 054712, doi:10.1063/1.2162536 (2006).

135 ten Wolde, P. R., Ruiz-Montero, M. J. & Frenkel, D. Numerical calculation of the rate of crystal nucleation in a Lennard-Jones system at moderate undercooling. *J. Chem. Phys.* **104**, 9932 (1996).

136 Juarez, J. J. & Bevan, M. A. Interactions and microstructures in electric field mediated colloidal assembly. *J. Chem. Phys.* **131**, 134704, doi:10.1063/1.3241081 (2009).

137 Wu, H. J. & Bevan, M. A. Direct Measurement of Single and Ensemble Average Particle-Surface Potential Energy Profiles. *Langmuir* **21**, 1244-1254, doi:10.1021/la047892r (2005).

138 Juarez, J. J., Feicht, S. E. & Bevan, M. A. Electric field mediated assembly of three dimensional equilibrium colloidal crystals. *Soft Matter* **8**, 94-103, doi:10.1039/c1sm06414b (2012).

139 Ermak, D. L. & McCammon, J. A. Brownian dynamics with hydrodynamic interactions. *J. Chem. Phys.* **69**, 1352-1360 (1978).

140 Grassia, P. S., Hinch, E. J. & Nitsche, L. C. Computer-Simulations of Brownian-Motion of Complex-Systems. *Journal of Fluid Mechanics* **282**, 373-403, doi:10.1017/S0022112095000176 (1995).

141 Brady, J. F. & Bossis, G. Stokesian Dynamics. *Ann. Rev. Fluid Mech.* **20**, 111-157, doi:10.1146/annurev.fl.20.010188.000551 (1988).

142 Jeffrey, D. J. & Onishi, Y. Calculation of the Resistance and Mobility Functions for 2 Unequal Rigid Spheres in Low-Reynolds-Number Flow. *J. Fluid Mech.* **139**, 261-290 (1984).

143 Bossis, G., Meunier, A. & Sherwood, J. D. Stokesian Dynamics Simulations of Particle Trajectories near a Plane. *Physics of Fluids A-Fluid Dynamics* **3**, 1853-1858 (1991).

144 Swan, J. W. & Brady, J. F. Simulation of hydrodynamically interacting particles near a no-slip boundary. *Physics of Fluids (1994-present)* **19**, -, doi:doi:http://dx.doi.org/10.1063/1.2803837 (2007).

145 Brenner, H. The Slow Motion of a Sphere Through a Viscous Fluid Towards a Plane Surface. *Chem. Eng. Sci.* **16**, 242-251, doi:10.1016/0009-2509(61)80035-3 (1961).

146 Goldman, A. J., Cox, R. G. & Brenner, H. Slow Viscous Motion of a Sphere Parallel to a Plane Wall -- I. Motion Through a Quiescent fluid. *Chem. Engr. Sci.* **22**, 637-651, doi:10.1016/0009-2509(67)80047-2 (1967).

147 Pethig, Y. H. a. R. Electrode design for negative dielectrophoresis. *Measurement Science and Technology* **2**, 1142 (1991).

148 Gardiner, C. W. *Handbook of Stochastic Methods for Physics, Chemistry, and the Natural Sciences*. 2nd edn, (Springer, 2009).

149 Damasceno, P. F., Engel, M. & Glotzer, S. C. Crystalline Assemblies and Densest Packings of a Family of Truncated Tetrahedra and the Role of Directional Entropic Forces. *ACS Nano* **6**, 609-614, doi:10.1021/nn204012y (2011).

150 Edwards, T. D., Yang, Y., Beltran-Villegas, D. J. & Bevan, M. A. Colloidal crystal grain boundary formation and motion. *Sci. Rep.* **4**, doi:10.1038/srep06132 http://www.nature.com/srep/2014/140820/srep06132/abs/srep06132.html#supplementary-information (2014).

151 Best, R. B. & Hummer, G. Diffusive Model of Protein Folding Dynamics with Kramers Turnover in Rate. *Physical Review Letters* **96**, 228104 (2006).

152 Jolliffe, I. T. *Principal Component Analysis*. (Springer, 2002).

153 Ferguson, A. L., Panagiotopoulos, A. Z., Kevrekidis, I. G. & Debenedetti, P. G. Nonlinear dimensionality reduction in molecular simulation: The diffusion map

approach. *Chemical Physics Letters* **509**, 1-11, doi:http://dx.doi.org/10.1016/j.cplett.2011.04.066 (2011).

154 Coifman, R., Kevrekidis, I., Lafon, S., Maggioni, M. & Nadler, B. Diffusion Maps, Reduction Coordinates, and Low Dimensional Representation of Stochastic Systems. *Multiscale Modeling & Simulation* **7**, 842-864, doi:10.1137/070696325 (2008).

155 Beltran-Villegas, D. J., Sehgal, R. M., Maroudas, D., Ford, D. M. & Bevan, M. A. Fokker-Planck analysis of separation dependent potentials and diffusion coefficients in simulated microscopy experiments. *J Chem Phys* **132**, 044707, doi:10.1063/1.3299731 (2010).

156 Smoukov, S. K., Gangwal, S., Marquez, M. & Velev, O. D. Reconfigurable responsive structures assembled from magnetic Janus particles. *Soft Matter* **5**, 1285-1292, doi:10.1039/B814304H (2009).

157 Grzelczak, M., Vermant, J., Furst, E. M. & Liz-Marzán, L. M. Directed Self-Assembly of Nanoparticles. *ACS Nano* **4**, 3591-3605, doi:10.1021/nn100869j (2010).

158 Bahukudumbi, P. *et al.* Colloidal Microstructures, Transport, and Impedance Properties within Interfacial Microelectrodes. *Appl. Phys. Lett.* **90**, 224102, doi:10.1063/1.2744480 (2007).

159 Bell, G. M., Levine, S. & McCartney, L. N. Approximate methods of determining the double-layer free energy of interaction between two charged colloidal spheres. *Journal of colloid and interface science* **33**, 335-359, doi:http://dx.doi.org/10.1016/0021-9797(70)90228-6 (1970).

160 Jeffrey, D. J. & Onishi, Y. Calculation of the Resistance and Mobility Functions for two Unequal Rigid Spheres in Low-Reynolds-Number Flow. *J. Fluid Mech.* **139**, 261-290, doi:10.1017/S0022112084000355 (1984).

161 Swan, J. W. & Brady, J. F. Simulation of hydrodynamically interacting particles near a no-slip boundary. *Physics of Fluid* **19**, 113306, doi:10.1063/1.2803837 (2007).

162 Coifman, R. R., Shkolnisky, Y., Sigworth, F. J. & Singer, A. Graph Laplacian Tomography From Unknown Random Projections. *IEEE Transactions on Image Processing* **17**, 1891-1899, doi:10.1109/TIP.2008.2002305 (2008).

163 Ferguson, A. L., Panagiotopoulos, A. Z., Debenedetti, P. G. & Kevrekidis, I. G. Systematic determination of order parameters for chain dynamics using diffusion maps. *Proceedings of the National Academy of Sciences* **107**, 13597-13602, doi:10.1073/pnas.1003293107 (2010).

164 Halperin, B. I. & Nelson, D. R. Theory of two dimensional melting. *Physical Review Letters* **41**, 121-124 (1978).

165 Lau, A. W. C. & Lubensky, T. C. State-dependent diffusion: Thermodynamic consistency and its path integral formulation. *Physical Review E* **76**, 011123 (2007).

166 Trangenstein, J. A. *Numerical Solution of Hyperbolic Partial Differential Equations* (Cambridge University Press, 2009).

167 Baumgartl, J. & Bechinger, C. On the limits of digital video microscopy. *Europhys. Lett.* **71**, 487-493 (2005).

168 Beltran-Villegas, D. J., Edwards, T. D. & Bevan, M. A. Self-Consistent Colloidal Energy and Diffusivity Landscapes in Macromolecular Solutions. *Langmuir* **29**, 12337-12341, doi:10.1021/la403261m (2013).

169 Beltran-Villegas, D. J. & Bevan, M. A. Free energy landscapes for colloidal crystal assembly. *Soft Matter* **7**, 3280-3285, doi:10.1039/c0sm01526a (2011).

170 Laing, C. R., Frewen, T. A. & Kevrekidis, I. G. Coarse-grained dynamics of an activity bump in a neural field model. *Nonlinearity* **20**, 2127 (2007).

171 Peters, B. & Trout, B. L. Obtaining reaction coordinates by likelihood maximization. *J Chem Phys* **125**, 054108, doi:doi:http://dx.doi.org/10.1063/1.2234477 (2006).

172 Ma, A. & Dinner, A. R. Automatic Method for Identifying Reaction Coordinates in Complex Systems. *The Journal of Physical Chemistry B* **109**, 6769-6779, doi:10.1021/jp045546c (2005).

173 Ozbay, E. The Magical World of Photonic Metamaterials. *Opt. Photonics News* **19**, 22-27, doi:10.1364/OPN.19.11.000022 (2008).

174 Stebe, K. J., Lewandowski, E. & Ghosh, M. Oriented Assembly of Metamaterials. *Science* **325**, 159-160, doi:10.1126/science.1174401 (2009).

175 Engheta, N. 150 Years of Maxwell's Equations. *Science* **349**, 136-137, doi:10.1126/science.aaa7224 (2015).

176 Kalsin, A. M. *et al.* Electrostatic Self-Assembly of Binary Nanoparticle Crystals with a Diamond-Like Lattice. *Science* **312**, 420-424, doi:10.1126/science.1125124 (2006).

177 Henzie, J., Grünwald, M., Widmer-Cooper, A., Geissler, P. L. & Yang, P. Self-Assembly of Uniform Polyhedral Silver Nanocrystals into Densest Packings and Exotic Superlattices. *Nat. Mater.* **11**, 131-137, doi:http://www.nature.com/nmat/journal/v11/n2/abs/nmat3178.html#supplementary-information (2012).

178 Nykypanchuk, D., Maye, M. M., van der Lelie, D. & Gang, O. DNA-Guided Crystallization of Colloidal Nanoparticles. *Nature* **451**, 549-552, doi:http://www.nature.com/nature/journal/v451/n7178/suppinfo/nature06560_S1.html (2008).

179 Shevchenko, E. V., Talapin, D. V., Kotov, N. A., O'Brien, S. & Murray, C. B. Structural Diversity in Binary Nanoparticle Superlattices. *Nature* **439**, 55-59, doi:http://www.nature.com/nature/journal/v439/n7072/suppinfo/nature04414_S1.html (2006).

180 Macfarlane, R. J. *et al.* Nanoparticle Superlattice Engineering with DNA. *Science* **334**, 204-208, doi:10.1126/science.1210493 (2011).

181 Cheng, Z., Russel, W. B. & Chaikin, P. M. Controlled Growth of Hard-Sphere Colloidal Crystals. *Nature* **401**, 893-895 (1999).

182 Biancaniello, P. L., Kim, A. J. & Crocker, J. C. Colloidal Interactions and Self Assembly Using DNA Hybridization. *Phys. Rev. Lett.* **94**, 058302 (2005).

183 Yan, J., Bloom, M., Bae, S. C., Luijten, E. & Granick, S. Linking Synchronization to Self-Assembly Using Magnetic Janus Colloids. *Nature* **491**, 578-581, doi:10.1038/nature11619 (2012).

184 Koenig, G. M., Lin, I.-H. & Abbott, N. L. Chemoresponsive Assemblies of Microparticles at Liquid Crystalline Interfaces. *Proc. Natl. Acad. Sci. U. S. A.* **107**, 3998-4003, doi:10.1073/pnas.0910931107 (2010).

185 Soyka, F., Zvyagolskaya, O., Hertlein, C., Helden, L. & Bechinger, C. Critical Casimir Forces in Colloidal Suspensions on Chemically Patterned Surfaces. *Phys. Rev. Lett.* **101**, 208301 (2008).

186 Swan, J. W. *et al.* Multi-Scale Kinetics of a Field-Directed Colloidal Phase Transition. *Proc. Natl. Acad. Sci. U. S. A.* **109**, 16023-16028, doi:10.1073/pnas.1206915109 (2012).

187 Kim, Y., Shah, A. A. & Solomon, M. J. Spatially and Temporally Reconfigurable Assembly of Colloidal Crystals. *Nat. Commun.* **5**, 4676, doi:10.1038/ncomms4676 (2014).

188 Armani, M. D., Chaudhary, S. V., Probst, R. & Shapiro, B. Using Feedback Control of Microflows to Independently Steer Multiple Particles. *J. Microelectromech. Syst.* **15**, 945-956, doi:10.1109/jmems.2006.878863 (2006).

189 Vezirov, T. A., Gerloff, S. & Klapp, S. H. L. Manipulating Shear-Induced Non-Equilibrium Transitions in Colloidal Films by Feedback Control. *Soft Matter* **11**, 406-413, doi:10.1039/C4SM01414F (2015).

190 Solis, E. O. P., Barton, P. I. & Stephanopoulos, G. Controlled Formation of Nanostructures with Desired Geometries. 2. Robust Dynamic Paths. *Ind. Eng. Chem. Res.* **49**, 7746-7757, doi:10.1021/ie1000778 (2010).

191 Klotsa, D. & Jack, R. L. Controlling Crystal Self-Assembly Using a Real-Time Feedback Scheme. *J. Chem. Phys.* **138**, 094502, doi:10.1063/1.4793527 (2013).

192 Branduardi, D., Gervasio, F. L. & Parrinello, M. From A to B in Free Energy Space. *J. Chem. Phys.* **126**, 054103 (2007).

193 Gast, A. P. & Russel, W. B. Simple Ordering in Complex Fluids - Colloidal Particles Suspended in Solution Provide Intriguing Models for Studying Phase Transitions. *Phys. Today* **51**, 24-30 (1998).

194 Anderson, V. J. & Lekkerkerker, H. N. W. Insights into phase transition kinetics from colloid science. *Nature* **416**, 811-815 (2002).

195 Poon, W. Colloids as Big Atoms. *Science* **304**, 830-831, doi:10.1126/science.1097964 (2004).

196 Pusey, P. N. & van Megen, W. Phase Behaviour of Concentrated Suspensions of Nearly Hard Colloidal Spheres. *Nature* **320**, 340-342 (1986).

197 Gasser, U., Weeks, E. R., Schofield, A., Pusey, P. N. & Weitz, D. A. Real-Space Imaging of Nucleation and Growth in Colloidal Crystallization. *Science* **292**, 258-262 (2001).

198 Schall, P., Cohen, I., Weitz, D. A. & Spaepen, F. Visualization of Dislocation Dynamics in Colloidal Crystals. *Science* **305**, 1944-1948, doi:10.1126/science.1102186 (2004).

199 Ackerson, B. J. & Clark, N. A. Shear-Induced Partial Tranlational Ordering of a Colloidal Solid. *Phys. Rev. A* **30**, 906-918 (1984).

200 Lumsdon, S. O., Kaler, E. W. & Velev, O. D. Two-Dimensional Crystallization of Microspheres by a Coplanar AC Electric Field. *Langmuir* **20**, 2108-2116, doi:10.1021/la035812y (2004).

201 Goldenberg, L. M., Wagner, J., Stumpe, J., Paulke, B.-R. & Görnitz, E. Simple Method for the Preparation of Colloidal Particle Monolayers at the Water/Alkane Interface. *Langmuir* **18**, 5627-5629, doi:10.1021/la025745s (2002).

202 Schermelleh, L., Heintzmann, R. & Leonhardt, H. A Guide to Super-Resolution Fluorescence Microscopy. *J. Cell Biol.* **190**, 165-175, doi:10.1083/jcb.201002018 (2010).

203 Leung, B. O. & Chou, K. C. Review of Super-Resolution Fluorescence Microscopy for Biology. *Appl. Spectrosc.* **65**, 967-980, doi:10.1366/11-06398 (2011).

204 Chen, Q. *et al.* 3D Motion of DNA-Au Nanoconjugates in Graphene Liquid Cell Electron Microscopy. *Nano Lett.* **13**, 4556-4561, doi:10.1021/nl402694n (2013).

205 Zheludev, N. I. & Kivshar, Y. S. From Metamaterials to Metadevices. *Nat. Mater.* **11**, 917-924 (2012).

206 Bowman, G., Pande, V. S. & Noe, F. *An Introduction to Markov State Models and Their Application to Long Timescale Molecular Simulation*. (Springer, 2014).

207 Marco, S., Frank, N. & Christof, S. On the Approximation Quality of Markov State Models. *Multiscale Model Simul.* **8**, 1154-1177, doi:10.1137/090764049 (2010).

208 Prinz, J.-H. *et al.* Markov Models of Molecular Kinetics: Generation and Validation. *J. Chem. Phys.* **134**, 174105, doi:10.1063/1.3565032 (2011).

209 Pande, V. S., Beauchanp, K. & Bowman, G. R. Everything you wanted to know about Markov State Models but were afraid to ask. *Methods* **52**, 99-105, doi:10.1016/j.ymeth.2010.06.002 (2010).

210 Chang, H., Fu, M., Hu, J. & Marcu, S. *Simulation-Based Algorithms for Markov Decision Processes*. (Springer-Verlag, 2006).

211 Bertsekas, D. P. *Dynamic Programming and Optimal Control*. 3rd edition edn, (Athena Scientific, 2012).

212 Chadès, I., Cros, M., Garcia, F. & Sabbadin, R. *Markov decision processes (MDP) toolbox*, 2009).

213 Adriani, P. M. & Gast, A. P. A Microscopic Model of Electrorheology. *Phys. Fluids* **31**, 2757-2768, doi:10.1063/1.866983 (1988).

214 Edwards, T. D., Yang, Y., Beltran-Villegas, D. J. & Bevan, M. A. Colloidal Crystal Grain Boundary Formation and Motion. *Sci. Rep.* **4**, 06132, doi:10.1038/srep06132 (2014).

215 Puterman, M. L. *Markov Decision Processes: Discrete Stochastic Dynamic Programming*. (John Wiley & Sons, 2014).

216 Zhang, H., Srolovitz, D. J., Douglas, J. F. & Warren, J. A. Characterization of Atomic Motion Governing Grain Boundary Migration. *Phys. Rev. B* **74**, 115404, doi:10.1103/PhysRevB.74.115404 (2006).

217 Skinner, T. O. E., Aarts, D. G. A. L. & Dullens, R. P. A. Grain-Boundary Fluctuations in Two-Dimensional Colloidal Crystals. *Phys. Rev. Lett.* **105**, 168301, doi:10.1103/PhysRevLett.105.168301 (2010).

218 Yuste, S. B. & Santos, A. A Heuristic Radial-Distribution Function for Hard Disks. *J. Chem. Phys.* **99**, 2020-2023 (1993).

219 Nagamanasa, K. H., Gokhale, S., Ganapathy, R. & Sood, A. K. Confined Glassy Dynamics at Grain Boundaries in Colloidal Crystals. *Proc. Natl. Acad. Sci. U. S. A.* **108**, 11323-11326, doi:10.1073/pnas.1101858108 (2011).

220 Zhang, H., Srolovitz, D. J., Douglas, J. F. & Warren, J. A. Grain Boundaries Exhibit the Dynamics of Glass-Forming Liquids. *Proc. Natl. Acad. Sci. U. S. A.* **106**, 7735-7740, doi:10.1073/pnas.0900227106 (2009).

221 Du, D., Li, D., Thakur, M. & Biswal, S. L. Generating an *in situ* Tunable Interaction Potential for Probing 2-D Colloidal Phase Behavior. *Soft Matter* **9**, 6867-6875, doi:10.1039/c3sm27620a (2013).

222 Ferraro, M. E., Bonnecaze, R. T. & Truskett, T. M. Graphoepitaxy for Pattern Multiplication of Nanoparticle Monolayers. *Phys. Rev. Lett* **113**, 085503 (2014).

223 Edwards, T. D., Yang, Y., Everett, W. N. & Bevan, M. A. Reconfigurable Multi-Scale Colloidal Assembly on Excluded Volume Patterns. *Sci. Rep.* **5**, 13612, doi:10.1038/srep13612

http://www.nature.com/articles/srep13612#supplementary-information (2015).

224 Beckham, R. E. & Bevan, M. A. Interfacial Colloidal Sedimentation Equilibrium I. Intensity Based Confocal Microscopy. *J. Chem. Phys.* **127**, 164708, doi:10.1063/1.2794340 (2007).

225 Beltran-Villegas, D. J., Schultz, B. A., Nguyen, N. H. P., Glotzer, S. C. & Larson, R. G. Phase behavior of Janus colloids determined by sedimentation equilibrium. *Soft Matter* **10**, 4593-4602, doi:10.1039/C3SM53136H (2014).

226 Liberek, K., Lewandowska, A. & Ziętkiewicz, S. Chaperones in Control of Protein Disaggregation. *EMBO J.* **27**, 328-335, doi:10.1038/sj.emboj.7601970 (2008).

227 Anekal, S. G., Bahukudumbi, P. & Bevan, M. A. Dynamic signature for the equilibrium percolation threshold of attractive colloidal fluids. *Phys. Rev. E* **73**, 020403, doi:10.1103/PhysRevE.73.020403 (2006).

228 Huang, Y. & Pethig, R. Electrode design for negative dielectrophoresis. *Meas. Sci. Technol.* **2**, 1142-1146, doi:10.1088/0957-0233/2/12/005 (1991).

229 Prinz, J.-H. *et al.* Markov models of molecular kinetics: Generation and validation. *The Journal of Chemical Physics* **134**, 174105, doi:10.1063/1.3565032 (2011).

230 Whitesides, G. M. & Grzybowski, B. Self-Assembly at All Scales. *Science* **295**, 2418-2421, doi:10.1126/science.1070821 (2002).

231 Whitesides, G. M. & Boncheva, M. Beyond molecules: Self-assembly of mesoscopic and macroscopic components. *Proceedings of the National Academy of Sciences* **99**, 4769-4774, doi:10.1073/pnas.082065899 (2002).

232 Arpin, K. A. *et al.* Multidimensional Architectures for Functional Optical Devices. *Advanced Materials* **22**, 1084-1101, doi:10.1002/adma.200904096 (2010).

233 Davis, K. E., Russel, W. B. & Glantschnig, W. J. Disorder-to-Order Transition in Settling Suspensions of Colloidal Silica: X-ray Measurements. *Science* **245**, 507-510, doi:10.2307/1704081 (1989).

234 Davis, K. E., Russel, W. B. & Glantschnig, W. J. Settling suspensions of colloidal silica: observations and X-ray measurements. *Journal of the Chemical Society, Faraday Transactions* **87**, 411-424, doi:10.1039/ft9918700411 (1991).

235 Woodcock, L. V. Reply: Entropy difference between crystal phases. *Nature* **388**, 236-236 (1997).

236 van Blaaderen, A., Ruel, R. & Wiltzius, P. Template-directed colloidal crystallization. *Nature* **385**, 321-324 (1997).

237 Fernandes, G. E., Beltran-Villegas, D. J. & Bevan, M. A. Spatially controlled reversible colloidal self-assembly. *The Journal of Chemical Physics* **131**, -, doi:doi:http://dx.doi.org/10.1063/1.3243686 (2009).

238 Biancaniello, P. L., Kim, A. J. & Crocker, J. C. Colloidal Interactions and Self-Assembly Using DNA Hybridization. *Physical Review Letters* **94**, 058302 (2005).

239 Juárez, J. J. & Bevan, M. A. Interactions and microstructures in electric field mediated colloidal assembly. *The Journal of Chemical Physics* **131**, -, doi:doi:http://dx.doi.org/10.1063/1.3241081 (2009).

240 Yang, Y., Gao, L., Lopez, G. P. & Yellen, B. B. Tunable Assembly of Colloidal Crystal Alloys Using Magnetic Nanoparticle Fluids. *ACS Nano* **7**, 2705-2716, doi:10.1021/nn400118e (2013).

241 Russel, W. B., Saville, D. & Schowalter, W. R. *Colloidal Dispersions*. (Cambridge University Press, 1992).

242 Gast, A. P., Hall, C. K. & Russel, W. B. Phase separations induced in aqueous colloidal suspensions by dissolved polymer. *Faraday Discussions of the Chemical Society* **76**, 189-201, doi:10.1039/dc9837600189 (1983).

243 Zahn, K. & Maret, G. Dynamic Criteria for Melting in Two Dimensions. *Physical Review Letters* **85**, 3656-3659 (2000).

244 Löwen, H., Palberg, T. & Simon, R. Dynamical criterion for freezing of colloidal liquids. *Physical Review Letters* **70**, 1557-1560 (1993).

245 Jack, R. L., Hagan, M. F. & Chandler, D. Fluctuation-dissipation ratios in the dynamics of self-assembly. *Physical Review E* **76**, 021119 (2007).

246 Klotsa, D. & Jack, R. L. Predicting the self-assembly of a model colloidal crystal. *Soft Matter* **7**, 6294-6303, doi:10.1039/c1sm05456b (2011).

247 Royall, C. P., Dzubiella, J., Schmidt, M. & van Blaaderen, A. Nonequilibrium Sedimentation of Colloids on the Particle Scale. *Physical Review Letters* **98**, 188304 (2007).

248 Beltran-Villegas, D. J., Sehgal, R. M., Maroudas, D., Ford, D. M. & Bevan, M. A. Colloidal cluster crystallization dynamics. *The Journal of Chemical Physics* **137**, - , doi:doi:http://dx.doi.org/10.1063/1.4754870 (2012).

249 Asakura, S. & Oosawa, F. On Interaction between 2 Bodies Immersed in a Solution of Macromolecules. *J. Chem. Phys.* **22**, 1255-1256 (1954).

250 Lekkerkerker, H. N. W. & Tuinier, R. *Colloids and the Depletion Interaction*. (Springer, 2011).

251 Marenduzzo, D., Finan, K. & Cook, P. R. The depletion attraction: an underappreciated force driving cellular organization. *J. Cell Bio.* **175**, 681-686, doi:10.1083/jcb.200609066 (2006).

252 Trokhymchuk, A., Henderson, D., Nikolov, A. & Wasan, D. T. Depletion and Structural Forces between Two Macrosurfaces Immersed in a Bidisperse Colloidal Suspension. *Journal of Colloid and Interface Science* **243**, 116-127, doi:http://dx.doi.org/10.1006/jcis.2001.7853 (2001).

253 Nikolov, A. D. & Wasan, D. T. Ordered micelle structuring in thin films formed from anionic surfactant solutions: I. Experimental. *Journal of Colloid and Interface Science* **133**, 1-12 (1989).

254 Badaire, S. p., Cottin-Bizonne, C. c. & Stroock, A. D. Experimental Investigation of Selective Colloidal Interactions Controlled by Shape, Surface Roughness, and Steric Layers. *Langmuir* **24**, 11451-11463, doi:doi:10.1021/la801718j (2008).

255 Zhao, K. & Mason, T. G. Suppressing and Enhancing Depletion Attractions between Surfaces Roughened by Asperities. *Phys. Rev. Lett.* **101**, 148301 (2008).

256 Edwards, T. D., Yang, Y. & Bevan, M. A. Reconfigurable Multi-Scale Colloidal Assembly on Excluded Volume Patterns. *in preparation* (2014).

257 Vrij, A. Polymers at Interfaces and the Interactions in Colloidal Dispersions. *Pure and Appl. Chem.* **48**, 471-483 (1976).

258 Bahukudumbi, P. & Bevan, M. A. Imaging Energy Landscapes using Concentrated Diffusing Colloidal Probes. *J. Chem. Phys.* **126**, 244702, doi:10.1063/1.2739548 (2007).

259 Iracki, T. D., Beltran-Villegas, D. J., Eichmann, S. L. & Bevan, M. A. Charged Micelle Depletion Attraction and Interfacial Colloidal Phase Behavior. *Langmuir* **26**, 18710–18717, doi:10.1021/la103701k (2010).

260 Edwards, T. D. & Bevan, M. A. Polymer Mediated Depletion Attraction and Interfacial Colloidal Phase Behavior. *Macromolecules* **45**, 585-594, doi:10.1021/ma202279x (2012).

261 Einstein, A. *Investigations on the Theory of the Brownian Movement*. (Courier Corporation, 1956).

262 Tsyboulski, D. A., Bachilo, S. M., Kolomeisky, A. B. & Weisman, R. B. Translational and Rotational Dynamics of Individual Single-Walled Carbon Nanotubes in Aqueous Suspension. *ACS Nano* **2**, 1770-1776, doi:10.1021/nn800364r (2008).

263 Hore, M. J. A. & Composto, R. J. Nanorod Self-Assembly for Tuning Optical Absorption. *ACS Nano* **4**, 6941-6949, doi:10.1021/nn101725j (2010).

264 Anderson, V. J. & Lekkerkerker, H. N. W. Insights into phase transition kinetics from colloid science. *Nature* **416**, 811-815 (2002).

265 Han, Y. *et al.* Brownian Motion of an Ellipsoid. *Science* **314**, 626-630, doi:10.1126/science.1130146 (2006).

266 Mukhija, D. & Solomon, M. J. Translational and rotational dynamics of colloidal rods by direct visualization with confocal microscopy. *Journal of colloid and interface science* **314**, 98-106, doi:10.1016/j.jcis.2007.05.055 (2007).

267 Solomon, M. J. & Spicer, P. T. Microstructural regimes of colloidal rod suspensions, gels, and glasses. *Soft Matter* **6**, 1391-1400, doi:10.1039/b918281k (2010).

268 Rotunno, M., Bellini, T., Lansac, Y. & Glaser, M. A. Phase behavior of polarizable spherocylinders in external fields. *J Chem Phys* **121**, 5541-5549, doi:doi:http://dx.doi.org/10.1063/1.1782411 (2004).

269 Donev, A. *et al.* Improving the Density of Jammed Disordered Packings Using Ellipsoids. *Science* **303**, 990-993, doi:10.1126/science.1093010 (2004).

270 Chaudhary, K., Juarez, J. J., Chen, Q., Granick, S. & Lewis, J. A. Reconfigurable assemblies of Janus rods in AC electric fields. *Soft Matter* **10**, 1320-1324, doi:10.1039/c3sm52418c (2014).

271 Broersma, S. Rotational Diffusion Constant of a Cylindrical Particle. *J Chem Phys* **32**, 1626-1631, doi:doi:http://dx.doi.org/10.1063/1.1730994 (1960).

272 Broersma, S. Viscous Force Constant for a Closed Cylinder. *J Chem Phys* **32**, 1632-1635, doi:doi:http://dx.doi.org/10.1063/1.1730995 (1960).

273 Batchelor, G. K. Slender-body theory for particles of arbitrary cross-section in Stokes flow. *Journal of Fluid Mechanics* **44**, 419-440 (1970).

274 Tirado, M. M., Martínez, C. L. & de la Torre, J. G. Comparison of theories for the translational and rotational diffusion coefficients of rod-like macromolecules. Application to short DNA fragments. *J Chem Phys* **81**, 2047-2052, doi:doi:http://dx.doi.org/10.1063/1.447827 (1984).

275 Aragon, S. R. & Flamik, D. High Precision Transport Properties of Cylinders by the Boundary Element Method. *Macromolecules* **42**, 6290-6299, doi:10.1021/ma900453c (2009).

276 Mansfield, M. L. & Douglas, J. F. Transport Properties of Rodlike Particles. *Macromolecules* **41**, 5422-5432, doi:10.1021/ma702839w (2008).

277 Gralinski, I., Neild, A., Ng, T. W. & Muradoglu, M. S. Sorting of Brownian rods by the use of an asymmetric potential. *J Chem Phys* **134**, -, doi:doi:http://dx.doi.org/10.1063/1.3537738 (2011).

278 Mestre, N. J. & Russel, W. B. Low-Reynolds-number translation of a slender cylinder near a plane wall. *J Eng Math* **9**, 81-91, doi:10.1007/bf01535390 (1975).

279 http://ryuon.sourceforge.net/twobody/errata.html.

280 Phillips, R. J., Brady, J. F. & Bossis, G. Hydrodynamic transport properties of hard-sphere dispersions. I. Suspensions of freely mobile particles. *Physics of Fluids (1958-1988)* **31**, 3462-3472, doi:doi:http://dx.doi.org/10.1063/1.866914 (1988).

281 Durlofsky, L., Brady, J. F. & Bossis, G. Dynamic Simulation of Hydrodynamically Interacting Particles. *Journal of Fluid Mechanics* **180**, 21-49, doi:Doi 10.1017/S002211208700171x (1987).

282 Hinch, E. J. Brownian motion with stiff bonds and rigid constraints. *Journal of Fluid Mechanics* **271**, 219-234, doi:doi:10.1017/S0022112094001746 (1994).

283 Löwen, H. Brownian dynamics of hard spherocylinders. *Physical Review E* **50**, 1232-1242, doi:10.1103/PhysRevE.50.1232 (1994).

284 Malevanets, A. & Kapral, R. Mesoscopic model for solvent dynamics. *J Chem Phys* **110**, 8605-8613, doi:doi:http://dx.doi.org/10.1063/1.478857 (1999).

285 De Corato, M., Greco, F., D'Avino, G. & Maffettone, P. Hydrodynamics and Brownian motions of a spheroid near a rigid wall. *J Chem Phys* **142**, 194901 (2015).

286 Swan, J. W. & Brady, J. F. Simulation of hydrodynamically interacting particles near a no-slip boundary. *Physics of Fluids* **19**, 113306, doi:10.1063/1.2803837 (2007).

287 Anekal, S. G. & Bevan, M. A. Interpretation of conservative forces from Stokesian dynamic simulations of interfacial and confined colloids. *J Chem Phys* **122**, -, doi:doi:http://dx.doi.org/10.1063/1.1830012 (2005).

288 Montesi, A., Morse, D. C. & Pasquali, M. Brownian dynamics algorithm for bead-rod semiflexible chain with anisotropic friction. *J Chem Phys* **122**, -, doi:doi:http://dx.doi.org/10.1063/1.1848511 (2005).

289 Doi, M. & Edwards, S. F. *The Theory of Polymer Dynamics*. (Oxford University Press, 1990).

290 Tirado, M. M., Martínez, C. L. p. & de la Torre, J. G. a. Comparison of theories for the translational and rotational diffusion coefficients of rod-like macromolecules. Application to short DNA fragments. *J Chem Phys* **81**, 2047, doi:10.1063/1.447827 (1984).

291 Lele, P. P., Swan, J. W., Brady, J. F., Wagner, N. J. & Furst, E. M. Colloidal diffusion and hydrodynamic screening near boundaries. *Soft Matter* **7**, 6844-6852, doi:10.1039/c0sm01466d (2011).

292 Goldman, A. J., Cox, R. G. & Brenner, H. Slow viscous motion of a sphere parallel to a plane wall—I Motion through a quiescent fluid. *Chemical*

Engineering Science **22**, 637-651, doi:http://dx.doi.org/10.1016/0009-2509(67)80047-2 (1967).

293 Sendner, C. & Netz, R. R. Hydrodynamic lift of a moving nano-rod at a wall. *EPL (Europhysics Letters)* **79**, 58004 (2007).

294 Sundararajan, S., Lammert, P. E., Zudans, A. W., Crespi, V. H. & Sen, A. Catalytic Motors for Transport of Colloidal Cargo. *Nano Letters* **8**, 1271-1276, doi:10.1021/nl072275j (2008).

295 Happel, J. & Brenner, H. *Low Reynolds number hydrodynamics: with special applications to particulate media*. (Springer, 1983).

296 Jeffrey, D. J. & Onishi, Y. Calculation of the resistance and mobility functions for two unequal rigid spheres in low-Reynolds-number flow. *Journal of Fluid Mechanics* **139**, 261-290, doi:doi:10.1017/S0022112084000355 (1984).

297 Dunstan, J., Miño, G., Clement, E. & Soto, R. A two-sphere model for bacteria swimming near solid surfaces. *Physics of Fluids (1994-present)* **24**, -, doi:doi:http://dx.doi.org/10.1063/1.3676245 (2012).

298 Batchelor, G. K. Brownian diffusion of particles with hydrodynamic interaction. *Journal of Fluid Mechanics* **74**, 1-29, doi:doi:10.1017/S0022112076001663 (1976).

299 Tirado, M. M. & de la Torre, J. G. Translational friction coefficients of rigid, symmetric top macromolecules. Application to circular cylinders. *J Chem Phys* **71**, 2581-2587, doi:doi:http://dx.doi.org/10.1063/1.438613 (1979).

300 Tirado, M. M. & de la Torre, J. G. Rotational dynamics of rigid, symmetric top macromolecules. Application to circular cylinders. *J Chem Phys* **73**, 1986-1993, doi:doi:http://dx.doi.org/10.1063/1.440288 (1980).

301 JEFFREY, D. J. & ONISHI, Y. THE SLOW MOTION OF A CYLINDER NEXT TO A PLANE WALL. *The Quarterly Journal of Mechanics and Applied Mathematics* **34**, 129-137, doi:10.1093/qjmam/34.2.129 (1981).

302 Hunt, A. J., Gittes, F. & Howard, J. The force exerted by a single kinesin molecule against a viscous load. *Biophysical Journal* **67**, 766-781, doi:http://dx.doi.org/10.1016/S0006-3495(94)80537-5 (1994).

303 Cox, R. G. & Brenner, H. Effect of finite boundaries on the Stokes resistance of an arbitrary particle Part 3. Translation and rotation. *Journal of Fluid Mechanics* **28**, 391-411, doi:doi:10.1017/S0022112067002150 (1967).

304 Sutton, R. S. & Barto, A. G. *Reinforcement learning: An introduction*. Vol. 1 (MIT press Cambridge, 1998).

15 CURRICULUM VITAE

Name: Yuguang Yang

Birth: Oct 09, 1988, Guilin, China

Address: Yuguang Yang may be contacted through Dr. M.A. Bevan at the
Chemical and Biomolecular Engineering Department, Johns
Hopkins University, Baltimore, MD 21218

Email Address: yangyutu123@gmail.com

Education: B.E., Polymer Engineering, Zhejiang University, China, 2011